Next-Generation Organic Blend Semiconductors for High Performance Solution-Processable Field Effect Transistors

by

Alexandra Frances Paterson

A thesis submitted in partial fulfilment of the degree of

Doctor of Philosophy

Department of Physics

Imperial College London

January 2017

Declaration

This thesis outlines the work carried out between October 2013 and December 2016 in the Experimental Solid State Physics group at Imperial College London under the supervision of Professor Thomas D. Anthopoulos and funded by Cambridge Display Technology. Unless otherwise stated, the material in this thesis is my own work. The work outlined in this thesis has not been submitted prior to this for any other degree at any other university.

The copyright of this thesis rests with the author and is made available under a Creative Commons Attribution Non-Commercial No Derivatives licence. Researchers are free to copy, distribute or transmit the thesis on the condition that they attribute it, that they do not use it for commercial purposes and that they do not alter, transform or build upon it. For any reuse or redistribution, researchers must make clear to others the licence terms of this work

Alexandra F. Paterson

January 2017

Abstract

Ambitions for transparent, lightweight, flexible and inexpensive electronic technologies that can be printed over large area substrates have driven substantial advances in the field of organic/printed electronics in recent years. Amongst the various technologies investigated, solution-processed, organic thin-film transistors (OTFTs) have received extraordinary attention, primarily due to the enormous potential for simple, cost-effective manufacturing. Two exciting research areas relevant to OTFT development that offer tremendous potential are those of the small-molecule/polymer organic semiconducting blends and the science and engineering of molecular doping. However, the lack of organic semiconducting blends that surpass the benchmark charge carrier mobility of 10 cm^2/Vs, and the numerous challenges associated with the practical utilisation of molecular doping, have prevented adaptation of OTFTs as a viable technology for application in the emerging sector of plastic electronics.

The work in this thesis focuses on an organic semiconducting system for OTFTs that addresses these two points. The first part of this thesis describes the development of advanced organic semiconducting blends, the so-called 3rd generation (3G) blend systems. Specifically, a new blend based on the small-molecule C_8-BTBT and the conjugated polymer C_{16}DT-BT is introduced. A third component, the molecular *p*-dopant, $C_{60}F_{48}$, is then added to the blend system and it is found to have remarkably positive effects on OTFT performance. The ternary blend system is then combined with a solvent-mixing approach, resulting in devices with an exceptional hole mobility value exceeding 13 cm^2/Vs. Through the use of complementary characterisation techniques, it is shown that key to this achievement is the unusual three-component material distribution, hinting at the existence of an unconventional doping mechanism. Furthermore, by considering alternative processing techniques, the maximum mobility of the resulting OTFTs is improved further to a value in excess of 23 cm^2/Vs.

The second part of the thesis focuses on the impact of *p*-doping in the ternary C_8-BTBT:C_{16}IDT-BT:$C_{60}F_{48}$ blend on other important operating characteristics of the OTFTs. The intentional and simple to implement doping process is shown to improve key device parameters such as bias-stress stability, parasitic contact resistance, threshold voltage and the overall device-to-device parameter variation (i.e. narrowing of the parameter spread). Importantly, the inclusion of the dopant is not found to adversely affect the nature of the C_8-BTBT crystal packing at the OTFT channel.

The final part of this thesis describes the incorporation of 3G blend-based OTFTs into fully functional logic electronic circuits. Hybrid inverter circuits (i.e. NOT gates) are fabricated at low temperatures from solution-phase by combining the high hole mobility C_8-BTBT:C_{16}IDT-BT:$C_{60}F_{48}$ blend OTFTs as the *p*-channel device and a novel In_2O_3/ZnO heterojunction metal oxide semiconducting system as the *n*-channel transistor. The resulting complementary inverters exhibit excellent signal gain and high noise margins, making this hybrid circuitry a promising contender for application in the emerging field of printed microelectronics.

Acknowledgement

First and foremost, I would like to thank my PhD supervisor Professor Thomas D. Anthopoulos for the opportunity to do a PhD in his research group; I have learnt even more than I'd hoped for during this process and I am grateful for his fantastic ideas, advice, patience and contagious enthusiasm. I would also like to thank Cambridge Display Technology for funding my PhD, and in particular thank Dr Daniel Tobjork for all of his correspondence. I am also very grateful to Professor Martin Heeney, Dr Zhuping Fei, Dr Olga Solomeshch and Professor Nir Tessler, as the work in this thesis would not have been possible without their skilfully crafted materials.

I have had a wonderfully enjoyable and intellectually stimulating time at Imperial College London thanks to everyone in the Advanced Materials and Devices group. I would particularly like to thank Dr Master Yen-Hung Lin and Dr Hendrik Faber for their time, knowledgeable guidance and patience, and Nilushi Wijeyasinghe and Gwenhivir Wyatt-Moon for being with me on this journey.

I would like to extend my thanks to all of my collaborators, particularly Dr Ivan Isakov for the work we did together on hybrid inverters, and Muhammad R. Niazi and Professor Aram Amassian at King Abdullah University Saudi Arabia for the various measurements and the work we did during my visit in December 2015. I would also like to express my thanks to Carolyn Dale and Juraci Didone, who are at the heart of the EXSS group and have helped me greatly over the years.

I would like to thank my grandfather, Dr Gerard F. Hayes, for the discussions about polymer chemistry and solvents. Also my best friend, Dr Simon Tapster, for the late night scientific conversations.

I am very grateful for the consistent and essential support network that I have from my parents and my siblings. As always, each of them have supported me throughout this process in different ways, including carefully proof reading this thesis, helping to format this thesis, conference pep-talks, listening to my presentations and buying the London-priced drinks.

Last but by no means least, I would like to express my deepest thanks to my partner, Scott Shaw, for the Origin programming, the many late nights that he picked me up from the train station after I'd finished in the lab, listening, his enduring patience and support during this process, and his extraordinarily stimulating belief in me.

Table of Contents

List of Figures ix

List of Tables xi

Chapter 1 Introduction 1

1.1 Fundamental building block: The field-effect transistor 2

1.2 Plastic (organic) electronics: Introduction and motivations 5

1.3 Motivation: Organic field-effect transistors 7

1.4 Thesis outline 10

Chapter 2 Charge transport in organic semiconductors and devices 12

2.1 Organic semiconductor molecular and electronic structure 13

2.1.1 Conjugation and energy bands 13

2.1.2 Organic semiconducting materials 14

2.2 Charge transport models 15

2.2.1 Hopping (simple hopping, variable range hopping, percolation theory) 15

2.2.2 Band-like transport 17

2.2.3 Multiple trapping and release model: The significance of trap states in organic semiconductors 18

2.2.4 The origin of trap states in organic semiconductors 21

2.2.5 Summary 21

2.3 Field-effect transistors 22

2.3.1 Metal-insulator-semiconductor (MIS) capacitor 22

2.3.2 Thin-film transistor (TFT) 23

2.3.3 OTFT parameter extraction 26

2.3.4 The dielectric and the semiconductor/dielectric interface 29

2.3.5 Contact resistance and the metal/semiconductor interface 32

2.3.6 Integrated circuits: The NOT gate 33

Chapter 3 Background 35

3.1 Organic small-molecule/polymer blends for OTFT applications 36

3.1.1 Introduction 36

3.1.2 Background 36

3.1.3 Vertical phase separation 37

3.1.3.1 The Flory-Huggins theory 37

3.1.3.2 Small-molecule/polymer blend liquid-liquid phase separation 39

3.1.4 Small-molecule/polymer blend film morphology 41

3.1.4.1 Small-molecule formation 41

3.1.4.2 Processing techniques 42

3.1.5 Ambipolar blend OTFTs 42
3.1.6 Insulating polymer binders 43
3.1.7 Semiconducting polymer binders 44
3.1.7.1 1st generation blend 44
3.1.7.2 2nd generation blend 45
3.1.7.3 Energetic disorder in small-molecule/polymer blend systems 46
3.1.7.4 Next-generation blend systems 47
3.2 Molecular doping in OTFTs 48
3.2.1 Introduction 48
3.2.2 Mechanisms of molecular doping and doping materials 48
3.2.2.1 The standard model: Integer charge transfer 48
3.2.2.2 The alternative model: Charge transfer complex formation 50
3.2.3 The importance of molecular doping in OTFTs 52
3.2.3.1 Threshold voltage 52
3.2.3.2 Bias-stress stability 53
3.2.3.3 Mobility and conductivity 53
3.2.3.4 On-off ratio 55
3.2.3.5 Contact resistance 55
3.2.3.6 OTFT parameter extraction: Mobility 58
3.2.4 Molecular doping methods 60
3.2.4.1 Bulk doping 60
3.2.4.2 Contact doping and interlayer doping 60
3.2.4.3 Chemical vapour treatments 62
3.2.4.4 Modulation doping 62
3.3 Outlook 63
Chapter 4 Experimental methods 64
4.1 Thin film transistor fabrication 65
4.1.1 Substrate preparation 65
4.1.2 Contact evaporation 65
4.1.3 Self-assembled monolayers 66
4.1.4 Organic blend solution preparation 66
4.1.5 Spin coating 67
4.2 Electrical characterisation 68
4.2.1 Current-voltage characterisation 68
4.3 Materials characterisation 69
4.3.1 Atomic force microscopy 69
4.3.2 Polarised optical microscopy 69
4.3.3 Scanning electron microscopy 70
4.3.4 Kelvin probe and air photoemission 70
4.3.5 Time-of-flight secondary ion mass spectroscopy 71
4.3.6 In-plane wide-angle x-ray diffraction and grazing-incidence wide-angle X-ray scattering 71

Chapter 5 Introduction of 3rd generation organic semiconducting blend systems 72

5.1 3rd generation blend development and design 73

5.1.1 Introduction 73
5.1.2 The binary blend: Small-molecule/polymer 73
5.1.3 The ternary blend: Small-molecule/polymer/dopant 77
5.1.4 Alternative solvent systems 79
5.1.5 Morphological and structural characterisation 84
5.1.5.1 Polarised optical microscopy, atomic force microscopy and scanning electron microscopy 84
5.1.5.2 Waterfall -plane wide angle X-ray diffraction and time-of-flight secondary ion mass spectroscopy 88
5.1.6 Doping mechanisms in the C_8-BTBT:C_{16}IDT-BT:$C_{60}F_{48}$ ternary organic blend 90

5.2 The 3rd generation blend as a prospective system 90

5.2.1 Introduction 90
5.2.2 Alternative blend materials 91
5.2.3 3rd generation blend-based OTFTs with hole mobility values > 20 cm^2/Vs 93

5.3 Summary and conclusions 99

Chapter 6 The effects of molecular doping in 3rd generation organic blend thin-film transistors 101

6.1 Introduction 102

6.2 Effects of doping concentration on I-V characteristics 103

6.2.1 Mobility 104
6.2.2 Bias stress stability 105
6.2.3 Contact resistance 109
6.2.4 OTFT parameter analysis 110
6.2.4.1 μ_{lin}, μ_{sat}, SS and $I_{ON/OFF}$ 111
6.2.4.2 V_{ON} and V_T 112

6.3 Effects of molecular doping on blend morphology 115

6.4 Summary and conclusions 120

Chapter 7 Integrated Circuits: The practical application of 3rd generation blend-based OTFTs 123

7.1 Introduction 124

7.2 Metal oxide bilayers 125

7.3 Hybrid inverters (NOT gates) 126

7.3.1 Inverter fabrication 126
7.3.2 Inverter analysis 128

7.4 Summary and conclusions 130

Chapter 8 Conclusions and Outlook 131

8.1 Summary 132

8.2 Future work **134**
8.3 Outlook **136**

Bibliography **138**
Appendix A **161**
List of publications **161**

Appendix B **162**
Effect of solvent blending on 3rd generation blend microstructure **162**

Appendix C **165**
Content reuse permission licenses **165**

List of Figures

Figure 1.1: The first transistorised computer built in 1953. 2
Figure 1.2: A smartphone and its processor chip. 4
Figure 1.3: Examples of plastic-based technologies. 6
Figure 1.4: Bar chart showing market forecast 7
Figure 2.1: sp2 hybridisation, σ-bonds and π-bonds. 13
Figure 2.2: Schematic representation of conjugated segments within a polymer network. 16
Figure 2.3: Charge transport models. 19
Figure 2.4: Density of states for multiple trapping and release model. 20
Figure 2.5: The MIS capacitor. 23
Figure 2.6: Key OTFT architectures. 24
Figure 2.7: A schematic representation of a thin-film transistor 25
Figure 2.8: The different operating regimes of the OTFT 26
Figure 2.9: (a) Transfer characteristics and (b) output characteristics 29
Figure 2.10: Circuitry of a complementary logic inverter. 34
Figure 3.1: The Flory-Huggins theory. 38
Figure 3.2: Schematic of small-molecule/polymer blend vertical phase separation. 40
Figure 3.3: The 1st generation blend. 45
Figure 3.4: Conductive grain boundaries. 47
Figure 3.5: Schematic of integer charge transfer processes for p-doping in OSCs. 49
Figure 3.6: Examples of dopants for organic semiconductors. 50
Figure 3.7: Charge transfer complex formation. 51
Figure 3.8: Band diagram of a metal and semiconductor interface. 56
Figure 3.9: Schematic of various OTFT doping techniques. 61
Figure 4.1: Schematic of probe station equipment 69
Figure 5.1: C_8-BTBT, C_{16}IDT-BT, energy levels OTFT architecture. 75
Figure 5.2: Representative transfer curve for C_8-BTBT:C_{16}IDT-BT blend OTFTs. 76
Figure 5.3: $C_{60}F_{48}$ and 3rd generation blend energy diagram. 78
Figure 5.4: C_8-BTBT:C_{16}IDT-BT:$C_{60}F_{48}$(1%) blend OTFT processed from CB. 79
Figure 5.5: Tetralin effects on blend OTFT performance. 80
Figure 5.6: Tetralin:CB effects on blend OTFT performance. 81
Figure 5.7: Effects of different solvent systems on transfer characteristics and mobility. 82
Figure 5.8: C_8-BTBT:C_{16}IDT-BT:$C_{60}F_{48}$(1%) blend ratio and work function. 83
Figure 5.9: POM and AFM imaging. 85

Figure 5.10: Scanning Electron Microscopy images. 87
Figure 5.11: In-plane WAXD measurements. 88
Figure 5.12: C_8-BTBT:IDTT-BT:$C_{60}F_{48}$ blend devices 92
Figure 5.13: Effects of solution solution-ageing on transfer characteristics. 94
Figure 5.14: Effects of solution-ageing on saturation mobility. 95
Figure 5.15: Device variability in solution-aged OTFTs. 97
Figure 5.16: Effects of solution-ageing on film microstructure. 98
Figure 6.1: Pristine and doped 3rd generation blend OTFT comparison. 104
Figure 6.2: Saturation and linear mobilities 105
Figure 6.3: The effect of molecular doping on bias-stress stability. 108
Figure 6.4: The effect of molecular doping on contact resistance. 110
Figure 6.5: The effect of molecular doping on transfer characteristics. 111
Figure 6.6: Full analysis of OTFT operating parameters 113
Figure 6.7: The number of holes donated, Δh+, to the OTFT channel 115
Figure 6.8:The effect of molecular doping on microstructure. 116
Figure 6.9: GIWAXS data for various doped C_8-BTBT:C_{16}IDT-BT blend films. 118
Figure 6.10: Intensity vs q_z for various doped C_8-BTBT:C_{16}IDT-BT blend films 119
Figure 6.11: In-plane structures for various doped C_8-BTBT:C_{16}IDT-BT blend films 120
Figure 7.1: Complementary metal oxide n-channel TFTs. 126
Figure 7.2: Inverter circuit design. 127
Figure 7.3:Transfer characteristics of the two independent n-type and p-type TFTs 129
Figure 7.4: Quasistatic voltage transfer characteristics and signal gain 130

List of Tables

Table 6.1: A summary of the literature on bias-stress stability for blend OTFTs……107
Table 6.2: Full analysis of OTFT operating parameters……..…..……...114

Chapter 1

Introduction

***Electronics**, noun: "The science in dealing with the development and application of devices and systems involving the flow of electrons".*

1.1 Fundamental building block: The field-effect transistor

The original idea for the field-effect transistor (FET) came from Julius Lilenfield and is encapsulated in his patent in 1933. This idea was brought to life on the 23rd of December 1947 at Bell Labs in New Jersey USA, when John Bardeen, Walter Brattain, and William Shockley fabricated a field-effect transistor. By using a semiconductor (germanium), three electrodes and applying two electric fields, they made a solid-state electronic switch or amplifier. Bardeen, Brattain, and Shockley were later awarded the 1956 Nobel Prize in Physics for "*their researches on semiconductors and their discovery of the transistor effect*".

In 1954, the first silicon transistor was demonstrated at Bell Labs; this was achieved by doping silicon single-crystals so that the conductivity could be controlled. Silicon transistors were easier to fabricate than geranium transistors and therefore silicon became the semiconductor of choice. The field-effect transistor went on to replace the vacuum-tube triode that had been used for amplification and switching since 1907, leading to improvements in power consumption, size, lifetime, reliability and fabrication cost issues that riddled the early world of electronics. These improvements allowed more creative freedom when it came to designing electronic circuitry.

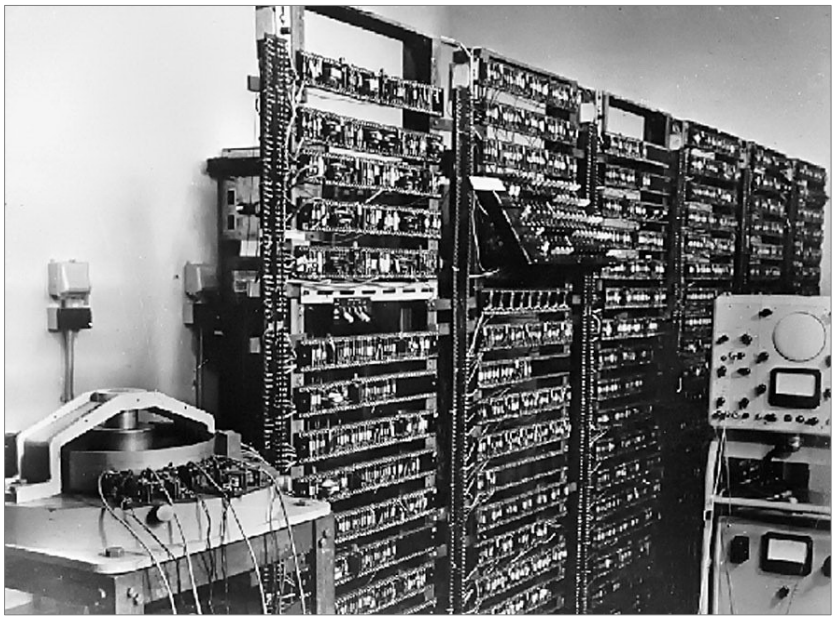

Figure 1.1: The first transistorised computer built in 1953. A photograph of the first computer built using newly developed transistors instead of vacuum tubes; this computer was built at The University of Manchester in 1953. (J. Wilcock, 2010, The Staffordshire University Computing Futures Museum Manchester Page) [1].

A combination of the new solid state field-effect transistors, and the development of the integrated circuit in 1958, began to take electronics from the large, unreliable single-components to the advanced, small microprocessor chips that are seen today. In 1965, Gordon Moore, the co-founder of Intel, published a paper in which, based on his observations, he predicted that every year transistors would get smaller so that the number of transistors on an integrated circuit would double every year [2]. This prediction was termed Moore's Law and was verified over the next few decades with significant impact.

One area where transistor miniaturisation has had a remarkable impact is computers; the transistor is the fundamental building block of the computers that have been responsible for many changes in everyday life. In 1953 the first transistor-based computer was built in Manchester in the UK; this computer contained 92 point-contact transistors and it was the size of a large room (Figure 1.1). As transistors reduced in size, the number of transistors in integrated circuits increased and the processing power increased. By the 1990's, computers could fit onto a desk, and were powerful enough that they became a widespread product in use in industry, business and homes.

Figure 1.2: A smartphone and its processor chip.(a) iPhone 7, (Currys, 2016, DSG Retail Limited) [3] (b) A10 Fusion chip that is used in the iPhone 7, containing over 3.3 billion transistors, (iPhone 7 Updates, 2016) [4].

Nowadays, personal computers are even smaller, portable, more powerful, and have excellent data storage and memory capabilities. The increasingly sophisticated, pocket-sized smartphone, which is widely available and economically viable has almost become a 'necessity' within certain societies. In September 2016, Apple released the iPhone 7 which contains a tremendous 3.3 x 10^9 transistors, and shows that the transistor is still at the heart of modern computers.

Electronic technology has undoubtedly changed humankind's standard and style of living; portable and personal electronic products in the home have completely transformed the functioning of daily lives, human connectivity, human communication/interaction, and how knowledge is documented, shared and used. It was the development and miniaturisation of the field-effect transistor that started the Digital Revolution and propelled the human species into the Information Age.

1.2 Plastic (organic) electronics: Introduction and motivations

As polymeric, or organic, materials are traditionally known to be insulators, one can imagine the excitement in the 1970's when it was discovered that polymers could conduct electricity. In 1977, Alan Heeger, Alan MacDiarmid and Hideki Shirakawa published their work on the discovery of "*doping-induced conductivity*" in polyacetylene [5] [6], and so began the field of plastic electronics. In 2000, Heeger, MacDiarmid and Shirakawa were jointly awarded the Nobel Prize in Chemistry for their discovery of conductive organic materials.

Plastic electronics have received great attention since this initial discovery, due to the range of exotic mechanical properties that they offer in contrast to prevalent inorganic semiconductor technologies [7] [8]. For example, plastics can be flexible, stretchable and processed from solution-phase over large areas in roll-to-roll newspaper-style printing. Plastics can also be processed from lower temperatures, and hence have lower economic costs than silicon. Another benefit of man-made, polymeric materials is that their properties can be tailored via the introduction of different chemical groups that vary overall molecular structures, giving rise to the idea of "*Make to Order*" (MTO) electronics [9] [10] [11].

Aspirations to achieve low temperature, solution processable, low-cost, flexible, stretchable, wearable, transparent, roll-to-roll printed electronics have resulted in extraordinary advances in the fundamental electronic properties of organic materials and electronic devices. Organic electronic devices have been earmarked for a wide range of applications, such as solar power generation, gas and chemical sensors, robotics, radio-frequency identification (RFID) tags, and display technologies [9].

Over the past few decades, there has been a significant amount of focus on making light emitting diodes [12] [13], photovoltaic cells [14] [15] and field-effect transistors [7] [16] from organic semiconductors. Organic light emitting diodes (OLEDs) have made a significant impact in the technology market and they are now widely available in many commercial, shop-bought products, such as mobile phone displays, televisions, digital cameras and other portable digital media. The overwhelming success of the OLED has been incredibly inspiring for the organic electronics field, which, for over a decade, has been generating fabulously alluring economic market predictions for a range of organic and printable technologies [17].

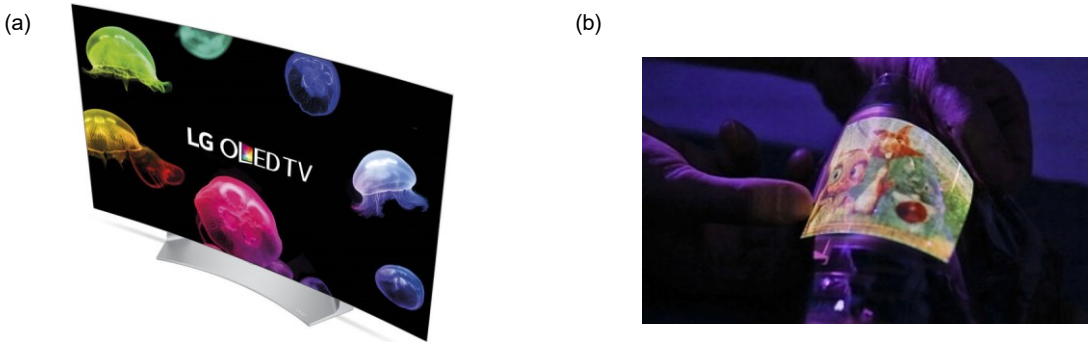

Figure 1.3: Examples of plastic-based technologies. (a) A curved, smart, 55-inch 3D OLED TV by LG, (Currys, 2016, DSG Retail Limited) [3]; curved and OLED TVs are widely available in many shops, including the electronic sections of large supermarket chains, (b) A prototype full-colour, flexible, 125 µm thick OTFT and OLED display by FlexEnable and Chunghwa Picture Tube (CPT), (FlexEnable, 2015, FlexEnable Ltd) [18].

Many recent predictions for the organic and printed electronics market include large contributions from both OLED displays which are not printed, and the increasingly popular conductive inks which are not organic. Market predictions also include alternative material families, such as high-performance, solution-processable metal oxides. It could be argued that some flexible organic technologies haven't entered the commercial market as quickly as the economic market predictions once suggested. But with the broad spectrum of multidisciplinary scientists who are working to achieve the commercial implementation of organic printable technologies, including those in academic groups and the 3000 companies spawned from the organic electronics field, as one idea fades out another idea is brought in.

One example of this is the idea of making everyday objects, such as household items, "smart" which has become very attractive in recent years. Smart objects fit into an overall vision, termed "the Internet of Things" (IoT), which describes a world where everyday objects, services, devices and systems are able to connect and network with each other. To make everyday items into smart technologies requires some kind of fundamental electronic functioning; this requires low-cost electronic circuitry, such as organic electronics, that can be easily embedded into everyday items and manufactured and sold on large scales.

Another area which has been highlighted to benefit from connectivity between devices is bioelectronics. For example, medical implants and devices that can communicate with each other and with medical professionals, creates a system that provides supporting information about patients, particularly those who do not necessarily need face-to-face appointments. A device network that provides this level of support to medical professionals, especially those working in increasingly strained healthcare systems in countries with ageing populations, could

be the latest in a long line of successful, informative medical technologies. For organic semiconductors, the emerging field of bioelectronics has ultimately gained significant popularity because of the compatibility between biological systems and organic materials. Applications such as diagnostic devices, drug delivery and tissue engineering are among the exciting prospects for new, organic based devices [19] [20].

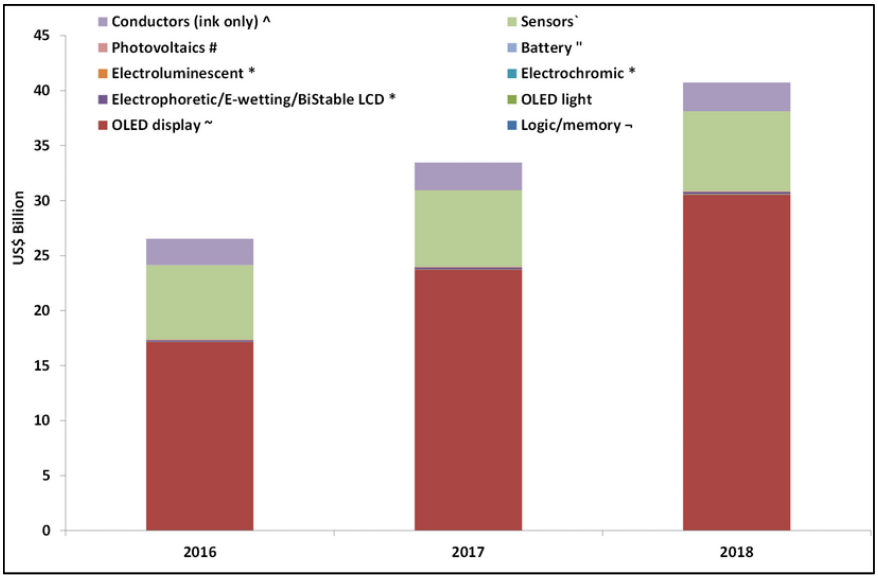

Figure 1.4: Bar chart showing market forecast published by IDTechEx in September 2016. The "printed, organic and flexible electronics" market is split into a range of components, with OLED displays and conductive inks being the most dominant. The report indicates that "stretchable electronics, logic and memory, thin film sensors are much smaller segments but with huge growth potential as they emerge from R&D". (R. Das and P. Harrop, 2016, IDTechEx) [21]

1.3 Motivation: Organic field-effect transistors

One of the primary focusses for organic electronics research over the past few decades has been the organic field-effect transistor (OFET), which was introduced by Koezuka et al. in 1987 by using polythiophene as the semiconductor component [22] [23]. The most common type of FET that is used for organics research is the thin-film transistor (TFT). The TFT was originally suggested by Weimer in 1962 [24] and over the years, the organic thin-film transistor (OTFT) has received tremendous attention.

Applications for OTFTs include light-emitting devices [25], bioelectronics sensing devices [9] and applications that would require low amounts of computing, such as electronic tags or memory devices. Another application – perhaps considered the primary aim for OTFTs – is the active matrix backplane in optical displays, as silicon TFTs have been very successful in this area. This gave rise to the popular idea of plastic, printed, flexible, organic

displays, such as fold-away televisions and electronic newspapers, made from OLEDs with an OTFT backplane.

There are some prototype flexible OLED displays with OTFT backplanes (shown in Figure 1.3 (b)), however this is one of the technologies that perhaps hasn't entered the commercial market as quickly or easily as was once expected. This is because there are still certain operational challenges that must be resolved for OTFT commercialisation to be realised, such as charge carrier mobility, stability, uniformity and contact resistance [9].

The charge carrier mobility value, which describes how quickly charges are able to move through a material under an external electric field, must ideally be as high as possible and a benchmark mobility of 10 cm^2/Vs is required for various industrial applications, such as active matrix backplanes in optical displays. Compared to other semiconducting materials, such as metal oxides and silicon, organic semiconductors are known to have intrinsically low mobilities, therefore achieving a high mobility has been one of the most popular OTFT aims, with research groups world-wide embarking on a race to produce the highest mobility devices [7] [26] [27].

In recent years, talk of high mobilities has adorned the field of organic electronics [28] [29] [30] [31] [32] [33] [34] [35]. Yet some of the highest values reported, with 43 cm^2/Vs being the maximum, have been unsettling due to questionable characteristics observed in the measured/interpreted data, as well as being unrepeatable. Indeed, recent work has confirmed that an artefact caused by contact resistance can lead to overestimated mobility values for some OTFT systems [36] [37].

However, compared to the OTFT mobility values only a few years ago, genuine, impressive and incredibly promising progress has been achieved. Not only do OTFT mobility values now surpass incumbent amorphous silicon-based technologies, but there are a few solution-processed systems that have passed the benchmark mobility of 10 cm^2/Vs. This is very promising and research must be maintained to continue this progress; this is now even more important considering that there is also competition from other materials, such as indium gallium zinc oxide (IGZO), which is now used for TFT backplanes, liquid crystal displays (LCDs) and OLEDs for laptops, tablets, smartphones and televisions.

Whilst solution-processed OTFT mobility values have started to enter the realm of industrial application, they can't be utilised unless the other critical parameters are also addressed. For example, TFTs are used as switches in both voltage-driven and current-driven applications. Voltage-driven applications, such as e-paper or liquid crystal displays, are much less demanding in that they require a controlled voltage to be applied. On the other hand, active

matrix organic light-emitting diode (AMOLED) display technologies – used commercially for smartphones, laptops, tablets, games consoles, smartwatches, digital cameras, media players and televisions – are current-driven. Here the OLED pixels are powered by current from an integrated backplane of TFTs, where a pixel may need to be driven for several hours at a time, supplying a continuous, stable current to the OLED. If this type of application were to use OTFTs then operational stability and device uniformity is of the utmost importance [7]. Another indispensable criterion is the contact resistance; not only has it been at the heart of the recent mobility overestimations, but in general it severely reduces the performance of OTFTs and it is an obstacle to OTFT miniaturisation.

In 2016, by using a time-resolved microwave conductivity (FI-TRMC) technique to avoid the problems associated with contacts in OTFTs, Tsutsui et al. measured mobilities of 170 cm^2/Vs for the organic semiconductor didodecyl[1]benzothieno[3,2-b][1]benzothiophene (C_{12}-BTBT). This is extraordinary; it finally puts the performance of organic materials in-line with its competitors, i.e. metal oxides (20-50 cm^2/Vs) and polycrystalline silicon (> 100 cm^2/Vs) [38]. As well as being remarkably promising for OTFTs, these results further highlight the issues related to the contacts in OTFTs and the necessity of an approach that resolves them.

One illustrious technique that is used to resolve contact resistance issues in inorganic contact-based electronics is doping. In fact, the eureka moment for the inorganic electronic technology was realising that conduction in silicon could be controlled by doping [39]. Doping has been established as a critical factor for modern electronics for many years, and in addition to revolutionising inorganic semiconductor technology, it brought about the field of organic electronics [5] [6]. Doping has also been key for developing efficient OLEDs and organic photovoltaics (OPVs).

Molecular doping in OTFTs has the potential to rectify the performance related issues that have been highlighted in this chapter, yet despite this, doping research for OTFTs is still "*lagging behind*" the research that has been undertaken for OLEDs and OPVs [40]. One of the primary issues of doping in OTFTs is that the introduction of a molecular dopant at high concentrations reduces the crystallinity of the semiconductor, and subsequently reduces the mobility [41].

In summary, organic semiconducting materials and OTFTs have made significant advances in recent years and they still offer great potential. By addressing the OTFT performance related issues it will be possible to capitalise on the intrinsic organic semiconductor property advances that have been made in recent years. Continued research into

high performance OTFTs, and particularly into doping techniques for OTFTs, is therefore extremely important for taking the next steps towards the realisation of OTFTs in commercial applications.

1.4 Thesis outline

One promising system for the commercial realisation of OTFTs is an organic semiconducting blend, consisting of a small-molecule and a polymer. Organic blends are simple, high performance, solution-processable systems that have received great attention, and in the past have achieved record breaking solution-processed mobility values. However, currently, there is one crucial question that remains regarding the organic blends: is it possible to further increase their performance to surpass the benchmark mobility of 10 cm^2/Vs? Achieving this level of performance with an organic blend would provide the field of organic electronics with a simple, low cost, high-performance OTFT system that can be manufactured using scalable processing techniques.

The aim of the work described in this thesis is to develop advanced organic semiconducting blends, the so-called 3rd generation blend systems, for high-performance OTFT applications. This objective was largely achieved through the addition of a molecular *p*-dopant in a traditional binary small-molecule/polymer blend system. The dopant is found to be the critical component in this particular blend system, resulting in a combination of high mobilities, improved operating parameters and what appears to be an unconventional doping mechanism. These factors strongly suggest that the ternary blend presented herein is a highly attractive model system for semiconductors in OTFTs.

The thesis is structured as follows: *Chapter 2* provides an overview of the theory behind organic semiconductors and OTFTs. *Chapter 3* gives an overview of the literature to-date on organic small-molecule/blend systems as well as the literature on molecular doping in OTFTs. *Chapter 4* follows by discussing the experimental techniques used for the work in this thesis.

Chapter 5 describes the development of a 3rd generation organic semiconducting blend and discusses the materials choice for the blend as well as the impact of the solvent choice. *Chapter 6* examines the role of the molecular dopant in the 3rd generation blend system in more detail, highlighting the relevance of this blend system in terms of the criteria for the realisation of OTFTs in commercial applications. *Chapter 7* continues by demonstrating the practical suitability of this system; a hybrid inverter circuit is realised by combining 3rd generation blend-based OTFTs with complementary metal oxide based TFTs. The thesis concludes in

Chapter 8 with a summary of the experimental work and the key achievements presented, while highlighting future research directions.

Chapter 2

Charge transport in organic semiconductors and devices

This chapter gives an overview of the theory behind organic semiconductors and the operating principles of organic thin-film transistors. The first part of the chapter outlines the origin of the semiconducting properties in conjugated organic systems, the models that are typically used to describe how charged carriers move through such systems, and the electronic trap states that are considered to govern charge transport in organic semiconductors. There then follows a discussion on the underlying operation of the thin-film transistor, the key experimental measurements, methods on how to extract critical device operating parameters and the role of the critical dielectric/semiconductor and metal/semiconductor interfaces. Finally, the operating principles of the NOT gate are introduced.

2.1 Organic semiconductor molecular and electronic structure

2.1.1 Conjugation and energy bands

Molecules tend to be classified as organic when there are long chains or rings of carbon atoms present. If the organic system is *conjugated*, i.e. consists of alternating double and single bonds between its carbon atoms, then it is known to exhibit semiconducting properties in a similar manner to inorganic semiconductors like silicon or germanium.

The basic building block of a conjugated system is the most common carbon isotope, which contains 6 neutrons, 6 protons and 6 electrons and has a ground state orbital structure of $1s^2\ 2s^2\ 2p^2$. By exciting an electron from the 2s state to the 2p state, as shown in Figure 2.1, the orbital configuration becomes $1s^2 2s^1 2p^3$. In this configuration, it is now possible for the 2s and 2p orbitals to overlap – or "*hybridize*" – to form three sp^2 hybrid orbits, that lie at 120° to one another in the same plane [42]. One remaining orbital, p_z, will contain one electron that lies perpendicular to the sp^2 orbital plane.

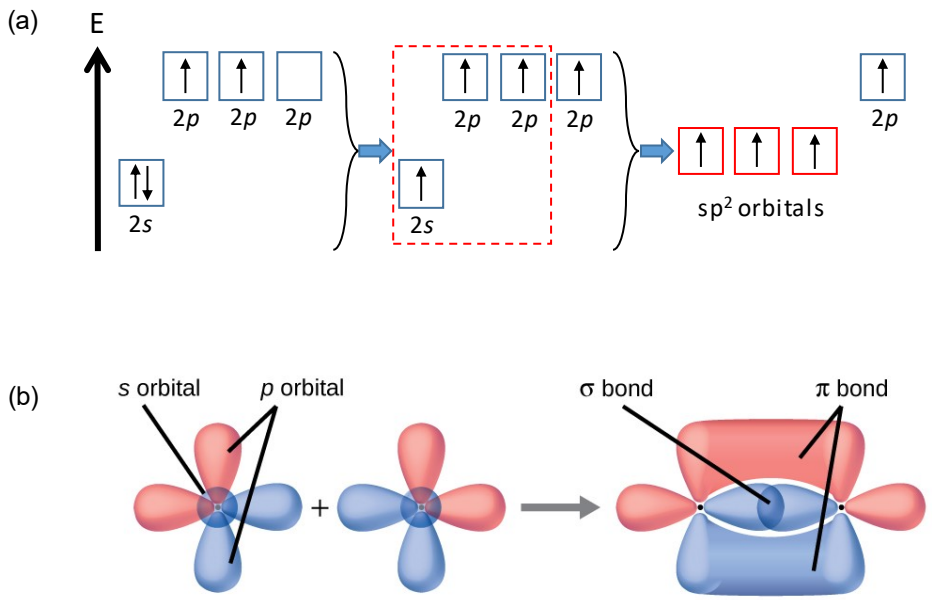

Figure 2.1: sp2 hybridisation, σ-bonds and π-bonds. (a) sp2 hybridisation of a carbon atom, (b) The formation of σ-bonds and π-bonds, reproduced from OpenStax, Chemistry (2016) [43].

If another carbon atom is brought into the picture, the sp2 orbitals of the neighbouring carbon atoms overlap to form strong covalent bonds, known as *σ-bonds*. The p_z orbitals of neighbouring atoms will also overlap, but they form weakly bound *π-bonds*, which unlike the

σ-bonds have delocalised wavefunctions. Introducing many more carbon atoms into this picture will produce a chain of σ-bonds and π-bonds between neighbouring carbon atoms. These two critical bonds ultimately provide organic semiconductors with two fundamental properties: (i) mechanical robustness from the strong σ-bonds that form a backbone and (ii) electrical performance from the delocalised π-bonds which allow the p-orbital electrons to move freely across the chain of carbon atoms.

Due to the constructive and destructive interference of overlapping p_z orbitals and the Pauli exclusion principle, regions of filled π-bonds and unfilled π*-bonds will exist above and below the sp2 backbone plane. It is the filled and unfilled π- and π*-bonds which act as pathways for the electrons to move through; these pathways are termed the *Highest Occupied Molecular Orbital* (HOMO) and *Lowest Unoccupied Molecular Orbital* (LUMO).

If the sp2 carbon atom backbone is conjugated and does not consist of identical bonds but rather a series of alternating double and single bonds, then there is a disruption to the periodicity of the carbon backbone. This disruption to the periodicity distorts the band structures, creating a Peierls distortion-induced gap between the HOMO and the LUMO levels by pushing up the energy of the empty electron states and pulling down the full electron states [44]. This will essentially create a gap, known as the *band gap*, E_G, which gives the material its semiconducting properties in an analogous manner to inorganic semiconductors. The HOMO and LUMO levels correspond to the inorganic *conduction band* and *valence band*, respectively.

2.1.2 Organic semiconducting materials

Some examples of conjugated molecules are benzene, fluorene and thiophene, which are used as building blocks for organic semiconductors. Molecular engineers add side groups to these conjugated molecules, which allow them to skilfully design and fabricate semiconductors with specific, tailor made properties. The side groups determine mechanical properties, such as solubility, as well as electrical properties; for example the electrical properties can be adjusted by adding groups that either withdraw or donate electrons. Side groups also determine the packing of the semiconductor. This is particularly important as improving the π-bond overlap between neighbouring conjugated units can improve the electronic coupling between neighbouring molecules, known as "*π-π stacking*" distances.

The organic semiconductors that are made from conjugated molecules and side groups tend to be split into two categories: (i) polymers, such as poly(triarylamine) (PTAA) and

poly(3-hexylthiophene-2,5-diyl) (P3HT), and (ii) small-molecules, such as pentacene and rubrene [45] [46]. These two material categories are fundamentally different – primarily due to their sizes – and therefore exhibit different material properties.

Polymers are made from molecular subunits that are repeated many times, creating very large molecules with covalently bonded carbon backbones. These polymer molecules are held together by weak van der Waals forces and their long structures mean that they form spaghetti-like microstructures that are either fully amorphous or, if it is energetically favourable, semi-crystalline. These specific microstructures give polymers their highly attractive flexible properties, but also mean that they lack intrinsic long-range order which is beneficial for the efficient movement of charged particles. On the other hand, small-molecules are able to pack together neatly to form highly crystalline structures, and therefore tend to have better electrical properties, but they are difficult to process from a solution.

As with inorganic semiconductors, organic semiconductors are defined by the polarity of their majority charge carriers. If negatively charged electrons are the majority charge carrier then the semiconductor is said to be *n-type*, and if positively charged holes are the majority charge carrier then the material is *p-type*. It is also possible for both types of carrier to flow within one material, in which case the semiconductor would be described as *ambipolar*. In the vast majority of cases, polymers are ambipolar and the polarity of the device that they are embedded into is determined by device engineering, which will be discussed further in Section 2.3.5.

2.2 Charge transport models

2.2.1 Hopping (simple hopping, variable range hopping, percolation theory)

A polymer molecule continuously changes along its length which leads to disruptions in its conjugation [47]. The disruptions in conjugation mean that it is better to treat the conjugated backbone as if it is broken into segments, as shown in Figure 2.2; this is the intrinsically disordered nature of a conjugated polymer system, where the delocalisation of π-electrons happens within the conjugated segments, rather than across a whole system. The conjugated segments can also vary considerably in length, leading to a variation in the bandgap energy [48].

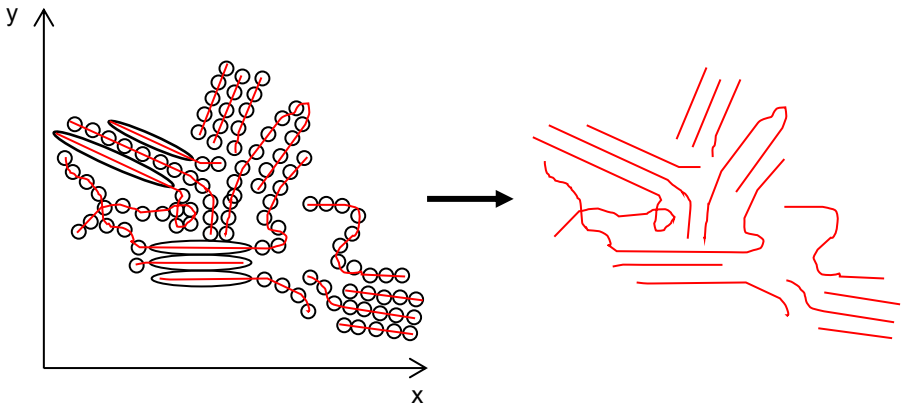

Figure 2.2: Schematic representation of conjugated segments within a polymer network. The circles represent units or moieties that are the building blocks of the backbone and the lines represent how the one long backbone is broken into conjugation segments of various lengths. Schematic reproduced with permission from reference [48].

A 3D network of conjugated polymer backbones, held together by weak van-der Waals electronic bonding, can be pictured as a disordered web of conduction pathways; localised states in the conjugated segments are able to "jump" or "hop" to neighbouring segments. For this reason, charged particles hopping through a series of localised states has been an accepted way of describing how charge carriers move through disordered polymers [49] [50].

The basis of a simple hopping-rate model for organic semiconductors emerged from the jump-rate model by Miller-Abrahams, which was originally used to describe hopping rates in weakly doped inorganic semiconductors, where phonon-induced electron hopping occurs between low levels of localised states [51]. Mott expanded this jump-rate model by considering that, although the charge carriers are localised, "*every now and then*" they are able to hop to another localised state with a variable range of hopping: either hopping over a large distance with a low activation energy, or a small distance requiring a high activation energy. This is known as the *Variable Hopping Range* (VHR) model [52]. The probability of a hop occurring between two sites that are separated in space by R and in energy by W is as follows:

$$P(R,W) = \exp\left(-a\,R - \frac{W}{k_{\mathrm{B}}T}\right)v \tag{2.1}$$

where T is the absolute temperature, k_B is the Boltzmann constant and a is a constant. By integrating over all energy states and distances, the total conduction is found to be dependent

on temperature in the following way:

$$\mu \propto \exp\left[-\left(\frac{T_0}{T}\right)^{\frac{1}{n+1}}\right] \tag{2.2}$$

where T is the absolute temperature, T_0 is a constant and n is the dimensionality of the system.

Vissenberg and Matters further evolved the hopping model by combining it with percolation theory [53]. Percolation theory was originally developed to describe the flow of a material through a porous matrix [54] and in this context is as follows: as described in Equation 2.1, at a certain temperature there is a probability that a charge carrier can hop to available energies, W, over a certain distance, R. This can be pictured as a conductive sphere with a hopping radius of R around the localised state. If there are only a few localised sites then the spheres will not be interconnected, or they may exist as small clusters of interconnectivity, but they won't exhibit any long-range connectivity. As the density of sites increases, the sizes of the clusters increase and begin to merge with one another, forming an interconnected pathway of conductive spheres. There is a critical number of sites at which the clusters will become a marginally connected pathway through which current is able to percolate.

In addition to the hopping model and percolation theory, Vissenberg and Matters incorporated a transistor model with an exponential distribution of tail states at the semiconductor-dielectric interface [53]. This gives a relationship between field-effect mobility (i.e. speed of the charge carriers due to the applied electric field), gate voltage and temperature:

$$\mu = \frac{\sigma_0}{e}\left(\frac{\pi(T_0/T)^3}{(2\alpha)^3 B_C \Gamma(1-T/T_0)\Gamma\,(1-T/T_0)}\right)^{T_0/T}\left(\frac{(C_i V_G)^2}{2k_B T_0 \varepsilon_S}\right)^{T_0/T-1} \tag{2.3}$$

where μ is the mobility, σ_0 is a conductivity prefactor specific to the material, e is elementary charge, B_c is critical criteria for percolation, C_i is the geometrical capacitance of the dielectric layer, V_G is the gate voltage and ε_S is the dielectric constant of the semiconductor and Γ is defined as:

$$\Gamma(z) = \int_0^\infty t^{z-1} e^{-t}\, dt \tag{2.4}$$

2.2.2 Band-like transport

In contrast, for well-ordered periodic crystal structures – such as those formed in inorganic semiconductors and highly-ordered organic crystals – charge carriers are considered

to be in potential wells within periodic boundary conditions. Solving the Schrodinger equation within these boundary conditions gives an energy distribution in two periodic bands. Within these two bands there is a region, E_G, that has no solution to the Schrodinger equation and therefore it is unphysical for charge carriers to exist there. The wavefunctions and hence electrons are delocalised throughout the bands which, due to the periodic unbroken nature of the structure, extend across the entire crystal. This type of transport model, unlike hopping, will lead to large conduction pathways and materials with potentially very high currents and mobilities.

The available states will be filled following Fermi-Dirac statistics, which describe the probability of a state with energy, E, being filled:

$$f(E) = \frac{1}{1 + \exp\left(\frac{E - E_{\mathrm{F}}}{k_{\mathrm{B}}T}\right)} \tag{2.5}$$

where E_F is the *Fermi level*. In addition, the field-dependent mobility for band-like charge transport is as follows:

$$\mu \propto \exp\left(\frac{1}{kT}\sqrt{\frac{E}{E_0}}\right) \tag{2.6}$$

where E is the electric field and

$$E_0 = \frac{\pi\varepsilon}{q} \tag{2.7}$$

with ε being the permittivity of the material and q the elementary charge.

2.2.3 Multiple trapping and release model: The significance of trap states in organic semiconductors

The previous section outlined two contrasting models to describe charge transport within materials of different structures. Hopping models are appropriate for highly disordered amorphous polymers [49] [50] [53] and band-like transport is appropriate for highly-ordered periodic crystals [55]. Yet in reality, neither of these two extremes are appropriate for the vast majority of organic semiconductors. In practice, a hybrid model that merges together extended states in bands and localised states in the bandgap is more appropriate for disordered, yet high-mobility, organic materials [50] [51] [56].

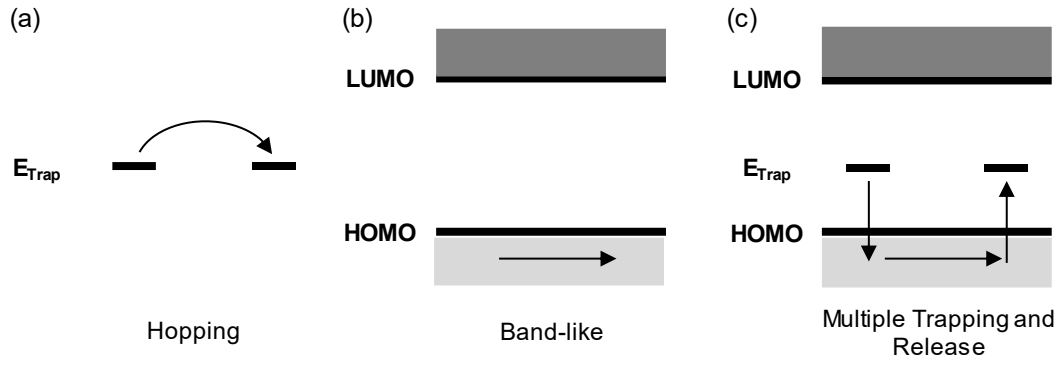

Figure 2.3: Charge transport models. (a) Hopping between localised states, (b) band-like charge transport, (c) multiple trapping and release (MTR) model that combines trap states with band-like charge transport.

Figure 2.3 shows the essence of the hybrid conduction model: band-like charge transport happens in the extended states – where it can contribute to electrical current – but the localised states are available to capture free charges and are termed *traps* [57]. This model is known as the *multiple trapping and release* (MTR) model, which was originally developed by Le Comber and Spear for amorphous silicon [51]. When a charge is captured by a trap, it is not able to contribute to electrical current [50], therefore the overall conductivity is very much dominated by the localised trap states that lie next to the band edge (HOMO/LUMO for *p*-type/*n*-type materials).

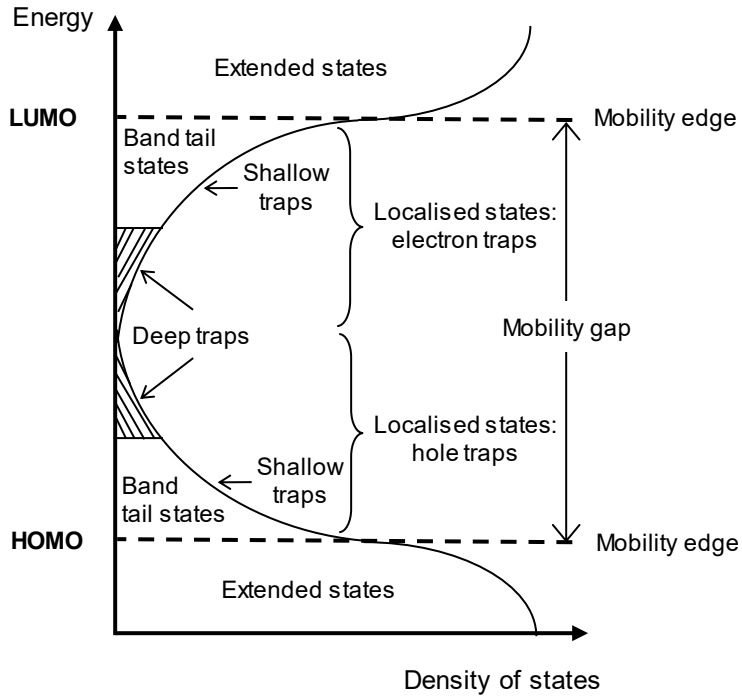

Figure 2.4: Density of states for multiple trapping and release model.

Although in general trapped charges do not contribute to electrical current, there is an exception to this rule if they can be made available via thermal excitation [9]. Traps can therefore be split into two categories dependent on their relative position to the band-edge and the time scales of carrier localisation: (i) localised states within k_BT of the band-edge are considered *shallow traps* and carriers can be thermally excited into/relaxed from the extended band states; (ii) traps that are greater than k_BT from the band-edge are *deep traps* and thermal excitation cannot activate carrier exchange [55].

Figure 2.4 shows the density of states (DOS) for an organic semiconductor using the MTR model. The distributions of trap (or "tail") states are exponential as this is suitable for many organic TFT applications, although the nature and form of the DOS is a debated topic as it is often distorted by experimental techniques [48]. Highly disordered systems will have a broad DOS whilst more ordered systems will have a much narrower DOS. Figure 2.4 also introduces a new term: the *mobility edge*. This term is used for MTR systems because – unlike band-like transport – there is no clear distinction between states that can contribute to electrical conductivity and states that can't, because the charges can be thermally excited into the transport levels.

Because thermally excited localised carriers can contribute to electrical current, an Arrhenius relationship can be used to describe the mobility of the charge carriers:

$$\mu = \mu_0 \exp\left(-\frac{E_\mathrm{A}}{k_\mathrm{B}T}\right) \tag{2.8}$$

where E_A is the activation energy required for a carrier to move from a localised state into an extended state. The mobility is therefore dependent on temperature and how the traps are distributed.

2.2.4 The origin of trap states in organic semiconductors

The incorporation of trap states into a band-like model has been very useful for describing electrical behaviours in organic materials, but where do these trap states originate from? In the 1950s, Anderson showed that disorder in the lattice, introduced by broken crystal symmetry, results in the localisation of wavefunctions and energy states being formed in the bandgap [48] [58]. Therefore the localised states within the forbidden bandgap are thought to originate from material defects and structural disorder. The trap states in single crystals, small-molecules and polymers generally come from the following:

- Single-crystals: Single-crystal structures are generally considered to be defect-less and exhibit band-like transport due to a clear distinction between extended states and traps. For single-crystals, traps are thought to arise from impurities.
- Small-molecules: In polycrystalline semiconductors such as small-molecules, broken bonds caused by structural defects disrupt the lattice and introduce energy states into the bandgap; strained bonds, which do not have neatly overlapping molecular orbitals, will also have the same effect [9]. Both broken and strained bonds are caused by structural defects. For example, structural defects that have attracted significant attention over the years are the grain boundaries in polycrystalline small-molecule films [50] [59].
- Polymers: There is a certain degree of statistical variation between polymer molecules, which results in a variety of bond angles and therefore local strained bonds, causing very poor orbital overlap and – as in the case of the small-molecule – leads to energy states in the bandgap [9].

2.2.5 Summary

Before moving on to the next section of this chapter, a few points should be made about charge transport models and traps. There are numerous charge transport models or variations

of models that have been developed to explain transport through disordered systems. Although MTR is suitable for a lot of organics work, due to the variety of microstructures and the temperature dependent behaviour of organic semiconductors [57], an open mind needs to be kept when considering which model is the most suitable for the semiconductor in question. Polymers come in a great variety of microstructures, from highly disordered amorphous semiconductors with no structure at all, to semicrystalline polymers with varying degrees of crystallinity from nanoscale, mesoscale or microscale crystallites [10] [60]. Small-molecules have a higher density of traps at the grain boundaries, rather than traps that are equally distributed throughout the polycrystalline film. In addition, the definition of a trap is not always clear-cut. For example, if the temperature is low enough – or if the trap density is high enough – then the charges can be transported through the DOS from trap to trap by tunnelling or hopping, therefore it is possible for "trapped" charges to be mobile [9]. Understanding the physics behind (i) how traps are generated and (ii) how trapping effects charge transport in organic semiconductors is fundamentally important for the future of organic electronic applications. For this reason, the nature of traps is being explored by some groups, who purposefully introduce traps into organic semiconductors [55] [61] [62], to better understand this complex topic.

2.3 Field-effect transistors

2.3.1 Metal-insulator-semiconductor (MIS) capacitor

At the heart of the thin-film transistor is the *metal-insulator-semiconductor* (MIS) *capacitor*. The MIS capacitor consists of an insulating layer, *dielectric*, sandwiched between a metal, *gate*, and a semiconductor, as shown in Figure 2.5 (a). When a voltage is applied across the MIS capacitor, termed the *gate voltage*, V_G, there are three different situations that can occur: (i) *accumulation*, (ii) *depletion* and (iii) *inversion*.

For a *p*-type semiconductor, when an opposite sign, i.e. negative, V_G is applied, the Fermi level (E_F) in the metal layer is raised from its equilibrium position by eV_G, as shown in Figure 2.5 (b). This attracts holes to the semiconductor/dielectric interface and causes holes to accumulate in a capacitive manner, known as accumulation mode. If a moderate positive V_G is applied to the same system then holes will be depleted from the semiconductor/dielectric interface resulting in a space-charge region, known as depletion mode. The final scenario for this system is one where a significant positive bias is applied and minority carriers are induced at the interface, changing the semiconductor from *p*-type to *n*-type, and hence this regime is known as *inversion mode* [51].

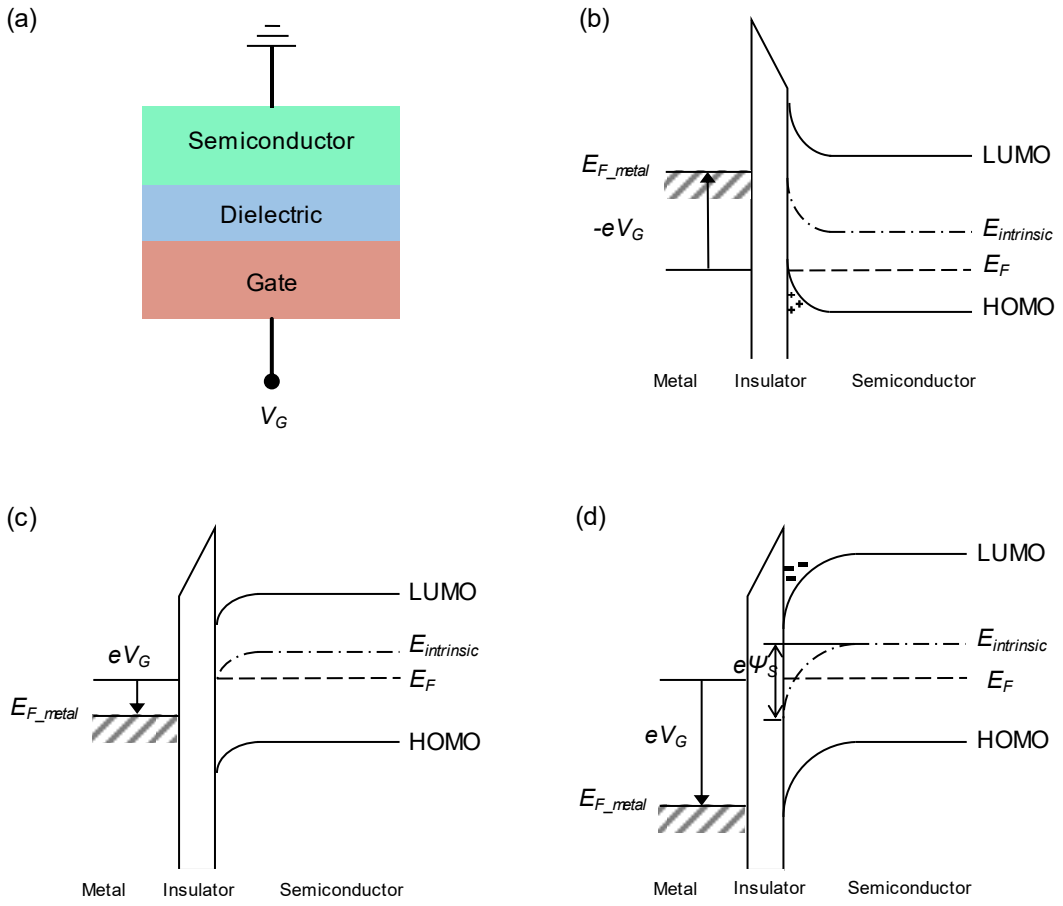

Figure 2.5: The MIS capacitor. (a) Schematic of a MIS capacitor and band diagrams of a MIS capacitor operating in (b) accumulation, (c) depletion and (d) inversion diagram. (H-F Meng, 2013, Polymer Electronics) [51].

2.3.2 Thin-film transistor (TFT)

If we consider the MIS capacitor and introduce two additional symmetric electrodes on the semiconductor side, as shown in Figure 2.6, then we have the beginnings of a three-terminal *thin-film transistor*. The two additional electrodes are known as the *source* and the *drain*.

Different TFT architectures can be formed depending on where the source and drain electrodes are positioned within the MIS capacitor. The architectures, which are known as *bottom-gate top-contact*, (BG-TC) *bottom-gate bottom-contact* (BG-BC) and *top-gate bottom-contact* (TG-BC), are shown schematically in Figure 2.6. Each structure has its own advantages in terms of ease of fabrication or TFT operational benefits, which will be discussed in further detail in Section 2.3.5.

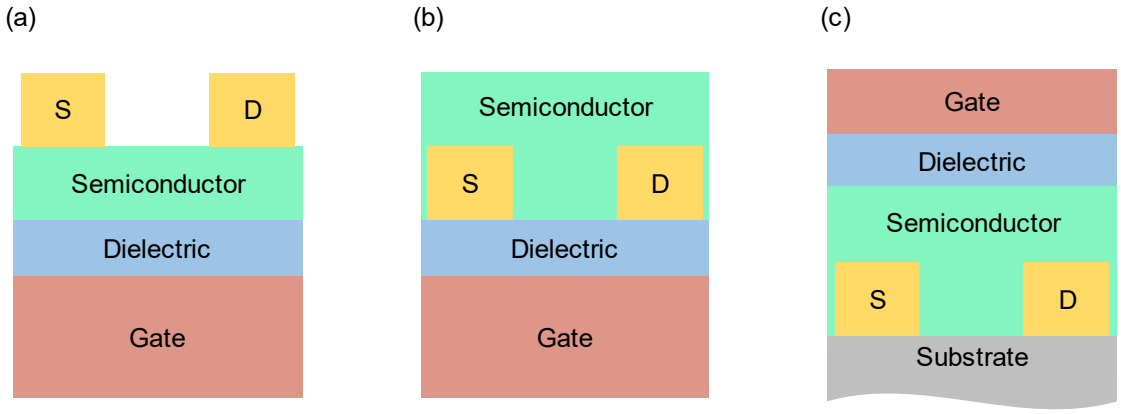

Figure 2.6: Key OTFT architectures. (a) Bottom-gate top-contact (BG-TC), (b) Bottom-gate bottom-contact (BG-BC) and (c) Top-gate bottom-contact (TG-BC).

OTFTs will usually operate in accumulation, but they are also known to operate in depletion and inversion modes [23] [63] [64]. For a typical accumulation operating mode, the source will be grounded at 0 V and V_G is biased such that charge carriers accumulate at the semiconductor/dielectric interface (as described for the MIS capacitor in Section 2.3.1). The layer of accumulated charge forms the transistor *channel*; this is the region in which all of the critical charge transportation occurs. The channel is only a few nanometres thick [10], and it has dimensions of *length*, L, and *width*, W, where both length and width are determined by the spatial arrangement of the source and drain. The areal density of charges that are accumulated in the channel, $Q_{channel}$, when V_G is applied can be described by a parallel plate capacitor model:

$$Q_{\text{channel}} = C_{\text{i}} \times V_{\text{G}} \tag{2.9}$$

where C_i is the capacitance of the dielectric layer.

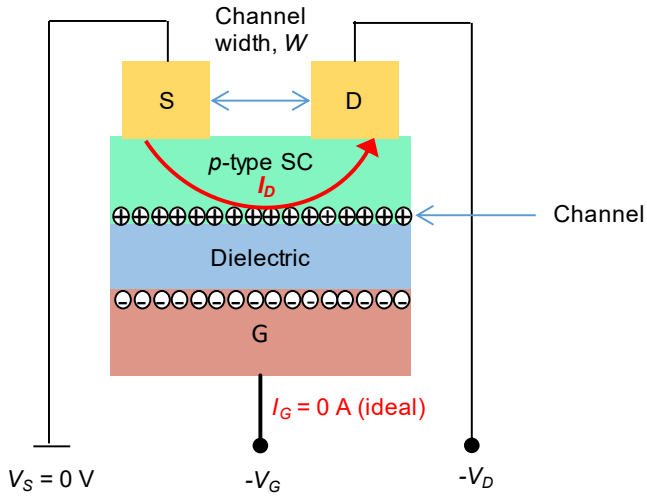

Figure 2.7: A schematic representation of a thin-film transistor, which is fundamentally based on a MIS capacitor with two additional electrodes.

Once a bias has been applied between the source and gate, V_G, and free holes/electrons have accumulated in the HOMO/LUMO at the channel, a second bias can be applied between the source and the drain terminals, known as the *drain voltage*, V_D. The free carriers will move under this secondary external electric field, being injected/extracted from the source/drain electrodes. The application of this second field, V_D, in addition to V_G therefore generates a current in the channel known as the *drain current,* I_D (Figure 2.7). V_G and V_D are ultimately used to modulate I_D.

The amount of V_D applied affects the resistance over the channel which subsequently affects how the charges in the channel are distributed. Based on this, there are three regimes that the transistor can operate in, which are demonstrated schematically in Figure 2.8.

If V_D = 0 V, then there will be no alteration to the accumulation layer at the semiconductor/dielectric interface (Figure 2.8 (a)), known as *cut-off*, where the channel remains as a uniform carrier concentration and I_D = 0 A.

As small amounts of V_D are applied, and 0 V < V_D << V_G, charges will start to be injected from the source and attracted to the drain. Under these conditions, there is a constant resistance across the channel, and the accumulated carrier concentration at the semiconductor/dielectric interface will vary linearly, and I_D therefore increases linearly with V_D. This is known as the *linear regime*.

If V_D is increased, such that $V_D \geq V_G > 0$ V, then a very high resistance region depleted of charge carriers begins to form next to the drain electrode. The high resistance region results in non-linear conductivity across the channel, known as the *saturation regime*.

It should be noted here that – in theory – when $V_D > 0$ V, the charges should only pass from the source to the drain and they should not be attracted towards the gate. However, in practice there may be a current flowing between the source and the gate, I_G, known as the *gate leakage* (shown in Figure 2.7).

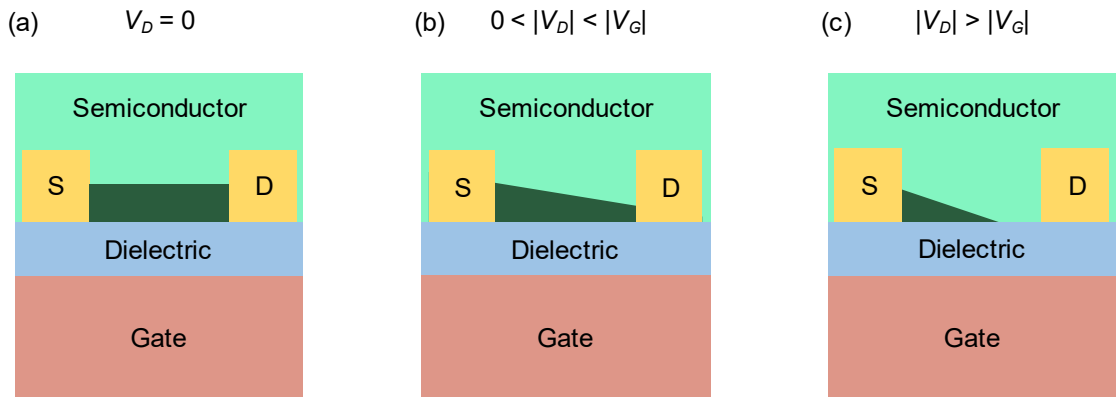

Figure 2.8: The different operating regimes of the OTFT depending on the drain voltage applied which affects the resistance of the channel and hence the distribution of charge carriers in the accumulation layer, (a) cut-off regime, (b) linear regime and (c) saturation regime

2.3.3 OTFT parameter extraction

If we assume that voltage varies gradually across the channel with the application of V_D then the *gradual-channel approximation* model can be employed. This model has been taken from inorganic metal-oxide semiconductor field-effect transistors (MOSFETs) and has been slightly modified for OTFTs [65]. By substituting the conditions shown in Figure 2.8, the gradual-channel approximation can be used to describe the current flowing through the channel and extract the critical OTFT operating parameters.

The qualitative situation outlined in Section 2.3.2 describes an ideal transistor, but in reality, following the MTR model described in Section 2.2.3, there are a number of trap states that need to be filled before mobile charge carriers can be induced at the semiconductor/dielectric interface. The voltage required to fill these traps and produce mobile charges is known as the *threshold voltage*, V_T. From Equation 2.9, the following therefore describes the density of mobile charges in the channel, Q_{mob}:

$$Q_{\text{mob}} = C_{\text{i}}(V_{\text{G}} - V_{\text{T}}) \tag{2.10}$$

As the charge carrier density depends on the position in the channel, *V(x)*, Equation 2.10 becomes:

$$Q_{\text{mob}} = C_{\text{i}}[V_{\text{G}} - V_{\text{T}} - V(x)] \tag{2.11}$$

Assuming that, under the external field V_D, drift current dominates the channel, then diffusion and gate leakage can be neglected (i.e. only consider the movement of charge carriers due to the applied field). The current through the channel, I_D, is then proportional to the width of the channel, W, the density of mobile charges, Q_{mob}, the electric field V at position x, $F(x)$, and the speed of the charge carriers due to the applied electric field, μ:

$$I_{\text{D}} = W\mu Q_{\text{mob}} F(x) \tag{2.12}$$

where

$$F(x) = \frac{dV}{dx} \tag{2.13}$$

and

$$\mu = \frac{v}{E} \tag{2.14}$$

where μ is the *mobility*, which is defined as the drift velocity, v, of the charge carriers in cm/s per applied electric field, E, in V/cm.

Substituting Equation 2.11 and 2.13 into Equation 2.12 gives:

$$I_{\text{D}} dx = W\mu C_{\text{i}}[V_{\text{G}} - V_{\text{T}} - V(x)]dV \tag{2.15}$$

and integrating over the potential difference range between the source and the drain, i.e. the channel length, L, gives:

$$\int_0^L I_{\text{D}} dx = W\mu \int_0^{V_D} C_{\text{i}}[V_{\text{G}} - V_{\text{T}} - V(x)]\, dV(x) \tag{2.16}$$

then:

$$I_{\text{D}} = \frac{WC_{\text{i}}}{L}\mu \times \left((V_{\text{G}} - V_{\text{T}}) \times V_{\text{D}} - \frac{V_{\text{D}}^2}{2} \right) \tag{2.17}$$

which is the gradual channel approximation. By approximating $V_D << V_G$ in Equation 2.17, the current between the source and drain during linear regime operation is given by the following:

$$I_{\mathrm{D}} = \frac{WC_{\mathrm{i}}}{L}\mu_{\mathrm{lin}} \times \left((V_{\mathrm{G}} - V_{\mathrm{T}}) \times V_{\mathrm{D}}\right) \tag{2.18}$$

Taking the first derivative of I_D with respect to V_G from Equation 2.18 gives the *linear mobility*, μ_{lin}, as:

$$\mu_{\mathrm{lin}} = \frac{L}{WC_{\mathrm{i}}V_{\mathrm{D}}}\frac{\partial I_{\mathrm{D_lin}}}{\partial V_{\mathrm{G}}} \tag{2.19}$$

To find the current in the saturation regime, $V_D = V_G - V_T$ can be substituted into the gradual channel approximation in Equation 2.17, as when V_D is greater than $V_G - V_T$, there is no noticeable increase in I_D (as shown in Figure 2.9):

$$I_{\mathrm{D}} = \frac{WC_{\mathrm{i}}}{2L}\mu_{\mathrm{sat}}C_{\mathrm{i}} \times (V_{\mathrm{G}} - V_{\mathrm{T}})^2 \tag{2.20}$$

From here, the *saturation mobility*, μ_{sat}, can be found either from the second derivative of Equation 2.20 with respect to V_G:

$$\mu_{\mathrm{sat}} = \frac{L}{WC_{\mathrm{i}}}\frac{\partial^2 I_{\mathrm{D}}}{\partial V_{\mathrm{G}}^2} \tag{2.21}$$

or by taking the first derivative of the square-root:

$$\mu_{\mathrm{sat}} = \frac{2L}{WC_{\mathrm{i}}}\left(\frac{\partial\sqrt{I_{\mathrm{D}}}}{\partial V_{\mathrm{G}}}\right)^2 \tag{2.22}$$

By combining the gradual channel approximation equations with experimental data, i.e. current-voltage measurements, the OTFT parameters can be extracted, giving a great insight into device operation. There are two key current-voltage measurements: (i) V_G is varied with constant V_D and the resultant I_D is measured, known as the *transfer characteristics* (Figure 2.9 (a)) and (ii) V_D is varied with constant V_G and the resultant I_D is measured, known as the *output characteristics* (Figure 2.9 (b)).

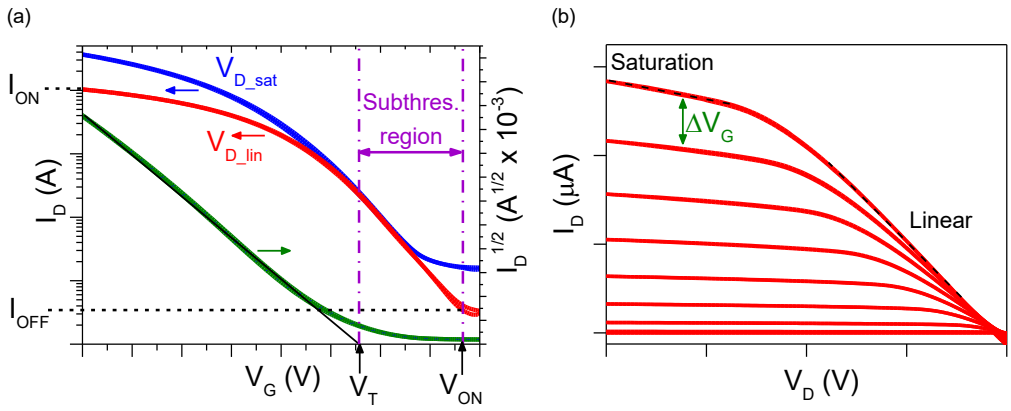

Figure 2.9: (a) Transfer characteristics and (b) output characteristics for a thin-film transistor.

The key parameters to extract from the experimental data are the *current on-off ratio*, $I_{ON/OFF}$, the threshold voltage, V_T, the *on voltage*, V_{ON}, the *subthreshold slope*, *SS*, the linear mobility, μ_{lin}, and the saturation mobility, μ_{sat}.

V_{ON} is described as the V_G at which I_D becomes greater than the *off-current*, I_{OFF}. The region between V_{ON} and V_T is known as the subthreshold region and here the subthreshold slope, *SS*, can be found using the following equation:

$$SS = \frac{\partial V_G}{\partial (log I_D)} \tag{2.23}$$

A steeper slope and a corresponding low value of *SS* is preferred, as this is indicative of a device that can switch on and off very quickly, acting as a fast electronic switch. A high $I_{ON/OFF}$ is also important for a clear distinction between the off and on states during switching, with $I_{ON/ON} > 10^6$ being a typical requirement for practical application. V_T can be calculated by plotting $\sqrt{I_D}$ vs V_G and extrapolating to find the *x*-axis intercept, as shown in Figure 2.9.

As V_T is considered to be the voltage required to fill traps in order to produce mobile charges in the channel, it is generally indicative of deep trap states. On the other hand, the *SS* is indicative of shallow trap states that need to be filled in order to raise I_D by one decade, as shown in Equation 2.23 [9].

2.3.4 The dielectric and the semiconductor/dielectric interface

The choice of dielectric is of the utmost importance to the entire operation of the OTFT. First and foremost, the dielectric plays the role of an insulator and it therefore must have a high

resistivity to ensure that there is low gate leakage. It must be able to sustain a reasonable amount of electric displacement and not become damaged/stop insulating at low electric fields, i.e. have a high dielectric breakdown, E_B.

Secondly, the dielectric determines the applied voltages that are required to operate the transistor. The requirement of low OTFT operating voltages is a popular topic, as to-date the vast majority of OTFTs require high operating voltages (> 50-60 V); this renders them unsuitable for low power commercial applications, which ideally require an operating voltage of less than 5V. Equation 2.17 indicates that increasing the capacitance of the dielectric can increase the drain current at lower operating voltages. With this in mind, the following equation states that the capacitance can be increased – and hence the operating voltage can be reduced – either by reducing the thickness of the layer or increasing the dielectric constant:

$$C_{\mathrm{i}} = \varepsilon_0 \left(\frac{k}{d}\right) \tag{2.23}$$

where k is the dielectric constant and d is the thickness.

Finally, as the OTFT channel only forms within a few nanometres of the semiconductor/dielectric interface [10], this interface itself is of critical importance [66]. For this reason, a lot of research has been done to try and improve, as well as understand the nature of, how the semiconductor/dielectric interface affects OTFTs [67] [68] [69]. In fact, in some cases it has been shown that this interface has more effect on charge trapping than the bulk semiconductor itself [70] [71] [72], and therefore has serious implications for OTFT performance and stability.

When considering the effects of the semiconductor/dielectric interface, the following factors need to be taken into account: (i) dielectric surface roughness, (ii) dielectric surface energy, (iii) dielectric surface polarity/hydrophobicity and (iv) the dielectric constant. The choice of OTFT architecture will determine which of these factors have the most prominent effects. For example, the bottom-gate (BG) structures shown in Figure 2.6 (a) and (b) have been popular for many years due to the accessibility of degenerately doped silicon wafer substrates which spontaneously form a layer of silicon dioxide via thermal oxidation. Here, the silicon acts as a gate and silicon dioxide acts as dielectric. As the semiconductor is deposited on top of the silicon dioxide dielectric, the dielectric surface energy and surface roughness will affect the formation of the semiconducting layer, and hence effect electrical performance [69]. To minimise the effects of dielectric roughness and surface energy, surface treatments can be used. As the work in this thesis focusses on top-gate (TG) structures, specific BG surface treatments

will not be covered here, but more information on this approach can be found in references [66], [73] and [69].

In a TG structure (Figure 2.6 (c)), other factors such as surface polarity and dielectric constant are more influential. For example, the surface polarity of the dielectric will have a significant influence on the electronic structure in the channel. In addition, if the dielectric surface introduces certain functional groups at the semiconductor/dielectric interface, then it is possible for charge trapping to occur here, hindering transport within the channel [74]. Dipole moments with random orientations at this interface can interact with charges in the channel, broadening the DOS at the channel; it is therefore possible that this region can have significantly more deep traps in comparison to the bulk semiconductor [75].

Charge trapping at the semiconductor/dielectric interface can reduce OTFT operating characteristics and cause hysteresis; the latter is typically seen in the transfer curve as higher or lower currents for the forwards sweep than the backwards sweep. Polar, non-crosslinked polymeric materials as dielectric layers are typically avoided in order to prevent unwanted hysteresis. This approach also helps prevent a shift in V_T during OTFT operation (known as the *bias-stress effect*, which will be discussed further in *Chapter 3* and *Chapter 6*) which can arise from moving ions. In addition, the surface of any material needs to be treated differently to the bulk properties, due to the presence of unterminated features such as dangling bonds, for example. Here, structural defects or even any impurities can lead to regions of lattice compression and – as outlined in Section 2.2.4 – this can introduce trap states from local areas of increased polarisation; indeed, it has been shown spectroscopically that deeps traps can be established by structural defects [74].

It should also be noted here that there are certain material property requirements that apply to the dielectric as well as the semiconductor. In order to realise the dream of OTFTs in commercial applications the materials that are used for OTFT semiconductors and dielectrics must be low cost, as well as solution-processable at low temperatures, so that they are compatible with printing techniques and flexible, plastic substrates. The solution-processability attribute also means that the dielectric must use an orthogonal solvent that dissolves the gate dielectric, but not the semiconductor; in other words, in TG structures when the dielectric layer is deposited on top of the semiconductor layer, the solvent used for the dielectric solution must not dissolve/damage the semiconductor. The high solubility of some organic semiconductors, particularly small-molecules, can make this difficult and therefore this limits the choice of dielectric materials.

2.3.5 Contact resistance and the metal/semiconductor interface

In *p*-type OTFTs operating in accumulation mode, holes are injected/extracted from the source/drain electrodes into the HOMO of the semiconductor. In order for the holes to be efficiently injected into the HOMO, the energy of the holes, which is determined by the *work function* of the metal electrode, φ_m, must be equivalent to the HOMO energy level. In the same way, for an *n*-type OTFT, the work function of the electrodes should match the LUMO energy level so that electrons are efficiently injected into the LUMO. For this reason, many polymeric materials are either *p*-type or *n*-type, and the polarity of the OTFT depends on the work function of the source and drain electrodes relative to the transport energy levels of the semiconductor.

If there is a difference in energy between the work function φ_m and the HOMO (LUMO) of the *p*-type (*n*-type) semiconductor, then this will create a potential barrier to charge injection and extraction. The metal/semiconductor interface is then considered a Mott-Schottky barrier, where the height of the barrier is determined by the difference between the HOMO (LUMO) and φ_m.

The existence of the potential barrier at the contacts is known as *contact resistance* and it significantly affects OTFT operation. Contact resistance effects can be seen in the output curve via a superlinear increase in the drain current when the drain voltage is close to zero; however, there are many other ways in which contact resistance manifests itself in the measurements, often with devastating consequences for the OTFT. If the contact resistance is very large, the transistor's operating characteristics are severely reduced due to a lack of injected charge carriers, quashing the mobility. Contact resistance is also problematic for minimising OTFT channel dimensions [76], because at small channel lengths the drain bias is prohibited from being applied over the whole channel [76]. Long channel dimensions are therefore primarily used in research for high-performance OTFTs.

The most common way to calculate the contact resistance is to use a scaling law method [77], which is as follows:

$$R_{\mathrm{ON}} = \frac{\partial V_{\mathrm{D_lin}}}{\partial I_{D_lin}} = r_{\mathrm{channel}} L + R_{\mathrm{C}} \tag{2.24}$$

where R_{ON} is the total resistance as a function of L, $r_{channel}$ is the channel resistance and

R_C is the contact resistance. $r_{channel}$ can also be used to calculate a corrected linear mobility, μ_C:

$$\mu_{\mathrm{c}} = \frac{1}{WC_{\mathrm{i}}} \frac{\partial ({r_{\mathrm{channel}}}^{-1})}{\partial V_{\mathrm{G}}} \tag{2.25}$$

The contact resistance barrier height can be minimised by choosing a metal with a suitable φ_m for the HOMO (LUMO) of the semiconductor. There are also other ways to improve the contact resistance, for example, by changing the OTFT architecture [76], increasing the channel dimensions, or using a contact modifying treatment. In terms of the OTFT architectures shown in Figure 2.6, the interface between the source and drain electrodes and the semiconductor can vary enormously. For example, the contact area in the BG-BC device shown in Figure 2.6 (b) is much smaller than the contact area in the BG-TC and TG-BC architectures in Figure 2.6 (a) and (c), resulting in higher contact resistance. In the cases for BG-TC and TG-BC (Figure 2.6 (a) and (c)), the apparent work function of the source and drain electrodes can be modified by using a *self-assembled monolayer* (SAM) that deliberately introduces a dipole at the metal surface, adjusting the potential barrier seen by the charge carriers. One example of a SAM that is widely used for source/drain modification in *p*-type OTFTs is the fluorinated thiol molecule pentafluorothiophenol (PFBT). Contact resistance in inorganic TFTs is reduced via semiconductor doping processes [51]; it can also be reduced using doping in OTFTs. This is discussed further in *Chapter 3*, along with the impact of contact resistance on mobility extraction.

2.3.6 Integrated circuits: The NOT gate

In order to use transistors in practical applications, they need to be incorporated into integrated circuits. The most fundamental component of any integrated digital logic circuit is an inverter, or a NOT gate. The NOT gate will return a high output from a low input – i.e. a high V_{OUT} will return a low V_{IN} – and vice versa.

Two transistors can be used to assemble an inverter in two ways: (i) using two TFTs of the same polarity, known as a unipolar inverter and (ii) using two TFTs of opposite polarity, known as a complementary inverter. A complementary logic inverter is shown in Figure 2.10; these inverters have greater noise margins, lower power consumption and larger gains, where the gain is defined as:

$$g = \frac{\partial V_{\mathrm{OUT}}}{\partial V_{\mathrm{IN}}} \tag{2.26}$$

Complementary logic inverters do, however, require a balanced performance from the *n*-type and *p*-type TFTs. This is currently a challenge for high performance all-organic

complementary inverters, as *p*-type semiconductors are known to far outperform *n*-type semiconductors due to the poor stability of easily oxidised *n*-type materials.

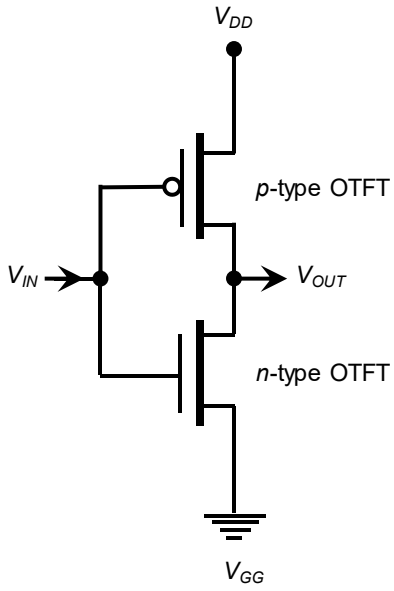

Figure 2.10: Circuitry of a complementary logic inverter.

Chapter 3

Background

This chapter gives an overview of the literature on two exciting topics associated with OTFTs. The first part of this chapter discusses organic small-molecule/polymer blend systems, which have attracted significant interest over the years and are highly promising candidates for use in OTFTs for numerous commercial applications. The second part reviews the literature on molecular doping in OTFTs. Doping has revolutionised inorganic semiconductor technology and has been key for developing efficient OLEDs and OPVs; molecular doping in OTFTs has the potential to rectify the current performance related issues, yet despite this, doping research for OTFTs is still "lagging behind" the research that has been undertaken for other organic devices. In summary, the literature review presented herein indicates that there is a gap in the market for two things: (i) advanced, 3rd generation organic blend systems that surpass the benchmark mobility of 10 cm^2/Vs, and (ii) further research into controlled doping techniques, particularly those that overcome lattice/microstructure interruptions from the dopant molecules and promote charge carrier transport.

3.1 Organic small-molecule/polymer blends for OTFT applications

3.1.1 Introduction

Blending materials to combine the beneficial properties of multiple components in a single system is not an uncommon process and has been known to mankind for many years [78]. In the field of organic electronics, blending organic semiconducting materials – both for enhanced mechanical and electronic properties – is used in solar cell [79] and OLED [80] applications, and is a popular choice for OTFTs. Although there are some blended OTFT systems that combine two polymers [81] [82], one particularly interesting and auspicious system is a blend consisting of a small-molecule and a polymer. The reason for blending these two materials together is as follows: small-molecules, known for their superior crystallinity and subsequent high mobilities, are renowned for being difficult to process from a solution phase [83] [84] [85]. On the other hand, polymers have exceptional solution-processing and film-forming qualities, but due to their comparatively disordered nature they generally have lower mobilities [85] [86]. Combining the two materials produces a system that is the best of both worlds, having the prominent electrical attributes associated with the small-molecule, as well as the film forming traits of the polymer binder [87] [88].

3.1.2 Background

In the early-to-mid 2000s, prior to the wealth of academic literature that is now available on OTFT small-molecule/polymer blends, it was well-known that blending organic semiconductors (OSCs) could indeed enhance integrity and stability, but the organic binder essentially "diluted" the electrical performance. For this reason, a reduction in mobility by at least an order of magnitude was expected from such systems [89].

In 2004, Brown et al. filed a patent that challenged this popular belief. They reported that, surprisingly, blending a semiconducting small-molecule with an insulating polymer binder does not have any impact on the mobility [89]. Furthermore, whilst spin-coating neat polyacene over large areas resulted in non-uniform films with poor device uniformity, the blending technique was seen to dramatically improve the quality of the film and device uniformity.

Brown et al. investigated the blend in a dual-gate TFT structure and high mobilities, associated with the small-molecule component, were only observed for the TG-BC structure. For this reason, it was hypothesised that the excellent performance of the TG-BC structure was

due to vertical phase separation of the small-molecule and the polymer, where the small-molecule segregated to the surface/air interface and hence the channel of TG-BC devices.

In 2006, a second follow-up patent filed by Ogier et al. demonstrated that by employing a semiconducting polymer binder into the blend system rather than an insulating polymer binder, significant improvements in the blend performance could be achieved. Ogier et al. hypothesised that this was due to an improved pathway between the source/drain contacts and the channel [90].

The two patents by Brown et al. and Ogier et al. laid the groundwork for the academic literature that was about to follow. They had highlighted the two most important aspects of the blend system: (i) the vertical phase separation of the two components [27] [88] [91] and (ii) the choice of polymer binder [87] [88].

3.1.3 Vertical phase separation

3.1.3.1 The Flory-Huggins theory

The Flory-Huggins theory is a lattice-based model widely used to predict what will happen when two polymers are mixed together. Consider two materials with different properties; material A consits of n_A moles and is contained in volume V_A, and material B consists of n_B moles and is contained within volume V_B. If the two materials are mixed together to occupy the combined volume of $V_A + V_B = V_{AB}$, then by considering the change in the *Gibbs free energy*, it can can determined whether the two materials will mix together or not. This change is known as the *Gibbs free energy of mixing*, ΔG_{mix}, where

$$\Delta G_{\mathrm{mix}} = G_{\mathrm{AB}} - (G_{\mathrm{A}} + G_{\mathrm{B}}) \tag{3.1}$$

with G_A and G_B being the Gibbs free energy of the separate states and G_{AB} is the Gibbs free energy of the mixed state.

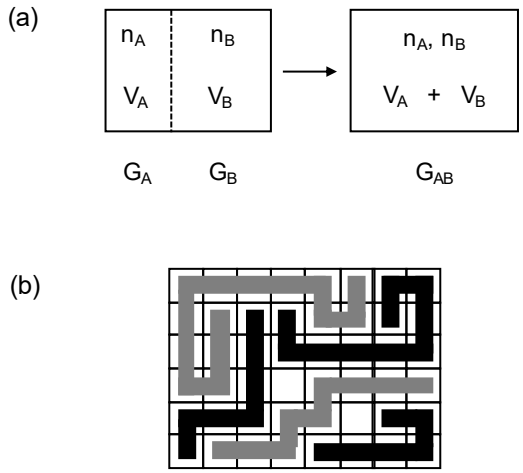

Figure 3.1: The Flory-Huggins theory. (a) The mixing of polymer A and polymer B (G. Strobl, 2007:p.106) [92], (b) a schematic of the lattice model used in the Flory-Huggins theory, where all polymer units occupy cells of the same volume in a regular lattice and all interactions can only occur between nearest neighbours (G. Strobl, 2007:p.110) [92].

The Flory-Huggins theory considers there to be two contributions to ΔG_{mix}, which ultimately determine what happens during (and after) the mixing process:

$$\Delta G_{\text{mix}} = -T\Delta S_t + \Delta G_{\text{loc}} \tag{3.2}$$

where T is the temperature of the system, ΔS_t is the translational entropy that describes the increase in entropy due to the movement of the polymer molecule centres of mass, and ΔG_{loc} is used to describe local interactions of the monomers. An increase in ΔS_t resulting in a decrease in the Gibbs free energy of mixing from the $-T\Delta S_t$ term, is always indicative of mixing. ΔG_{loc} depends on the specific character and properties of the monomers, where in general, equal or similar monomers are more likely to be attracted than unlike monomers.

The Flory-Huggins treatment then defines these two contributions as follows:

$$\frac{\Delta S_t}{R} = -n_{\text{A}} ln\phi_{\text{A}} - n_{\text{B}} ln\phi_{\text{B}} \tag{3.3}$$

$$\Delta G_{\text{loc}} = RT\frac{V}{v_c}\chi\phi_{\text{A}}\phi_{\text{B}} \tag{3.4}$$

where R is the *gas constant*, φ_A and φ_B are volume fractions of A and B (i.e. $\varphi_A = V_A/V$), v_c is the volume occupied by a reference monomer that is representative of the system and χ is the *Flory-Huggins parameter* which represents the local change in free energy per reference unit.

Combining Equations 3.2, 3.3 and 3.4 gives the Flory-Huggins expression:

$$\Delta G_{\text{mix}} = RTV\left(\frac{\phi_A}{v_A}\ln\phi_A + \frac{\phi_B}{v_B}\ln\phi_B + \frac{\chi}{v_c}\phi_A\phi_B\right) \tag{3.5}$$

where v_A and v_B are molar volumes for polymers A and B respectively, i.e. $n_A = V(\varphi_A/v_A)$ and $n_B = V(\varphi_B/v_B)$. Assuming that all polymer units, regardless of which polymer they belong to, occupy the same cell volume in a regular lattice and all interactions can only occur between nearest neighbours, the Flory-Huggins expression (Equation 3.5) can be used to describe the miscibility of two materials, where positive χ values result in incompatability and negative χ values result in mixing [92].

By using the Flory-Huggins theory, phase diagrams can be constructed to predict if polymers will coexist and what conditions are required for their coexistance. This can give information on what temperatures and compositions will lead to stable, meta-stable and unstable states and if/how phase separation occurs.

In terms of OTFT applications, ΔG_{mix} and χ have not only been used to study the evolution of small-molecule/polymer blend films, such as blends made from 6,13-bis(triisopropylsilylethynyl) pentacene (TIPS-pentacene) and poly(alpha-methylstyrene) (PaMS) [93], but they have also been used to enhance the performance of OTFTs. For example, Cho et al. found that if they maximised ΔG_{mix} and χ by choosing an appropriate polymer binder and varying the blend volume fractions, they could improve the performance of TIPS-pentacene-based blend OTFTs [94].

3.1.3.2 Small-molecule/polymer blend liquid-liquid phase separation

For solution-processable small-molecule/polymer blends, there is an additional component present in the system – the solvent. The presence of the solvent tends to complicate the mixing process, as it introduces additional interactions which need to be taken into account. As a result of these complicated interactions, the phase-separation can be affected by blend ratio, solvent choice and solution concentration/viscosity.

A solution-phase small-molecule/polymer blend will undergo liquid-liquid phase separation after it has been deposited. There are two routes by which liquid-liquid phase separation can occur: (i) spinodal decomposition or (ii) nucleation and growth [27] [95]. The former case is a spontaneous process, occuring due to the miscibiliy of the blend components, which is commonplace for many polymer/polymer blends. The latter case is determined by the component that nucleates first.

In small-molecule/polymer blends, nucleation and growth processses tend to dominate liquid-liquid phase separation. Nucleation can either be homogeneous, where nuclei spontaneously appear in a meta-stable state, or heterogeneous, where the new phase appears at impurity particles or on a surface. For a small-molecule/polymer/solvent mixture, as the solution becomes supersaturated by, for example, a change in temperature or a change in solution concentration (i.e. solvent evaporation), the small-molecule component will tend to nucleate first and does so at the surface/air interface. The nucleation leads to a change in the Gibbs free energy, which drives solidification; smooth solid-liquid interfaces typically advance by the growth of lateral ledges that can result from surface nucleation or from dislocations that are intersecting the interface [96] [97].

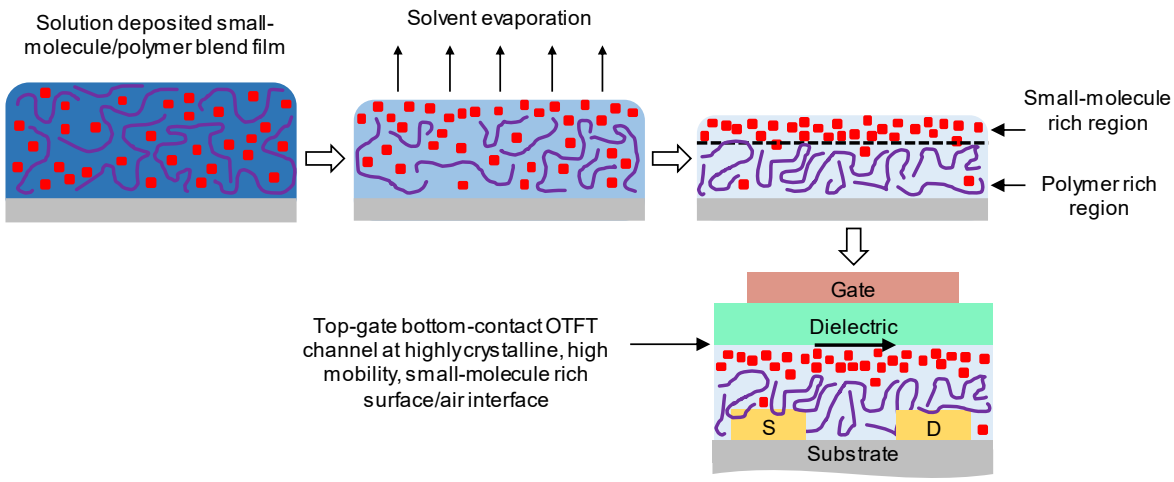

Figure 3.2: Schematic of small-molecule/polymer blend vertical phase separation. The phase separation, which leaves a layer of small-molecule on top of a layer of polymer binder is ideally suited to top-gate bottom-contact architectures, where the channel is at the surface/air interface.

For a small-molecule/polymer blend, the end result of the nucleation and growth phase separation is usually a layer of small-molecule on top of a layer of polymer, i.e. vertical phase separation. The fact that the highly crystalline, high mobility small-molecule tends to crystallise at the surface/air interface in these blend systems means that they are ideally suited to top-gate structures, where the channel is at the top surface of the semiconductor film (Figure 3.2).

However, this can be an obvious limitation if one wishes to produce bottom-gate TFTs. For this reason, studies have been undertaken with the aim of controlling the vertical phase separation so that the small-molecule nucleates at the surface/substrate interface, rather than the surface/air interface. A number of groups have successfully demonstrated this by considering factors such as the blend ratio, processing conditions and the polymer binder [98] [99]. One example is by Zhao et al., who nicely demonstrated that trilayer stratification

(i.e. small-molecule/polymer/small-molecule) can be achieved in a blend made from 2,8-difluoro-5,11-bis(triethylsilylethynyl)an-thradithiophene (diF-TES ADT) and poly(triarylamine) (PTAA) by varying the spin-coating parameters. Using this approach, they produced BG-TC OTFTs with mobilities > 2 cm^2/Vs, concluding that the drying kinetics of this particular system determine how the diF-TES ADT is ejected during film formation [95]. Another example by He. et al demonstrated that phase separation could be switched between lateral and vertical in TIPS-pentacene blends by varying the alkyl length of the polyacrylate binder [100].

3.1.4 Small-molecule/polymer blend film morphology

Given the strong structure-property relationship exhibited in OSCs, a lot of OTFT research has focussed on methods to control/dictate the morphology and molecular arrangement of OSCs using reproducible and reliable methods. Because small-molecule/polymer blends offer a wide range of morphologies compared to any single material system, they have received a great amount of interest in this area. The diverse range of morphologies that blend systems have to offer depends on a range of factors such as: degree of polymer crystallinity, system miscibility, solvent choice, solvent evaporation rate, solution viscosity, polymer binder, diffusivity, choice of fabrication technique, temperature treatment, substrate/surface properties and interactions such as surface tension and wetting [94] [101].

3.1.4.1 Small-molecule formation

The size of the crystallites/grains in solution-processed small-molecule thin-films has been an attractive topic over the years [102] [103]. Efficient charge transport is enabled in ordered crystallites but inhibited and trapped at the disordered grain boundaries [104], therefore high mobilities generally correlate with larger grain sizes [105].

For solution processing techniques, the sizes of the small-molecule crystallites are determined by solvent evaporation rates. This means that for processes such as spin-coating, where the film formation happens on very short timescales, nucleation rates are increased and the grain sizes are significantly reduced due to the severe kinetic limitations imposed by the fast solvent evaporation. For these reasons, ways for reducing nucleation rates during solution-processing have been highly sought after.

One simple way of reducing nucleation rates, controlling the growth processes and hence improving the film-forming properties is to blend the small-molecule with a polymer. For this reason, the well-known, highest mobility small-molecules have been widely researched

in small-molecule/polymer blend systems, i.e. TIPS-pentacene [106] [107] [108] [109], rubrene [110] [111], dif-TES ADT [112] [113] and C_8-BTBT [33] [114].

A number of variables have been found to have a strong influence on how small-molecules nucleate in blend systems, such as solvent choice (including poor solvent introduction) [83] [110] [115] [116], blend ratio [91] [98], processing and substrate temperature [33] [98] [110], surface treatment/wetting [94] [117] [118], and indeed the polymer binder in terms of molecular weight and whether it has amorphous or semi-crystalline properties [99] [119] [120] [110] [121].

3.1.4.2 Processing techniques

Further control over the formation of the blend has been achieved by using external processing techniques. Over the years, the versatility of the blend system has been demonstrated through its use in a wide range of fabrication techniques. Examples of fabrication techniques include: spray deposition [122] [123], line-printing [124], air-brushing [125], ink-jet printing [98], dipping processes [106], vertical flow [107], blade coating [115] [117] and off-centre spin-coating [126]. Blade coating – which is a solution processing technique that is suited to large scale application with minimal waste – has recently shown some particularly interesting blend results. For example, using diF-TES ADT and TIPS-pentacene blends, Niazi et al. highlighted that the blend nucleation and growth processes are different in blade coating than spin-coating [117]. They take this work one step further in a later publication; by carefully controlling the processing conditions of the blade coating technique, they report diF-TES ADT:PS blend OTFTs with mobilities close to the mobility values that have been reported for diF-TES ADT single crystal OTFTs [115] [127].

Another option for controlling blend crystallisation is to introduce an additive into the blend, which was first demonstrated in 2005 by Stingelin-Stutzmann et al, who used a vitrifying species to control the crystallisation of rubrene blended with UHMW-PS [128]. Other examples include work by Chen et al., who saw that the introduction of additives within the polymer binder resulted in new TIPS-pentacene polymorphs with excellent long-range order, leading to enhanced charge transport properties without the need for extra equipment to externally align the blend OSC [129].

3.1.5 Ambipolar blend OTFTs

An alternative application for the blend systems is to combine a *p*-type OSC with an *n*-type OSC, producing blends for ambipolar OTFTs. In fact, this was one of the primary uses for the blend system in the early days of small-molecule/polymer blend academic

literature [130]. One early example is where Babel et al. blended a *p*-type small-molecule, copper phthalocyanine (CuPc) with an *n*-type polymer, poly(benzobisimidazobenzophenanthroline) (BBL) in 2004 [131]. Although in the past this approach appeared to hinder the *p*-type and *n*-type mobilities rather than enhance them [87], ambipolar blend OTFTs with improved performance have been demonstrated since then [132] [133].

3.1.6 Insulating polymer binders

There is a wealth of literature for small-molecules – particularly TIPS-pentacene – that have been blended with insulating polymer binders such as PαMS, PMMA and PS. First and foremost, insulating polymer binders can, quite simply, be used to improve the film formation and device uniformity [120].

Secondly, insulating binders – both amorphous and semi-crystalline – have been used to understand, explore and control blend morphology and phase separation [121].

Finally, the vertical phase separation of an insulating polymer and a semiconducting small-molecule lends itself very neatly to the self-assembly of an OSC and dielectric layer. This type of one-step deposition processing has been demonstrated in OTFTs on numerous occasions [134] [135] [136]. One of the interesting aspects of this approach is the intimate contact between the insulating polymer and small-molecule after phase separation. The contact at this interface has been shown to have a pronounced effect, known as a "zone refinement effect". During vertical phase separation, there is a preference for any impurity species to remain in the polymer-rich layer, removing them from the interface and hence the channel, where they would otherwise inhibit charge transport and OTFT performance [126] [137] [138].

For example, Yuan et al. [126] blended the high-mobility small-molecule C_8-BTBT with polystyrene for use in their new application process, which they called off-centre spin-coating (OCSC). They observed higher mobilities for the C_8-BTBT blended with PS than the neat C_8-BTBT, due to the vertical phase separation of the blended system, which results in a very thin layer of PS between the C_8-BTBT OSC and poly(4-vinylphenol) (PVP) dielectric. The PS tends to segregate towards the PVP surface as this is the energetically favourable option, given the differences in surface energy between the C_8-BTBT and PVP, and it is suggested that this ultrathin layer of PS may help to reduce surface traps at the semiconductor/dielectric interface, which otherwise would have been caused by the polar hydroxyl groups in the PVP. Similar effects were indicated by Niazi et al. whilst blade coating diF-TES ADT:PS blend BG-BC OTFTs; they note an improvement in the subthreshold slope for the blend compared to

the neat small-molecule and attribute this to a reduction in interfacial trap density at the semiconductor dielectric/interface [115].

3.1.7 Semiconducting polymer binders

But the pivotal question when it comes to any OTFT system is: how is the mobility affected? Mobility values are an area where small-molecule/polymer blends have been remarkably successful; there are two prominent blends that stand-out as pioneering, with both achieving record breaking solution-processed mobility values: (i) the *1st generation blend*, (ii) the *2nd generation blend*.

3.1.7.1 1st generation blend

In 2009 Hamilton et al. developed a blend made from diF-TES ADT and PTAA, which exhibited record breaking solution-processed hole mobility values of μ_{sat} = 2.4 cm^2/Vs [87]. The mobilities for the diF-TES ADT:PTAA blend were double the value of neat spin-coated diF-TES ADT films [139] and also higher than diF-TES ADT blended with an insulating polymer binder (PαMS). This system demonstrated the significance of the blending process as well as using a semiconductor polymer over an insulating polymer.

Hamilton et al. also highlighted the importance of the unique vertically phase separated microstructure by using vertical profiling techniques and investigating the blend film in a dual-gate TFT architecture (Figure 3.3 (d)). Not only did the top-gate OTFTs show increased mobility due to the layer of high-mobility small-molecule at the channel, but better hysteresis and threshold voltages were observed, indicating that blending improved energetic disorder.

This was the first blend in the academic literature to demonstrate the importance of the semiconducting polymer binder, and did so by achieving record carrier mobilities. The diF-TES ADT:PTAA blend system has been popular since its development in 2009 [95] [113] and has been termed the 1st generation blend.

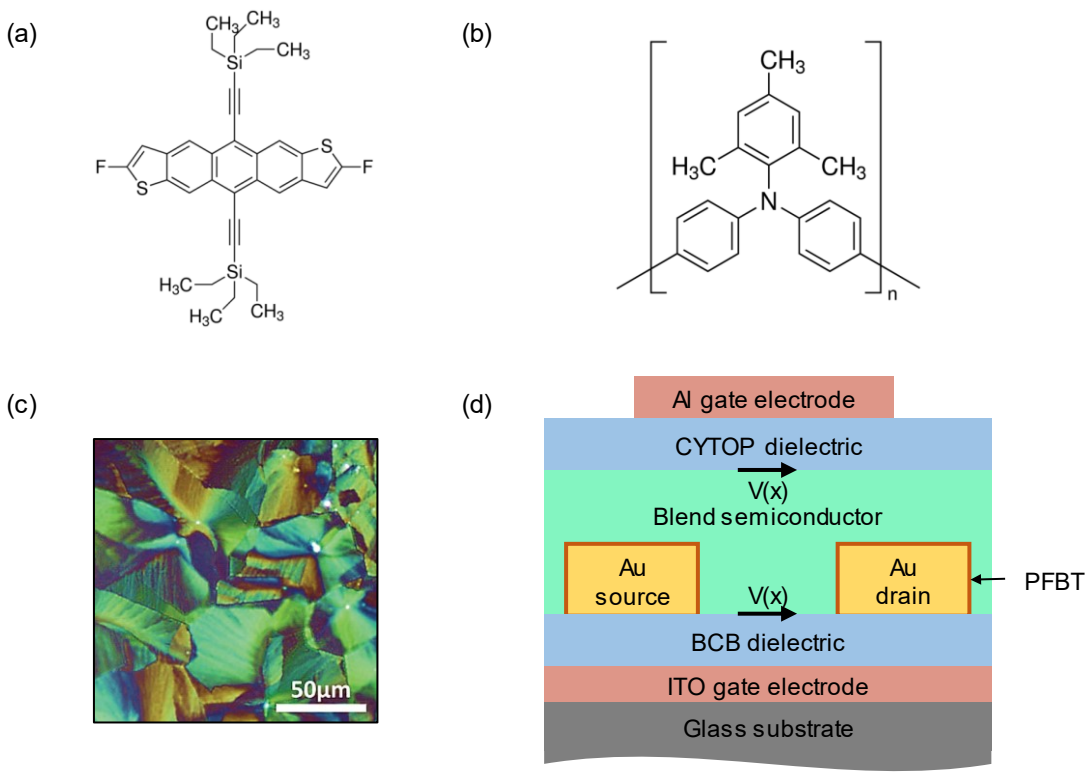

Figure 3.3: The 1st generation blend. (a) the small-molecule diF-TES ADT, (b) the polymer binder PTAA, (c) a polarised optical microscope image of the phase separated blend film (reproduced with permission from reference [140]), and (d) a schematic of the dual gate structure used by Hamilton et al in [87].

3.1.7.2 2nd generation blend

In 2012 the 2nd generation blend was introduced by Smith et al. This blend used the same small-molecule as the 1st generation blend, diF-TES ADT, but combined it with a higher performing semiconducting polymer binder, poly(dialkyl-fluorene-co-dimethyl-triarylamine) (PF-TAA) [88]. The diF-TES ADT:PF-TAA blend was processed in exactly the same way as the 1st generation blend, i.e. the same deposition technique, spin-coating recipe, solvent and concentration, but the mobility was more than double the value of the 1st generation blend, increasing from 2.4 cm^2/Vs to > 5 cm^2/Vs.

Smith et al. had demonstrated record breaking solution-processed OTFT mobilities by changing the polymer binder in the 1st generation blend [88]. These important results suggest that the polymer does not only impact charge transport properties by aiding film formation, morphology and nucleation/growth kinetics of the small-molecule, but that it also has an intrinsic role in the blend OTFT electrical performance.

To shed some light on the success of the 2nd generation blend system, Smith et al. highlighted that the intrinsic mobility of the polymer binder may enhance charge transport between the diF-TES ADT-rich regions at the surface/air interface, in addition to providing a more effective pathway between the source/drain contacts and the channel. They also discussed the importance of energy level matching throughout the system, i.e. between the small-molecule, Au electrodes and the polymer binder.

3.1.7.3 Energetic disorder in small-molecule/polymer blend systems

There are some important points about the small-molecule/polymer blend system that have been highlighted by the 1st generation and 2nd generation blends. If a simple solution deposition technique, i.e. spin-coating, is taken as a base point, then the important points can be summarised as follows:

1. If a small-molecule is blended with an insulating polymer binder, it will demonstrate better film forming and hence electrical performance properties than its small-molecule counterpart.
2. If the insulating polymer binder is exchanged for a semiconducting polymer binder, then this will increase the mobility of the blend (shown with the 1st generation blend).
3. If the semiconducting polymer binder is exchanged for an alternative semiconducting polymer binder with better electrical properties, this will further increase the mobility of the blend (shown with the 2nd generation blend).

Because of this, further studies have been undertaken to investigate why these systems and their unique phase separated microstructures are so successful.

One such study was by Hunter and Anthopoulos, who investigated the 1st generation blend processed in two slightly different ways: one film was annealed at a higher temperature, which produced small diF-TES ADT crystallites, and another film was annealed at lower temperatures to slow the evaporation rate, resulting in large crystalline domains. Surprisingly, they found that there was no difference in OTFT performance between the two morphologies.

To investigate this further, they used conducting probe atomic force microscopy to look at the two versions of the diF-TES ADT:PTAA films, which gave unusual and interesting results: the grain boundaries – which are known to inhibit charge transport in OSCs [141] (and indeed it has been shown previously that trapping at the grain boundaries dominates the transport in both of these blend microstructures [91]) – appeared to be highly conductive. What was even more interesting was that this high conductivity was only observed in the blend films, not for the neat blend components. They also observed conductive grain boundaries in blends

made from TIPS-pentacene:PTAA as well as diF-TES ADT:PTAA, suggesting inter-grain connectivity from the mixed-phase grain boundaries may well be a generic effect of a small-molecule/polymer blend.

The effects of blending on trap states were further elucidated by Hunter et al., who used low temperature measurements to show that, although there is an increase in the average trap energy, there is a narrower trap distribution in the diF-TES ADT:PTAA blend than in the neat diF-TES ADT devices.

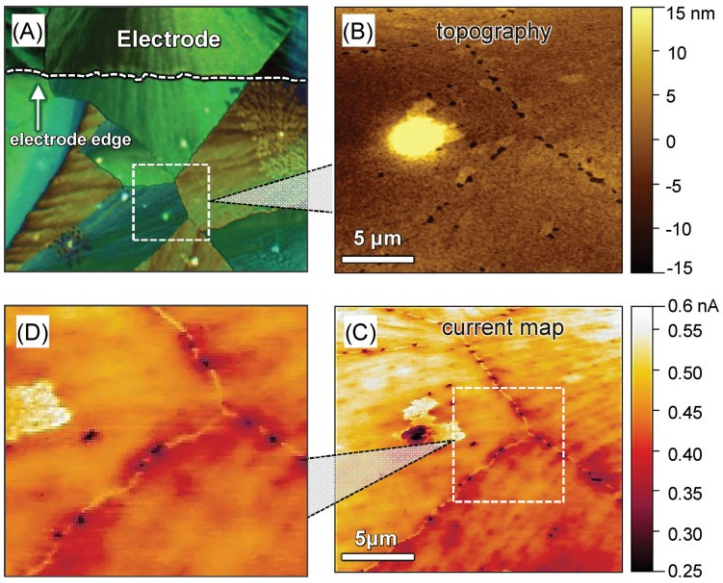

Figure 3.4: Conductive grain boundaries. (a) Polarised optical microscope image of diF-TES ADT:PTAA blend, (b) atomic force microscopy image of the grain boundaries in the region highlighted in (a), (c) lateral-transport current map of the area shown in (b) demonstrating electrically connected crystallites, (d) current map of the region highlighted in (c), showing grain boundaries as "conductive filaments". Reproduced with permission from reference [140].

3.1.7.4 Next-generation blend systems

The remarkable effects on energetic disorder from a simple blending technique are one of the reasons that the organic small-molecule/polymer blend has been such a popular choice for OTFTs. The 1st and 2nd generation blends received great attention when they were published and became renowned for their influence on mobility. Given the recent improvements in mobility values from other organic semiconducting systems for OTFT applications, there is one interesting question that remains about the small-molecule/polymer blend: is it possible to further increase its performance to surpass the benchmark mobility of 10 cm^2/Vs?

3.2 Molecular doping in OTFTs

3.2.1 Introduction

The eureka moment for the inorganic electronic technology that has shaped our everyday lives was realising that conduction in silicon could be controlled by doping [39]. Doping has therefore been established as a critical factor for modern electronics for many years. Furthermore, in 1977 the field of organic electronics originated from the Nobel prize winning discovery of conductivity in polyacetylene, which was brought about by doping [5] [6].

However, despite the known significance of this technique, the controlled, intentional doping of OTFTs has yet to be realised with the same substantial impact that it has had for inorganics due to practical utilisation issues. Although doping in OTFTs has been investigated, this particular area is underdeveloped, especially when compared to organic photovoltaics (OPVs) [142] [143] [144] and commercially available organic light-emitting diodes (OLEDs) [39] [41] [145], where doping been crucial for their development.

For OTFTs to be used in industrial applications, for example, current-driven OLED active matrix displays, operating characteristics such as mobility, stability, threshold voltage, charge injection/contact resistance and operating voltages must be improved [7]. In recent years we have seen promising demonstrations of how doping can impact these critical characteristics [35] [64] [146] [147] [148] [149] [150] [151] and theoretically, molecular doping may have the potential to be an all-round solution for the performance related issues that are currently hindering the commercial application of OTFTs.

3.2.2 Mechanisms of molecular doping and doping materials

3.2.2.1 The standard model: Integer charge transfer

The standard model for doping in OSCs is analogous to doping in inorganic semiconductors, i.e. a dopant is purposefully introduced to either remove/donate electrons from/to the energy levels of an OSC. In the case of *p*-type organic systems, charge carriers are removed from the highest occupied molecular orbital (HOMO) of the semiconductor to the lowest unoccupied molecular orbital (LUMO) of the dopant (see Figure 3.5). In the case of *n*-type doping the opposite occurs, integer charges are transferred from the LUMO of the OSC to the HOMO of the dopant. This charge transfer process leaves a localised charge carrier on the dopant and a mobile charge carrier within the OSC matrix, which increases the concentration of either holes ($HOMO_{OSC} \rightarrow LUMO_{dopant}$) or electrons

($LUMO_{dopant}$ → $HOMO_{OSC}$). The increase in the number of charge carriers will subsequently shift the Fermi level (E_F) towards the transport band [5].

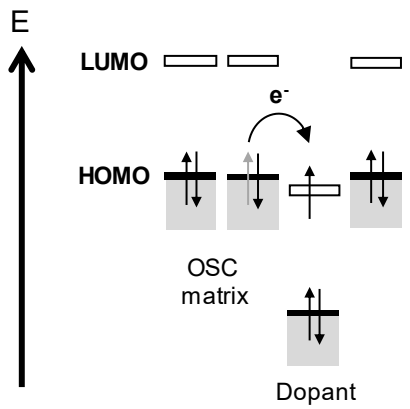

Figure 3.5: Schematic of integer charge transfer processes for *p*-doping in OSCs.

To be effective, the integer charge transfer process requires a dopant with energy levels that are well matched to the OSC, to allow electron transfer into or out of the OSC matrix as shown schematically in Figure 3.5. Up until now this has been the main driving force in terms of design criteria for dopants [152]. In the case of *p*-type dopants, the main aim is to have an *electron affinity* (EA) as high as possible; fluorination has been a critical tool for this, with increasing fluorination leading to an increase in EA [5] [153] [154]. Examples of *p*-dopants include 2,3,5,6-Tetrafluoro-7,7,8,8-tetracyanoquinodimethane (F_4-TCNQ) [155], $C_{60}F_{36}$ [156] and $C_{60}F_{48}$ [157] [158].

The requirement for well-matched energy levels is a key reason for the large discrepancy between the number of *p*-type dopants available and *n*-type dopants available. *N*-type dopants require a high HOMO level so that it is above the LUMO level of the OSC matrix. As high HOMO levels can lead to oxygen instability, air-stable precursor materials or alkali metals have often been used for *n*-dopants instead of high HOMO level materials [39] [159] [160]. Examples of *n*-dopants include 4-(2,3-Dihydro-1,3-dimethyl-1H-benzimidazol-2-yl)-N,N-dimethylbenzenamine (N-DMBI) [161] and cesium fluoride [162].

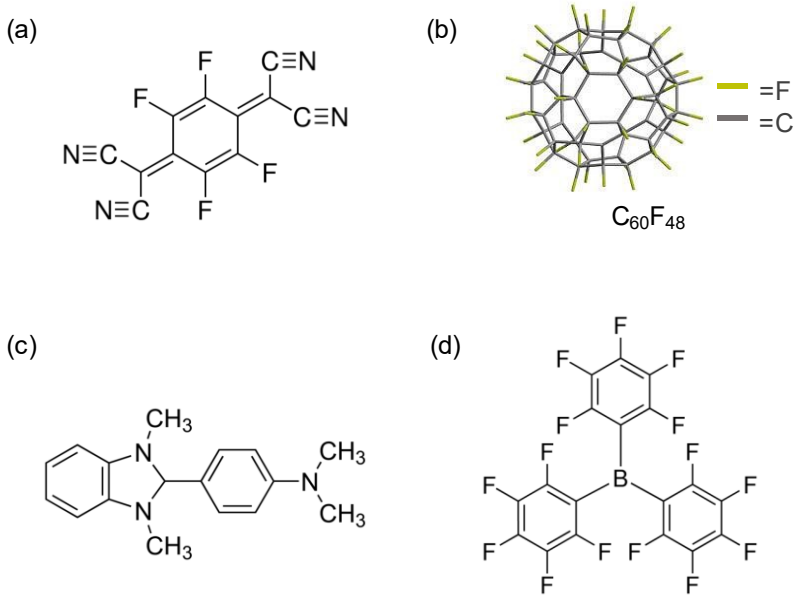

Figure 3.6: Examples of dopants for organic semiconductors. (a) 2,3,5,6-Tetrafluoro-7,7,8,8-tetracyanoquinodimethane (F_4-TCNQ), (b) $C_{60}F_{48}$, (c) 4-(2,3-Dihydro-1,3-dimethyl-1H-benzimidazol-2-yl)-N,N-dimethylbenzenamine (N-DMBI), (d) BCF.

3.2.2.2 The alternative model: Charge transfer complex formation

In recent years there has been some debate over the fundamental processes governing doping mechanisms in OSCs. Many dopants for OSCs are unexpectedly inefficient and, given the underlying differences between inorganic and organic semiconductors, further thought has gone into whether something other than integer transfer is happening.

Mendez et al have suggested an alternative model where, instead of an integer charge being transferred from the dopant to the host OSC, a supramolecular or ground-state charge transfer complex is formed via the hybridization of frontier molecular orbitals [5] [163]. In other words, for *p*-doping, there is a hybridization of the OSC HOMO and the dopant LUMO [164] [165] [163] [166] and the formation of this charge transfer complex results in an unoccupied molecular orbital in the bandgap of the bulk OSC [5] [151].

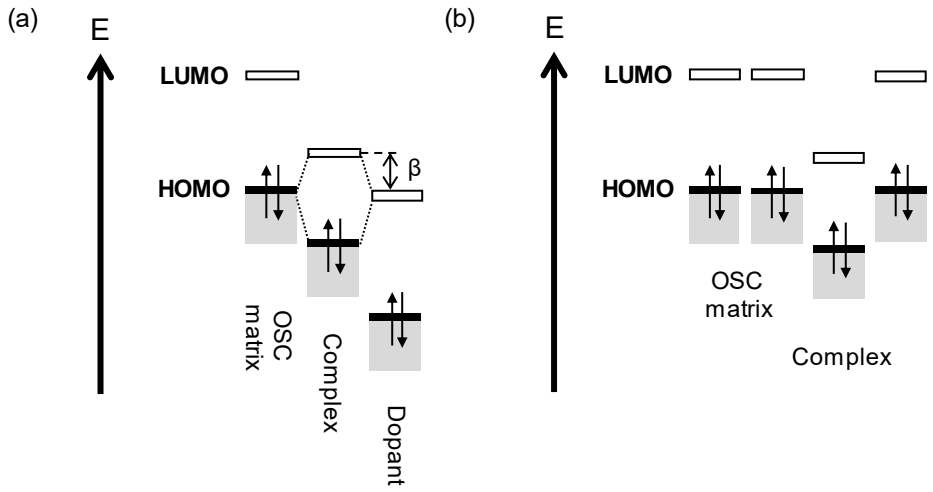

Figure 3.7: Charge transfer complex formation. (a) Schematic of the alternative model suggested by Mendez et al in [163], where hybridisation occurs between the HOMO of the OSC and the LUMO of the dopant for p-doping, forming a supramolecular complex; the intermolecular resonance integral, β, which is important for dopant design concepts is also indicated. (b) Unoccupied states in the band-gap of the host OSC matrix as a result of the complex formation. Reproduced with permission from reference [163].

Similar doping mechanisms have been shown by, for example, Han et al., where the formation of a complex between a host OSC and a dopant leads to the formation of empty levels/orbitals inside the bulk OSC bandgap. However, rather than there being a hybridization of the OSC HOMO and the dopant LUMO, Han et al. found that the formation of a Lewis acid-base complex between a nitrogen lone-pair on a host polymer and tris(pentaflourophenyl)borane ($B(C_6F_5)_3$ (Figure 3.6 (d)) had the same unconventional doping effect [151]. This work produced promising results, increasing the OTFT mobility by 11 fold and demonstrating a nice trend between the OTFT characteristics and doping concentration. There is another example of Lewis acid-base complex doping by Zalar et al., who added a Lewis acid, $B(C_6F_5)_3$, to a Lewis basic conjugated polymer, poly[(4,4-diethylhexyldithieno[3,2-b:2′,3′-d]silole)-2,6-diyl-alt-(1,4-pyridyl)-4,7-diyl] (DTS-Py), and observed an increase in the mobility values in hole-only diode devices [167].

In comparison to the integer transfer model, the alternative complex-formation model opens up the design criteria for molecular dopants. This will ultimately broaden the palette of dopants available, which in the long run should increase the opportunities for successfully doping OTFTs. Mendez et al. carried out experiments to test the most promising design strategy for complex-formation doping. It was found that increasing the EA of the *p*-dopant alone was not sufficient by itself, and that, in addition, the *intermolecular resonance integral*, *β*, must be minimised [5] [168].

Han et al. argue that doping via the formation of a Lewis acid-base is a much easier situation for molecular engineers and chemists to design materials for. To substantiate their point, they purposefully used polymers that would be difficult to dope via conventional integer charge transfer [151].

3.2.3 The importance of molecular doping in OTFTs

Trap states in OSCs are detrimental to charge transport and device operation. Introducing a molecular dopant to an OSC can donate charge carriers to trap states, and therefore is a very simple and powerful way to deactivate unwanted trap states, decrease energetic disorder and narrow the DOS.

There are a number of ways that trap states effect OTFT operation, which are manifested in experimental measurements and the critical operating parameters. When a *p*-type thin-film transistor operates in accumulation mode, holes accumulate at the semiconductor/dielectric interface as V_G is applied. The accumulation of holes causes the OSC Fermi level (E_F) to shift further towards the HOMO level. As E_F moves, deep and shallow trap states are filled en route, until the E_F passes the mobility edge and into the extended states, where the holes are mobile and therefore the OTFT can be switched on.

Based on this model, trap states significantly affect the following in OTFTs: (i) charge carriers available for conductivity, and hence $I_{ON/OFF}$ and mobility, (ii) the amount of voltage required to move E_F past the localised trap states to the delocalised states that contribute to the channel current, i.e. the threshold voltage, V_T, and on voltage, V_{ON}, and (iii) the speed at which the transistor can turn on, i.e. the subthreshold slope, *SS*. Charge trapping during device operation also affects the stability and lifetime of an OTFT, manifested as the bias-stress effect, and causes hysteresis.

This section therefore discusses the impact that molecular doping has on trap states and its influence on the key OTFT operating parameters.

3.2.3.1 Threshold voltage

V_T is associated with deep trap states in the OSC that, unlike shallow traps within kT of the transport level, are not able to contribute to charge transport [9]. In an ideal OTFT, there are no trap states, $V_T = 0$ V and mobile charge carriers are available as soon as V_G is applied. But in reality, trap states exist, and so device engineering is used to optimise V_T.

For example, one way to improve V_T is to alter the thickness of the OTFT channel [40]. Another approach for improving V_T is molecular doping. By using a dopant to donate charge

carriers to the OSC, deep trap states can be filled, which improves V_T and reduces the energetic disorder in the system [169]. For this reason, a shift in V_T towards positive (/negative) voltages is one of the key signs of a doped *p*-type (/*n*-type) OTFT system.

There are many examples of a threshold voltage shift/reduction in OTFTs that have been doped; for example, poly(3-hexylthiophene-2,5-diyl) (P3HT) polymer OTFTs doped with F_4-TCNQ, [155] small-molecule OTFTs such as TIPS-pentacene doped with tris(1-(trifluoroacetyl)-2-(trifluoromethyl)ethane-1,2-dithiolene) ($Mo(tfd\text{-}COCF_3)_3$) [170], and pentacene doped with F_4-TCNQ, [171] F_6TCNNQ, [64] and MoO_x.[172]

3.2.3.2 Bias-stress stability

The *bias-stress effect* is a shift in V_T over time associated with charge carriers becoming trapped. The charges can either be trapped in the dielectric, at the semiconductor/dielectric interface, at grain boundaries or within the bulk semiconductor [74] [173] [174]. Therefore, if charge trapping sites can be deactivated by introducing a molecular dopant, this would suggest that the dopant has an effect on bias-stress stability.

Indeed, improvements in operational stability have been demonstrated in both *p*-type, *n*-type and ambipolar doped OTFTs [160] [161] [162] [175] [176]. For example, Khim et al demonstrated improvement in bias-stress stability for phenyl-C61-butyric acid methyl ester (PCBM) that had been doped with both CsF, to produce an *n*-channel, and F_4-TCNQ, to produce a *p*-type, in ambipolar OTFTs [162]. Another example of doping improved bias-stress stability is the work by Rossbauer et al who investigated *n*-doping with N-DMBI in an assortment of organic materials (C_{60}, C_{70}, [60]PCBM, [70]PCBM and indene-C_{60} bis-adduct) and show that doping has a significant effect on the bias-stress stability of the TFTs [161]. Hein et al. also improved the bias-stress degradation in *p*-type TFTs by three orders of magnitude by doping pentacene with 2,2'-(perfluoronaphthalene-2,6-diylidene)dimalononitrile (F_6-TCNNQ) [176].

3.2.3.3 Mobility and conductivity

Molecular doping can increase conductivity in OTFTs by several order of magnitude by passivating charge traps in the system, increasing the free charge carriers available at lower V_G [5] [161] [177] [178] and generating free charge carriers [166] [179].

An increase in conductivity is beneficial because it reduces the resistance, and hence reduces Ohmic losses, in the bulk OSC [5] [40]. In addition, the conductivity is related to mobility in the following way:

$$\sigma = ep\mu_h \tag{3.6}$$

where e is the *elementary charge*, p is the concentration of holes and μ_h is the hole mobility. Therefore, increasing the conductivity can increase the mobility.

Doping has been used to improve mobility on several occasions [81] [180] [181] [182]. For example: Mendez et al. increased the conductivity of C_{10}-BTBT by passivating traps with low concentrations of F_4-TCNQ [177]; Olthof et al. used *n*-doping to passivate charge traps in C_{60}, increasing conductivity which corresponded to an increase in mobility by 3 orders of magnitude [177]; Rossbauer et al. also increased the mobility of *n*-type C60 and C70 to around 2 cm^2/Vs by filling traps with the dopant N-DMBI [161] and Han et al. demonstrated a mobility increase by 11 fold with the addition of $B(C_6F_5)_3$ to poly(6,6,12,12-tetraoctyldiindeno[1,2-b:1,2-e]pyrazine-co-2,5-thiophene) (IP-T) and poly(6,6,12,12-tetraoctyldiindeno[1,2-b:1,2-e]pyrazine-co-2,5-thieno[3,2-b]thiophene) (IP-TT) due to the passivation of traps [151].

Having said that, the introduction of a dopant to an OSC system can lead to disturbances in the crystal packing of the host OSC lattice, which can introduce disorder and interrupt charge transport. This can be seriously detrimental for the mobility, regardless of the theoretical potential that doping has for improving the mobility or indeed any of the other OTFT parameters [40].

In inorganic systems dopants are neatly introduced into a periodic crystal lattice structure by substituting individual atoms. This contrasts with intrinsically disordered polymeric semiconductors where introducing a dopant can disturb the chain order, and lead to the reorganisation of a polymer, resulting in polymer chain defects such as bipolarons, polarons and solitons [183]. The packing of crystalline small-molecule semiconductors can also be heavily disturbed by dopant molecules. Therefore, in organic systems, the host OSC lattice is very sensitive to local disruptions and often there isn't a proportional relationship between the amount of dopant added and the resultant conductivity.

Doping efficiency in organic materials depends on a number of factors, such as the host OSC lattice structure, doping homogeneity and the nature of the chosen dopant [183]. In fact, organic systems tend to require much higher doping concentrations than inorganics [183], sometimes so high that the same level of doping in inorganic materials would result in metallic properties [39]. Increasing the amount of dopant increases the likelihood of disturbing the OSC host and in some cases this can also lead to problems with polymer solubility, or mechanical properties such as flexibility [183] [184], in addition to a decrease in the mobility [40] [185].

For instance, Han et al. used $B(C_6F_5)_3$ to dope polymers IP-T and IP-TT and they saw a reduction in mobility at high doping concentrations because the dopant had introduced

energetic disorder and structural defects into the OSC [151] [166]. Similarly, Ha and Kahn show that the crystal lattice of pentacene doped with low concentrations of F_4-TCNQ does not change compared to the pristine pentacene, as the dopant molecules neatly diffuse into lattice vacancies [186]. Yet at higher F_4-TCNQ concentrations above 1% mol. wt, Kleemann et al. show that the crystallinity of the pentacene lattice is significantly reduced [187]. This reduction in crystallinity manifests itself as a decrease in the size of the pentacene crystallites and a corresponding decrease in mobility. These effects were emphasised further with the addition of an even bulkier molecular dopant, F_6-TCNNQ. Another *p*-dopant that has demonstrated this trend is $C_{60}F_{36}$; Pahner et al. show that at high doping concentrations, there is an increase in the density of states [188]. Aziz et al. also showed that the strong charge-transfer interaction between P3HT and F_4-TCNQ can result in significant changes to the microstructure [166].

3.2.3.4 On-off ratio

An increase in conductivity due to molecular doping can also have an impact on $I_{ON/OFF}$. An increase in the on-current is desirable; on the other hand, if the semiconductor becomes too conductive, the off-current also increases. This will decrease $I_{ON/OFF}$, potentially pushing the value away from the commercial requirement of $I_{ON/OFF} = 10^6$ [146] [147]. That being said, there are some examples where $I_{ON/OFF}$ is improved in doped systems [81] [151].

3.2.3.5 Contact resistance

The work function, φ, is the energy required to take a hole or electron from the Fermi level, E_F, to the vacuum level, E_0. Typically, the work function value for the metal contact, φ_m, and the OSC, φ_s, will not be the same ($\varphi_m - \varphi_s \neq 0$), and therefore when the metal and the semiconductor come into contact, the energy of the electrons added to the metal is not the same as the energy of the electrons added to the semiconductor.

This energetic difference at the metal/semiconductor interface is reduced by holes or electrons flowing from the semiconductor to the metal, shifting E_F in the semiconductor so that $E_{F_OSC} = E_{F_metal}$. The flow of electrons from the semiconductor to the metal forms a region at the interface of the semiconductor that is depleted of any charge carriers (known as the *depletion region* or *space-charge region*). Ionised atoms are left behind and hence a 'built-in' electric field exists at the interface, which creates a potential barrier, known as a Schottky barrier, that must be overcome if electrons are to move from the metal to the semiconductor.

This causes significant problems for the operation of a TFT, where one of the first stages of operation relies on the ability to inject charge carriers from the source electrode into the semiconductor.

For a *p*-type semiconductor, the *height of the Schottky barrier*, φ_B, is determined by the energy difference between the work function of the metal, φ_m, compared to the HOMO of the OSC:

$$q\phi_{\mathrm{B}} \equiv q\phi_{\mathrm{m}} - qE_{HOMO} \tag{3.7}$$

where q is charge and E_{HOMO} is the energy of the HOMO level. The built-in electric field from the depletion region causes holes/electrons to move away from the semiconductor interface, resulting in holes/electrons close to the interface having a higher energy than the holes/electrons in the bulk. This creates a *built-in voltage*, φ_i, which is determined by the difference between φ_m and φ_s:

$$q\phi_{\mathrm{i}} \equiv q\phi_{\mathrm{m}} - q\phi_{\mathrm{s}} = q\phi_{\mathrm{B}} - (E_{\mathrm{F}} - E_{\mathrm{HOMO}})_{\mathrm{bulk}} \tag{3.8}$$

To improve contact resistance in OTFTs, the height of the Schottky barrier, φ_B, can be reduced by choosing a metal contact with a similar φ_m to the OSC transport level, as described in *Chapter 2*. However, the choice of materials available is often limited; for example, metals that typically have suitable work functions for electron injection in *n*-type OTFTs are very reactive and unsuitable for use in ambient conditions.

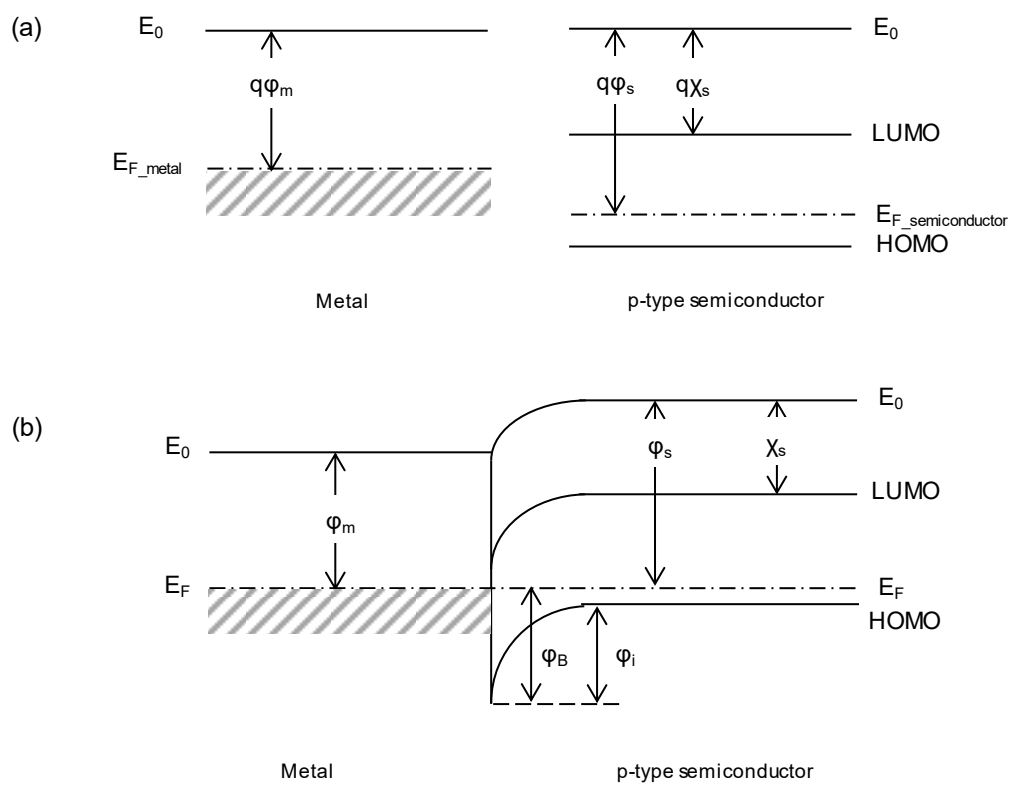

Figure 3.8: Band diagram of a metal and semiconductor interface. In (a), the two materials are not in contact and in (b) they are in contact.

Alternatively, the Schottkey contacts can be transformed into Ohmic contacts. There are two ways that this can be done:

1. Choose $\varphi_m > \varphi_s$ for a *p*-type semiconductor, and $\varphi_m < \varphi_s$ for an *n*-type semiconductor. In the case of *p*-type OSCs, the energy of the system is reduced by the flow of holes from the metal into the semiconductor, as opposed to the holes/electrons from the semiconductor to metal in the situation that has been described above. This causes accumulation near the surface rather than depletion, resulting in an Ohmic contact.
2. Reduce the width of the depletion region so that it is thin enough to allow tunnelling in both directions, i.e. form a quasi-Ohmic contact with very little resistance.

Point 1 is, of course, an intrinsic property of the metal used for the contacts in TFTs, and therefore depends on the choice of material used for device engineering.

On the other hand, point 2 can be achieved by molecular doping and this is the approach widely used by the inorganic semiconductor industry [40]. When a dopant is introduced into a semiconducting system, free charge carriers are generated. Depending on whether the free charge carriers are holes or electrons, the Fermi level will move towards the HOMO or the LUMO, respectively. The shift in E_F results in a change in φ_s, because:

$$\phi_{\mathrm{s}} \equiv (E_0 - E_{\mathrm{F}})/q \tag{3.9}$$

which therefore changes the built in voltage, φ_i, from Equation 3.8.

Using Poisson's equation and the depletion approximation gives the relationship between φ_i and the depletion region as:

$$\phi_{\mathrm{i}} = \phi_{\mathrm{m}} - \phi_{\mathrm{s}} = \frac{1}{2}\frac{qN_d}{k\epsilon_0}{x_d}^2 \tag{3.10}$$

where N_d is the doping density, k is Coulomb's law constant, ϵ_0 is the permittivity of free space and x_d is the width of the depletion region. Rearranging Equation 3.10 gives the width of the depletion layer as:

$$x_d = \sqrt{\frac{2k\epsilon_0\phi_i}{qN_d}} \tag{3.11}$$

which depends on both φ_i and N_d. For example, if the doping density, N_d, is very large then x_d becomes very small. If x_d is small enough ($x_d \leq$ 25-50 Å) then a low resistance quasi-Ohmic contact forms and tunnelling can occur, compared to large barrier widths where injection occurs by thermionic emission.

Doping the OSC can therefore enable efficient charge injection in OTFTs regardless of the barrier height from the mismatch between φ_m and the OSC transport level. This is achieved by reducing the depletion layer width and hence reducing contact resistance [171] [189]. For example, doping dependent depletion region width was shown by Olthof et al. who measured x_d in N,N,N′,N′N′,N′-tetrakis(4-methoxyphenyl)-benzidine doped with F_4-TCNQ via co-evaporation, using Ag, ITO and PEDOT:PSS as the electrode materials [190].

3.2.3.6 OTFT parameter extraction: Mobility

As outlined in *Chapter 2*, the gradual channel approximation model is used to find the key parameters of OTFTs:

$$I_{\mathrm{D}} = \frac{W}{L} C_{\mathrm{i}} \mu_{\mathrm{app}} \left(V_{\mathrm{G}} - V_{\mathrm{T}} - \frac{V_{\mathrm{D}}}{2} \right) V_{\mathrm{D}} \tag{3.12}$$

where $V_D < V_G - V_T$. Using this model, both V_T and the apparent mobility, μ_{app}, are extracted from the ratio of the current change at the output, to the voltage change at the input, i.e. the *transconductance,* g_m, where:

$$g_m = \frac{\partial I_{\mathrm{D}}}{\partial V_{\mathrm{G}}} = \frac{W}{L} C_i \mu_{\mathrm{app}} V_{\mathrm{D}} \tag{3.13}$$

Due to the contact resistance discussed in Section 2.3.5 and Section 3.2.3.5, there will be a potential drop across the channel. The total resistance can be described by Ohm's law as:

$$R_{\mathrm{total}} = \frac{V_{\mathrm{D}}}{I_{\mathrm{D}}} = R_{\mathrm{ch}} + R_{\mathrm{C}} \tag{3.14}$$

which gives

$$R_{\mathrm{ch}} I_{\mathrm{D}} = V_{\mathrm{D}} - R_{\mathrm{C}} I_D \tag{3.15}$$

If this potential drop due to the contact resistance is substituted for V_D in the gradual channel approximation model (Equation 3.12), and the small term $V_D/2$ is neglected, then an expression can be obtained for I_D in the linear regime that takes into account the contact resistance, R_C:

$$I_{\mathrm{D}} = \frac{V_{\mathrm{D}}}{R_{\mathrm{C}} + \frac{1}{\frac{W}{L} C_{\mathrm{i}} \mu_{\mathrm{int}} (V_{\mathrm{G}} - V_{\mathrm{T}})}} \tag{3.16}$$

Combining this equation with the gradual channel approximation gives a relationship between the μ_{app} and μ_{int}:

$$\mu_{\text{app}} = \mu_{\text{int}} \times \frac{1}{1 + R_{\text{c}} \frac{W}{L} C_{\text{i}} \mu_{\text{int}} (V_{\text{G}} - V_{\text{T}})} \tag{3.17}$$

This tells us that due to contact effects, $\mu_{app} < \mu_{int}$, and this is particularly prominent when the device has a short channel length. This is well-known for OTFTs and in general, this is always the case.

However, in recent years, a spate of high OTFT mobility values have been reported that have proven to be unreproducible [126]. These unreproducible mobility values are well-known in the field and they have recently been nicely explained by Uemura et al. [36]. If Equation 3.14 is rearranged to find V_D this gives:

$$V_{\text{D}} = I_{\text{D}} (R_{\text{c}} + R_{\text{ch}}) \tag{3.18}$$

which can be substituted into Equation 3.13, giving

$$g_{\text{m}} = \frac{\partial I_{\text{D}}}{\partial V_{\text{G}}} = -\frac{V_{\text{D}}}{(R_{\text{ch}} + R_{\text{c}})^2} \left(\frac{\partial R_{\text{ch}}}{\partial V_{\text{G}}} + \frac{\partial R_{\text{c}}}{\partial V_{\text{G}}} \right) \tag{3.19}$$

This shows that when the channel resistance is low, there is a high sensitivity to contact resistance dependency on V_G (i.e. $\delta R_c/\delta V_G$). This can lead to a large artefact in g_m from a nonlinear increase in the drain current at low V_G, resulting in $\mu_{app} > \mu_{int}$.

This artefact in the transconductance manifests itself as a peak in mobility with V_G when the second derivative analysis method is used, and/or a 'double slope' if the $\sqrt{I_D}$ method is used. Using the former, μ_{app} is overestimated by taking the peak at a single V_G value. Using the latter, μ_{app} is overestimated by taking the steepest gradient from the low V_G region. Therefore, if there is a large change in the contact resistance with V_G, then μ_{app} can appear greater than μ_{int}, which can result in overestimations of the mobility. This is particularly the case for high mobility OTFTs and has indeed been the cause of a number of inaccurately reported mobilities.

Uemura et al. demonstrated this behaviour experimentally using vacuum evaporated 2,9-didecyl-dinaphtho[2,3-b:2′,3′-f]thieno[3,2-b]thiophene (C_{10}DNTT) and extracting μ_{int} using a *gated four-point probe* (gFPP) method and calculating μ_{app} using the typical two-probe transmission line method (TLM) [36]. They find that there is a large deviation in μ_{int} and μ_{app}, with the most extreme case being a factor of 10 difference, showing that peaks in the saturation μ_{app} could reach as high as 100 cm^2/Vs. They then anneal the C_{10}DNTT which improves the

metal/semiconductor interface, critically improving the contact resistance and subsequently bringing the peaks in μ_{app} down to values of μ_{int}. In other words, they show how significant mobility overestimations can be made.

Important points that Uemura et al. highlight are that this overestimation is more significant at higher channel lengths and in the saturation regime, as well as that the contact resistance dependency on V_G may not be shown in the output curves as might be expected (i.e. R_C issues may not be shown by nonlinearities at low V_D). The best way to show whether the TFT in question is suffering from a large change in the contact resistance is to plot I_{D_lin} vs V_G and look at whether this line is straight (ideal), or where it has an "s-shaped" bend (g_m artefact).

Addressing the issue of contact resistance, using methods such as molecular doping, is therefore highly important for mobility extraction for two reason: (i) it can lead to $\mu_{app} < \mu_{int}$ and (ii) in high performance systems it can lead to an artefact in g_m where, if there is a sharp decrease in the contact resistance compared to a decrease in the channel resistance, $\mu_{app} > \mu_{int}$.

3.2.4 Molecular doping methods

3.2.4.1 Bulk doping

One simple method which allows easy control over the doping levels, is to directly mix a dopant into the host OSC. A stable and bulky dopant (e.g. $C_{60}F_{36}$) would be ideal for this approach, as some dopants can have a tendency to diffuse throughout the film (e.g. F_4-TCNQ), leading to unwanted TFT characteristics [40] [156].

Although there are successful examples of this doping technique [151] [161], because of the high risk of a molecular dopant interfering with a OSC host lattice and decreasing the mobility, bulk doping is an approach that is rarely used. Therefore, over the years a number of alternative doping methods have been employed [40], which will be discussed in the remainder of Section 3.2.4.

3.2.4.2 Contact doping and interlayer doping

To avoid lattice interruptions, which ultimately increase disorder in an OSC system, the most common method for doping OTFTs is to introduce an extra layer into the structure [40]. In general, there are two ways to do this, as shown with the help of Figure 3.9 (a-c).

Figure 3.9 (a) shows one approach, contact doping, where a layer of either pure dopant or dopant/semiconductor mix is deposited at the source and drain metal/semiconductor interface [191] [192]. Contact doping is a remarkably successful, widely studied technique for

reducing contact resistance in OTFTs (for the reasons outlined in Section 3.2.3.5), and there are many examples in the literature of this technique being used [172] [182] [191] [192] [193] [194] [195]. Self-assembled monolayers (SAMs), such as pentafluorothiophenol (PFBT) [67] [195] [196] [197] [198], and injection layers, such as molybdenum(VI) oxide (MoO3) [199] [200], have become commonplace in an OTFT fabrication laboratory.

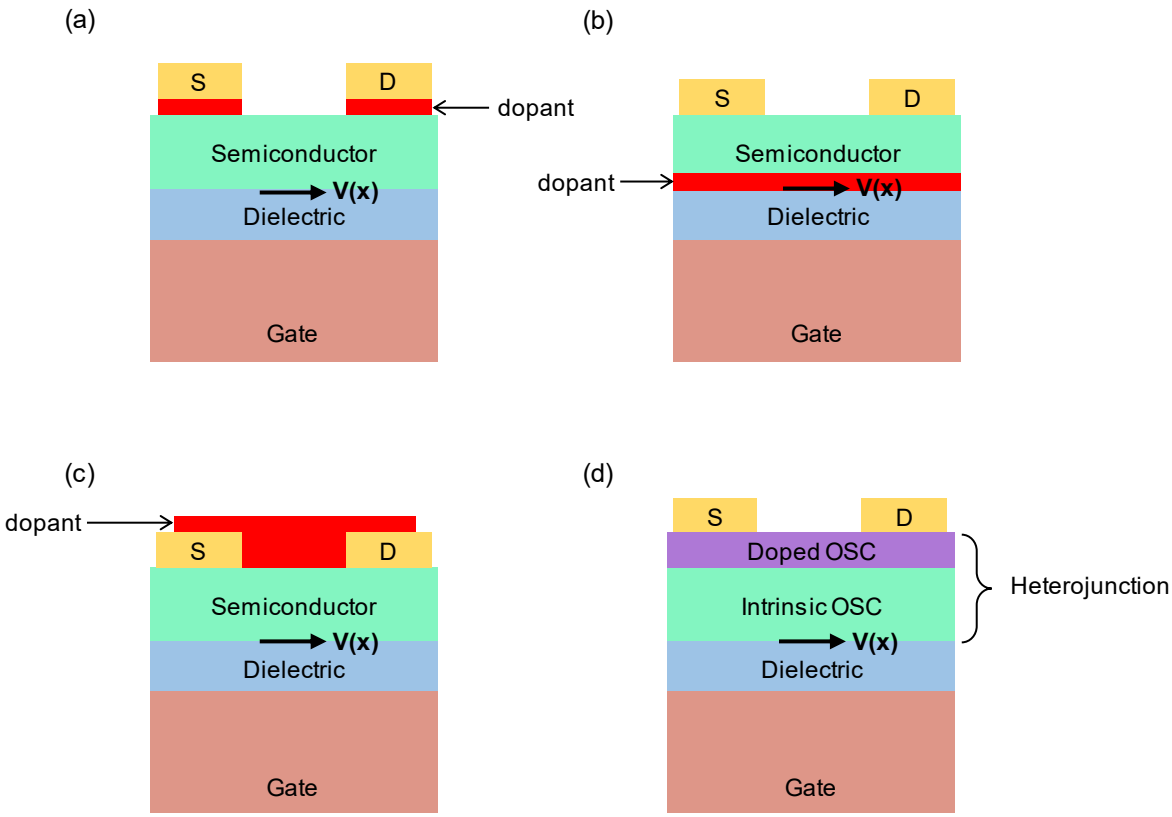

Figure 3.9: Schematic of various OTFT doping techniques. (a) contact doping, (b) a layer of dopant above and (c) below the OSC, (d) an organic heterojunction designed for modulation/remote doping.

Figure 3.9 (b) and (c) show an alternative approach, where a dopant interlayer is inserted either above or below the OSC. This approach has been shown to increase conductivity and shift the threshold voltage [40] [147] [169] [201]. The threshold voltage shift has been shown to be highly dependent on the thickness of the dopant layer because:

$$V_T \approx V_{FB} + \frac{eN_A d_{dop}}{C_i} \tag{3.20}$$

where V_{FB} is the flat-band voltage (i.e. the voltage required to induce flat energy levels between the metal and OSC), e is the elementary charge, N_A is the density of ionised dopants, d_{dop} is the thickness of the doped layer and C_i is the capacitance per unit area. Therefore, the

thickness of the dopant layer must be carefully optimised, as demonstrated by Lüssem et al. [64], or the thickness of the OSC must be optimised, as demonstrated by Hählen et al. [202], depending on where the dopant layer is placed in the chosen OTFT structure.

Depositing a SAM between the dielectric and OSC is another interlayer approach that has been shown to cause a shift in V_T, due to the introduction of a molecular dipole at the OSC/dielectric interface, altering the voltage required for flat band conditions.

3.2.4.3 Chemical vapour treatments

Another way to dope OTFTs is to use a chemical vapour treatment [203] [204]. One example is by Lee et al., who start their work by highlighting the need for a method to dope OSCs without the resistivity/nanomorphology being affected and hence mobility inhibited [35]. They suggest chemical vapour treatment is a good option and subsequently use this approach to dope poly[4-(4,4-dihexadecyl-4H-cyclopenta[1,2-b:5,4-b′]dithiophen-2-yl)-alt-[1,2,5]thiadiazolo-[3,4-c]pyridine] (PCDTPT) that had been externally aligned. Using an iodine (I2) vapour treatment, they report an increase in carrier density, a shift in V_T and a reduction in the contact resistance, as well as increased mobility values. In addition to performance improvement, this is also a good example of how OTFT gas-based doping could lend itself to chemical/gas sensor applications [205] [206].

Another gas that has been known for many years to dope organic materials is oxygen. This has been demonstrated in many situations [207] [208] [209] [210] [211] [212] but it can lead to unintentional and uncontrolled doping in atmospheric environments.

3.2.4.4 Modulation doping

In the field of inorganic electronics, a process known as modulation doping is used whereby the dopant is not located within the channel, but the dopant-induced free carriers are still able to populate the channel. This results in spatial separation between the dopant and the free charge carriers and hence avoids adverse scattering effects. Modulation doping is used in, for example, AlGaAs/GaAs heterostructures and modulation-doped field effect transistors (MODFETs).

Realising modulation doping in OTFTs would mean that the dopant molecules would not reduce OSC crystallinity at the channel, which is important because is currently one of the biggest setbacks for doping in OTFTs [40]. Modulation doping-like techniques are therefore an extremely attractive option for organic electronics, but examples of modulation doping mechanisms in OTFTs are few and far between. One example is by Zhoa et al., who designed

an organic hererojuction with aligned energy levels in contact with an OTFT channel (Figure 3.9 (d)) [213]. The heterojunction is comprised of a layer of N,N'-diphenyl-N,N'-bis(1-naphthyl)-1,1'-biphenyl-4,4'-diamine (α-NPD) that has been doped with $Mo(tfd)_3$ (labelled "*p*-doped α-NPD") on top of a layer of pentacene. The free holes are generated in the *p*-doped α-NPD and remotely transferred to the pentacene channel because the *ionisation energy* (IE) of the pentacene is equivalent to the work function of the *p*-doped α-NPD; this subsequently increases OTFT conductivity without the dopant acting as a trapping or scattering centre.

3.3 Outlook

Small-molecule/polymer blends and molecular doping are two of the most promising areas for realising OTFTs in commercial applications. Independently, they are popular techniques that are known to reduce energetic disorder and improve OTFT performance.

By reviewing the literature on small-molecule/polymer blends and molecular doping in OTFTs, *Chapter 3* has highlighted that there is a gap in the market for two things: (i) advanced, 3rd generation organic semiconducting blends that surpass the benchmark mobility of 10 cm^2/Vs, and (ii) further research into OTFT doping techniques, particularly those that overcome lattice/microstructure interruptions from the dopant molecules and promote charge carrier transport [40].

Although this chapter has considered and reviewed small-molecule/polymer blend systems and molecular doping separately, a patent filed by Anthopoulos in 2012 discussed *p*-doping the 1st generation blend, where the *p*-dopant appeared to have minimal effect on the crystalline domains in the blend thin-film. This suggests that there may be some interesting effects from combining the two approaches.

Chapter 4

Experimental methods

The following chapter summarises the experimental methods that are used in this thesis. As outlined in Chapter 3, small-molecule/polymer blends are often incorporated into staggered top-gate, bottom-contact (TG-BC) organic thin-film transistor architectures to maximise the impact of the vertical phase separation. Therefore, this chapter begins by discussing the fabrication of organic blend OTFTs in TG-BC structures. It then discusses electrical and materials characterisation techniques which are used to analyse the OTFTs and semiconductor films.

4.1 Thin film transistor fabrication

4.1.1 Substrate preparation

Borofloat® glass substrates with dimensions 20 x 20 mm are used as the underlying substrates for device fabrication. The glass substrates are subjected to a rigorous cleaning procedure in four different solutions. Firstly, the glass substrates are submerged in a deionised water and soap (≈1% DECON-90) solution and ultrasonicated for between 10-20 minutes. The DECON-90 solution is used to modify the surface energy of the glass substrate, which ensures that the blend film properly wets the surface of the glass substrate. The glass substrates are then exposed to running water to rinse off the soap solution and ultrasonicated for 10-20 minutes in a fresh water solution to remove any DECON-90 residue.

The substrates are then ultrasonicated in acetone for 10-20 minutes. The acetone is primarily used to remove any DECON-90 residue, but may itself leave some residue on the glass substrate. Therefore, a final step of 10-20 minutes sonication in 2-propanol (IPA) is required, which, although a less aggressive cleaner, will remove any remaining acetone. The substrates then need to be removed from the IPA solution and dried with a high pressure nitrogen gas gun, rather than allowing the IPA to evaporate, as that may leave streaks on the surface.

4.1.2 Contact evaporation

After cleaning the glass substrates, the next step for TG-BC transistors is to deposit the source and drain electrodes onto the glass. For *p*-type organic semiconductors, gold (Au) is a good choice for the source/drain metal due to its work function value of $\varphi_m \approx$ -5.1 eV, which compares well to the HOMO level of many *p*-type organic semiconductors. For example, the small molecule 2,7-Dioctyl[1]benzothieno[3,2-b][1]benzothiophene (C_8-BTBT) has a HOMO value ranging between -5.04 eV and -5.4 eV [214] [215].

To improve adhesion, a thin layer of aluminium (Al) can be deposited between the glass and the Au. Using an Al adhesion layer can make electrical characterisation easier as it prevents the Au from being scratched off the glass substrate. However, this approach requires caution as the injection properties can be affected due to the work function of the Al ($\varphi_m \approx$ -4.1 eV) which is inadequate for many *p*-type organic semiconductors. Additionally, any mismatched or non-ideal overlap of the Al/Au bilayer can affect the TFT injection properties. For the work in this thesis, the source and drain electrodes are either 40 nm of Au, or 40 nm of Au with a 5 nm Al adhesion layer.

To deposit the source and drain electrodes, a thermal evaporator is used. Crucibles containing the metal of choice are electrically heated while the substrates are suspended above in a frame. A shadow mask is positioned on the surface of the substrate so that the evaporated metal is only deposited in the exposed areas, enabling patterning of the metal. The shadow mask patterning is dependent upon the type of mask used, allowing transistors with different channel dimensions to be fabricated. The most commonly used masks for this work have 50 TFTs per 20 x 20 mm substrate, with channel lengths varying from 20 – 200 µm and channel widths varying from 500 – 2000 µm.

Once the main evaporation chamber is under vacuum ($\approx 10^{-6}$ mbar), the rate of evaporation is monitored by an oscillating quartz crystal whilst a feedback loop allows regulation by controlling the amount of current passing through the crucible.

In addition to depositing the source and drain electrodes, the thermal evaporator is also used to deposit the gate electrode as the final step of the TG-BC TFT fabrication. Although the thickness and material used for the gate is not as crucial as it is for the source and drain, typically 50 nm of Al is used for the gate electrode which is deposited after the dielectric has been deposited. A different shadow mask is used for this step.

4.1.3 Self-assembled monolayers

The φ_m of the source and drain electrodes are of critical importance to the operation of the TFT. In addition to choosing a metal with appropriate intrinsic characteristics, the source and drain electrode apparent φ_m can be modified by using a self-assembled monolayer (SAM) which deliberately introduces a dipole at the metal surface and thereby adjusts the potential barrier seen by the charge carriers. As mentioned in *Chapter 2*, fluorinated thiol molecules are widely used for this purpose in *p*-type OTFTs. Throughout this work, pentafluorothiophenol (PFBT) is used on Au electrodes as a work function modifier. For this treatment, a 5 mmol L^{-1} solution of PFBT in isopropanol is used and the substrates with the Au source/drain electrodes are submerged in the solution for a minimum of 5 minutes.

4.1.4 Organic blend solution preparation

The primary focus of this thesis is the development of the 3rd generation blend, to explore the impact of the dopant in this system and also investigate the suitability of the 3rd generation blend for practical applications. This section will therefore specifically outline the solution preparation for the 3rd generation blend.

The 3rd generation blend is made from the small-molecule 2,7-Dioctyl[1]benzothieno[3,2-b][1]benzothiophene (C_8-BTBT), the polymer indacenodithiophene-benzothiadiazole (C_{16}IDT-BT) and the fluorinated fullerene dopant $C_{60}F_{48}$. The blend solution optimum concentration is 10 mg/ml and it is made with two solvents, chlorobenzene (CB) and 1,2,3,4-Tetrahydronaphthalene (tetralin), which are both purchased from Sigma Aldrich.

The C_8-BTBT:C_{16}IDT-BT and $C_{60}F_{48}$ solutions are made separately, so that the amount of dopant can be added depending on the doping concentration required. Firstly, the C_8-BTBT:C_{16}IDT-BT solution is made at a ratio of 25% small-molecule to 75% polymer in a solvent solution that is 50% tetralin and 50% CB. The C_8-BTBT was purchased from 1-Material, whereas the C_{16}IDT-BT was synthesised at Imperial College London by Dr Weimin Zhang, Dr Zhuping Fei and Professor Martin Heeney (number average molecular weight 66.5 Kg mol^{-1}). Then, a separate solution of $C_{60}F_{48}$ is prepared in chlorobenzene. The fluorinated fullerene dopant, $C_{60}F_{48}$, was synthesised at Technion, Israel Institute of Technology by Dr Olga Solomeshch and Professor Nir Tessler.

When the dopant solution is added to the C_8-BTBT:C_{16}IDT-BT solution, it must be added so that the overall concentration is kept at 10 mg/ml and the total solution is made from 50% tetralin and 50% chlorobenzene. A stirring bar should be used to prepare the solution and it will be ready to spin coat after stirring for 2 hours. Before spin coating, the blend solution should be gently heated and stirred at 60°C for 15-30 minutes.

4.1.5 Spin coating

Spin coating is a common method that has been used for many decades as a solution deposition technique to produce thin-films and static spin-coating is used here to deposit both the semiconductor and dielectric films. As a deposition technique, spin coating is well known for its simplicity as well as repeatability, speed and film uniformity.

Once the solution has been deposited at the centre of the substrate, the spinning wheel can be rotated at high speeds. The centripetal acceleration causes the liquid to spread across the substrate, dispersing any excess solution from the edges of the substrate. A combination of the centripetal force and surface tension ‘pulling’ the liquid evenly covers the surface of the substrate leaving a thin-film. The final thin-film thickness and other properties depend on a number of factors, such as: the boiling point of the solvent used, solution viscosity, spin-speed, solution concentration and surface tension. As the solvent usually evaporates relatively quickly during spin coating, there often is not much time for any of the molecular ordering that may be

offered by other solution deposition techniques. Therefore, post-deposition treatments such as annealing are sometimes employed [216]. For consistency and due to the toxicity of some of the solvents used in this work, all spin coating was undertaken in an inert nitrogen atmosphere in a glovebox.

For TG-BC OTFTs, the semiconductor is spin-coated first. The 20 x 20 mm glass substrate with the evaporated source/drain electrodes is placed in the centre of the spinning wheel and a small amount of the blend solution is dropped onto the substrate using a pipette. The amount of solution required depends on the viscosity of the liquid, but as a rule of thumb, typically 70 µl of the C_8-BTBT:C_{16}IDT-BT:$C_{60}F_{48}$ blend solution is required to produce a 65 nm thick OSC film on a 20 x 20 mm substrate, where the film thickness was measured using a Bruker Dektak. A two-step spin coating recipe is used: 1) 500 rpm for 10 seconds and 2) 2000 rpm for 30 seconds. The films are then annealed at 120°C for 5 minutes and quenched to room temperature.

The next step is to deposit the dielectric layer. Throughout this work, either the fluoropolymer Cytop, or a polytetrafluoroethylene (PTFE) polymer dielectric layer (Teflon™ AF2400) have been used. Both dielectrics use solvents that are orthogonal to the organic semiconducting materials employed in this work, so there is no damage to the semiconductor layer when the dielectric is deposited. As both of the dielectric solutions are significantly more viscous than the blend solutions, a larger quantity of dielectric solution needs to be pipetted onto the substrate and spin-coated at a slower spin speeds.

For the Cytop, a one-step spin coating recipe of 2000 rpm for 60 seconds will produce a film thickness of ≈900 nm. The AF2400 solutions are prepared in-house at a concentration of ≈25 mg/ml and take several days of heating and stirring to dissolve. To produce a ≈335 nm film of AF2400, the following spin coating recipe can be used as a guide: 1) 500 rpm for 20 seconds and 2) 1000 rpm for 30 seconds. However, a separate dielectric film should always be made so that the thickness can be measured and the areal capacitance calculated for each set of devices. Both dielectrics need to be annealed at 50°C for 1 hour after spin-coating.

4.2 Electrical characterisation

4.2.1 Current-voltage characterisation

Either an Agilent B2902 or a Keithley 4200 source measurement unit (SMU) – which are made up of voltmeters, ammeters and amplifiers – was used as a semiconductor parameter analyser to measure the transfer and output characteristics. The SMUs are connected to three

probes which are easily moved into accurate positions using mechanical micromanipulators. These probes make contact with the source, drain and gate electrodes, so that voltages can be applied and currents can be measured. With the data collected from these measurements, the equations in *Chapter 2* (Section 2.3.3) can be used to extract key OTFT parameters.

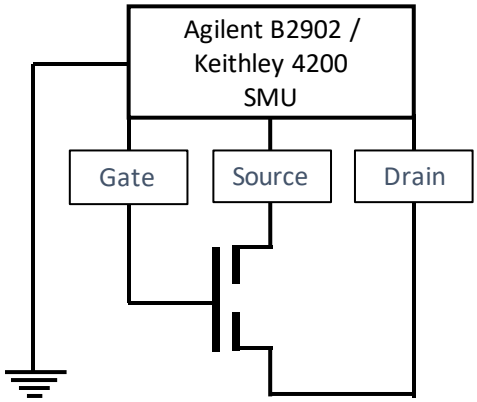

Figure 4.1: Schematic of probe station equipment for measuring I-V characteristics of TFTs.

4.3 Materials characterisation

4.3.1 Atomic force microscopy

Atomic force microscopy (AFM) is a highly accurate and useful imaging tool. An Agilent 5500 scanning probe microscope operating in tapping mode was used to study the surface topography and phase of the semiconductor thin-films with nanoscale resolution. The AFM consists of a small cantilever which moves across the surface at a constant vibration frequency. Any interplay that the tip has with the surface will result in a change in the vibration frequency, which is detected by a change in a laser reflected from the cantilever; this change is measured by a photodiode and the output signal depicts an outline of the sample surface. Once the imaging has taken place, Gwyddion 2.39 software is used for statistical and image analysis.

4.3.2 Polarised optical microscopy

The polarised optical microscope (POM) is an effective tool which uses crossed polarisers and a series of lenses for examining crystalline microstructures that exhibit birefringence. This instrument has been of the utmost importance for the development of the work in this thesis, as the POM can very quickly provide a wealth of information about the crystallisation of small-molecules.

Birefringent materials exhibit anisotropic properties whereby they have different refractive indices along two different optical axes. If linearly polarised light passes through the sample down an axis between these two birefringent axes, the light changes polarisation and produces two electric field components travelling perpendicular to each other and out of phase. This phase difference is caused by the light having two different refractive indices in the crystal and therefore the two electric field components travel at different speeds; these waves are known as ordinary and extraordinary waves. The light is re-emitted (either by reflection or transmission) after it has travelled through the sample and it is then passed through a polariser set at 90° to the initial polariser, i.e. crossed polarisers. In order to pass through the crossed polarisers, the light must have changed polarisation. If this is the case then the phase difference between the ordinary and extraordinary waves will create an interference pattern, providing an image of the microstructure.

4.3.3 Scanning electron microscopy

The scanning electron microscope (SEM) uses a focussed beam of electrons moving in a raster scan fashion to construct images of the surface topography of thin-films. The SEM imaging of the films in this thesis were measured with an operating voltage of 5 kV, whilst under vacuum in a LEO Gemini 1525 Field Emission Scanning Electron Microscope (FESEM). This imaging technique is particularly helpful when surface irregularities hinder AFM imaging.

4.3.4 Kelvin probe and air photoemission

The Kelvin probe (KP) – also known as surface potential microscopy – is a non-contact, non-destructive technique that detects the potential difference between a material surface and a probe tip. The potential difference causes the KP tip to move, forming a vibrating capacitor and allowing the work function of the surface to be measured. This therefore makes the KP a key instrument for detecting any doping in organic semiconductors.

For this thesis, the work function and HOMO levels of doped organic thin-film samples relative to pristine organic thin-film samples, as well as their constitutive parts, were measured using KP and air photoemission (APS) techniques, respectively, using a KP Technology SKP5050/APS02 and silver was used as a reference material. The APS measurements are undertaken by using incident light (wavelength between 6.2 and 4.4 eV) to scan the sample, whilst observing the photocurrent response; the HOMO level can then be extracted from this data using Fowler analysis [217]. Due to the high sensitivity of both techniques to thin-film surface conditions, atmospheric conditions such as temperature and humidity should be

monitored and controlled whilst undertaking KP and APS measurements, as well as measuring directly after thin-film fabrication.

4.3.5 Time-of-flight secondary ion mass spectroscopy

Time-of-flight secondary ion mass spectroscopy (ToF-SIMS) is a highly sensitive technique used to analyse the surface of a material with pulses of ion beams. The pulsed ion beam removes molecules that are present on the outer surface of the material sample, revealing information about the depth profiling of the sample.

For this work, depth profiling of the semiconducting organic blend thin-films were performed using an IONTOF ToF-SIMS V, where 2.5 kV Ar cluster (1000 atoms, ≈1 nA) sputter beams were rastered over a 300 x 300 µm sample area. The measurements were done at a pressure of 10^{-10} Torr, and a Bi_3^+ (≈0.5 pA) beam was used to collect negative ions from the centre of the sputter crater (i.e. the 200 x 200 µm region).

4.3.6 In-plane wide-angle x-ray diffraction and grazing-incidence wide-angle X-ray scattering

One of the most popular photon-based techniques for material characterisation is X-ray imaging. Over the past few decades, knowledge regarding the interaction of X-rays with matter has been thoroughly developed, allowing the exploitation of X-rays in a number of critical tools designed to investigate the microstructure of various materials [218].

When a material has crystalline characteristics, the regularly spaced lattice planes will act as scattering centres for an incident beam of X-rays. The resultant diffraction pattern gives information about the chemical composition, lattice spacing, crystal packing and alignment, and lattice stress. In this thesis two X-ray techniques have been employed: in-plane (Bragg-Brentano geometry) wide-angle x-ray diffraction (WAXD) and grazing-incidence wide-angle X-ray scattering (GIWAXS).

For the WAXD measurements, a Rigaku Ultima+ diffractometer was used with a CuKα monochromated line ($\lambda = 0.154$ nm), with an anode voltage of 40 kV and filament current of 30 mA. The WAXD measurements and analysis in this work were done by Professor George Vourlias and Professor Panos A. Patsalas at Aristotle University of Thessaloniki.

For the grazing-incidence wide-angle X-ray scattering (GIWAXS), the measurements were carried out at D-line, Cornell High Energy Synchrotron Source (CHESS) at Cornell University by Muhammad R. Niazi from King Abdullah University of Saudi Arabia.

Chapter 5

Introduction of 3rd generation organic semiconducting blend systems

This chapter describes the development of a 3rd generation organic semiconducting blend. Here, the small-molecule 2,7-dioctyl[1]benzothieno[3,2-b][1]benzothiophene (C_8-BTBT) and polymer indacenodithiophene-benzothiadiazole (C_{16}IDT-BT) are blended together and a third component, the molecular p-dopant $C_{60}F_{48}$, is introduced. The introduction of $C_{60}F_{48}$ has a significant effect on the performance of the blend OTFTs – and when this ternary blend is combined with a solvent-mixing approach – hole mobility values exceeding 13 cm^2/Vs are achieved. In the final part of this chapter it is shown that, not only could this ternary system be used as a model system for other materials combinations, but by adopting alternative processing techniques the hole mobility of 3rd generation blend-based OTFTs can be even further improved to values exceeding 23 cm^2/Vs.

5.1 3rd generation blend development and design

5.1.1 Introduction

Small-molecule/polymer blends are one of the most auspicious systems to date for realising OTFTs in future plastic-based microelectronic applications. In 2009, the 1st generation blend was designed by Hamilton et al. by blending the small-molecule 2,8-difluoro-5,11-bis(triethylsilylethynyl)anthradithiophene (diF-TES ADT) with the semiconducting polymer poly(triarylamine) (PTAA), engendering blend OTFTs with mobility values of 2.4 cm^2/Vs [87].

Three years later in 2012, the 2nd generation blend was developed by Smith et al. by replacing the PTAA with a higher performance polymer binder, poly(dialkyl-fluorene-co-dimethyl-triarylamine) (PF-TAA), in the original diF-TES ADT blend system, achieving impressively high mobilities of over 5 cm^2/Vs [88] as well as demonstrating critical design requirements for the blend system.

With the recent rise in charge carrier mobility values of organic materials, which now surpass the benchmark mobility of 10 cm^2/Vs required for industrial application, there is one critical question that remains about the organic blend: is it possible to further increase its performance to values that are commensurable to state-of-the-art OTFTs? [28] [30] [32] [34] [35] Such a development would provide the field of organic electronics with a high-performance system that can be manufactured using simple, low cost and scalable processing techniques, thereby making OTFTs a viable technology for use in plastic electronics.

The aim of this chapter is to answer this important question, and in doing so the development of a 3rd generation organic semiconducting blend with mobilities exceeding 13 cm^2/Vs is reported. In addition, future work is suggested, demonstrating the 3rd generation blend as a prospective system with great potential for further research to be undertaken.

5.1.2 The binary blend: Small-molecule/polymer

Over the past two decades, the performance of individual organic semiconducting materials has improved significantly, meaning that there is now a wealth of small-molecules and polymers to choose from when designing an organic blend system. Specifically, for small-molecules, the family of highly soluble 2,7-dialkyl[1]benzothieno[3,2-b] [1]benzothiophenes (Cn-BTBTs) semiconductors have demonstrated very impressive electrical properties [219].

From this family of materials, the commercially available liquid crystal 2,7-dioctyl[1]benzothieno[3,2-b][1]benzothiophene (C_8-BTBT) (shown in Figure 5.1 (a)) has established itself as one of the most promising semiconducting organic materials, achieving some of the highest mobility OFETs to date, when fabricated under certain conditions [28] [30], due to its superb molecular ordering that results in extensive intermolecular overlapping for efficient charge transfer [28] [30] [219]. C_8-BTBT is also highly soluble in a range of organic solvents and therefore – along with its electrical characteristics – it is an excellent choice as a component for an organic blend.

After selecting C_8-BTBT as the small-molecule, a range of polymers were explored as polymer binders for a C_8-BTBT-based organic blend system; these polymers included polyfluorene (PTO), poly(triaryl amine) (PTAA), poly(vinyl alcohol) (PVA), polystyrene (PS), poly(alpha-methylstyrene) (PαMS), diketopyrrolopyrrole-dithienylthieno[3,2-b]thiophene (DPP-DTT) and indacenodithiophene-benzothiadiazole (C_{16}IDT-BT). From the selection of polymers, it was found that the latter polymer binder, C_{16}IDT-BT, produced the most promising OTFT blend transistors.

As outlined in *Chapter 3,* the choice of polymer binder is critically important for the success of a small-molecule/polymer blend system. Conjugated polymers with indacenodithiophene as a co-polymer and benzothiadiazole as a co-monomer have recently been shown to exhibit exceptional electrical properties [220] [221]; as such, C_{16}IDT-BT has achieved mobilities of up to 3.6 cm^2/Vs and has been of great interest to the organic electronics field because – surprisingly – it exhibits no long-range order and the remarkable performance appears due to its rigid backbone structure [222]. This impressive intrinsic performance is one of the key factors that makes C_{16}IDT-BT the strongest choice out of the polymer binders. In addition, as with C_8-BTBT, C_{16}IDT-BT has good solubility, as well as a HOMO level that is a reasonably good match to the C_8-BTBT HOMO level (Figure 5.1 (b)) [201, 214]. Therefore, for the blend system in this work, C_{16}IDT-BT was chosen as the complementary polymer binder for the small-molecule C_8-BTBT.

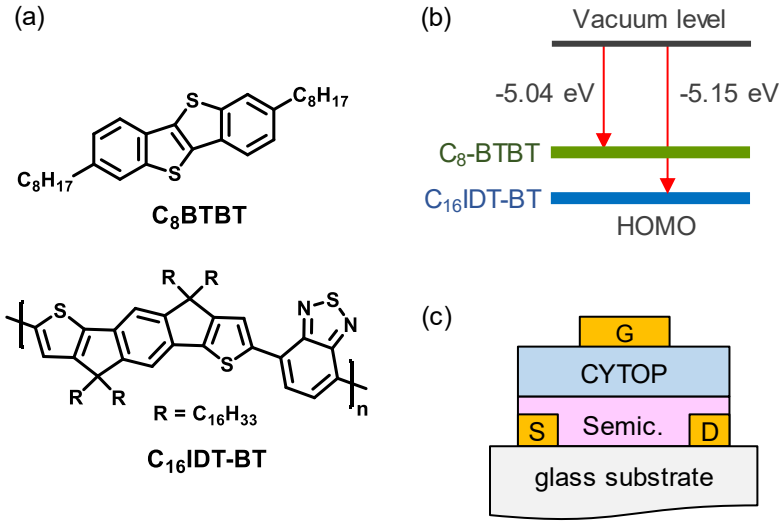

Figure 5.1: C_8-BTBT, C_{16}IDT-BT, energy levels OTFT architecture. (a) The chemical structures of 2,7-dioctyl[1]benzothieno[3,2-b][1]benzothiophene (C_8-BTBT) and indacenodithiophene-benzothiadiazole (C_{16}IDT-BT), (b) Energy level diagram showing complementary HOMO levels of C_8-BTBT and C_{16}IDT-BT as measured by air photoemission spectroscopy and (c) top-gate bottom-contact (TG-BC) architecture used to investigate the organic blend.

As the organic solvent chlorobenzene (CB) is the solvent of choice for C_{16}IDT-BT [220] [221] [222], initial investigations for the C_8-BTBT:C_{16}IDT-BT blend were carried out using CB. It has been shown on several occasions that the ratio of small-molecule to polymer, as well as the overall solution concentration, is of huge importance [88] [95] [139]. Therefore, the C_8-BTBT and C_{16}IDT-BT were investigated at a range of different ratios in a top-gate bottom-contact (TG-BC) transistor configuration, with channel lengths (L) from 30 µm to 100 µm and a channel width (W) of 1 mm.

It was found that if the C_8-BTBT content in the blend was greater than or less than 25% of the total weight of the blend materials, the mobility of the blend OTFTs decreased. Furthermore, if the C_8-BTBT content was more than 25% then the OTFTs had more prominent *n*-type characteristics, as well as a lower $I_{ON/OFF}$ due to an increase in the film thickness and alteration of the bulk conductivity. When the amount of C_8-BTBT was greater than 50%, significant cracks, small crystallites and uneven surfaces were observed in the blend films, resulting in lower mobility OTFTs. Reducing the small-molecule content to 25% appears to improve the miscibility between the small-molecule and the polymer, which encourages a continuous layer of C_8-BTBT at the surface/air interface. However, if the C_8-BTBT content is any lower than 25% then very faint, thin C_8-BTBT crystallites are observed and the mobility of the system is reduced. Similar blend films and OTFT performance trends were observed with the solution concentration, i.e. if the blend solution concentration was above 10 mg/ml then the

film thickness increased and distorted the formation of the C_8-BTBT crystallites, whereas below 10 mg/ml limited produced very thin films and poor C_8-BTBT crystal thickness.

Therefore, from these preliminary investigations, it was found that the best blend ratio for producing the highest performing devices was 25% C_8-BTBT to 75% C_{16}IDT-BT at a 10 mg/ml total solution concentration.

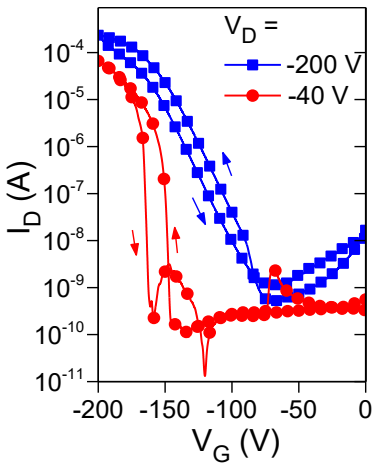

Figure 5.2: Representative transfer curve for C_8-BTBT:C_{16}IDT-BT blend OTFTs. Devices are made from CB with 25% small-molecule and 75% polymer in a 10 mg/ml concentrtaion solution; this device has channel length 80 µm and width 1000 µm and has been tested at V_D = -40 V and V_D = -200 V at room temperature in a nitrogen atmosphere.

A representative transfer curve for the C_8-BTBT:C_{16}IDT-BT blend devices in CB is shown in Figure 5.2. It is clear from this transfer curve that these as-made blend devices exhibit non-ideal properties, requiring high operating voltages as well as suffering from hysteresis. There are a few ways to potentially explain the transport behaviour observed here: (i) the high operating voltages can be attributed to the 900 nm thick Cytop dielectric layer and the low dielectric constant (=2.1) associated with this fluropolymer, and (ii) the origin of the hysteresis could be due to significant energetic disorder.

Energetic disorder has been seen previously in the 1st generation blend system and is attributed to the presence of deep trap states within the semiconductor [91]. The high gate fields shown in Figure 5.2 are required to fill such trap states before the channel current can be switched-on, but once the as-made blend devices enter saturation, they are able to maintain large channel currents, which is characteristic of OTFT material systems with high mobilities. The presence of the trap states could be due to microstructural defects within the system [91] and/or the 100 meV difference between the HOMO level energies of the C_8-BTBT and the

C_{16}IDT-BT (Figure 5.1). Other causes of trap states could be the molecular weight distribution of the C_{16}IDT-BT and/or chemical impurities [223]. In addition, Figure 5.2 shows that the as-prepared blend OTFTs are ambipolar with prominent *p*-type characteristics.

Despite the nonidealities in the transfer characteristics, there is a key observation that demonstrates the potential of this materials system and the combination of this particular small-molecule/polymer blend: compared to mobilities of the single-system control devices, C_8-BTBT (=2.6 cm^2/Vs) and C_{16}IDT-BT (=3.1 cm^2/Vs), the blend has a higher maximum hole mobility of $\mu_{sat} \approx 4.7$ cm^2/Vs. This indicates that by blending C_{16}IDT-BT with C_8-BTBT, C_8-BTBT grain boundary passivation can be achieved. Grain boundary passivation is characteristic of small-molecule/polymer blend systems and similar effects have been observed at the grain boundaries in the 1st generation and 2nd generation blends [87] [88]. In this case, C_{16}IDT-BT appears to have improved charge carrier transport between C_8-BTBT-rich regions at the OTFT channel, which would explain the higher mobilities.

5.1.3 The ternary blend: Small-molecule/polymer/dopant

Chapter 3 highlighted that introducing a molecular dopant to an OSC is a very simple and powerful way to deactivate unwanted trap states, decrease energetic disorder and improve OTFT operating characteristics. Therefore, the hypothesis regarding energetic disorder and trap states in the as-prepared C_8-BTBT:C_{16}IDT-BT blend was further investigated by introducing a molecular dopant, with the aim of intentionally *p*-doping the blend system. It is also expected that the *p*-dopant molecules in the ternary blend system will increase the charge carrier density by accepting electrons and leaving behind positively charged holes. Therefore, as well as improvements in the operating characteristics, doping mechanisms should also cause a reduction in the *n*-type behaviour shown in Figure 5.2.

Different molecular dopants were thus investigated in the C_8-BTBT:C_{16}IDT-BT blend, with the most promising candidate being the fluorinated fullerene derivative, $C_{60}F_{48}$ (Figure 5.3) [224] [225] [226]. Because of its large electron affinity, and large molecular size able to withstand diffusivity, $C_{60}F_{48}$ has already been successfully used as a *p*-dopant in various carbon-based materials [157] [158] [227] [228].

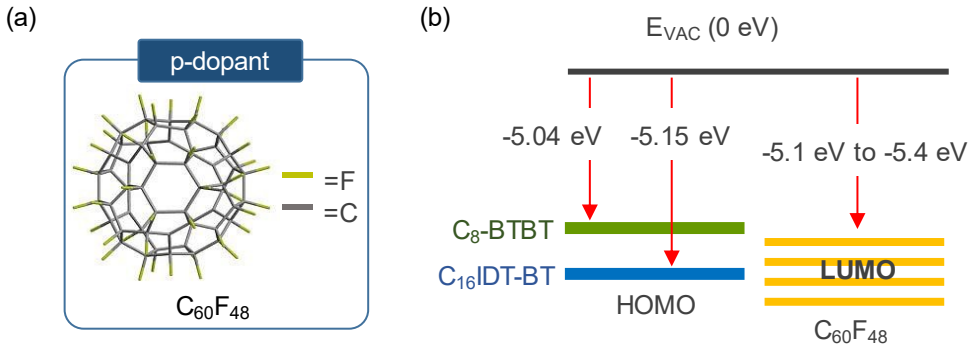

Figure 5.3: $C_{60}F_{48}$ and 3rd generation blend energy diagram. (a) The chemical structure of $C_{60}F_{48}$ used as a molecular dopant, (b) Energy level diagram showing C_8-BTBT and C_{16}IDT-BT HOMO levels measured using air photoemission spectroscopy compared to the range of published LUMO energies for $C_{60}F_{48}$ [157] [158] [227] [228].

A range of $C_{60}F_{48}$ molar weight (wt.) percentages were investigated (0.01%, 0.1%, 1%, 5%, and 10%) in the C_8-BTBT:C_{16}IDT-BT blend. As the amount of $C_{60}F_{48}$ in the blend was gradually increased, the OTFT operating characteristics were seen to gradually change and evolve; the threshold voltage began to shift towards positive biases, the hysteresis gradually improved, *n*-type behaviour was supressed, I_{ON} increased and – eventually – I_{OFF} began to increase. By varying the doping concentration, it was found that 1% molar wt. $C_{60}F_{48}$ had the most significant effect on the transistors. Representative transfer characteristics for the C_8-BTBT:C_{16}IDT-BT CB blend devices made from 25% small-molecule and 75% polymer, doped with 1% molar wt. $C_{60}F_{48}$, are shown in Figure 5.4. Compared to the transfer characteristics from the as-made devices (Figure 5.2), there are striking improvements due to the addition of the dopant, particularly in the operating voltages and hysteresis. However, the most noticeable effect is the impressive enhancement in the saturation mobility, which now reaches a maximum value of 7.8 cm^2/Vs, (an average of 5.3 cm^2/Vs calculated from 10 transistors). This is higher than any mobility value that has been reported for OTFTs made with the single-component semiconductors C_8-BTBT and C_{16}IDT-BT.

There are three indications that the improvements in the transistors are due to *p*-doping: (i) a shift in the threshold voltage, (ii) increasing the $C_{60}F_{48}$ concentration to over 1% increases hole concentration, which subsequently increases the off-current and reduces the on/off ratio, (iii) the *n*-type behaviour has been quashed due to $C_{60}F_{48}$ molecules acting as deep electron traps.

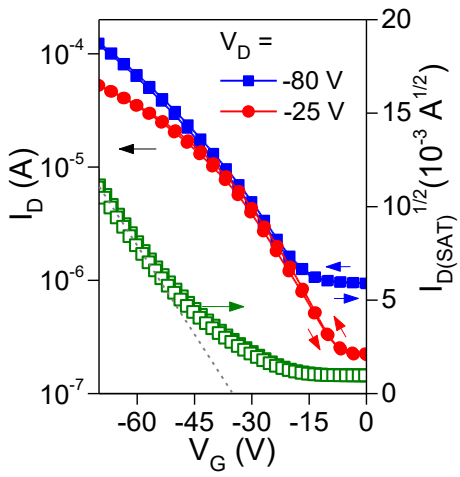

Figure 5.4: C_8-BTBT:C_{16}IDT-BT:$C_{60}F_{48}$(1%) blend OTFT processed from CB. Transfer characteristics for a device with channel length 80 µm and width 1000 µm, tested at V_D = -25 V and V_D = -80 V in a nitrogen atmosphere and at room temperature.

5.1.4 Alternative solvent systems

The solvent is an important parameter for solution-processed organic semiconductors. The choice of solvent has a huge influence on crystal size/formation due to its role in crystallisation kinetics and the thermodynamics underpinning film-formation. This is important for organic semiconductors as they have a strong property-structure relationship, and larger crystalline regions generally represent lower structural disorder, and hence improved electronic properties. Optimising the solvent offers an opportunity to form different shapes and sizes of crystals; different solute-solvent interaction energies, where solute molecules can be adsorbed onto the faces of the growing crystals, can alter the normal growth rate of different crystal faces [229], [230]. Therefore solvent variation has been used extensively in crystal engineering for different applications in a wide range of industries [27] [83, 232] [96] [231]. Over the years, solvents, or multi-solvent systems, have also been used to tailor the morphology of OSC films and hence optimise the electrical performance [83] [115] [233] [234] [235] [236] [237].

A range of solvents compatible to both C_8-BTBT and C_{16}IDT-BT were therefore explored as alternatives to the CB for the *p*-doped C_8-BTBT:C_{16}IDT-BT:$C_{60}F_{48}$ blend: chloroform, tetrahydrofuran (THF), anisole, dimethylformamide (DMF) and 1,2,3,4-tetrahydronaphthalene (tetralin). Each of these solvents were tested individually, as well as combined with one another at a range of ratios to investigate the effects of solvent mixtures on the blend microstructure and OTFT performance (Appendix B).

For example, representative transfer characteristics for the OTFTs processed from tetralin are shown in Figure 5.5. The devices have low threshold voltages and demonstrate hysteresis-free operation, but the mobility values are significantly reduced in comparison to the transistors devices made using CB, with the hole saturation mobilities between 0.1 and 1.6 cm^2/Vs.

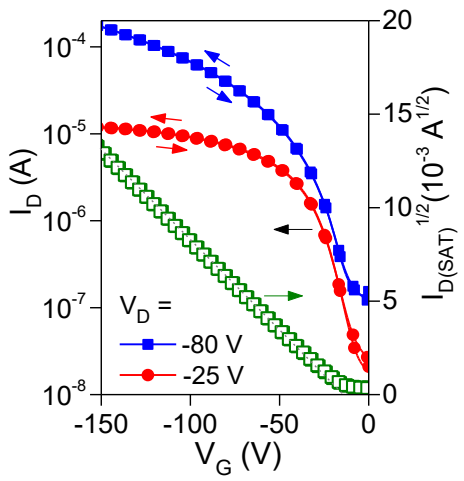

Figure 5.5: Tetralin effects on blend OTFT performance. Representative transfer characteristics for C_8-BTBT:C_{16}IDT-BT:$C_{60}F_{48}$(1%) blend OTFT processed from tetralin. The device has channel length 80 µm and width 1000 µm and has been tested at V_D = -25 V and V_D = -80 V in a nitrogen atmosphere and at room temperature.

Despite the low mobilities of the single-solvent tetralin devices, it was found that by using a solution made from 50% tetralin and 50% CB (tetralin:CB), not only did the device-to-device uniformity and channel current on–off ratio ($I_{ON/OFF} > 10^3$) of the C_8-BTBT:C_{16}IDT-BT:$C_{60}F_{48}$(1%) blend OTFTs significantly improve compared to the CB devices, but the maximum saturation hole mobility was dramatically improved to values in excess of 13 cm^2/Vs, (an average of 9.4 cm^2/Vs calculated over 16 transistors). Figure 5.6 shows representative transfer and output characteristics for a TG-BC C_8-BTBT:C_{16}IDTBT:$C_{60}F_{48}$(1%) blend transistor fabricated from the tetralin:CB solution, annealed at 120°C and quenched to room temperature.

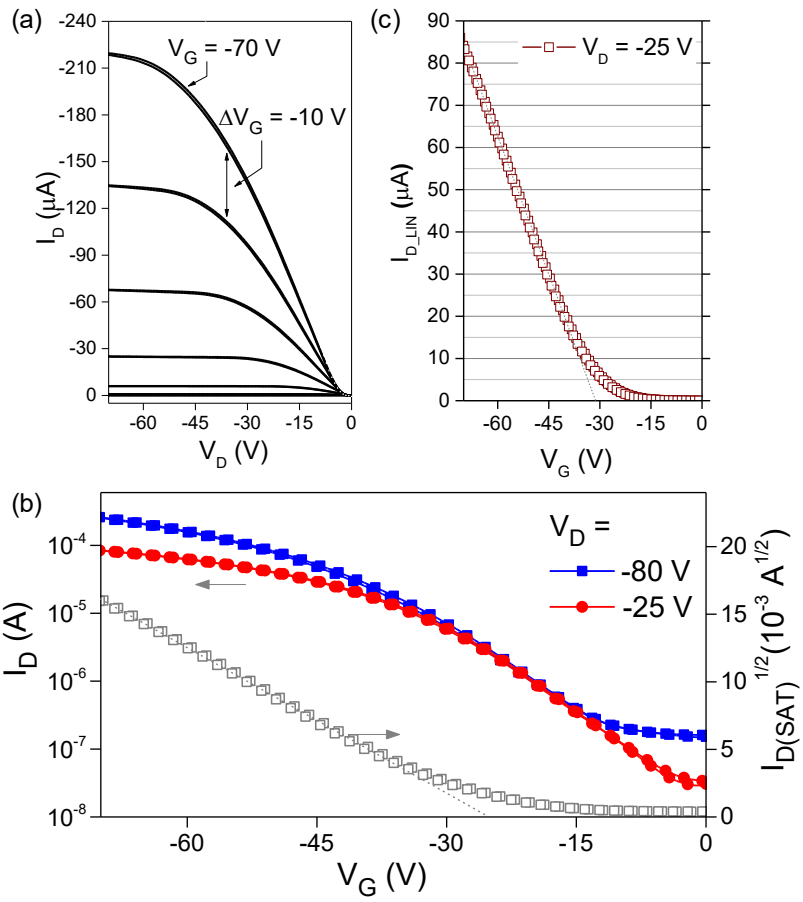

Figure 5.6: Tetralin:CB effects on blend OTFT performance. (a) Representative output characteristics and (b) transfer characteristics for the *p*-doped C_8-BTBT:C_{16}IDT-BT:$C_{60}F_{48}$ processed from tetralin:CB; this device has channel length 80 μm and width 1000 μm and has been tested at V_D = -25 V and V_D = -80 V at room temperature in a nitrogen atmosphere, (c) A linear scale plot of the drain current in the linear regime (V_D = -25 V) vs. gate voltage for the same device shown in (a), exhibiting no "s-shaped" characteristics.

The evolution, spreads and mean values of the hole mobilities for the tetralin:CB, tetralin and CB solvent systems are summarised in Figure 5.7 (a). These results indicate that a tetralin:CB solvent blend, combined with a molecular *p*-dopant, significantly improves the operating characteristics of the C_8-BTBT:C_{16}IDT-BT blend OTFTs.

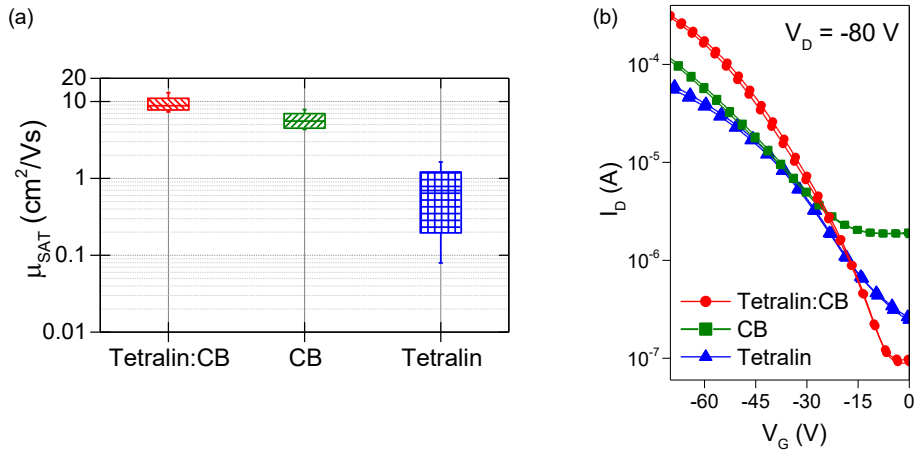

Figure 5.7: Effects of different solvent systems on transfer characteristics and mobility. (a) A box-and-whisker plot showing the differences in saturation mobilities for the tetralin:CB, CB and tetralin solutions, (b) The representative transfer characteristics measured at V_D = -80 V are compared for the three different solvent systems, demonstrating an increase in maximum current, subthreshold slope and $I_{ON/OFF}$ for the tetralin:CB OTFTs.

Figure 5.8 (a) shows the impact of the small-molecule/polymer ratio on saturation mobility in the C_8-BTBT:C_{16}IDTBT:$C_{60}F_{48}$(1%) tetralin:CB blend. As with the single-solvent CB devices, it was found that a blend ratio of 25% small-molecule to 75% polymer generated OTFTs with optimum performance. The reason for this could be due to an improved miscibility between the two blend materials, which improves the quality of the film formed following solvent evaporation.

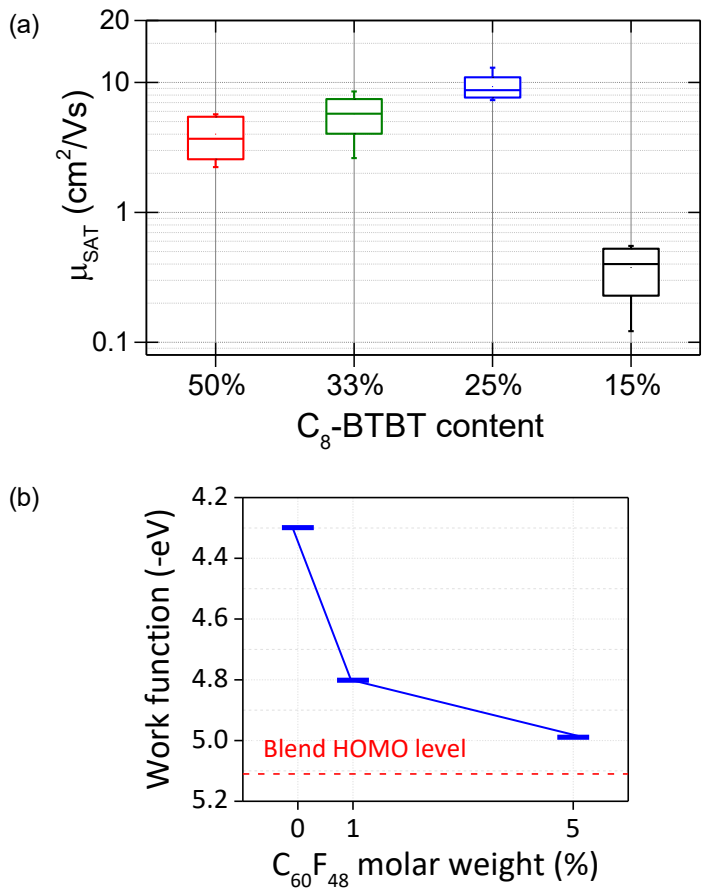

Figure 5.8: C_8-BTBT:C_{16}IDT-BT:$C_{60}F_{48}$(1%) blend ratio and work function. (a) Box-and-whisker plot to show the effect of the blend ratio on saturation mobilities for the C_8-BTBT:C_{16}IDT-BT:$C_{60}F_{48}$(1%) tetralin:CB blends, (b) Kelvin Probe and air photoemission measurements for the 25% C_8-BTBT blend showing the work function moving towards the HOMO level in the C_8-BTBT:C_{16}IDT-BT blend with the addition of $C_{60}F_{48}$; the work function deepens with increasing molar weight percentage of $C_{60}F_{48}$, indicative of *p*-doping processes.

In addition to the transfer characteristics, further evidence to show that the C_8-BTBT:C_{16}IDT-BT blend has been *p*-doped by $C_{60}F_{48}$ has been obtained using Kelvin probe (KP) measurements. Figure 5.8 (b) shows the change in the C_8-BTBT:C_{16}IDT-BT blend work function as a function of $C_{60}F_{48}$ concentration. Compared to the as-made pristine C_8-BTBT:C_{16}IDT-BT blend, the addition of $C_{60}F_{48}$ at 1% molar wt. results in a large shift in the work function (0.5 eV). Increasing the amount of $C_{60}F_{48}$ even further in the blend reduces the work function by another 0.2 eV (to 4.9 eV). As expected in a *p*-doped system, the HOMO energy level, measured by atmospheric photoemission spectroscopy (APS), does not change.

5.1.5 Morphological and structural characterisation

The choice of solvent has had a noticeable impact on the C_8-BTBT:C_{16}IDT-BT:$C_{60}F_{48}$(1%) blend OTFTs. To find out more about why this is the case, various morphological and structural characterisation techniques were used to investigate what may be causing the differences in electrical performance.

5.1.5.1 Polarised optical microscopy, atomic force microscopy and scanning electron microscopy

The morphologies of the blends from the three different solvent systems were explored using polarized optical microscopy (POM), atomic force microscopy (AFM), and scanning electron microscopy (SEM) techniques, to probe any differences between the films.

As expected, the POM images in Figure 5.9 show that the C_8-BTBT:C_{16}IDT-BT:$C_{60}F_{48}$(1%) blends made from tetralin:CB, CB, and tetralin exhibit solvent-dependent microstructures [27] [115] [229] [230]. The tetralin:CB films in Figure 5.9 (a) appear to have C_8-BTBT-rich crystalline regions of long, random shapes, whereas the CB films in Figure 5.9 (b) are composed of more typical spherulite-like crystallites. In contrast, Figure 5.9 (c) shows that the tetralin films have formed highly discontinuous bi-layer structures.

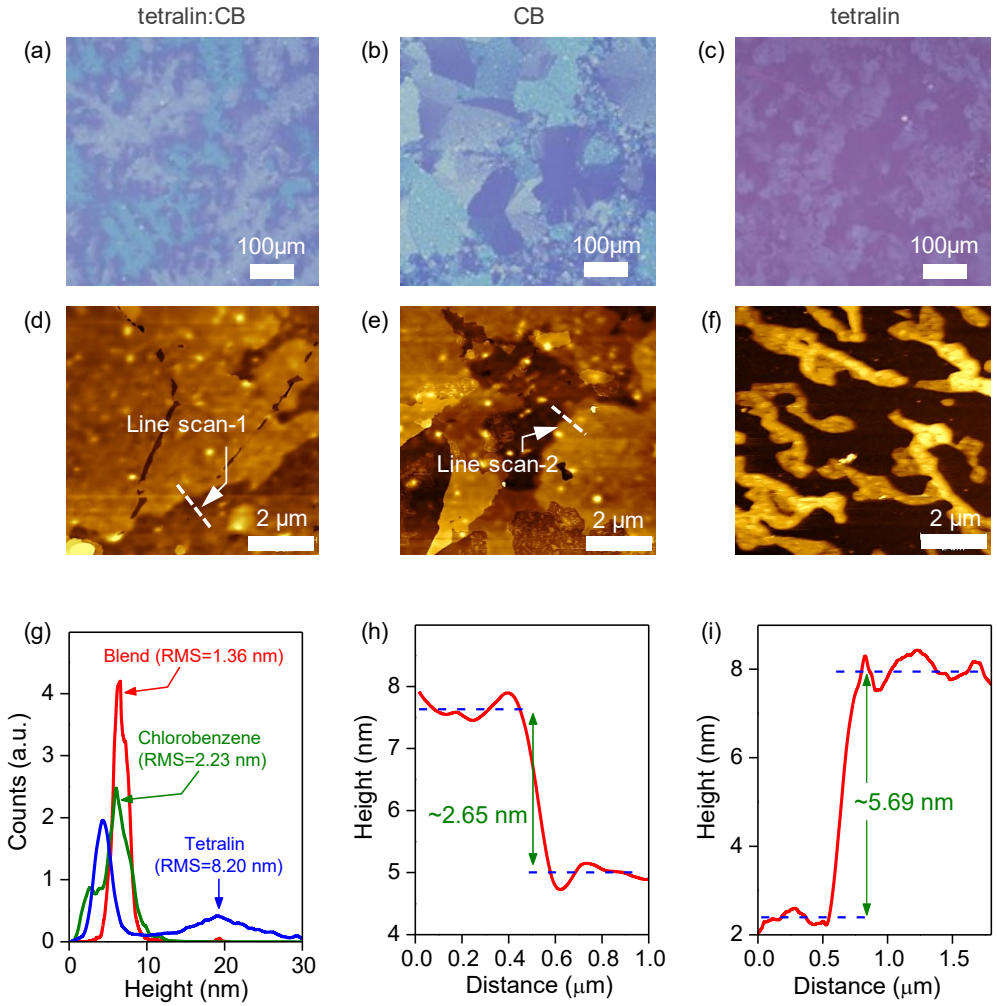

Figure 5.9: POM and AFM imaging. Polarised optical microscope images of (a) 50% tetralin 50% CB, (b) CB and (c) tetralin C_8-BTBT:C_{16}IDT-BT:$C_{60}F_{48}$(1%) films and their respective atomic force microscope (AFM) images in (d-f). Histograms in (g) showing surface height distributions with corresponding root mean squared (RMS) values for the 3 different solvent systems. Line-scan 1 in (h) showing molecular terracing for image (d), and line-scan 2 in (i) corresponding to figure (e).

The solvent-dependent morphologies were investigated further using AFM; Figure 5.9 (d-g) shows the AFM imaging and statistical height distributions. The root mean square (RMS) surface roughness values shown in Figure 5.9 (g) indicate that the tetralin:CB films have significantly smoother topography with a lower RMS and narrower distribution of heights, compared to the CB and tetralin films, which exhibit multimodal distributions. The multimodal distributions in the CB and tetralin films are indicative of the presence of plateaus and valleys. In the case of the tetralin film, the bi-layer structure could be due to the fact that tetralin has a high boiling point (207°C), which gives the C_8-BTBT a lot of time following spin-coating to diffuse, phase separate and dewet from the higher viscosity polymer, which results in the polycrystalline domains shown in Figure 5.9 (c). CB, on the other hand, has a

lower boiling point (131°C), and the tetralin:CB and CB films are both characterised by continuous polycrystalline upper-layers of C_8-BTBT.

Figure 5.9 (h) shows a line scan for the surface of the tetralin:CB film that has been extracted from the AFM measurements. This data indicates that the C_8-BTBT upper-layer in the tetralin:CB films have formed molecular terraces with height 2.65 (±0.2) nm; such molecular terracing has been shown before in high-mobility C_8-BTBT-based OTFT literature [28] [30] [219] [238]. Figure 5.9 (i) shows that similar terracing is also seen in the CB layers, however, here it appears to be 2-3 molecules thick (=5.69 (±0.2) nm). In contrast, no molecular terracing is seen in the tetralin films.

It is fair to ask why the CB films that have a good coverage/continuous upper layer of C_8-BTBT, reasonably sized spherulite-like crystallites (Figure 5.9 (b)), and some molecular terracing (albeit terracing of multiple molecules) do not produce OTFTs with mobilities as high as the tetralin:CB film. SEM imaging gives a good insight into why this may be the case; Figure 5.10 shows the SEM images, where Figure 5.10 (c) shows that the CB films have significant perforations in the C_8-BTBT crystallites. These perforations are likely to be thermally-induced cracks. Thermally-induced cracks are known to form in liquid crystalline small-molecules and, in particular, they are known to inhibit charge transport in C_8-BTBT-based systems, preventing higher mobilities from being accessed [34, 239].

On the other hand, the films processed from tetralin:CB shown in Figure 5.10 (a) and Figure 5.10 (b) do not have any cracks and appear to be continuous. Although it is difficult to say for certain without further experimentation, it is possible that the differences in the morphology between the CB and tetralin:CB films are due to residual-solvent effects [121] [240].

Finally, the SEM images show that the films processed from tetralin exhibit strong phase separation and a bi-modal structure that correlates with the POM images. The cracks and bi-modal structures seen in the CB and tetralin films respectively have most likely resulted in the lower mobilities that have been measured for these single-solvent systems. SEM imaging has also been done for the pristine (0% $C_{60}F_{48}$) tetralin:CB films (Figure 5.10 (a)) and there appears to be very little difference between the morphology of the pristine film and the high mobility *p*-doped film.

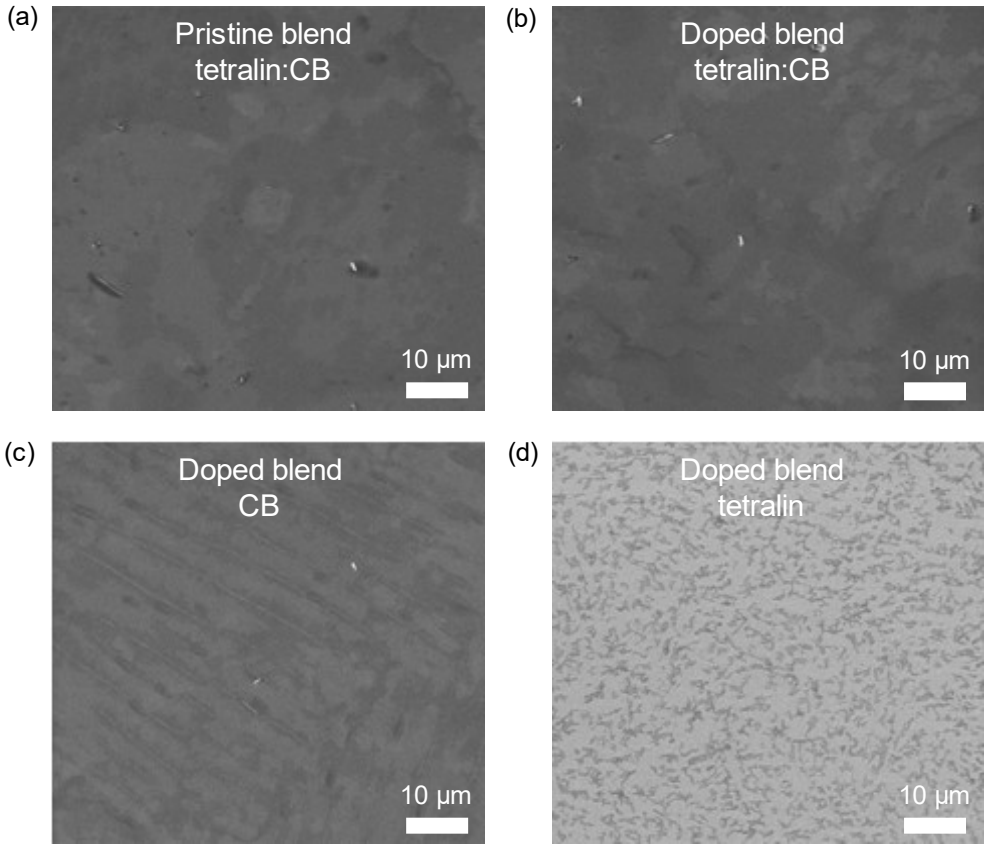

Figure 5.10: Scanning Electron Microscopy images. (a) the pristine C_8-BTBT:C_{16}IDT-BT blend made from a 50% tetralin 50% CB solution, and *p*-doped C_8-BTBT:C_{16}IDT-BT:$C_{60}F_{48}$(1%) blend films processed from (b) 50% tetralin 50% CB, (c) neat chlorobenzene and (d) neat tetralin solutions. The images of the pristine and doped tetralin:CB blends show very little difference in surface morphology.

5.1.5.2 Waterfall -plane wide angle X-ray diffraction and time-of-flight secondary ion mass spectroscopy

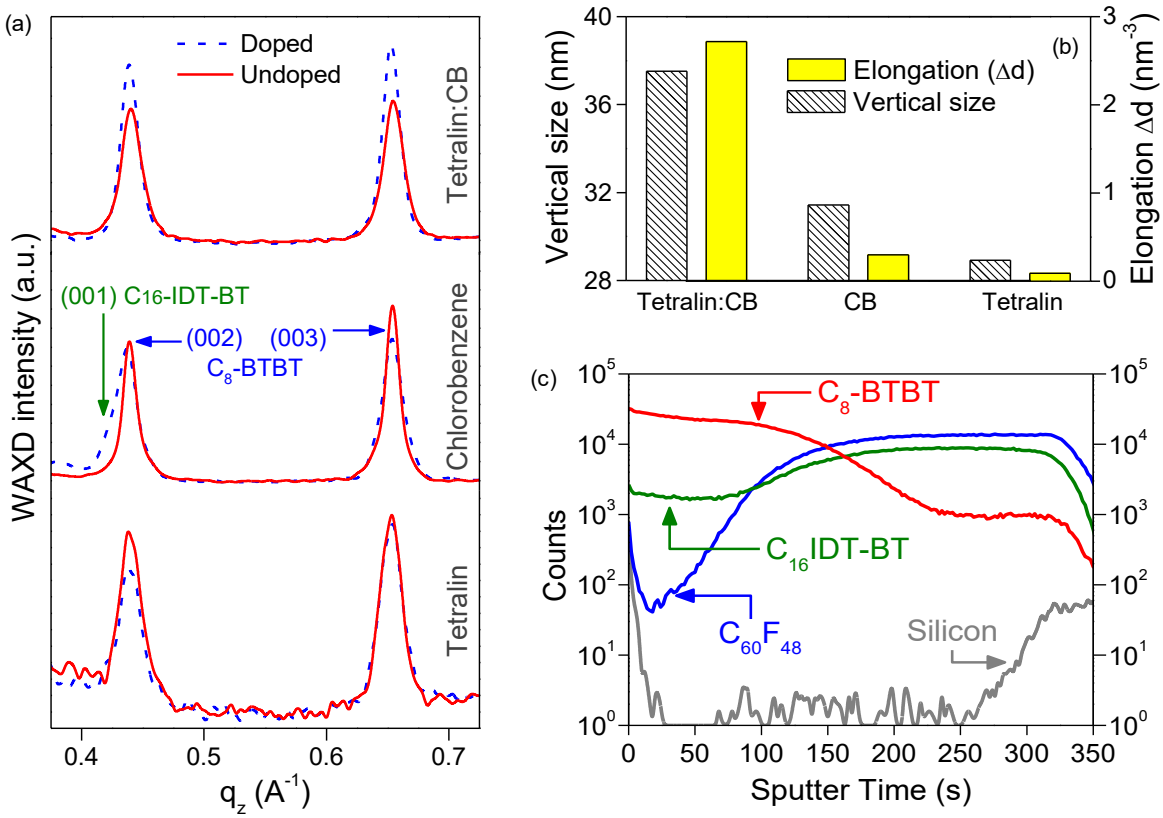

Figure 5.11: In-plane WAXD measurements. (a) WAXD for the blend processed from the three different solvents (i.e. tetralin:CB, CB and tetralin). The solid line represents the pristine blend films (C_8-BTBT:C_{16}IDT-BT) and the dashed line represents the doped (C_8-BTBT:C_{16}IDT-BT:$C_{60}F_{48}$(1%)) films, (b) the (003) lattice plane spacing elongation (Δd) of the C_8-BTBT and the z-direction (i.e. vertical) crystallite size for the C_8-BTBT processed from the three solvent systems, (c) Time-of-flight secondary ion mass spectrometry (ToF-SIMS) measurement data for the best performing *p*-doped C_8-BTBT:C_{16}IDT-BT:$C_{60}F_{48}$(1%) blend films made from tetralin:CB solvent solution.

The layered crystallinity shown in C_8-BTBT – demonstrated by the molecular terracing shown in Figure 5.9 (h) – is known to encourage charge transport in the x-y plane [30] [241]. Therefore, an in-plane wide-angle X-ray diffraction (WAXD) technique was used to examine the crystal structure in the charge carrier direction i.e. the blend film surface. Doped and pristine films processed from the three solvent systems (CB, tetralin, tetralin:CB) were shown to be crystalline, each having main peaks that identify with the C_8-BTBT (Figure 5.11 (a)).

Some variations do exist between samples in terms of the C_8-BTBT in-plane crystallite size (i.e. lamellar stacking dimensions) and corresponding d-spacing; a Lorentzian peak fit

analysis was used to quantify these variations, which is summarised in the histogram in Figure 5.11 (b). The use of the tetralin:CB solvent-mix leads to improved crystallinity in the C_8-BTBT:C_{16}IDT-BT films, as well as longer spatial separation between the lattice planes. This suggests that the improved crystallinity in the *z*-direction – along with the enhanced continuity in the *x*-*y* plane that has been shown by both the AFM and SEM imaging (Figures 5.9 and 5.10) – could indeed result in the improved electrical characteristics of the OTFTs made from the *p*-doped C_8-BTBT:C_{16}IDT-BT:$C_{60}F_{48}$(1%) blend from tetralin:CB solutions. However, the improved crystallinity in the growth direction/*z*-direction is less significant than the differences in the *x*-*y* plane morphology shown in the AFM topography measurements. It is therefore reasonable to suggest that the improvements in the *x*-*y* plane long-range order have a more significant contribution to the overall improvement of the OTFTs.

Finally, time-of-flight secondary ion mass spectrometry (ToF-SIMS) was used to investigate the vertical phase separation of the highest mobility C_8-BTBT:C_{16}IDT-BT:$C_{60}F_{48}$(1%) films fabricated from tetralin:CB. Figure 5.11 (c) shows Poisson corrected ion signals for the individual molecular components (i.e. C_8-BTBT, C_{16}IDT-BT and $C_{60}F_{48}$) plotted as a function of the sputter time (where the air interface is at x = 0s). The C_8-BTBT signal decreases and C_{16}IDT-BT signal increases with time as the beam sputters through the depth of the blend film; there is a step-wise change in the elemental content, which suggests that there is a pseudo-bilayer microstructure present in the blend film, where the C_8-BTBT has separated to the surface-air interface with the C_{16}IDT-BT in the lower part of the film. This type of vertically phase separated microstructure – where the small-molecule is present on the surface of the film – is characteristic of the small-molecule/polymer blend systems and it is ideal for top-gate OTFTs (see *Chapter 3*) [87] [88] [91].

In addition, the ToF data rather interestingly suggests that the $C_{60}F_{48}$ signal is almost entirely within the C_{16}IDT-BT polymer that is positioned at the lower part of the film, i.e. the blend-substrate interface, which (for a top-gate structure) means that the $C_{60}F_{48}$ is not present at the channel. It is possible that this has happened because the $C_{60}F_{48}$ is more soluble in the C_{16}IDT-BT than in the C_8-BTBT, and/or the $C_{60}F_{48}$ has been expelled by the crystallisation of the C_8-BTBT, causing vertical phase separation of the small-molecule and the $C_{60}F_{48}$ to occur. Although this information suggests that the $C_{60}F_{48}$ is primarily found within the C_{16}IDT-BT, Figure 5.11 (c) also shows that at sputter time x = 0 s, a strong $C_{60}F_{48}$ signal is found at the surface-air interface. It is expected that the presence of an F-rich compound at the surface-air interface would reduce the surface energy of the blend system and therefore this type of phase separation is logically coherent. However, it is also possible that the physical gaps/perforations present in the top-layer of crystalline C_8-BTBT might allow the C_{16}IDTBT:$C_{60}F_{48}$(1%) layer to

be accessed by the sputtering beam even at sputter time x = 0 s; this would lead to ions associated with the C_{16}IDTBT and $C_{60}F_{48}$ compounds being observed near to the surface.

5.1.6 Doping mechanisms in the C_8-BTBT:C_{16}IDT-BT:$C_{60}F_{48}$ ternary organic blend

The unusual distribution of the materials within the system indicates that there may be some unconventional doping mechanisms operating in this blend. Although Figure 5.3 (b) suggests that the C_8-BTBT should be more easily doped based on its HOMO level energy, as the dopant appears to be distributed entirely within the polymer, this would suggest that the free holes are being generated either in the C_{16}IDT-BT and/or in the proximity of the mixed C_8-BTBT:C_{16}IDT-BT:$C_{60}F_{48}$(1%) interface.

If this is the case, then there are a few ways in which the generated free holes could contribute to the current in the channel: (i) by deactivating the hole traps existing in the pristine OTFTs, (ii) by enabling hole transport pathways between C_8-BTBT-rich domains in the polycrystalline small-molecule upper-layer because there is improved conductivity in the C_{16}IDT-BT (in a similar manner to the 1st generation grain boundary effects), (iii) by free holes being remotely transferred to the channel, in a similar manner to modulation doping in inorganics.

Although it is too early to say for certain which of these mechanisms is the most dominant, it does appear that the dramatic improvement in the mobility and charge transport characteristics in the C_8-BTBT:C_{16}IDT-BT:$C_{60}F_{48}$(1%) blend are due to synergetic effects from multiple processes, with the prevailing mechanism most likely to be hole trap deactivation.

5.2 The 3rd generation blend as a prospective system

5.2.1 Introduction

The rest of this chapter highlights two reasons for this 3rd generation blend as a prospective system.

Firstly, the C_8-BTBT:C_{16}IDT-BT:$C_{60}F_{48}$(1%) blend could be a model system for other small-molecule/polymer/dopant blends. Indeed, doping mechanisms in another ternary blend of diF-TESADT:PTAA *p*-doped with Mo tris-[l,2-bis(trifluoromethyl)ethane-l,2-dithiolene] (MoTDT) have been observed in the patent literature [149].

Secondly, it has been shown that single-crystal C_8-BTBT OTFTs can achieve maximum mobilities of 31.3 cm^2/Vs [30]. Based on this, it's feasible that, with further research

into processing optimisation, the performance of the 3rd generation blend system could be improved even further.

5.2.2 Alternative blend materials

Over the past few years, there have been exciting improvements in the intrinsic properties of polymeric semiconducting materials [29, 242-244]. One of these polymers is indacenodithieno[3,2-b]thiophene--benzothiadiazole (IDTT-BT) which was designed by Zhang et al. IDTT-BT has been shown to have hole mobilities of 2.6 cm^2/Vs, which are dramatically improved to 8.7 cm^2/Vs when used in conjunction with a copper thiocyanate (CuSCN) injection layer [245]. IDTT-BT was designed to be a revised version of C_{16}IDT-BT, with improved performance from extended conjugated segments and increased π-orbital overlap on the polymer chains. Because IDTT-BT has similar characteristics and solubility to C_{16}IDT-BT, it is an ideal alternative polymer to try in the 3rd generation blend.

As a preliminary investigation, IDTT-BT was used as a direct replacement for the polymer-binder (C_{16}IDT-BT) in the optimised C_8-BTBT:C_{16}IDT-BT blends (i.e. at 25% C_8-BTBT and 75% IDTT-BT, 10 mg/ml concentration and a solvent solution of 50% tetralin and 50% CB). Figure 5.12 (a) is a representative transfer curve for the C_8-BTBT:IDTT-BT blend without any dopant; again, high operating voltages are required and hysteresis is exhibited, demonstrating similar energetic disorder that was seen in the C_8-BTBT:C_{16}IDT-BT blend. Ambipolar characteristics are also observed in this system. A maximum hole saturation mobility of ≈2 cm^2/Vs is achieved for these pristine transistors, which is reasonable considering that the blend is not at all optimised.

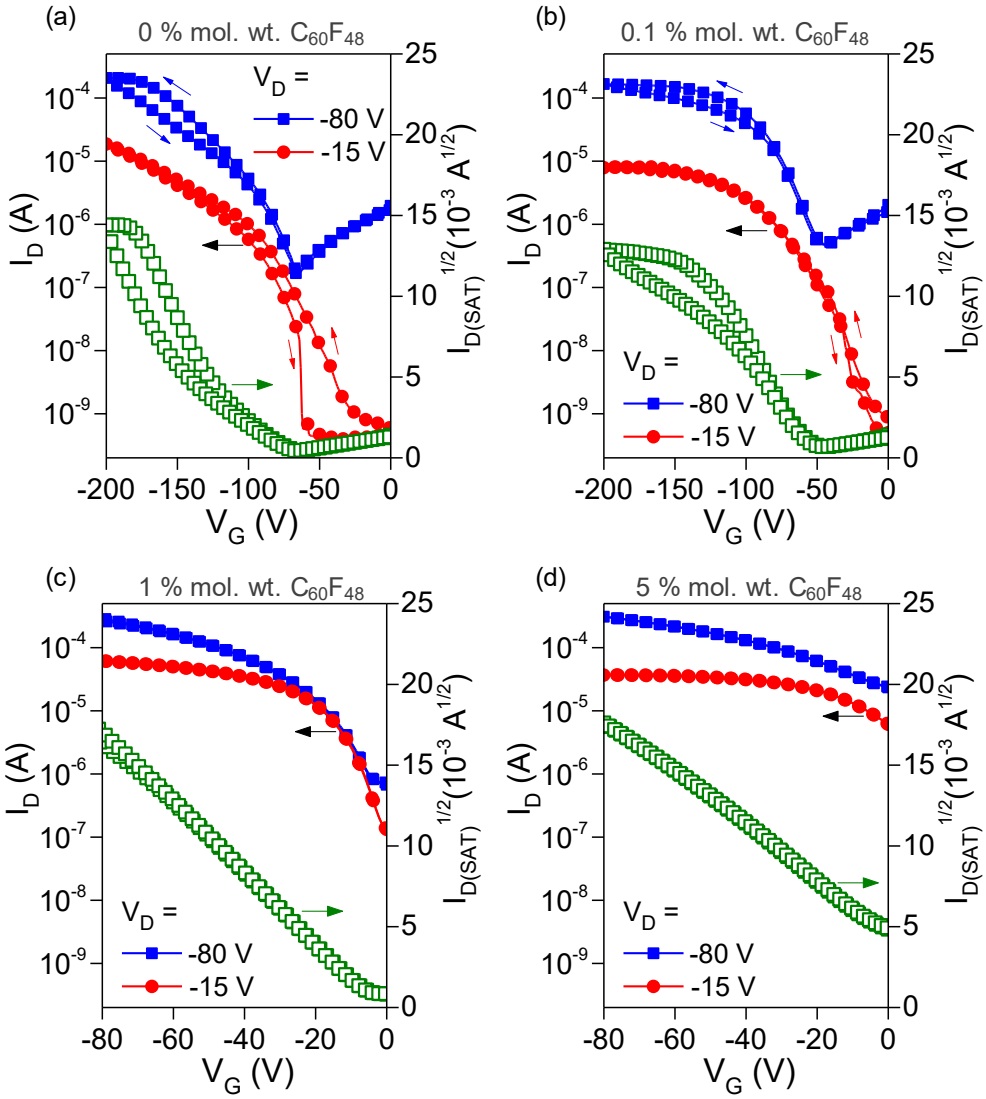

Figure 5.12: C_8-BTBT:IDTT-BT:$C_{60}F_{48}$ blend devices, fabricated by directly replacing the C_{16}IDT-BT polymer binder in the optimised 3rd generation blend with IDTT-BT. The C_8-BTBT:IDTT-BT blend has been doped at a range of ratios to observe molecular doping trends: (a) 0% $C_{60}F_{48}$, (b) 0.1% $C_{60}F_{48}$, (c) 1% $C_{60}F_{48}$, (d) 5% $C_{60}F_{48}$.

Figure 5.12 shows the effect of introducing $C_{60}F_{48}$ as a molecular dopant at a range of molar weight percentages (0.1%, 1% and 5%). The trend exhibited is remarkably similar to the C_8-BTBT:C_{16}IDT-BT blend: a shift in the threshold voltage, an increase in off-current at high doping percentages (Figure 5.12 (d)), ambipolar characteristics are now predominantly *p*-type and the mobility of the 1% $C_{60}F_{48}$ blend has increased to ≈4 cm^2/Vs. A further increase of the dopant to 5% results in a drop in the maximum saturation mobility, down to ≈2.5 cm^2/Vs.

The important aspects of this preliminary study are the doping mechanisms shown in the transfer curves, the significant improvement in the transfer characteristics and the mobility

improvement for the 1% mol. wt. doped blend compared to the pristine blend. The results imply that the improvements in energetic disorder due to the addition of a dopant could be applicable to other organic blend systems; optimisation of the dopant concentration, blend ratio, solvents and spin-coating recipe would certainly be required to yield optimum performance for this system.

5.2.3 3rd generation blend-based OTFTs with hole mobility values > 20 cm^2/Vs

Improving molecular ordering in OSCs is important because it improves the overlap of π-orbitals and charge transport via π-π interactions. Over the years, a number of ways have been concocted to improve molecular ordering of solution-processed OSCs, for example, designing new materials [219] [245], new solution-deposition approaches [30] [31] [246] [247], and surface-based treatments such as grooves in the substrate [248] [249] [250].

In addition to chemical synthesis and new deposition/processing techniques, in-solution (i.e. pre-deposition) techniques have attracted attention; for example, carefully selected solvents [251] [252], solution-ageing [253] and ultrasonication [253] have all been shown to induce/promote small regions that have short-range order over a few molecular units in solution-phase polymers, known as *aggregates*.

For example, poly(3-hexylthiophene-2,5-diyl) (P3HT) is a semi-crystalline conjugated polymer containing both amorphous regions (highly disordered), as well as semi-ordered regions such as crystallites (large regions with long-range ordering) or aggregates. In such heterogeneous microstructures the charge transport predominantly occurs in the ordered regions and hence the presence of aggregation in a polymer system is highly important and any methods to induce such ordered regions are very attractive [254]. Indeed, ultrasonication-, solvent- and ageing- induced aggregation have all been used to improve the charge carrier mobility in P3HT [252] [253].

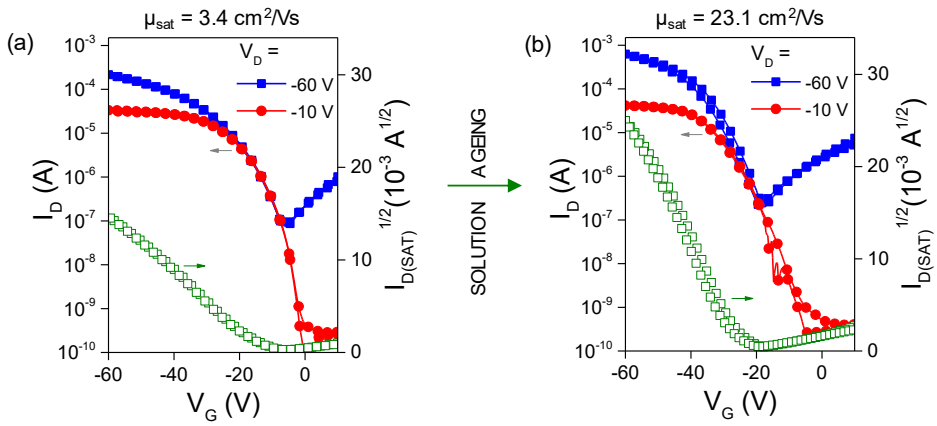

Figure 5.13: Effects of solution solution-ageing on transfer characteristics. (a) Transfer characteristics for a C_8-BTBT:C_{16}IDT-BT:$C_{60}F_{48}$(0.1%) blend device processed from a freshly prepared solution, (b) Transfer characteristics for a C_8-BTBT:C_{16}IDT-BT:$C_{60}F_{48}$(0.1%) blend device processed from a solution that had been aged in an inert nitrogen atmosphere for 2 months. Both devices have channel dimensions L = 80 µm and W = 1000 µm, have source/drain electrodes made from a bilayer of 5 nm of Al and 40 nm of Au, and have PTFE (AF2400) as the polymer dielectric layer. The blend is made in a tetralin:CB solution, which was previously found to be optimum for this system.

Solution-ageing effects were therefore explored in the C_8-BTBT:C_{16}IDT-BT:$C_{60}F_{48}$ blend to investigate if there are any effects similar to the "*time-dependent self-assembly*" and aggregation effects that have been seen in other organic systems. Solutions of the C_8-BTBT:C_{16}IDT-BT blend (at 25% small-molecule and 75% polymer in tetralin:CB solutions) doped at a range of concentrations (from 0% to 1%) were stored in an inert nitrogen atmosphere for 2 months. Fresh and aged OTFTs were then fabricated in a TG-BC configuration, with the same moderate solution heating, spin-coating recipe and post-deposition annealing treatment that have been used throughout this chapter and as detailed in *Chapter 4*.

The results were significant, especially for the 0.1% $C_{60}F_{48}$ blend. Figure 5.13 shows transfer characteristics for the C_8-BTBT:C_{16}IDT-BT:$C_{60}F_{48}$(0.1%) devices made from freshly prepared solutions (Figure 5.13 (a)) and devices made from solutions that had been aged for 2 months (Figure 5.13 (b)). Clear differences can be seen between the two devices, particularly in terms of the on-currents, which correlate with a staggering difference in mobility: the fresh OTFT in Figure 5.13 (a) has μ_{sat} = 3.4 cm^2/Vs, whereas the aged OTFT in Figure 5.13 (b) has an extremely high hole mobility value μ_{sat} = 23.1 cm^2/Vs.

A total of 30 transistors were measured for the fresh C_8-BTBT:C_{16}IDT-BT:$C_{60}F_{48}$(0.1%) blend and the aged C_8-BTBT:C_{16}IDT-BT:$C_{60}F_{48}$(0.1%) blend to give a statistical overview of the effects of the solution-ageing on saturation mobility; the mobility value spreads are shown in Figure 5.14. For the fresh OTFTs, the average hole

mobility over 30 TFTs was found to be =2.7 cm^2/Vs. In contrast, the average hole mobility for 30 TFTs made from the aged solution was significantly higher at =11.5 cm^2/Vs. Despite the significant increase in the average hole mobility after solution-ageing, there is a large difference between the maximum hole mobility value (=23.1 cm^2/Vs) and the average mobility value (=11.5 cm^2/Vs), which is due to poor device uniformity of the aged devices, which will be discussed later in this chapter.

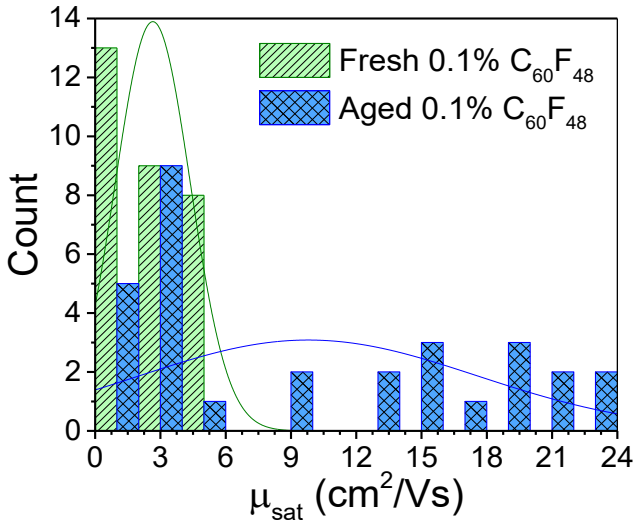

Figure 5.14: Effects of solution-ageing on saturation mobility. A histogram showing the difference in saturation mobility values for 30 freshly prepared C_8-BTBT:C_{16}IDT-BT:$C_{60}F_{48}$(0.1%) blend devices compared to 30 aged C_8-BTBT:C_{16}IDT-BT:$C_{60}F_{48}$(0.1%) blend devices, indicating the improvement as well as the variability in the performance of the aged blend.

If there are aggregates forming in the solution-phase polymer over time, then there are a number of factors that could affect why and how aggregation occurs, such as the presence of the small-molecule and the dopant molecules in the solution, as well as both the chlorobenzene and the tetralin solvents. Due to the number of variables, further materials characterisation and experimental work is required to understand the processes that are occurring over time in this complex solution; therefore, at this point in time it is difficult to ascertain the exact reasons for the superior performance of the aged blend solutions compared to the fresh blend solutions.

Having said that, there are a few clues within the transfer curves that allow some speculation on one of the mechanisms that might be at play. For example, the significant increase in mobility for the aged devices comes hand-in-hand with a shift in the threshold voltage towards negative voltages. For 30 devices, the threshold voltage has shifted by ≈-12 V, from an average V_{T_fresh} =-13.5 V, to an average V_{T_aged} =-25.3 V. V_T is associated with trap

states that need to be filled before mobile charge carriers can be induced in the OTFT channel. Therefore, a shift/reduction in V_T (i.e. towards positive voltages in the case of a *p*-type OTFT) is typically an indication of doping mechanisms in OTFTs, as the dopant may donate free charge carriers to fill trap states; indeed, one of the indications of doping in the 3rd generation blend system is that V_T shifts towards positive biases with the addition of the $C_{60}F_{48}$ in the C_8-BTBT:C_{16}IDT-BT blend.

Here, V_T has shifted towards negative biases in the aged C_8-BTBT:C_{16}IDT-BT:$C_{60}F_{48}$(0.1%) OTFTs when compared to the fresh 0.1% $C_{60}F_{48}$ OTFTs, potentially indicating a 'reversal' of the doping processes. In fact, if the aged OTFTs are compared to the pristine C_8-BTBT:C_{16}IDT-BT blend TFTs (i.e. 0% $C_{60}F_{48}$) of the same configuration, then the V_T values are very similar: over 30 devices, the average V_T for the pristine system is $V_{T_pristine}$ = -23.8 V compared to an average of $V_{T_0.1\%_aged}$ =-25.3 V for the aged system. This shift may imply that the dopant is not playing the same role as it is in the freshly made C_8-BTBT:C_{16}IDT-BT:$C_{60}F_{48}$(0.1%) devices. The 'reversal' of the doping mechanisms suggest that the dopant may have been displaced within the solution over time. However, the presence of the dopant could still be contributing to the electrical characteristics by, for example, enabling improved charge injection and contact resistance.

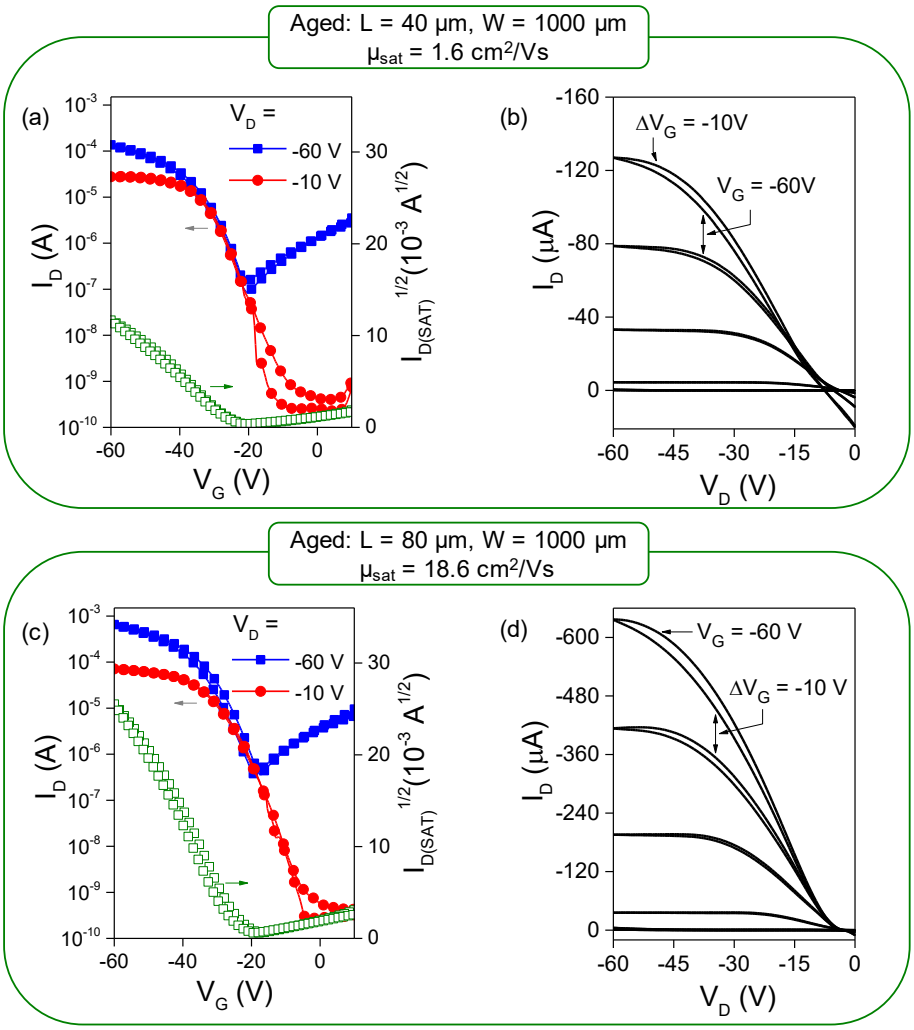

Figure 5.15: Device variability in solution-aged OTFTs. Transfer and output characteristics are shown for two aged C_8-BTBT:C_{16}IDT-BT:$C_{60}F_{48}$(0.1%) blend devices fabricated on the same substrate with channel width 1000 µm. The OTFT in (a) and (b) has a channel length of 40 µm and a saturation mobility of 1.6 cm^2/Vs. The OTFT in (c) and (d) has a channel length of 80 µm and a saturation mobility of 18.6 cm^2/Vs.

Figure 5.15 shows transfer and output curves from two devices made from the aged C_8-BTBT:C_{16}IDT-BT:$C_{60}F_{48}$(0.1%) blend solution; the OTFT in Figure 5.15 (a) and (b) has μ_{sat} = 1.6 cm^2/Vs and the OTFT in Figure 5.15 (a) and (b) has μ_{sat} = 18.6 cm^2/Vs. Contact resistance is often exhibited by nonlinearities in the low V_D region of OTFT output curves and indeed, there is a difference in the output curves of the aged OTFTs with high mobilities (for example, Figure 5.15 (d)) compared to those with low mobilities (for example, Figure 5.15 (a)). After studying the output curves for all of the transistors, the results suggest that the lowest performing TFTs suffer from contact resistance more significantly than the highest performing TFTs. Therefore, if the dopant has been displaced during the solution-ageing process, the dopant molecules may be non-uniformly dispersed, improving contact resistance for some

TFTs but not for others, resulting in significant device variation. In addition, the performance varies greatly within groups of devices that have the same channel length, as opposed to only measuring low/high mobilities for short/long channel lengths. For example, the highest mobility of 23.1 cm^2/Vs was measured for a device with channel length 100 µm, but there is also a device with the same 100 µm channel length that has a mobility of 3.5 cm^2/Vs.

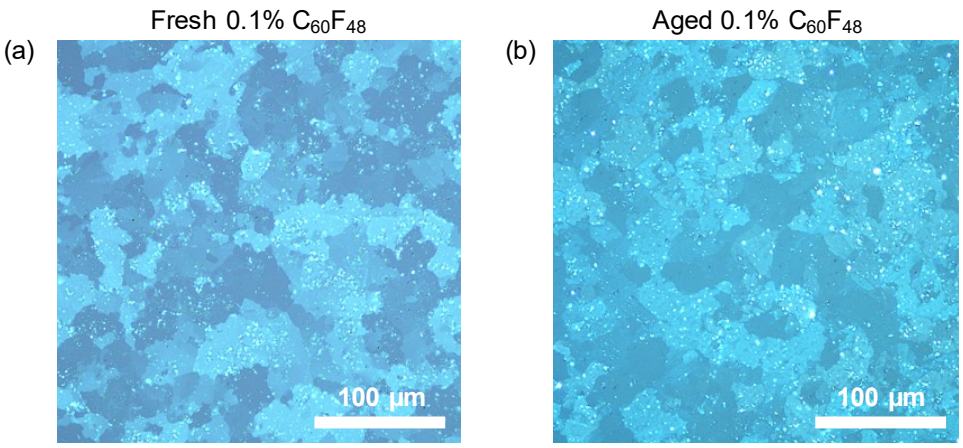

Figure 5.16: Effects of solution-ageing on film microstructure. Polarised optical microscope images of (a) freshly prepared C_8-BTBT:C_{16}IDT-BT:$C_{60}F_{48}$(0.1%) devices, and (b) 2 month aged C_8-BTBT:C_{16}IDT-BT:$C_{60}F_{48}$(0.1%) devices.

Other differences between the fresh and aged transfer characteristics are that, for the aged OTFTs, there is moderate hysteresis and an increase in the subthreshold slope. The average subthreshold slope value calculated over 30 OTFTs for the aged devices is $SS_{aged} \approx 3.7$, compared to $SS_{fresh} \approx 2.2$ calculated over 30 devices for the fresh OTFTs.

As both hysteresis and the subthreshold slope are often associated with shallow traps at the semiconductor/dielectric interface [9], POM was used to examine and compare the surface morphologies of the fresh and aged C_8-BTBT:C_{16}IDT-BT:$C_{60}F_{48}$(0.1%) blend films. Figure 5.16 shows the POM images, with no clear difference between the two blend films. At this stage the data indicates that the improvement in mobility is not due to a change in the morphology, although further insight could be gathered from other characterisation techniques, such as AFM and SEM, that enable a more detailed investigation of the microstructure.

One thing that is clear in the POM images, however, is that both of the films appear to have a high number of 'agglomerations' dispersed throughout the films within the C_8-BTBT crystallites. The agglomerations appear to be structural defects and therefore would be expected to act as charge trapping sites. To achieve mobilities > 20 cm^2/Vs with a microstructure such as this is highly unusual. This suggests that by considering other processing techniques that

avoid the formation of the structural defects/agglomerations, the performance of the aged blend may be improved even further.

Overall, the data suggests that there is great promise for the aged 3rd generation blend system, and further experiments should be undertaken to understand the blend solution-ageing mechanisms and improve the device uniformity.

5.3 Summary and conclusions

In summary, this chapter reports the development of a 3rd generation organic blend system, which exhibits maximum hole saturation mobility values exceeding 13 cm^2/Vs. A key factor that has led to the success of this system is the addition of a molecular *p*-dopant, $C_{60}F_{48}$, in a small-molecule/polymer blend.

Two promising materials, the small-molecule C_8-BTBT and the conjugated polymer C_{16}IDT-BT, were chosen to design a new small-molecule/polymer blend system. At an optimised blend ratio of 25% small-molecule to 75% polymer and concentration of 10 mg/ml, the as-made TG-BC blend devices exhibit mobilities of up to 4.7 cm^2/V, exceeding the performance of the single material components and thereby demonstrating the potential of this particular mixture of materials. However, despite the promising high mobilities, the OTFT transfer curves suggest that this system suffers from severe energetic disorder as the devices exhibit a range of nonideal transfer characteristics, such as hysteresis, high threshold voltages and high operating voltages.

With the aim of reducing the energetic disorder in this system, intentional *p*-doping is investigated. The molecular dopant $C_{60}F_{48}$ at 1% molar weight is found to have a significant impact on the transport properties of the OTFTs: a significant shift in V_T, reduced hysteresis, reduced operating voltages, *n*-type behaviour suppressed and – most importantly – increase in the maximum saturation mobility to 7.8 cm^2/Vs.

By combining the C_8-BTBT:C_{16}IDT-BT:$C_{60}F_{48}$(1%) ternary blend with a solvent blend made from 50% tetralin and 50% chlorobenzene, the mobility is improved even further, achieving maximum values mobility values over 13 cm^2/Vs with an average of 9.4 cm^2/Vs calculated over 16 transistors. In order to shed some light on the success of the tetralin:CB system, blend films made from tetralin:CB were compared to films made from the single solvents, CB and tetralin, using a range of materials characterisation techniques (POM, AFM, SEM and WAXD). Compared to the single solvent systems, the tetralin:CB system was found to improve crystallinity in both the *x*-*y* plane as well as the *z*-direction, with the *x*-*y* plane improvements having the most prominent effects on the OTFT electrical characteristics; in

particular, tetralin:CB films exhibited molecular terracing and a continuous, perforation-free topography with a lower RMS and narrower distribution of heights.

ToF-SIMS was then used to investigate the phase separation of the best performing ternary blend. The results uncovered an unusual distribution of the blend materials, where the dopant is found to reside within the polymer layer. For TG-BC device architecture, this implies that there is spatial separation between the dopant molecules and the OTFT channel, suggesting that unconventional doping mechanisms may govern the unique ternary blend system and hinting at a possible modulation doping technique for OTFTs.

This chapter concludes by highlighting future work for the 3rd generation blend system. Firstly, it is suggested that this ternary blend system could be used as a model system for other small-molecule/polymer/dopant blends. Preliminary experimental results are shown for an alternative C_8-BTBT:IDTT-BT:$C_{60}F_{48}$ blend, where the transfer characteristics demonstrate a reduction in energetic disorder and similar performance trends with the addition of a dopant. Finally, the performance of the 3rd generation blend-based OTFTs are dramatically improved by ageing C_8-BTBT:C_{16}IDT-BT:$C_{60}F_{48}$(0.1%) blend solutions for 2 months, achieving exceptional hole mobilities of up to 23.1 cm^2/Vs. These results highlight the ternary organic blend as a prospective system for OTFTs, with great potential for further research to be undertaken.

Chapter 6

The effects of molecular doping in 3rd generation organic blend thin-film transistors

The experimental work outlined in the previous chapter suggests that the key to the success of the ternary C_8-BTBT:C_{16}IDT-BT:$C_{60}F_{48}$ blend system is the inclusion of a molecular dopant. Molecular doping has been highlighted as a powerful technique with the potential to resolve many performance related issues that must be addressed if OTFTs are to be realised in commercial applications; Chapter 6 therefore explores the effect of the dopant on all of the critical operating parameters in the blend OTFTs. It is found that doping not only dramatically improves the mobility, but also the bias-stress stability, parasitic contact resistance, device uniformity and threshold voltage. Finally, material characterisation techniques suggest that the inclusion of the dopant in the small-molecule/blend system does not affect crystallinity of the C_8-BTBT at the channel.

6.1 Introduction

The dream of OTFTs being used to make flexible, commercially available electronics will only become a reality once a number of performance related factors have been addressed. One crucial figure of merit for OTFT performance is the mobility; in recent years, OTFT mobility values have made remarkable improvements, not only surpassing amorphous silicon, but also surpassing the benchmark mobility of 10 cm^2/Vs which pushes OTFTs into the realm of industrial application [30] [34] [245] [255]. Given the impressive progress that has been made with the mobility, focus is turning towards a variety of other operational hurdles that need to be overcome.

One of those operational hurdles is lifetime stability. OTFT instability is manifested as a shift in the threshold voltage, V_T, and change in the on-current with the application of gate and/or drain voltage over time; this is known as the bias-stress effect [70] [256] [257]. Bias-stress is recognised to be caused by charge trapping during device operation [70] [257] [9] [55] [161] [258] [259] either in the dielectric, at the semiconductor/dielectric interface, at grain boundaries or within the bulk semiconductor [74] [173] [174]. The impact of such instabilities have severe implications for real-life applications outside of the laboratory. For example, in the AMOLED displays described in *Chapter 1*, the brightness of the TFT driven OLED will deteriorate over time if there is a decline in the TFT on-current [257]. Therefore it is a fundamental requirement that any high performance organic system must be stable throughout the duration of its expected use. In addition, V_T itself is an indispensable criterion, as the precise control of low V_T values is a fundamental requisite for practical integrated circuits with low operating voltages [169] [260].

Contact resistance is another important consideration for the implementation of OTFTs in practical applications. As outlined in *Chapter 2* and *Chapter 3*, contact resistance can severely reduce the performance of OTFTs because the drain bias is prohibited from being applied over the channel due to the potential barriers at the source and drain electrodes [76]. It also creates a serious disadvantage for the miniaturisation of OTFTs, as well as causing mobility overestimations in some high performance OTFTs [36] [77].

The experimental work outlined in the previous chapter suggests that the key to the success of the 3rd generation blend system described is the inclusion of the molecular dopant $C_{60}F_{48}$ in a small-molecule/polymer blend of C_8-BTBT and C_{16}IDT-BT. As discussed in *Chapter 3*, it has been shown in the literature that doping organic semiconductors for OTFT applications can improve bias-stress stability and threshold voltage by deactivating charge trapping sites, [161] [162] as well as improve contact resistance by reducing the width of the

depletion layer at the metal/semiconductor interface [35] [182] [193] [261] [262]. This chapter will therefore explore the credibility of the 3rd generation blend-based OTFTs in terms of the important operating parameters, with a particular focus on how they are affected by molecular doping.

It is found that doping not only improves mobility, but it also reduces the contact resistance by a factor of ten, improves bias-stress stability, reduces the threshold voltage and improves device uniformity. Finally, POM and GIWAXS data show that the dopant does not appear to have an effect on the film morphology/crystal packing of the C_8-BTBT at the channel interface. Overall, the data in this chapter demonstrates that the 3rd generation blend is a highly attractive model system for the realisation of OTFTs in future plastic electronic applications.

6.2 Effects of doping concentration on I-V characteristics

Top-gate, bottom contact transistors were fabricated on 20x20 mm glass substrates for the C_8-BTBT:C_{16}IDT-BT blend (i.e. pristine blend) and the C_8-BTBT:C_{16}IDT-BT:$C_{60}F_{48}$(1%) blend (i.e. best performing doped blend). Both blends were prepared at the optimised 25% small-molecule to 75% polymer in the optimised 50% tetralin and 50% CB solvent solutions, for the reasons outlined in *Chapter 5*. A polytetrafluoroethylene (PTFE) polymer dielectric layer (AF2400) was then deposited on top of the blend layers to produce a 320 nm thick dielectric, which was subsequently annealed at 50°C for an hour.

Representative transfer and output curves for both the pristine and best performing blends with the AF2400 dielectric are shown in Figure 6.1. Compared to the Cytop dielectric data in *Chapter 5*, there is reduced hysteresis for the pristine blend, which may be attributed to an improved semiconductor/dielectric interface when using the AF2400 compared to the Cytop [263]. The *SS* values are also improved for both blends, which is another indication of an improved semiconductor/dielectric interface. The pristine blend requires lower operating voltages, which is due to the thinner layer of AF2400 compared to Cytop (Cytop ≈ 900 nm and AF2400 ≈ 320 nm) as both dielectrics have a similar dielectric constant ($\varepsilon_{CYTOP} \approx 2.05$ and $\varepsilon_{AF2400} \approx 1.91$). In addition, V_{ON} and V_T have been reduced (i.e. shifted towards positive voltages), signifying an improvement in injection properties because of the Au source/drain electrodes without an Al adhesion layer. All other previously reported findings are the same in terms of adding the dopant, i.e. improved mobility, a strong shift in threshold voltage and supressed electron transport [255].

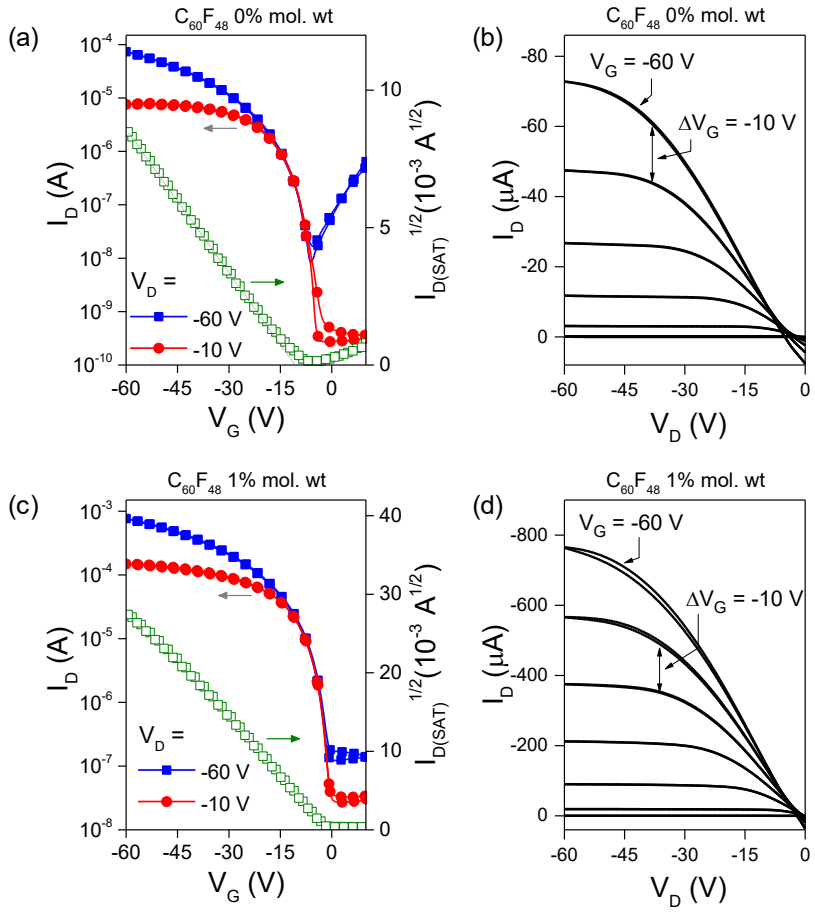

Figure 6.1: Pristine and doped 3rd generation blend OTFT comparison. Representative (a) transfer and (b) output characteristics of the best performing C_8-BTBT:C_{16}IDT-BT:$C_{60}F_{48}$(1%) blend; and representative (c) transfer and (d) output characteristics of the pristine C_8-BTBT:C_{16}IDT-BT blend.

6.2.1 Mobility

The previous chapter largely focussed on statistical data for how the solvent, rather than the dopant, affected the mobility. Therefore, 50 TFTs, for each of the pristine blend and the best performing blend, were measured to give a broader statistical image of the effect of molecular doping on mobility.

Figure 6.2 shows box and whisker plots for the linear and saturation mobilities of the two blends, with the whiskers being the 10-90 percentiles. From 50 TFTs, the average saturation mobility for the pristine blend is ≈1.4 cm^2/Vs compared to an average of ≈7.8 cm^2/Vs for the doped blend. The maximum mobilities for the pristine and doped blends are ≈4.2 cm^2/Vs and ≈12.8 cm^2/Vs respectively. A similar trend is seen with the linear mobilities, where the average linear mobility for the pristine blend of ≈1 cm^2/Vs increased to an average

of ≈5.3 cm^2/Vs for the doped blend. It is also clear that for both blends, there is reasonably large device to device variation over the 50 devices, which will be addressed later in this chapter.

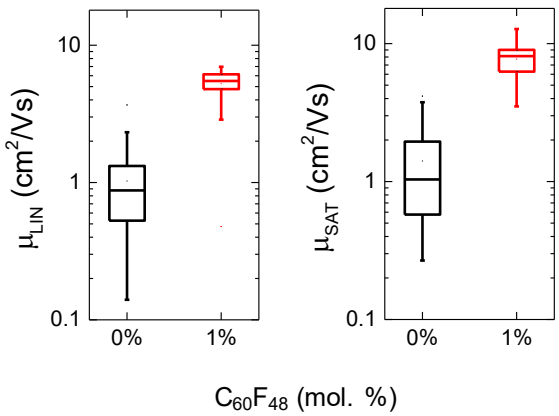

Figure 6.2: Saturation and linear mobilities for the best performing C_8-BTBT:C_{16}IDT-BT:$C_{60}F_{48}$(1%) blend compared to the pristine C_8-BTBT:C_{16}IDT-BT blend.

6.2.2 Bias stress stability

The statistical data also indicates a strong shift in V_T, from an average of $V_T \approx$ -10.5 V calculated from 50 TFTs in the pristine system to an average $V_T \approx$ -2.1 V calculated from 50 TFTs in the best performing system. As a shift in V_T due to the inclusion of a molecular dopant suggests that holes have been donated to fill deep trap states [9] [169], the presence of the dopant may influence bias-stress stability, which is caused by charge trapping during OTFT operation [161] [160].

To investigate whether intentional doping has deactivated charge trapping sites that are responsible for bias-stress stability, both the pristine and the best performing doped blend were investigated and compared in bias stress tests. OTFTs with channel length 80 µm and width 1000 µm for both blends were subjected to 20,000 seconds of gate and drain bias (V_D = -10 V and V_G = -40 V) in a nitrogen atmosphere. At the end of the bias-stress tests, the drain current measured at V_G = -60 V for the pristine blend had deteriorated by 17.7%, and the drain current measured at the same V_G = -60 V for the best performing blend deteriorated by 4.2%. The change in threshold voltage after stressing was $\Delta V_{T_pristine}$ = -1.34 V for the pristine blend and ΔV_{T_doped} = -0.91 V for the doped blend. Therefore, there is a slight change in the performance over time, with the doped blend exhibiting the least change.

Table 6.1 summarises the literature on bias-stress stability for blend OTFTs. Compared to the other organic blend systems, the 3rd generation blend performs very well; both the pristine

and doped blends have been stressed for a comparatively substantial period of time, yet they are able to maintain similar performance levels throughout the duration of the bias-stress tests. This is very promising and, in particular, because the best performing doped blend has a high mobility and hence high drain currents, it is suitable for a range of electronic and/or optoelectronic applications.

Active Material	Process Temp. (°C)	Mobility (cm^2/Vs)	Dielectric Material	Geometric Capacitance (nF/cm^2)	Gate Stress (V)	Drain Stress (V)	Electric Flux Density (C/cm^2)	Stress Time (s)	ΔV_T (V)	Trap Density (cm^{-2})	Ref.
C_8-BTBT:C_{16}IDT-BT:$C_{60}F_{48}$(1%)	120	7.8	AF2400	5.28	-40	-10	2.11×10^{-7}	20,000	0.91	3.00×10^{10}	**This work**
C_8-BTBT:C_{16}IDT-BT	120	1.4	AF2400	5.28	-40	-10	2.11×10^{-7}	20,000	1.34	4.42×10^{10}	
C_8-BTBT:PS	100	25	PVP:HDA	12	-15	0	1.80×10^{-7}	3,000	~5	3.75×10^{11}	**[126]**
TIPS-Pentacene: i-PMMA	110	n/a	Al_2O_3	~80	-15	0	1.20×10^{-6}	5,000	3	1.50×10^{12}	**[264]**
TIPS-Pentacene: PTAA	~100	1.1×10^{-2}	Al_2O_3	78.6	-8	-8	6.29×10^{-7}	3,600	~1.5	7.37×10^{11}	**[265]**
TIPS-Pentacene: PTAA	~100	0.20	CYTOP	2.3	-50	-50	1.15×10^{-7}	3,600	~2	2.88×10^{10}	**[265]**
TIPS-Pentacene: PTAA	~100	0.52	CYTOP/ Al_2O_3	34.8	-8	-8	2.78×10^{-7}	3,600	~0.4	8.70×10^{10}	**[265]**
TIPS-Pentacene: PTAA	~100	0.24	CYTOP/ Al_2O_3	34.8	-8	-8	2.78×10^{-7}	7,200	~0.2	4.35×10^{10}	**[266]**
diF-TES ADT: PαMS (2:1)	~90	~0.16	SiO_2	17.3	-20	-0.1	3.46×10^{-7}	7,200	12	1.30×10^{12}	**[267]**
diF-TES ADT: PαMS (2:2)	~90	~0.16	SiO_2	17.3	-20	-0.1	3.46×10^{-7}	7,200	8	8.65×10^{11}	**[267]**
PCDTPT:PC_{61}BM	200	0.5	SiO_2	11.5	-10	-80	1.15×10^{-7}	300	0.8	5.75×10^{10}	**[268]**
PCDTPT:PC_{61}BM	200	0.5	SiO_2	11.5	-30	-80	3.45×10^{-7}	300	0.2	1.44×10^{10}	**[268]**
diF-TES ADT: PTAA	120	1.7	CYTOP	2.1	-50	-50	1.05×10^{-7}	18,000	10	1.31×10^{11}	**[123]**

Table 6.1: A summary of the literature on bias-stress stability for blend OTFTs.

Figure 6.3 shows the data from the stress-bias measurements, where the V_T shift/instability of both blends plateaus over time. This is expected from such measurements due to a reduction in the trapping rate as the trap states become occupied. To characterise the bias-stress effect in more detail, a stretched exponential function is typically fitted to the experimental data using the following equation [7] [173] [123]:

$$\Delta V_{\mathrm{T}}(t) = \Delta V_0 \left\{ 1 - \exp\left[-\left(\frac{t}{\tau}\right)^{\beta} \right] \right\} \tag{6.1}$$

where $\Delta V_0 = V_G - V_{T_initial}$, with $V_{T_initial}$ being the threshold voltage prior to any application of bias stress, τ is the *relaxation time* and β is the *stretching parameter*, where β is a value between 0 and 1.

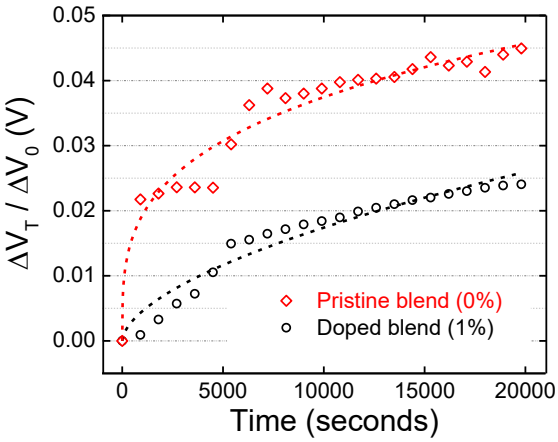

Figure 6.3: The effect of molecular doping on bias-stress stability. Experimental data (shapes) and stretched exponential fittings (dashed lines) used to extrapolate the $\boldsymbol{\beta}$ and τ parameters for the best performing doped blend (C_8-BTBT:C_{16}IDT-BT:$C_{60}F_{48}$(1%)) and pristine blend (C_8-BTBT:C_{16}IDT-BT) devices. The devices were subjected to 20,000 seconds of bias stress at V_D = -10 V and V_G = -40 V, in an inert nitrogen atmosphere.

In Figure 6.3, the experimental data is represented by shapes and the stretched exponential fittings are represented by dashed lines; the latter have been used to extrapolate the β and τ parameters. For the doped system, the stretching parameter is β_{doped} = 0.58 and the relaxation time is τ_{doped} = 1 x 10^7, compared to a stretching parameter of $\beta_{pristine}$ = 0.29 for the pristine system and a relaxation time of $\tau_{pristine}$ = 7 x 10^8. The coefficient of determination, R^2, is 0.947 and 0.946 for the doped and pristine systems respectively. A greater value of β (i.e. β closer to 1) for the doped system compared to the pristine system indicates a less stretched bias-stress response time, i.e. a more uniform distribution of trapping sites next to the HOMO level [269]. In addition, the relaxation time, τ, is seen to decrease with the addition of

the dopant. This implies that the trapping mechanisms within the doped system happen on a shorter timescale. Therefore, along with an improved average V_T shift in the best performing doped blend, the most plausible explanation for this data is that the $C_{60}F_{48}$ has deactivated deep trap sites by donating holes. The fact that molecular doping can influence lifetime stability has valuable practical implications for OTFTs.

6.2.3 Contact resistance

Operational stability is also known to be associated with the contacts, because charge trapping can occur in deep trap states at the contacts, as well as in the bulk or at the dielectric/semiconductor interface [270] [271] [272] [273]. As discussed in *Chapter 2* and *Chapter 3*, the contact resistance is well known to have a huge influence on OTFT operation [274] [275]. Reducing contact resistance is highly important for OTFT operation, miniaturisation [36] and accurate parameter analysis [36] [37].

Molecular doping has been highlighted as a technique for reducing contact resistance in OTFTs [171] [182] [193] [261]. Therefore, it is important to consider whether the dopant has affected the contact resistance in the blend OTFTs. A scaling law method can be used to extrapolate contact resistance values from output characteristics using the following linear expression: [276]

$$R_{\mathrm{ON}} = \frac{\partial V_{\mathrm{D_lin}}}{\partial I_{\mathrm{D_lin}}} = r_{\mathrm{channel}} L + R_{\mathrm{C}} \tag{6.2}$$

where L is the channel length, R_{ON} is the total device resistance measured as a function of L, $r_{channel}$ is the resistance across the channel and R_C is the resistance at the contacts. Measurements were taken from transistors with channel lengths ranging from 20 µm to 200 µm for the C_8-BTBT:C_{16}IDT-BT blend with $C_{60}F_{48}$ doping concentrations of 0%, 0.05%, 0.1%, 0.5% and 1%. The contact resistance (R_CW) values were calculated as a function of gate bias and the results are shown in Figure 6.4. There is a strong relationship between molecular doping and contact resistance; it is also clear that R_C is dependent on gate voltage, which is expected for this type of TG-BC staggered architecture [91] [277].

The largest effect on R_C is between 0% and 0.1% mol. wt. $C_{60}F_{48}$, where the contact resistance is reduced by 82.5% from $R_C \approx 263$ kΩ to $R_C \approx 46$ kΩ (R_C is taken from V_G = -50 V). When the doping is increased to 1% mol. wt. R_C is reduced further to ≈16 kΩ. The improvement in R_C highlighted in these results offers another explanation for the superior mobility values in the best performing blend compared to the pristine blend.

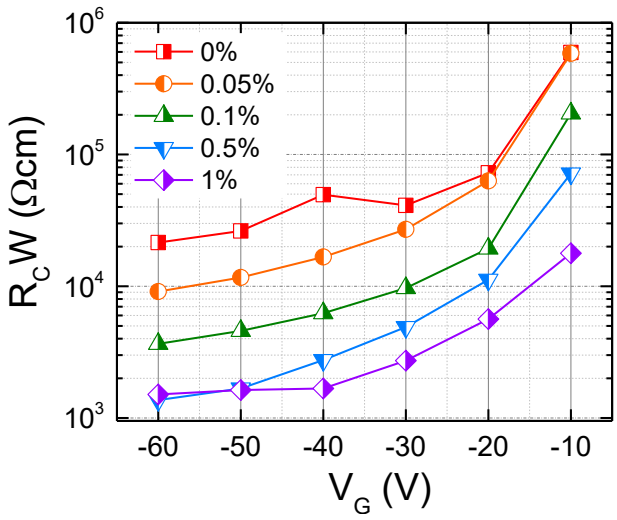

Figure 6.4: The effect of molecular doping on contact resistance. Graph showing contact resistance dependency on gate bias, calculated for the C_8-BTBT:C_{16}IDT-BT blend with 0%, 0.05%, 0.1%, 0.5% and 1% molar weight $C_{60}F_{48}$.

6.2.4 OTFT parameter analysis

To conclude the overall picture of how the dopant influences the *I-V* characteristics of the 3rd generation blend system, transfer characteristics and the key operating parameters μ_{lin}, μ_{sat}, V_T, V_{ON}, $I_{ON/OFF}$ and *SS* were explored at 0%, 0.05%, 0.1%, 0.5%, and 1% mol. wt. $C_{60}F_{48}$.

Firstly, the transfer characteristics were studied. For OTFTs that have been *p*-doped there are several things expected in the transfer characteristics: an increase in the on-current and off-current, a shift in V_T to positive gate voltages and any *n*-type behaviour to be suppressed [161].

Figure 6.5 highlights the revealing features of the representative transfer characteristics for 0%, 0.05%, 0.1%, 0.5% and 1% mol. wt. $C_{60}F_{48}$ devices with channel length and width 80 µm and 1000 µm respectively. There is a clear trend of changes occurring in the transfer characteristics with increasing doping concentration. For example, Figure 6.5 (a) shows the drain current associated with the linear regime with V_D held at -10 V (see Figure 6.1 (b) and (d) for representative output characteristics); there is a steady increase in the on-current for each increase in the doping ratio. In terms of the off-current, it is largely the same for 0%, 0.05%, 0.1% $C_{60}F_{48}$ mol. wt., but at 0.5% it increases by a factor of 10 and increases even further at 1%. The increase in the on- and off-current is associated with an increase in charge carrier density due to dopant donating free holes to the system, which results in an increased bulk

conductivity [161] [185]. Indeed, the same effects and trends are seen at a higher drain voltage associated with saturation regime (V_D = -60V) as shown in Figure 6.5 (b).

The dopant can also be seen to act as an electron trap (Figure 6.5 (b)). For example, at lower doping percentages (0%, 0.05% and 0.1%) electron transport can be seen, but at the higher doping percentages (0.5% and 1%) the devices are predominantly *p*-type, indicating that if the doping concentration is high enough then the dopant will withdraw electrons from the system. Lastly, Figure 6.5 (c) shows the evolution of $\sqrt{I_D}$ with doping ratio, demonstrating an increase in I_D, a shift in V_T, as well as an increase in μ_{sat}.

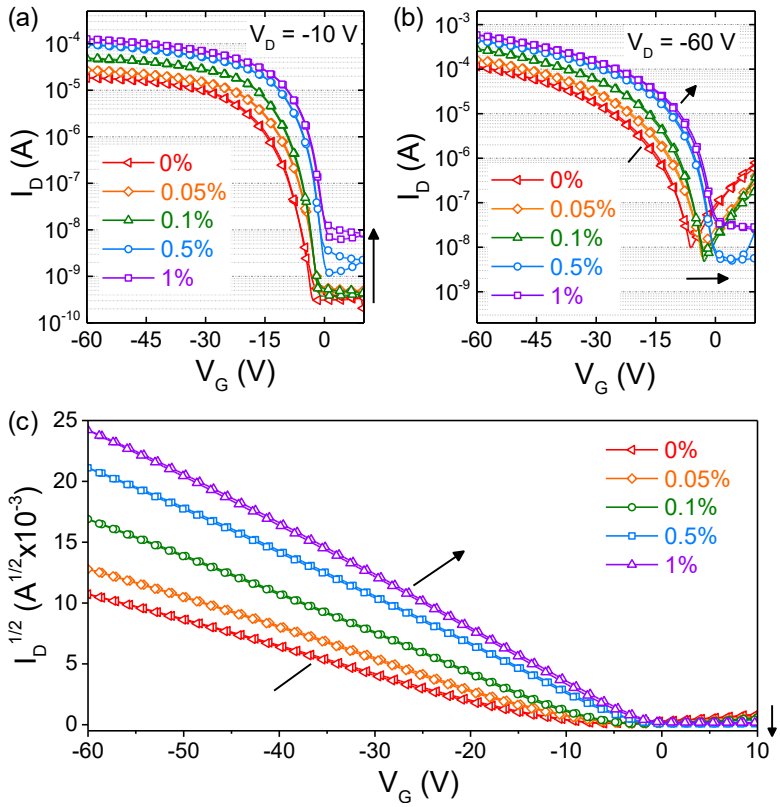

Figure 6.5: The effect of molecular doping on transfer characteristics. Transfer characteristics for the C_8-BTBT:C_{16}IDT-BT blend with 0%, 0.05%, 0.1%, 0.5% and 1% molar weight $C_{60}F_{48}$: (a) at V_D = -10 V, (b) at V_D = -60 V, (c) the square root of I_D which do not exhibit a "double-slope" and have been used to calculate both V_T and μ_{sat}. The channel length is 80 µm and width 1000 µm for each TFT.

6.2.4.1 μ_{lin}, μ_{sat}, SS and $I_{ON/OFF}$

For each doping concentration, 10 transistors with channel lengths ranging from 30 µm to 100 µm at a fixed width of 1000 µm, were measured and analysed. The results are shown graphically in Figure 6.6 and numerically in Table 6.2 to give a clear idea of the parameter spreads and how the trends of each parameter develop with doping concentration.

Figure 6.6 (a) and (b) show a clear evolution of the mobility values with the doping ratio, confirming that – along with other data in this thesis – the 1% mol. wt. $C_{60}F_{48}$ produces maximum mobility in this system. For example, the average saturation mobilities do not show any great change at the lower doping ratios, i.e. the 0.05% and 0.1% average saturation mobilities are 1.9 cm^2/Vs and 1.6 cm^2/Vs respectively; a slight increase to 2.7 cm^2/Vs is seen at 0.5%, but the noticeable improvement in mobility comes at 1% when the average μ_{sat} becomes 8.2 cm^2/Vs.

There is also a noticeable improvement in device uniformity with molecular doping. Device uniformity is important for integrated circuitry where numerous devices are employed on the same circuit [9]. Here, the most noticeable difference is at 0.5% $C_{60}F_{48}$, where the device uniformity is improved for μ_{lin}, μ_{sat}, V_{ON}, V_T, *SS* and $I_{ON/OFF}$. Indeed, the OTFT parameter data indicates that exploring doping percentages between 0.5% and 1% $C_{60}F_{48}$ could yield further improvements in device uniformity, in particular for *SS* and $I_{ON/OFF}$. Therefore, the data indicates that exploring between 0.5% and 1% mol. wt. $C_{60}F_{48}$ could combine the high mobilities associated with the doping at 1%, as well as enhanced device to device uniformity associated with the doping at 0.5%.

Further to the above, there are some other observations for *SS* (Figure 6.6 (f)) and $I_{ON/OFF}$ (Figure 6.6 (e)). Mainly, these are the only parameters that do not seem to be strongly affected by doping. In fact, for both *SS* (Figure 6.6 (f)) and $I_{ON/OFF}$ (Figure 6.6 (e)), it is the 0.5% $C_{60}F_{48}$, not 1% $C_{60}F_{48}$, which yields the best average values as well as the best device uniformity. As outlined in *Chapter 2*, some of the underlying issues for improving the values of *SS* and $I_{ON/OFF}$ lie outside the capacity of the bulk semiconductor. Therefore, both parameters can be addressed by considering aspects of device engineering, such as the dielectric layer [278] and the semiconductor/dielectric interface [279].

6.2.4.2 V_{ON} and V_T

Finally, V_{ON} and V_T are investigated as a function of doping concentration. Because it is important for transistors to switch on quickly and efficiently when a gate bias is applied, V_{ON} and V_T must ideally be as close to 0 V as possible. Figure 6.6 (c) and Figure 6.6 (d) indicate a strong relationship between the doping ratio V_T and V_{ON} respectively, with both shifting towards 0 V as the doping concentration increases, and plateauing after 0.5% $C_{60}F_{48}$. The plateau is more pronounced for V_{ON} than V_T, i.e., $V_{ON_0.5\%} \approx$ -1.4 V and $V_{ON_1\%} \approx$ -1.5 V compared to $V_{T_0.5\%} \approx$ -3.3 V and $V_{T_1\%} \approx$ -1.9 V.

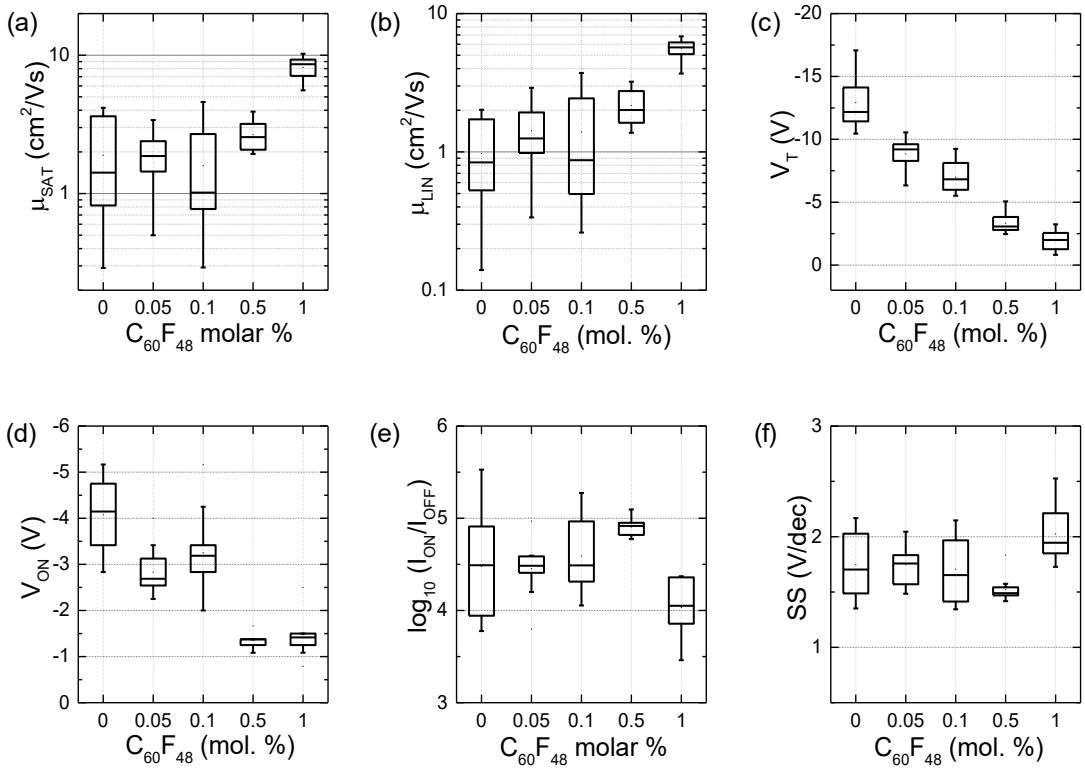

Figure 6.6: Full analysis of OTFT operating parameters for C_8-BTBT:C_{16}IDT-BT blend with 0%, 0.05%, 0.1%, 0.5% and 1% molar weight $C_{60}F_{48}$: (a) saturation mobility, (b) linear mobility, (c) threshold voltage, (d) on voltage, (e) on-off current, (f) subthreshold slope.

Linear mobility (cm^2/Vs)									
0%		0.05%		0.1%		0.5%		1%	
Average	Min-Max	Average	Min-Max	Average	Min-Max	Average	Min-Max	Average	Min-Max
1.0	0.1-2.0	1.4	0.3-2.9	1.4	0.3-3.7	2.2	1.4-3.2	5.6	3.7-6.8
Saturation mobility (cm^2/Vs)									
0%		0.05%		0.1%		0.5%		1%	
Average	Min-Max	Average	Min-Max	Average	Min-Max	Average	Min-Max	Average	Min-Max
1.9	0.3-4.2	1.9	0.5-3.4	1.6	0.3-4.6	2.7	1.9-3.9	8.2	5.6-11.2
Modulus V_T (V)									
0%		0.05%		0.1%		0.5%		1%	
Average	Min-Max	Average	Min-Max	Average	Min-Max	Average	Min-Max	Average	Min-Max
13.1	10.5-17.1	8.9	10.5-6.3	7.1	9.2-5.8	3.3	5.1-2.5	1.9	3.2-0.8
Modulus V_{ON} (V)									
0%		0.05%		0.1%		0.5%		1%	
Average	Min-Max	Average	Min-Max	Average	Min-Max	Average	Min-Max	Average	Min-Max
4.1	5.2-2.8	2.8	4.0-2.3	3.3	5.2-2.0	1.4	1.7-1.1	1.5	2.5-0.8
Subthreshold Slope (V/dec)									
0%		0.05%		0.1%		0.5%		1%	
Average	Min-Max	Average	Min-Max	Average	Min-Max	Average	Min-Max	Average	Min-Max
1.7	2.2-1.4	1.7	2.0-1.5	1.7	2.1-1.3	1.5	1.8-1.4	2.0	2.5-1.7
$I_{ON/OFF}$									
0%		0.05%		0.1%		0.5%		1%	
Average	Min-Max	Average	Min-Max	Average	Min-Max	Average	Min-Max	Average	Min-Max
7×10^4	6×10^3 - 3×10^5	3×10^4	6×10^3 - 9×10^4	6×10^4	1×10^4 - 2×10^5	8×10^4	6×10^4 - 1×10^5	1×10^4	3×10^3 - 2×10^4

Table 6.2: Data corresponding to full analysis of OTFT operating parameters in Figure 6.6.

Taking a close look at V_T is important for practical implications, and in addition, V_T also offers valuable information about doping mechanisms. As V_T is the voltage required to fill deep trap states before mobile charge carriers can be induced at the channel [23] [50] [57], the observed shift in V_T with doping ratio can therefore be used to approximate the total number of holes donated by the $C_{60}F_{48}$ to the channel with the following:

$$\Delta h^+ = \frac{C_i \left| V_{\mathrm{TH(pristine)}} - V_{\mathrm{TH(doped)}} \right|}{h} \tag{6.3}$$

where C_i is the geometric capacitance of the dielectric layer and e is the charge of an electron.

Figure 6.7 is a graphical representation of the number of donated holes with the doping ratio, which follows a steady increase up to 0.5% $C_{60}F_{48}$ before starting to plateau towards 1%, similar to the trend observed for the contact resistance (Figure 6.4) as well as the other calculated device parameters (Figure 6.6). This indicates that the donation of holes corresponds

with an improvement in R_C and OTFT operating parameters, up to the point where the number of donated holes begins to saturate.

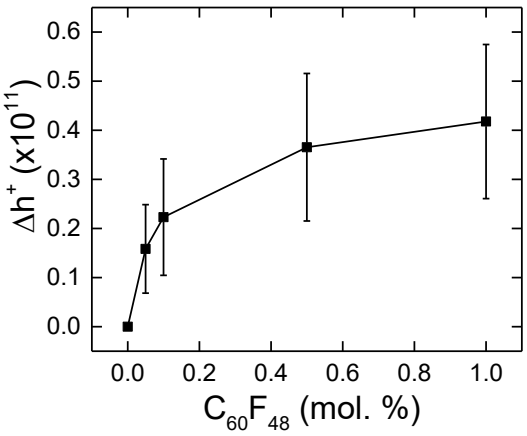

Figure 6.7: The number of holes donated, Δh+, to the OTFT channel as a function of doping ratio.

6.3 Effects of molecular doping on blend morphology

So far in this chapter, molecular doping effects on electrical characteristics have been considered, but the rest of this chapter will focus on how the molecular dopant affects the microstructure/morphology of the blend. It is well known that the quality and ordering of the OSC microstructure can determine and/or influence OTFT performance, due to defects in the semiconductor acting as charge trapping sites [278] [280] [281]. For this reason, a wealth of OTFT research and literature has focussed on new fabrication techniques, such as surface treatments (for example, grooved or rubbed substrates) and directional deposition techniques, with the aim of improving the quality and anisotropic order of organic semiconductors deposited using solution-processing techniques [282]. Indeed, the importance of morphology and crystallinity was shown in *Chapter 5*, when a range of solvent systems were explored as part of the development of the C_8-BTBT:C_{16}IDT-BT:$C_{60}F_{48}$ blend.

Because ordering in organic semiconductors is so important, one of the biggest hurdles for doping in OTFTs is that dopant molecules have a strong tendency to interfere with the OSC host lattice, subsequently reducing crystallinity and mobility [41]. For this reason, bulk doping techniques, such as the approach used in this work, are infrequently used and alternative doping methods are typically employed, such as contact doping [172] [182] [191] [192] [193] [194] [195] and chemical vapour doping [205] [206]. This was discussed in further detail in

Chapter 3. It is therefore important to address the whether the $C_{60}F_{48}$ has had any effect on the microstructure of the C_8-BTBT:C_{16}IDT-BT blend.

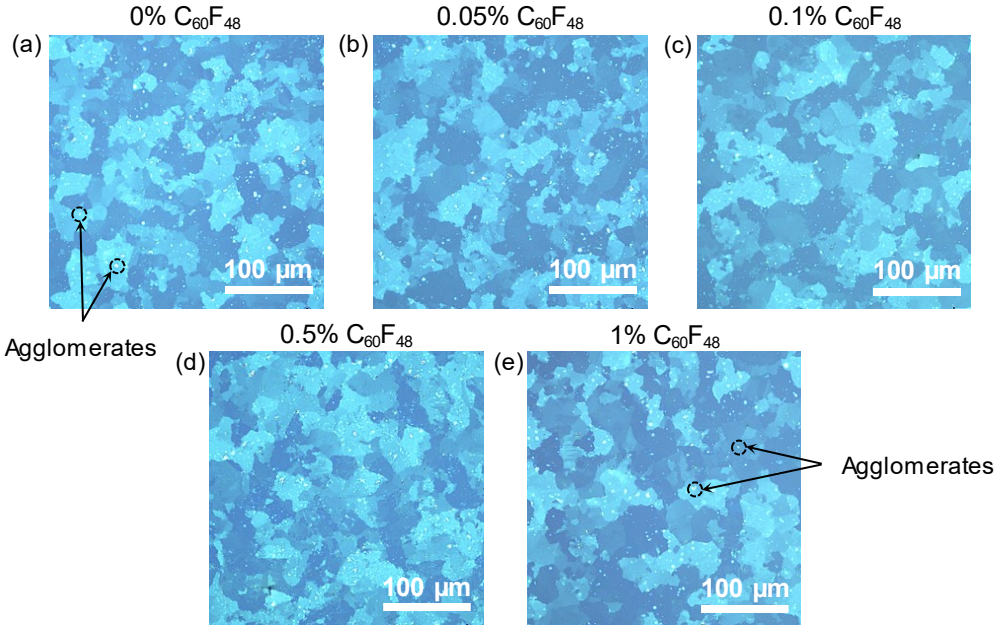

Figure 6.8:The effect of molecular doping on microstructure. Polarised optical microscope images of the C_8-BTBT:C_{16}IDT-BT blend with varying amounts of dopant, $C_{60}F_{48}$: a) 0%, b) 0.05%, c) 0.1%, d) 0.5%, e) 1%. The doping concentration does not appear to have any effect on the microstructure.

The first step taken to explore the microstructure with doping concentration was using polarised optical microscopy (POM). Figure 6.8 shows the C_8-BTBT:C_{16}IDT-BT films with $C_{60}F_{48}$ at 0%, 0.05%, 0.1%, 0.5% and 1% molar weight. Although there is some variation in the morphology due to the intrinsic nature of the films, there is very little difference between these images. After studying a number of blend films for each doping concentration, it appears that the dopant has no noticeable effect on the crystalline domains.

Another interesting observation is the high density of agglomerates distributed within all of the blends, regardless of the presence/amount of dopant. These agglomerates, or defects, were highlighted in the solution-ageing studies in *Chapter 5*, as they would be expected to behave as charge trapping centres, severely limiting charge transportation and hence the performance of TFTs. Therefore, to achieve high mobilities with this morphology is surprising [102] [117] [283] [284]. The poor morphology may offer another explanation as to why this system has such high energetic disorder in the first place, in addition to the reasons outlined in *Chapter 5*.

The agglomerations will also affect the quality of the semiconductor/dielectric interface and therefore may shed some light on the *SS* values discussed earlier, because *SS* is strongly

dependent on trapping at the semiconductor/dielectric interface [279]. The fact that the poor morphology at the semiconductor/dielectric interface is unchanged with the addition of the dopant may explain why there is no improvement in *SS*, even though there is a dramatic difference in μ_{lin}, μ_{sat}, V_{ON}, and V_T. The poor morphology also highlights some other key points regarding this system: (i) the powerful role that the dopant is playing in this 3rd generation blend system, and (ii) the potential that this system could have with further processing optimisation to remove the agglomerations and improve the morphology.

As the POM images indicate that the $C_{60}F_{48}$ dopant does not change the C_8-BTBT crystallisation, the crystal structure and molecular packing was investigated in further detail using grazing incidence wide angle X-ray scattering (GIWAXS). The blend thin-films investigated contain $C_{60}F_{48}$ at 0%, 0.1%, 1% and 5% mol. wt., with 5% being included for the GIWAXS studies as higher doping concentrations are more likely to introduce lattice disorder [187] [188].

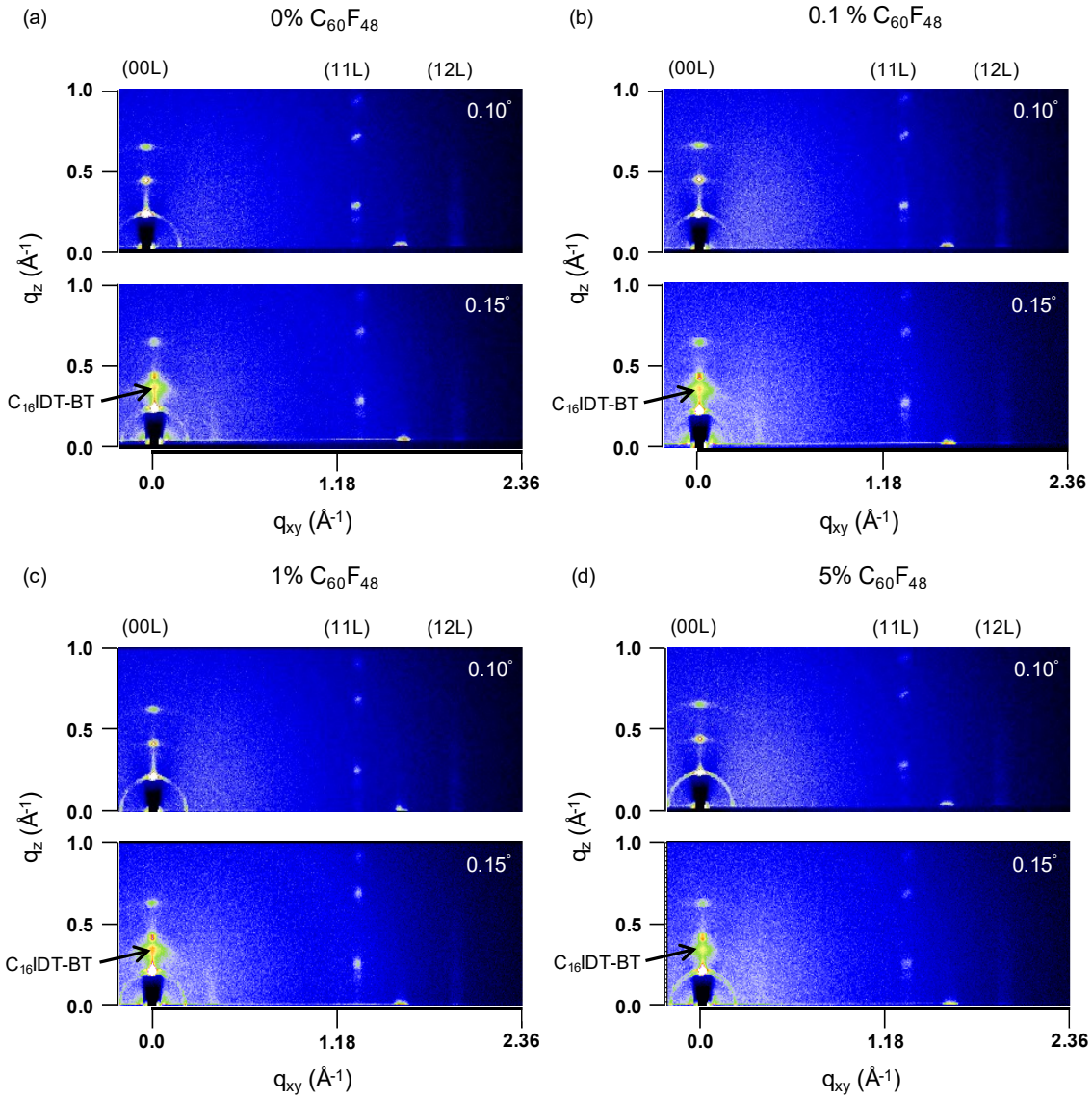

Figure 6.9: GIWAXS data for various doped C_8-BTBT:C_{16}IDT-BT blend films. (a) 0%, (b) 0.1%, (c) 1% and (d) 5% mol. wt. $C_{60}F_{48}$ blends are shown at two grazing incidence angles, 0.10° and 0.15°.

The blend films were investigated at various grazing incidence angles (0.05°, 0.10°, 0.15°) with the critical angle found to be 0.15°. All of the blend films are found to exhibit high lamellar ordering, which is shown by the presence of (00*l*) peaks (*l* = 1, 2, 3) with interplanar spacing of d = 2.8 nm for (001) Bragg Sheet (q_z = 2.23 nm^{-1}) (Figure 6.9). These results are irrespective of the dopant concentration and this predominant out of plane ordering is consistent with other published C_8-BTBT literature [285].

In Figure 6.10, intensity vs q_z has been plotted for two different angles of incidence, one of which is below the critical angle (0.10°) and the other is the critical angle (0.15°). This data not only highlights that the dopant does not affect the crystallinity of blend films, but also

provides information about the vertical profiling of the four doped blends, specifically the qualitative composition in the top few nm of the films; Figure 6.10 (a) shows that for grazing angles below the critical incidence angle (i.e. 10°) the C_{16}IDT-BT signature at q_z = 3.63 nm^{-1} is not present, but in Figure 6.10 (b) it is present at 0.15°. This suggests that the polymer is not present in the top few nm of the film and that it has segregated to the bottom of the film for all of the doping concentrations.

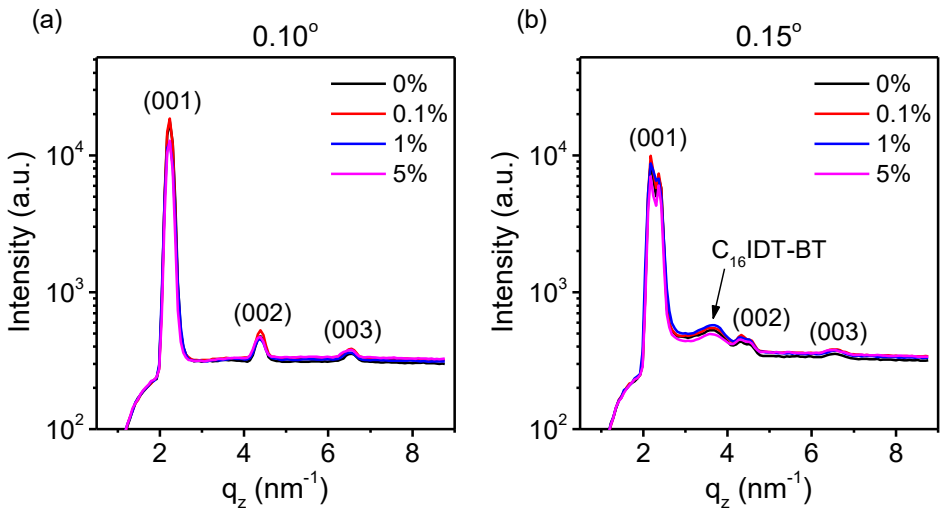

Figure 6.10: Intensity vs q_z for various doped C_8-BTBT:C_{16}IDT-BT blend films (0%, 0.1%, 1% and 5% mol. wt. $C_{60}F_{48}$) at two different angles of incidence: (a) below the critical angle (0.10°), and (b) the critical angle (0.15°). The peak associated with the C_{16}IDT-BT is only present in (b), indicating that the polymer is not present at the surface/air interface.

Finally, the in-plane structures of the four blend films are investigated. Figure 6.11 (a) compares the q_{xy} position for all of the films, with the dashed line highlighting that there is no shift in the in-plane peak position for any of the blend films. There does appear to be slight intensity weakness at very high doping concentrations (5% mol. wt. $C_{60}F_{48}$), which could either be due to a reduction in crystallinity or to reduced C_8-BTBT layer thickness. Further experiments and depth profiling would need to be undertaken to assess this in detail. To compliment the q_{xy} position data, Figure 6.11 (b) shows that there is also no shift in the q_z values for the blend films. Overall, this data indicates that the packing of the C_8-BTBT at the surface/air interface has not been altered by the presence of the dopant.

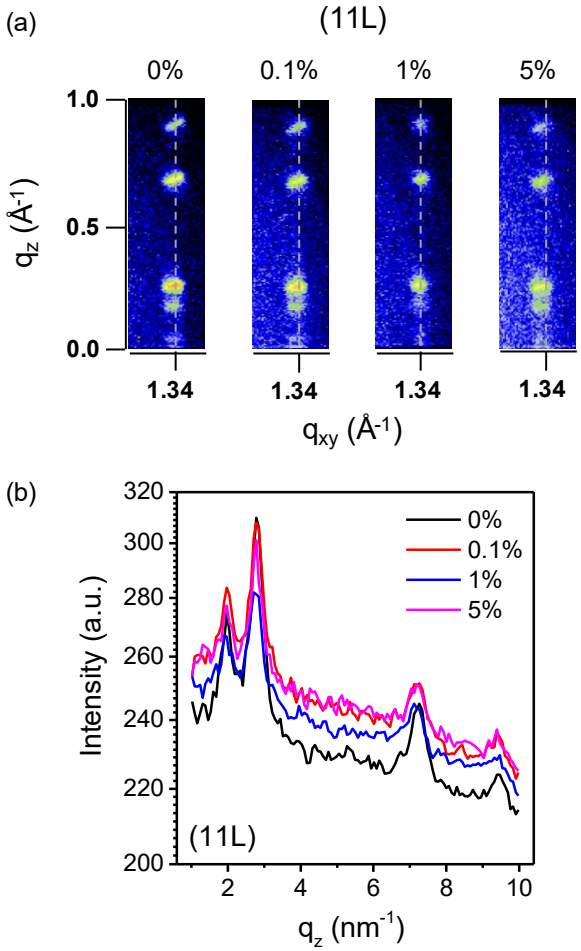

Figure 6.11: In-plane structures for various doped C_8-BTBT:C_{16}IDT-BT blend films (0%, 0.1%, 1% and 5% mol. wt. $C_{60}F_{48}$) where (a) compares the q_{xy} position, with the dashed line highlighting that there is no shift in the in-plane peak, and (b) shows that there is also no shift in the q_z values, suggesting that crystal packing is not altered by the presence of the $C_{60}F_{48}$.

The lack of disturbance to the C_8-BTBT crystal packing could possibly be explained by the ToF-SIMS data in *Chapter 5*, which highlights an unusual vertical phase separation resulting in the dopant residing in the polymer at the blend/substrate interface. To know this for certain, further experiments would be required to investigate vertical profiling in the blends.

6.4 Summary and conclusions

This chapter investigated the impact of molecular doping on the key OTFT operating parameters in the 3rd generation C_8-BTBT:C_{16}IDT-BT:$C_{60}F_{48}$ blend. As *Chapter 5* primarily dealt with statistics on how the choice of solvent affected the mobility, this chapter began with

a statistical overview of how molecular doping affects the mobility. For 50 OTFTs per blend, the saturation mobility is found to increase from an average of 1.4 cm^2/Vs in the pristine blend to an average of 7.8 cm^2/Vs in the best performing blend.

The bias-stress stability is then investigated for the pristine and the best performing blends, finding that, although both blends compare well to the literature on bias-stress stability for organic blend TFTs, the doped system is more stable than the pristine system. This stability, as well as the high mobilities and drain current, of the doped system makes it ideal for a range of electronic and optoelectronic applications.

The next critical operating parameter investigated is contact resistance. It is found that there is a strong correlation between the inclusion of the dopant and the contact resistance, where the contact resistance in the pristine system is found to be $R_C = 263$ kΩ, which is reduced by a factor of ≈10 to $R_C = 16$ kΩ in the best performing blend devices.

The overall picture of how the dopant affects the electrical characteristics concludes by presenting transfer curves for a broad range of doping concentrations, showing a clear trend in the evolution of the transfer characteristics that is expected from *p*-doped systems. In addition, corresponding statistical analysis of μ_{lin}, μ_{sat}, V_T, V_{ON}, $I_{ON/OFF}$ and SS are presented for 10 OTFTs, where μ_{lin}, μ_{sat}, V_T, and V_{ON} are seen to improve with increasing doping concentration.

Overall, molecular doping has clearly had a great impact on the key OTFT operating parameters in the 3rd generation blend, not just the mobility. *Chapter 5* hypothesised that the prevailing mechanism for the dramatic improvements in performance is most likely to be hole trap deactivation. The strong relationship between the doping ratio and V_T, which steadily shifts towards positive gate biases with increasing doping concentrations, is supporting evidence for this hypothesis. In addition, comparing the stretching parameter and relaxation time extrapolated from the bias-stress data indicates that there is a more uniform distribution of trapping sites for the doped system, as well as trapping mechanisms happening on a shorter timescale. The V_T shift is used to calculate the number of holes donated to the channel, with the trend indicating that hole donation results in an improvement in R_C, μ_{lin}, μ_{sat}, V_T, and V_{ON}.

A further hypothesis made in *Chapter 5* was that free holes may be remotely transferred to the channel, in a similar manner to modulation doping in inorganics. Modulation doping would suggest that there is spatial separation between the dopant molecules and the free charge carriers, avoiding adverse scattering/crystal packing effects at the channel. Therefore, if this is the case, one of the signs that might be expected is that the dopant does not interfere with the OSC crystal structure at the channel.

POM and GIWAXS were therefore used to investigate this further and it appears that, indeed, the dopant does not interrupt the C_8-BTBT lattice structure at the channel interface of the blend film. Although further investigations are required, this could be due to the unusual distribution of the materials in the 3rd generation blend, where the dopant molecules are found to reside within the polymer binder layer away from the channel (see *Chapter 5*).

One of the main setbacks for doping in OTFTs is that high doping concentrations have a tendency to reduce OSC crystallinity [40] This chapter has shown that the 3rd generation blend reported in this thesis is a high mobility, high stability, low contact resistance, low threshold voltage, repeatable system with a structure that appears to enable doping mechanisms without the dopant molecules interrupting the host lattice at the channel, making it a very attractive model system for the future realisation of OTFTs in plastic electronic applications.

Chapter 7

Integrated Circuits: The practical application of 3rd generation blend-based OTFTs

The previous chapter identified the 3rd generation blend as a highly promising model system in terms of the critical operating parameters that currently hinder the deployment of OTFTs in commercial applications. The next step to demonstrating the potential and practicality of 3rd generation blend-based OTFTs is to show that the technology can be used to realise simple functional circuits. In this chapter, C_8-BTBT:C_{16}IDT-BT:$C_{60}F_{48}$(1%) devices are combined with n-channel In_2O_3/ZnO heterojunction TFTs to form hybrid inverter circuits. The approach allows integration of p-channel and n-channel TFTs with balanced carrier mobilities in the range 5-10 cm^2/V. Importantly, the inverters are fabricated on the same substrate and demonstrate promisingly high signal gains of >30 V/V and wide noise margins of ~70%, validating the potential of this hybrid technology for large-area electronics applications.

7.1 Introduction

Integrated circuits were invented in 1958 by Jack Kilby at Texas Instruments, a discovery which was awarded the Nobel Prize in Physics in 2010 [286]. Since this initial discovery they have been used extensively in many applications, for example, in microcontrollers, microprocessors, digital and analogue logic circuits and data converters [287]. At the heart of the digital integrated circuit is the inverter, or NOT gate, which is designed to return a high output from a low input and can be built using two transistors in two different ways: (i) using two transistors of the same polarity, known as a unipolar inverter and (ii) using two transistors of opposite polarity, known as a complementary inverter. Inorganic integrated circuits in commercially available appliances are widely made using the latter; they are known as complementary metal-oxide-semiconductor (CMOS) inverters, as they are made up of symmetrical, complementary pairs of *n*-type and *p*-type metal-oxide-semiconductor field-effect transistors (MOSFETs) [288]. Compared to unipolar logic, the dual-polarity CMOS logic circuits have lower power consumption, greater noise margins, higher gains and switching speeds and high manufacturing yield for large-scale industrial integration [289]. Hence if the 3rd generation blend can be incorporated into a complementary inverter, then it demonstrates the potential for its application in future commercial technologies.

To make a complementary inverter requires a *p*-type and an *n*-type transistor which have corresponding threshold voltages and equitable mobility values [17]. A complementary *n*-type system must therefore be identified in order to make integrated circuits with the *p*-type 3rd generation blend. It is well known in the organics community that the *p*-type performance for organic materials far outperforms the *n*-type performance, so a high mobility (≥ 10 cm^2/Vs) solution-processed organic *n*-type system is not available at the time of writing. As such, other material families must be considered that are – critically – equally suited for low-cost, solution-processable, low-temperature deposition techniques.

One suitable materials family is the metal oxides, which are inherently *n*-type materials, with only a few examples of *p*-type metal oxides being demonstrated to date [290] [291]. Lin et al. demonstrated that by using a bilayer of indium oxide (In_2O_3) and zinc oxide (ZnO), mobility values of 5-11 cm^2/Vs could be obtained [292]. In addition to these high mobility values, the processing was undertaken at low temperatures and from solution-phase, making this metal oxide bilayer system an ideal counterpart for the 3rd generation blend.

Such "hybrid" inverter systems that combine *p*-type organic systems and *n*-type metal oxide systems have been demonstrated previously in the literature [293] [294] [295] [296]. However, in the majority of cases these hybrid circuits require high processing temperatures

which conflict with the goal of electronics on flexible plastic substrates [297], or they require expensive vacuum-based fabrication techniques such as atomic layer deposition (ALD) [298] and sputtering [294] [296] [299], which conflict with the objective of low-cost electronics. Although advances have been made towards such systems that are both low-cost and compatible with flexible plastic substrates, these circuits are often based on systems with imbalanced or moderate electron and hole mobilities [300] [301] [302] [303].

The hybrid inverters demonstrated herein, comprised of *p*-type 3rd generation C_8-BTBT:C_{16}IDT-BT:$C_{60}F_{48}$(1%) organic blend and an *n*-type In_2O_3/ZnO metal oxide bilayer, exhibit promising high signal gains > 30 V/V and wide noise margins of 70%. In addition, they are solution-processable at low temperatures (<200 °C) and show balanced, high mobilities of 5-10 cm^2/Vs, validating the potential of this system for large-area electronics applications.

7.2 Metal oxide bilayers

The metal oxides that are the most widely studied as *n*-type semiconductors for TFTs are Ga_2O_3, ZnO, In_2O_3 and their alloys [297] [304]. These metal oxides are capable of producing TFTs with very high mobilities, but it is particularly arduous to access such high mobility values whilst processing from solution phase at low temperatures (<200 °C) [291] [305] [306]. A number of approaches have therefore been investigated with the aim of overcoming this particular limitation, for example, photonic annealing, combustion synthesis and chemical doping [305] [306] [307] [308] [309]. In 2015 Lin et al. demonstrated that one such way of improving the electron mobility whilst depositing at low temperatures was to employ a In_2O_3/ZnO bilayer architecture at the TFT channel [292]. Figure 7.1 shows transfer curves for the single materials, In_2O_3 and ZnO, compared to the In_2O_3/ZnO heterojunction. It is clear that the In_2O_3/ZnO TFTs have higher on-currents than both of the In_2O_3 and ZnO single material systems, which indicates a higher electron mobility for the bilayer system. This is indeed the case: the mobility values for 10 ZnO and 10 In_2O_3 TFTs were 1 cm^2/Vs and 2 cm^2/Vs respectively, but increase dramatically to 5-11 cm^2/Vs for 10 of the In_2O_3/ZnO TFTs. Such a remarkable improvement in the mobility is attributed to a chemically sharp heterointerface that is observed between the In_2O_3 and ZnO layers, shown in the inset in Figure 7.1, where two distinct polycrystalline layers of In_2O_3 and ZnO can be seen. Such a high quality heterointerface is believed to lead to the formation of a sheet of free electrons that are confined to this region, allowing the extended states in the In_2O_3 conduction band to be accessed, resulting in band-like charge transportation [292].

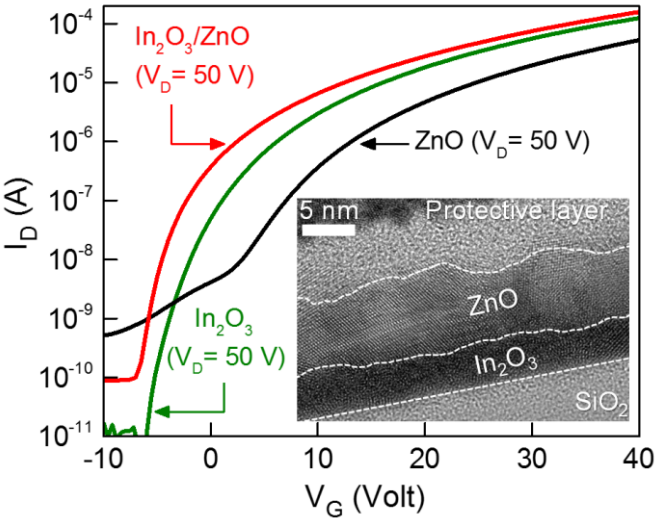

Figure 7.1: Complementary metal oxide *n*-channel TFTs. Representative transfer characteristics for single layers of In_2O_3 and ZnO, compared to a In_2O_3/ZnO bilayer TFT. All TFTs have channel dimensions L = 50 µm and W = 1000 µm. The inset is a cross-sectional high-resolution transmission electron microscopy image of the isotope In_2O_3/ZnO heterointerface.

7.3 Hybrid inverters (NOT gates)

7.3.1 Inverter fabrication

Now that an *n*-channel with an appropriate mobility has been selected, the next step to demonstrating the potential of 3rd generation blend-based OTFTs for commercial applications is to fabricate complimentary NOT gates, with a 3rd generation blend as the *p*-channel, and the In_2O_3/ZnO bilayers as the *n*-channel.

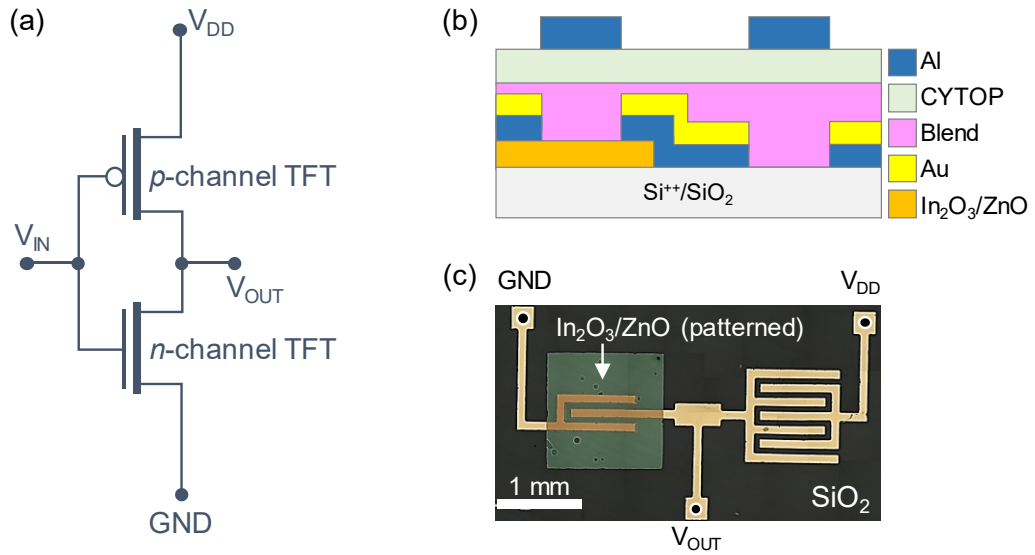

Figure 7.2: Inverter circuit design. (a) A complementary logic inverter circuit diagram, (b) a schematic representation of the cross-section of the hybrid complementary inverter with *n*-channel and *p*-channel TFTs fabricated on the same substrate, (c) An optical microscope image of the structure shown in (c) prior to the deposition of the 3rd generation blend and after the metal oxide layer has been patterned.

In order to establish the functional integration of the two systems, both channels were fabricated on the same substrate. Figure 7.2 shows a schematic of the proposed physical layout, which consists of a bottom-gate top-contact (BG-TC) structure for the *n*-channel In_2O_3/ZnO bilayer semiconductor, and a top-gate bottom-contact (TG-BC) architecture for the *p*-channel C_8-BTBT:C_{16}IDT-BT:$C_{60}F_{48}$(1%) OTFT.

The TG-BC structure is critical for the small-molecule/polymer blends, as outlined in *Chapter 3,* as these systems are known to vertically phase separate during solution-processsing and the excellent performance of organic blend systems is attributed to such a structure. The 3rd generation blend employed here has been shown to be no exception to the rule and as shown in *Chapter 5*, the small-molecule migrates to the surface/air interface, forming a layer of highly crystalline, high mobility C_8-BTBT on top of a layer of C_{16}IDT-BT binder. This morphology makes this system ideally suited to a top-gate structure so that the channel is present at the small-molecule layer, which is the underlying reason for using a TG-BC for the blend in the inverter structure.

As the *n*-channel TFTs will be in a BG-TC configuration, degenerately *n*-doped silicon wafers were used so that the 400 nm SiO_2 can be used as the dielectric layer, and the Si can act as the gate. The cleaning procedures for the silicon substrates are the same as those outlined in *Chapter 4* for glass substrates. To prepare the metal oxide precursor solutions, indium nitrate

hydroxide was dissolved in 2-methoxyethanol to produce 20 mg/ml solutions. For the zinc oxide, 10 mg/ml solutions were made by dissolving zinc oxide nanoparticles in 50 wt% ammonium hydroxide. The In_2O_3 precursor solution was then spin-coated onto the Si^{++}/SiO_2 substrate at 4000 rpm for 30 s and annealed for 1 hour at 200°C in an ambient environment. The In_2O_3 deposition was followed by spin-coating the ZnO at 4000 rpm for 30 s, annealing again for 1 hour at 200°C, to form the In_2O_3/ZnO bilayer.

Once the In_2O_3/ZnO bilayer had been deposited, photolithography was used to pattern the metal oxide semiconductor. This was done in order to minimise parasitic effects between the In_2O_3/ZnO bilayer and the C_8-BTBT:C_{16}IDT-BT:$C_{60}F_{48}$(1%) during operation. Conventional photolithography was carried out using Microposit S1813 photoresist with MF-26A developer; in order to remove the developed areas, 37% hydrochloric acid was used, and acetone was used to remove any residual resist that remained.

Now that the gate, dielectric and semiconductor are in place for the *n*-channel metal oxide, the next step is to deposit source/drain electrodes to complete the BG-TC structure. The deposition of the *n*-channel S/D electrodes was combined with the deposition of the S/D electrodes for the TG-BC *p*-channel organic devices. Source and drain electrodes consisting of 10 nm Al and 30 nm Au were therefore deposited on top of the $Si^{++}/SiO_2/In_2O_3$/ZnO structure. The use of the Al is twofold: to act as an adhesion layer for the Au and also to act as an electron injecting layer for the *n*-channel TFTs. The Au acts as a hole-injecting material and – as in previous chapters – the Au S/D electrodes were treated with 2,3,4,5,6-Pentafluorothiophenol (PFBT) to modify the work function [88]. The C_8-BTBT:C_{16}IDT-BT:$C_{60}F_{48}$(1%) blend was then prepared and deposited following the procedure outlined in *Chapter 4*. Cytop is then used as a gate dielectric for the TG-BC organic *p*-channel devices and to complete the fabrication, a 40 nm layer of Al was thermally evaporated on top of the semiconductor as a gate for the *p*-channel TFTs.

7.3.2 Inverter analysis

Figure 7.3 shows the transfer characteristics of the two independent *n*-type and *p*-type TFTs. In order to get the similar transfer characteristics and on-currents (that are shown in Figure 7.3), the dielectric capacitance values, thicknesses of the two different dielectrics (Cytop and SiO_2) and channel dimensions for both TFTs were adjusted and finely-tuned; the widths are 1000 μm and 7000 μm for the *n*- and *p*-channels respectively, with both channel lengths being 100 μm. Both types of TFT exhibit electron and hole saturation mobility values between 5-10 cm^2/Vs. Not only do these high mobility values indicate the potential of these hybrid

circuits, at the time of writing they are also the highest values reported for solution-processed *n*-type metal oxide and *p*-type organic inverter TFTs fabricated on the same substrate.

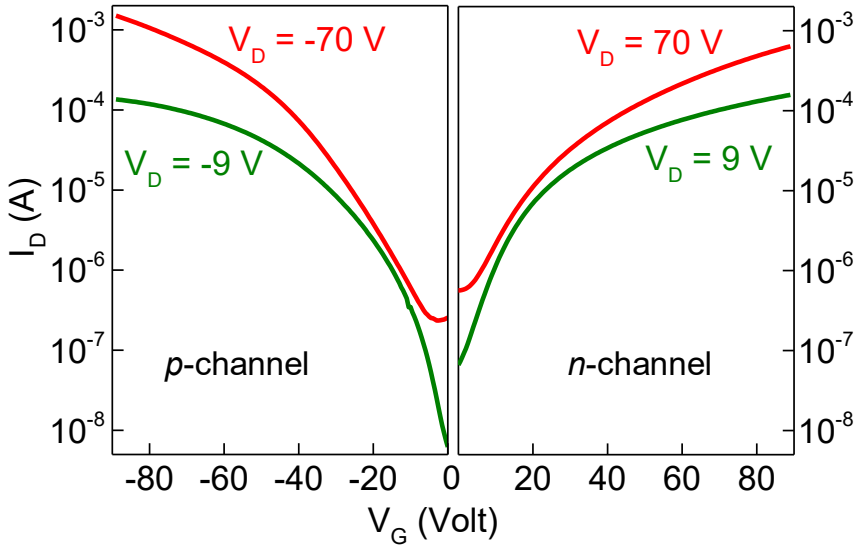

Figure 7.3:Transfer characteristics of the two independent *n*-type and *p*-type TFTs measured after the inverter fabrication.

Once the individual transistors had been tested and balanced mobilities confirmed, the inverter circuits were characterised. The two figures of merit for inverters are the *signal gain* and the *noise margin*. The signal gain is defined as [17]:

$$g = \frac{\partial V_{\mathrm{OUT}}}{\partial V_{\mathrm{IN}}} \tag{7.1}$$

where V_{OUT} (V) is the output voltage, V_{IN} (V) is the input voltage, and g is the signal gain (V/V) which must be > 1 to continue signal propagation in large integrated circuits that are made of many logic gates. The noise margin describes how immune the circuit is to noise, i.e. if a wide range of input values can produce a valid output.

The quasistatic voltage transfer characteristics (VTC) for the hybrid inverter are shown in Figure 7.4, along with a number of signal gain curves that have been measured across a range of voltages (V_{DD}). The inset in Figure 7.4 is a polarised optical microscope image showing the hybrid integrated circuit. Exemplary inverter operation is demonstrated by this hybrid system; almost ideal rail-to-rail output voltage (V_{OUT}) swing is exhibited with a sharp transition, where V_{OUT} is double the value of V_{IN} (i.e. $V_{IN} = V_{OUT}/2$), particularly at $V_{OUT} > 20$ V. Such behaviour results in high differential signal gain values > 30 V/V for $V_{DD} \geq 30$ V, shown by the shaded

areas in Figure 7.4. Finally, the noise margins for this hybrid circuit are 70% for $V_{DD} \geq 20$ V, demonstrating that this circuit has a high resilience to input signal noise. The combination of a high signal gain and high noise margin make this hybrid system very promising and clearly demonstrates the potential of such a system for printed microelectronic applications [289].

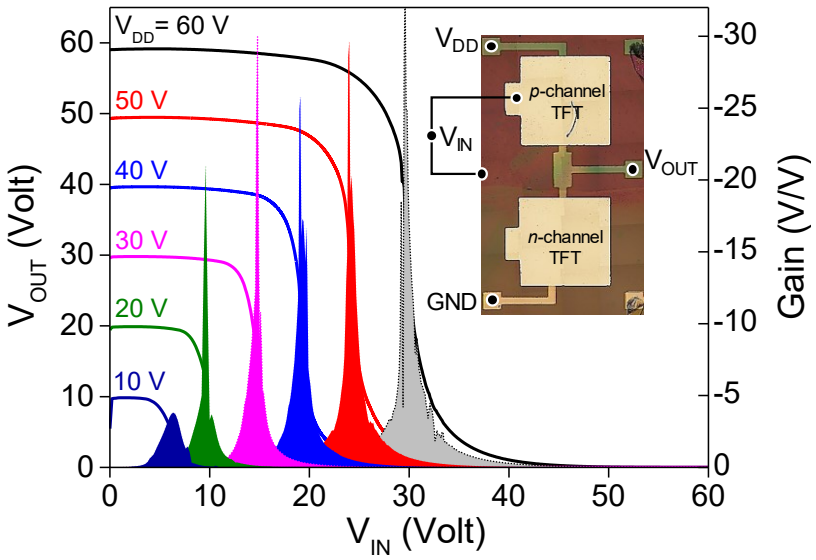

Figure 7.4: Quasistatic voltage transfer characteristics and signal gain (shaded areas) for the complementary hybrid inverter.

7.4 Summary and conclusions

In summary, the potential of 3rd generation blend-based OTFTs for real life applications has been demonstrated by fabricating hybrid integrated circuits. The 3rd generation C_8-BTBT:C_{16}IDT-BT:$C_{60}F_{48}$(1%) blend was used as a *p*-channel and – as a complementary counterpart – high performance metal oxide heterojunctions of In_2O_3/ZnO were employed for the *n*-channel. Both material systems were processed on the same substrate from solution-phase at low-temperatures (< 200 °C) that are compatible with a number of plastic substrates and hence the ultimate ambition of flexible electronics. The electron and hole saturation mobilities exhibited were between 5-10 cm^2/Vs, which are the highest values reported to-date for solution-processed *n*-type metal oxide and *p*-type organic inverter TFTs fabricated on the same substrate. The hybrid inverters exhibit excellent performance, with noise margins over 70% and high differential signal gain values > 30 V/V. The combination of high signal gain and high noise margins – as well as low temperature solution processing – make this hybrid system very promising and demonstrates its potential for use in scalable, cost effective, printed microelectronic applications.

Chapter 8

Conclusions and Outlook

This chapter provides a summary of the experimental work presented in this thesis and highlights future work and outlook. In brief, the thesis describes the development of 3rd generation ternary organic semiconducting blends and their application in OTFTs. The resulting devices offer remarkably enhanced hole mobility, improved operating stability, low contact resistance, and reduced threshold voltage; all important prerequisites for practical utilisation of any transistor technology in commercial applications. Additionally, the 3rd generation blend system exhibits an unusual phase-separated microstructure, which appears to enable doping but without any apparent adverse effect on the layer's crystalline microstructure (e.g. introduction of defects). Overall, the work contributes to the advancement of the small-molecule/polymer blends and highlights molecular doping as a key enabling technology for the development of advanced organic microelectronics.

.

8.1 Summary

The experimental work in *Chapter 5* reports on the development of a 3rd generation organic blend system. To begin with, two promising materials, the small-molecule C_8-BTBT and the conjugated polymer C_{16}IDT-BT, were chosen to design a new small-molecule/polymer blend system. At a blend ratio of 25% small-molecule to 75% polymer and concentration of 10 mg/ml in chlorobenzene, the mobility value is greater than the maximum mobilities that have been achieved by either of the single materials, thereby demonstrating the potential of this unique materials combination.

Although the mobility of the C_8-BTBT:C_{16}IDT-BT blend OTFTs is improved, the transfer characteristics exhibit nonideal properties, suffering from high V_T, hysteresis and high operating voltages. A potential explanation for this behaviour is that the system suffers from severe energetic disorder due to a number of trap states that may arise from, for example, microstructural defects, the difference between the HOMO levels of the C_8-BTBT and C_{16}IDT-BT, chemical impurities and molecular weight distribution of the polymer binder.

In order to investigate the energetic disorder hypothesis further, intentional molecular doping was explored in the C_8-BTBT:C_{16}IDT-BT blend OTFTs. Indeed, the molecular dopant, $C_{60}F_{48}$, at a molar weight percentage of 1% was found to have dramatic effects on the hole transport properties: a significant shift in V_T, reduced hysteresis, reduced operating voltages, *n*-type behaviour completely suppressed and – most significantly – an increase in the maximum saturation mobility.

A range of solvents and solvent blends were then investigated in the blend system. It was found that by using a solvent blend containing 50% tetralin and 50% chlorobenzene (tetralin:CB) for the C_8-BTBT:C_{16}IDT-BT:$C_{60}F_{48}$(1%) blend, dramatic improvements in the mobility could be made, achieving a maximum mobility greater than 13 cm^2/Vs, with an average of 9.4 cm^2/Vs calculated over 16 transistors.

A range of materials characterisation techniques (POM, AFM, SEM and WAXD) were used to investigate the differences between the single solvent systems (i.e. tetralin and chlorobenzene) and the tetralin:CB system. It was found that the tetralin:CB solvent blend improves crystallinity in the *x-y* plane as well as the *z*-direction, with the *x-y* plane improvements being found to have the most prominent effects; in particular, tetralin:CB films exhibited molecular terracing and a continuous, perforation-free topography with a lower RMS and narrower distribution of heights.

Due to the importance of the vertical phase separation in small-molecule/polymer blend systems, a ToF-SIMS technique was used to investigate the phase separation of the highest mobility C_8-BTBT:C_{16}IDT-BT:$C_{60}F_{48}$(1%) films fabricated from tetralin:CB. The ToF-SIMS data indicates an unusual distribution of materials where the dopant appears to be distributed within the polymer layer and not present at the OTFT channel. This indicates that there is some spatial separation between the dopant molecules and the channel, suggesting that unconventional doping mechanisms may be underpinning the dramatic performance improvements of the ternary blend OTFTs.

Chapter 5 concludes by highlighting future work for the 3rd generation blend system. Firstly, preliminary studies were carried out with an alternative polymer binder, IDTT-BT, in a C_8-BTBT:IDTT-BT:$C_{60}F_{48}$ blend. Although further optimisation work is certainly required, the results show the same promising performance trends as in the C_{16}IDT-BT-based system, indicating a reduction in energetic disorder. Secondly, a solution-ageing approach was investigated, which resulted in exceptionally high mobilities up to 23.1 cm^2/Vs for a C_8-BTBT:C_{16}IDT-BT:$C_{60}F_{48}$(0.1%) blend. These results demonstrate the 3rd generation ternary organic blend as a prospective system with great potential for further research to be undertaken.

Chapter 6 investigates the impact of molecular doping on the key OTFT operating parameters in the C_8-BTBT:C_{16}IDT-BT:$C_{60}F_{48}$ blend, starting with a statistical overview of how the dopant affects the mobility. Molecular doping is found to improve the mobility from an average of 1.4 cm^2/Vs (0% $C_{60}F_{48}$) to an average of 7.8 cm^2/Vs (1% $C_{60}F_{48}$) for 50 OTFTs per blend.

Bias stress was then investigated for the pristine and the best performing blends, finding that although both blends compare well to the literature, the doped system is more stable than the pristine system. The bias-stress data suggests that the dopant causes a narrowing of the trap distribution in addition to trapping on shorter timescales. These results are supportive of a hypothesis made in *Chapter 5*, where it was suggested that trap deactivation from the molecular dopant is the primary mechanism for OTFT improvements.

Contact resistance was the next critical operating parameter to be investigated over a broad range of doping concentrations, finding that the contact resistance is reduced by a factor of ≈10 in the best performing blend compared to the pristine blend. A similarly strong relationship with molecular doping was also found for μ_{lin}, μ_{sat}, V_{ON} and V_T, as well as a clear trend in the transfer characteristics, which is expected from *p*-doped systems. The strong relationship between the doping ratio and V_T also supports the trap-filling hypothesis, and the observed shift in V_T is subsequently used to calculate holes donated to the channel.

Chapter 6 finishes by using POM and GIWAX to investigate the effect of the dopant on the morphology/crystallinity. Remarkably, the results indicate that the dopant does not interrupt the C_8-BTBT lattice structure at the channel interface of the blend film.

Overall, *Chapter 6* shows that the 3rd generation blend reported in this thesis is a high mobility, high stability, low contact resistance, low V_T, repeatable system with an unusual structure that enables doping mechanisms yet the dopant molecules do not adversely disrupt the organic semiconductor crystal packing at the OTFT channel. This makes the 3rd generation ternary organic blend an extremely attractive model system for the future realisation of OTFTs in commercial applications.

The final experimental chapter, *Chapter 7*, showed that the 3rd generation blend-based OTFTs can indeed be used in practical applications. The C_8-BTBT:C_{16}IDT-BT:$C_{60}F_{48}$(1%) blend was incorporated into a hybrid inverter circuit, using a metal oxide In_2O_3/ZnO bilayer as a complementary *n*-channel. Dielectric thicknesses and TFT channel lengths were used to balance the performance of the two complementary TFTs, which were both deposited from solution-phase at low temperatures. The two TFTs exhibited electron and hole saturation mobility values between 5-10 cm^2/Vs, which are the highest values reported to-date for solution-processed *n*-type metal oxide and *p*-type organic inverter TFTs fabricated on the same substrate.

The hybrid inverters exhibit excellent performance, with noise margins over 70% and high differential signal gain values > 30 V/V. The combination of a high signal gain and high noise margin make this hybrid system very promising and clearly demonstrates the potential of this system and 3rd generation blend-based OTFTs for printed microelectronic applications.

8.2 Future work

The work outlined in this thesis strongly suggests that further research into ternary organic blend systems will certainly be fruitful.

Alternative combinations of small-molecules, polymers and dopants need to be explored. This includes exploring the effects of molecular doping in existing blends, such as the 1st and 2nd generation blends, as well as investigating new, alternative dopants – such as BCF mentioned in *Chapter 3* – in the 3rd generation blend that has been presented here. In addition to investigating molecular dopants in existing blends, molecular doping should be used as a tool for developing new *p*-type blends from other combinations of small-molecules and polymers. For example, C_8-BTBT:PTAA and diF-TES ADT:C_{16}IDT-BT blends have moderate performance as binary blends may but may benefit from introducing a molecular dopant; this

can be done by introducing dopants at a range of mol. wt. % from 0% to 5% and monitoring the performance of the OTFTs. *Chapter 5* highlighted that a small-molecule/polymer blend made from C_8-BTBT and IDTT-BT has great potential if further optimisation is carried out. The first steps for this optimisation should be varying the spin-speed, solution concentration and investigating a range of solvents, as well as continue to investigate the effects of other molecular dopants.

The development of new blends shouldn't be limited to *p*-type materials; *n*-type ternary blends should also be explored. For instance, *n*-dopants can be introduced into the 3rd generation blend to investigate whether the electron transport highlighted in *Chapter 5* and *Chapter 6* can be encouraged further. New combinations of both *n*-type and *p*-type materials should also be investigated with the aim of developing ambipolar blends, such as a high-performance ambipolar blend system where the polarity can be tweaked and controlled using *n*-dopants and *p*-dopants.

Alternative processing conditions should be investigated for the C_8-BTBT:C_{16}IDT-BT:$C_{60}F_{48}$ blend; POM imaging revealed that the blend microstructure appears to be strewn with defects, or 'agglomerations'; it is therefore rather surprising that a system with this apparent level of disorder produces high saturation mobilities. By considering alternative solution-deposition techniques, such as blade coating and bar coating, the performance may be enhanced even further by improving the morphology.

Another interesting processing condition that can be explored is post-deposition annealing. Theoretically, if a crystalline material, such as C_8-BTBT, is melted and re-crystallised from the melt then it is possible to use the re-crystallisation temperature to control the formation and the size of the crystallites. If the re-crystallisation occurs at a temperature close to but below the melting point, then the nucleation rate will significantly decrease and the growth rate will increase, hence producing larger crystals than films re-crystallised at low temperatures, or quenched to room temperature.

As such, very large C_8-BTBT crystals can be grown in C_8-BTBT-based blends if the blend films are annealed after spin-coating using one of the following approaches: (i) heating the blend film above the C_8-BTBT melting point (108–112°C) and turning down the hotplate to slowly reduce the temperature of the blend film, and (ii) heating the blend film above the C_8-BTBT melting point and then transferring the substrate to another hotplate set to a specific temperature just below the C_8-BTBT melting point.

For the C_8-BTBT:C_{16}IDT-BT:$C_{60}F_{48}$ blend, these annealing techniques were not found to not have any affect on the underlying layer of C_{16}IDT-BT in the blend film, but they can

have a dramatic affect on the size of the C_8-BTBT crystallites at the upper layer of the blend film. However, despite an increase in crystallite size, the OTFTs annealed in this manner had highly variable mobilities which were noticeably lower than the OTFTs presented in this thesis. Further experimentation on this promising topic would therefore certainly be required, with a particular focus on overcoming repeatability issues and the difficulties in controlling the temperature of the surroundings so that large single crystals – greater than the OTFT channel dimensions – can be grown in a controlled manner for high mobility OTFTs. In addition to exploring the annealing temperature of the 3rd generation blend, other polymer binders (such as those listed in *Chapter 5*, *Section 5.1.2*) should be investigated with the C_8-BTBT at a range of annealing temperatures. The polymer binder has a significant influence how the C_8-BTBT crystallites grow from the melt and therefore the polymer binder can be used as a tool for controlling this technique further. Other solution deposition techniques should also be combined with the controlled annealing, as well as investigating other solvents.

There are other processing parameters that should be considered for the C_8-BTBT:C_{16}IDT-BT:$C_{60}F_{48}$ blend, for example, it was shown that mobilities up to 23.1 cm^2/Vs can be achieved by using a solution-ageing technique. To investigate these solution-ageing effects further, C_8-BTBT:C_{16}IDT-BT:$C_{60}F_{48}$ blend solutions doped at a range of molar wt. concentrations (0%, 0.01%, 0.05%, 0.1%, 0.5%, 1%, 2% and 5%) should be tested in OTFTs on a weekly or biweekly basis for 2 months. This data will highlight the trends in OTFT performance improvement with solution-ageing; the contact resistance must also be analysed for each set of data to monitor contact resistance change over time. Between OTFT fabrication, the solutions should be stored in a dark place in the glovebox in an inert nitrogen atmosphere. In addition to the transistor data, a 'dummy' solution should be prepared to detect any fluctuations or changes in the solution concentration. This can be done by weighing the dummy solution each week to see if any solvent has evaporated over time.

Finally, further work should be undertaken to understand the unconventional doping mechanism governing the 3rd generation blend, including depth profiling and computer modelling. The development of new blends will also shed further light on the doping processes involved in ternary organic blend systems.

8.3 Outlook

For many years, the organic small-molecule/polymer blend has been a very popular system for OTFTs because of the remarkable effects of this simple technique. For example, the blend offers improved film formation, interfacial trap density reduction and grain boundary

passivation. The work in this thesis highlights an additional interesting property of the blend, whereby the introduction of a molecular dopant in the traditional binary small-molecule/polymer blend dramatically improves the electrical properties by reducing energetic disorder. At the same time, the dopant does not appear to interrupt the OSC lattice and reduce crystallinity or mobility due to the unique, non-uniform distribution of the dopant molecules.

In fact, the mobility is significantly increased with the addition of the dopant, exceeding 13 cm^2/Vs, which pushes the organic blend into the realm of industrial applications. This system therefore addresses the two points that were highlighted in the literature review in *Chapter 3*, that there is a gap in the market for (i) advanced, 3rd generation organic semiconducting blends that surpass the benchmark mobility of 10 cm^2/Vs, and (ii) further research into OTFT doping techniques, particularly those that overcome organic semiconductor lattice/microstructure interruptions and promote charge carrier transport. Furthermore, the 3rd generation blend developed in this thesis is shown to be a stable, low contact resistance, low V_T, repeatable system, that is also demonstrated in a hybrid inverter circuit. This makes this blend system a highly attractive, relevant model system for the realisation of OTFTs in future applications.

The science and engineering of doping has been so relevant to the success of modern electronics; likewise the small-molecule/polymer organic semiconducting blends have been a key player in OTFT development. Combining these two fundamental approaches has had a highly desirable and significant impact on OTFT performance. Furthermore, the unusual phase separation of the 3rd generation blend system hints at the existence of an underlying unconventional mechanism, suggesting a potential modulation doping technique for OTFTs.

Overall, the work in this thesis has shown that there is a bright future ahead for the ternary organic blend in the development of advanced organic microelectronics.

Bibliography

1. Wilcock J. The Staffordshire University Computing Futures Museum Manchester Page 2010 [Available from: http://www.fcet.staffs.ac.uk/jdw1/sucfm/manchester.htm].
2. Moore GE. Cramming more components onto integrated circuits (Reprinted from Electronics, pg 114-117, April 19, 1965). Proceedings of the Ieee. 1998;86(1):82-5.
3. Currys. LG 55EG910V Smart 3D 55" Curved OLED TV: DSG Retail Limited; 2016 [Available from: http://www.currys.co.uk/gbuk/tv-and-home-entertainment/televisions/televisions/lg-55eg910v-smart-3d-55-curved-oled-tv-10144246-pdt.html.]
4. iPhone 7 Updates. iPhone 7 Pictures – Concepts, Leaks And Rumors iPhone 7 Updates; 2016 [Available from: http://www.iphone7updates.org/iphone-7-pictures-concepts-leaks-rumors/4736/#].
5. Mendez H, Heimel G, Opitz A, Sauer K, Barkowski P, Oehzelt M, et al. Doping of Organic Semiconductors: Impact of Dopant Strength and Electronic Coupling. Angewandte Chemie-International Edition. 2013;52(30):7751-5.
6. Shirakawa H, Louis EJ, MacDiarmid AG, Chiang CK, Heeger AJ. Synthesis of electrically conducting organic polymers: halogen derivatives of polyacetylene, (CH). Journal of the Chemical Society, Chemical Communications. 1977(16):578-80.
7. Sirringhaus H. 25th Anniversary Article: Organic Field-Effect Transistors: The Path Beyond Amorphous Silicon. Advanced Materials. 2014;26(9):1319-35.
8. Dong H, Fu X, Liu J, Wang Z, Hu W. 25th Anniversary Article: Key Points for High-Mobility Organic Field-Effect Transistors. Advanced Materials. 2013;25(43):6158-82.
9. Salleo A. Electronic Traps in Organic Semiconductors. Organic Electronics: Wiley-VCH Verlag GmbH & Co. KGaA; 2013. p. 341-80.
10. Salleo A. Charge transport in polymeric transistors. Materials Today. 2007;10(3):38-45.
11. Fakhouri SM, Zhang L, Briseno AL. Solar flare. Materials Today. 2011;14(12):623.
12. Gather MC, Köhnen A, Meerholz K. White Organic Light-Emitting Diodes. Advanced Materials. 2011;23(2):233-48.
13. Murawski C, Leo K, Gather MC. Efficiency Roll-Off in Organic Light-Emitting Diodes. Advanced Materials. 2013;25(47):6801-27.
14. Leo K. Organic photovoltaics. Nature Reviews Materials. 2016;1:16056.
15. Youn H, Park HJ, Guo LJ. Organic Photovoltaic Cells: From Performance Improvement to Manufacturing Processes. Small. 2015;11(19):2228-46.
16. Sirringhaus H. Device Physics of Solution-Processed Organic Field-Effect Transistors. Advanced Materials. 2005;17(20):2411-25.

17. Baeg K-J, Caironi M, Noh Y-Y. Toward Printed Integrated Circuits based on Unipolar or Ambipolar Polymer Semiconductors. Advanced Materials. 2013;25(31):4210-44.

18. FlexEnable. Press release: FlexEnable and CPT partnership signals the industrialisation of truly flexible AMOLED displays: FlexEnable Limited; 2015 [Available from: http://www.flexenable.com/newsroom/press-release-flexenable-and-cpt-partnership-signals-the-industrialisation-of-truly-flexible-amoled/].

19. Malliaras G, Abidian MR. Organic Bioelectronic Materials and Devices. Advanced Materials. 2015;27(46):7492-.

20. Someya T, Bao Z, Malliaras GG. The rise of plastic bioelectronics. Nature. 2016;540(7633):379-85.

21. Das R, Harrop P. Printed, Organic & Flexible Electronics Forecasts, Players & Opportunities 2016-2026: IDTechEx; 2016 [Available from: http://www.idtechex.com/research/reports].

22. Koezuka H, Tsumura A, Ando T. Field-effect transistor with polythiophene thin film. Synthetic Metals. 1987;18(1):699-704.

23. Horowitz G, Hajlaoui R, Bouchriha H, Bourguiga R, Hajlaoui M. The Concept of “Threshold Voltage” in Organic Field-Effect Transistors. Advanced Materials. 1998;10(12):923-7.

24. Weimer PK. The TFT A New Thin-Film Transistor. Proceedings of the IRE. 1962;50(6):1462-9.

25. Cicoira F, Santato C. Organic Light Emitting Field Effect Transistors: Advances and Perspectives. Advanced Functional Materials. 2007;17(17):3421-34.

26. Labram JG, Lin Y-H, Anthopoulos TD. Exploring Two-Dimensional Transport Phenomena in Metal Oxide Heterointerfaces for Next-Generation, High-Performance, Thin-Film Transistor Technologies. Small. 2015;11(41):5472-82.

27. Smith J, Hamilton R, McCulloch I, Stingelin-Stutzmann N, Heeney M, Bradley DDC, et al. Solution-processed organic transistors based on semiconducting blends. Journal of Materials Chemistry. 2010;20(13):2562-74.

28. Yuan YB, Giri G, Ayzner AL, Zoombelt AP, Mannsfeld SCB, Chen JH, et al. Ultra-high mobility transparent organic thin film transistors grown by an off-centre spin-coating method. Nat Commun. 2014;5: 3005.

29. Kim G, Kang S-J, Dutta GK, Han Y-K, Shin TJ, Noh Y-Y, et al. A Thienoisoindigo-Naphthalene Polymer with Ultrahigh Mobility of 14.4 cm2/V·s That Substantially Exceeds Benchmark Values for Amorphous Silicon Semiconductors. J Am Chem Soc. 2014;136(26):9477-83.

30. Minemawari H, Yamada T, Matsui H, Tsutsumi J, Haas S, Chiba R, et al. Inkjet printing of single-crystal films. Nature. 2011;475(7356):364-7.

31. Diao Y, Tee BCK, Giri G, Xu J, Kim DH, Becerril HA, et al. Solution coating of large-area organic semiconductor thin films with aligned single-crystalline domains. Nat Mater. 2013;12(7):665-71.

32. Tseng HR, Phan H, Luo C, Wang M, Perez LA, Patel SN, et al. High-Mobility Field-Effect Transistors Fabricated with Macroscopic Aligned Semiconducting Polymers. Advanced Materials. 2014;26(19):2993-8.

33. Kwon S, Kim J, Kim G, Yu K, Jo Y-R, Kim B-J, et al. Organic Single-Crystal Semiconductor Films on a Millimeter Domain Scale. Advanced Materials. 2015:DOI:10.1002/adma.201502980.

34. Iino H, Usui T, Hanna J-i. Liquid crystals for organic thin-film transistors. Nature communications. 2015;6:6828.

35. Lee BH, Bazan GC, Heeger AJ. Doping-Induced Carrier Density Modulation in Polymer Field-Effect Transistors. Advanced materials. 2016;28(1):57-62.

36. Uemura T, Rolin C, Ke T-H, Fesenko P, Genoe J, Heremans P, et al. On the Extraction of Charge Carrier Mobility in High-Mobility Organic Transistors. Advanced Materials. 2016;28(1):151-5.

37. Bittle EG, Basham JI, Jackson TN, Jurchescu OD, Gundlach DJ. Mobility overestimation due to gated contacts in organic field-effect transistors. Nature communications. 2016;7.

38. Tsutsui Y, Schweicher G, Chattopadhyay B, Sakurai T, Arlin J-B, Ruzié C, et al. Charge Carrier Mobility: Unraveling Unprecedented Charge Carrier Mobility through Structure Property Relationship of Four Isomers of Didodecyl[1]benzothieno[3,2-b][1]benzothiophene (Adv. Mater. 33/2016). Advanced Materials. 2016;28(33):7291-.

39. Walzer K, Maennig B, Pfeiffer M, Leo K. Highly efficient organic devices based on electrically doped transport layers. Chemical Reviews. 2007;107(4):1233-71.

40. Lüssem B, Keum C-M, Kasemann D, Naab B, Bao Z, Leo K. Doped Organic Transistors. Chemical Reviews. 2016.

41. Lüssem B, Riede M, Leo K. Doping of organic semiconductors. physica status solidi (a). 2013;210(1):9-43.

42. Pauling L. THE NATURE OF THE CHEMICAL BOND. APPLICATION OF RESULTS OBTAINED FROM THE QUANTUM MECHANICS AND FROM A THEORY OF PARAMAGNETIC SUSCEPTIBILITY TO THE STRUCTURE OF MOLECULES. J Am Chem Soc. 1931;53(4):1367-400.

43. CNX O. OpenStax, Chemistry: BC Open Textbooks, Pressbooks; 2016 [Available from: http://cnx.org/contents/85abf193-2bd2-4908-8563-90b8a7ac8df6@9.311].

44. Politis JK, Nemes JC, Curtis MD. Synthesis and characterization of regiorandom and regioregular poly(3-octylfuran). J Am Chem Soc. 2001;123(11):2537-47.

45. Bendikov M, Wudl F, Perepichka DF. Tetrathiafulvalenes, oligoacenenes, and their buckminsterfullerene derivatives: The brick and mortar of organic electronics2004. 4891-945 p.

46. Facchetti A. Semiconductors for organic transistors. Materials Today. 2007;10(3):28-37.

47. Wong KF, Skaf MS, Yang C-Y, Rossky PJ, Bagchi B, Hu D, et al. Structural and Electronic Characterization of Chemical and Conformational Defects in Conjugated Polymers. The Journal of Physical Chemistry B. 2001;105(26):6103-7.

48. Tessler N, Preezant Y, Rappaport N, Roichman Y. Charge Transport in Disordered Organic Materials and Its Relevance to Thin-Film Devices: A Tutorial Review. Advanced Materials. 2009;21(27):2741-61.

49. Waragai K, Akimichi H, Hotta S, Kano H, Sakaki H. Charge transport in thin films of semiconducting oligothiophenes. Physical Review B. 1995;52(3):1786-92.

50. Horowitz G. Tunneling Current in Polycrystalline Organic Thin-Film Transistors. Advanced Functional Materials. 2003;13(1):53-60.

51. Meng H-F. Polymer Electronics. Singapore: Pan Standford Publishing; 2013.

52. Paasch G, Lindner T, Scheinert S. Variable range hopping as possible origin of a universal relation between conductivity and mobility in disordered organic semiconductors. Synthetic Metals. 2002;132(1):97-104.

53. Vissenberg M, Matters M. Theory of the field-effect mobility in amorphous organic transistors. Physical Review B. 1998;57(20):12964-7.

54. Broadbent SR, Hammersley JM. Percolation processes. Mathematical Proceedings of the Cambridge Philosophical Society. 1957;53(03):629-41.

55. Chen Y, Podzorov V. Bias Stress Effect in “Air-Gap” Organic Field-Effect Transistors. Advanced Materials. 2012;24(20):2679-84.

56. Stallinga P. Electronic Transport in Organic Materials: Comparison of Band Theory with Percolation/(Variable Range) Hopping Theory. Advanced Materials. 2011;23(30):3356-62.

57. Stallinga P, Gomes HL. Thin-film field-effect transistors: The effects of traps on the bias and temperature dependence of field-effect mobility, including the Meyer–Neldel rule. Organic Electronics. 2006;7(6):592-9.

58. Anderson PW. Absence of Diffusion in Certain Random Lattices. Physical Review. 1958;109(5):1492-505.

59. Horowitz G, Hajlaoui ME, Hajlaoui R. Temperature and gate voltage dependence of hole mobility in polycrystalline oligothiophene thin film transistors. Journal of Applied Physics. 2000;87(9):4456-63.

60. Salleo A, Kline RJ, DeLongchamp DM, Chabinyc ML. Microstructural Characterization and Charge Transport in Thin Films of Conjugated Polymers. Advanced Materials. 2010;22(34):3812-38.

61. Dacuña J, Desai A, Xie W, Salleo A. Modeling of the effect of intentionally introduced traps on hole transport in single-crystal rubrene. Physical Review B. 2014;89(24):245302.

62. Huang BC, Lin YJ. Effect of the induced electron traps by oxygen plasma treatment on transfer characteristics of organic thin film transistors. Applied Physics Letters. 2011;99(11).

63. Zhu M, Liang G, Cui T, Varahramyan K. Depletion-mode n-channel organic field-effect transistors based on NTCDA. Solid-State Electronics. 2003;47(10):1855-8.

64. Lüssem B, Tietze ML, Kleemann H, Hoßbach C, Bartha JW, Zakhidov A, et al. Doped organic transistors operating in the inversion and depletion regime. Nature communications. 2013;4.

65. Brotherton SD. Introduction to Thin Film Transistors: Physics and Technology of TFTs. Switzerland: Springer; 2013.

66. Facchetti A, Yoon MH, Marks TJ. Gate Dielectrics for Organic Field-Effect Transistors: New Opportunities for Organic Electronics. Advanced Materials. 2005;17(14):1705-25.

67. DiBenedetto SA, Facchetti A, Ratner MA, Marks TJ. Molecular Self-Assembled Monolayers and Multilayers for Organic and Unconventional Inorganic Thin-Film Transistor Applications. Advanced Materials. 2009;21(14-15):1407-33.

68. Braga D, Horowitz G. High-Performance Organic Field-Effect Transistors. Advanced Materials. 2009;21(14-15):1473-86.

69. Sun X, Di C-a, Liu Y. Engineering of the dielectric-semiconductor interface in organic field-effect transistors. Journal of Materials Chemistry. 2010;20(13):2599-611.

70. Choi HH, Kang MS, Kim M, Kim H, Cho JH, Cho K. Decoupling the Bias-Stress-Induced Charge Trapping in Semiconductors and Gate-Dielectrics of Organic Transistors Using a Double Stretched-Exponential Formula. Advanced Functional Materials. 2013;23(6):690-6.

71. Mathijssen SGJ, Spijkman M-J, Andringa A-M, van Hal PA, McCulloch I, Kemerink M, et al. Revealing Buried Interfaces to Understand the Origins of Threshold Voltage Shifts in Organic Field-Effect Transistors. Advanced Materials. 2010;22(45):5105-9.

72. Mathijssen SGJ, Kemerink M, Sharma A, Cölle M, Bobbert PA, Janssen RAJ, et al. Charge Trapping at the Dielectric of Organic Transistors Visualized in Real Time and Space. Advanced Materials. 2008;20(5):975-9.

73. Possanner SK, Zojer K, Pacher P, Zojer E, Schürrer F. Threshold Voltage Shifts in Organic Thin-Film Transistors Due to Self-Assembled Monolayers at the Dielectric Surface. Advanced Functional Materials. 2009;19(6):958-67.

74. Sirringhaus H. Reliability of Organic Field-Effect Transistors. Advanced Materials. 2009;21(38-39):3859-73.

75. Richards T, Bird M, Sirringhaus H. A quantitative analytical model for static dipolar disorder broadening of the density of states at organic heterointerfaces. The Journal of Chemical Physics. 2008;128(23):234905.

76. Marinkovic M, Belaineh D, Wagner V, Knipp D. On the Origin of Contact Resistances of Organic Thin Film Transistors. Advanced Materials. 2012;24(29):4005-9.

77. Meijer EJ, Gelinck GH, van Veenendaal E, Huisman B-H, de Leeuw DM, Klapwijk TM. Scaling behavior and parasitic series resistance in disordered organic field-effect transistors. Applied Physics Letters. 2003;82(25):4576-8.

78. Robeson LM. Polymer Blends: A Comprehensive Review: Hanser; 2007.

79. Scaccabarozzi AD, Stingelin N. Semiconducting:insulating polymer blends for optoelectronic applications-a review of recent advances. Journal of Materials Chemistry A. 2014;2(28):10818-24.

80. Claudia Arias A. Vertically Segregated Polymer Blends: Their Use in Organic Electronics. Journal of Macromolecular Science, Part C. 2006;46(1):103-25.

81. Lu GH, Blakesley J, Himmelberger S, Pingel P, Frisch J, Lieberwirth I, et al. Moderate doping leads to high performance of semiconductor/insulator polymer blend transistors. Nature communications. 2013;4.

82. Goffri S, Muller C, Stingelin-Stutzmann N, Breiby DW, Radano CP, Andreasen JW, et al. Multicomponent semiconducting polymer systems with low crystallization-induced percolation threshold. Nat Mater. 2006;5(12):950-6.

83. Hwang DK, Fuentes-Hernandez C, Berrigan JD, Fang Y, Kim J, Potscavage WJ, Jr., et al. Solvent and polymer matrix effects on TIPS-pentacene/polymer blend organic field-effect transistors. Journal of Materials Chemistry. 2012;22(12):5531-7.

84. Guo D, Miyadera T, Ikeda S, Shimada T, Saiki K. Analysis of charge transport in a polycrystalline pentacene thin film transistor by temperature and gate bias dependent mobility and conductance. Journal of Applied Physics. 2007;102(2):023706.

85. Dimitrakopoulos CD, Malenfant PRL. Organic thin film transistors for large area electronics. Advanced Materials. 2002;14(2):99-117.

86. McCulloch I, Heeney M, Bailey C, Genevicius K, MacDonald I, Shkunov M, et al. Liquid-crystalline semiconducting polymers with high charge-carrier mobility. Nat Mater. 2006;5(4):328-33.

87. Hamilton R, Smith J, Ogier S, Heeney M, Anthony JE, McCulloch I, et al. High-Performance Polymer-Small Molecule Blend Organic Transistors. Advanced Materials. 2009;21(10-11):1166-71.

88. Smith J, Zhang WM, Sougrat R, Zhao K, Li RP, Cha DK, et al. Solution-Processed Small Molecule-Polymer Blend Organic Thin-Film Transistors with Hole Mobility Greater than 5 cm2/Vs. Advanced Materials. 2012;24(18):2441-6.

89. Brown BA, Veres J, Anemian RM, Williams RT, Ogier SD, Leeming SW. Organic semiconducting layer formulations comprising polyacenes and organic binder polymers. Google Patents; 2005.

90. Ogier SD, Veres J, Zeidan M. Electronic short channel device comprising an organic semiconductor formulation. Google Patents; 2007.

91. Smith J, Hamilton R, Qi Y, Kahn A, Bradley DDC, Heeney M, et al. The Influence of Film Morphology in High-Mobility Small-Molecule:Polymer Blend Organic Transistors. Advanced Functional Materials. 2010;20(14):2330-7.

92. Strobl GR. The Physics of Polymers: Concepts for Understanding Their Structures and Behaviour: Springer; 1997.

93. Michels JJ. Surface-Directed Spinodal Decomposition of Solvent-Quenched Organic Transistor Blends. ChemPhysChem. 2011;12(2):342-8.

94. Cho SY, Ko JM, Lim J, Lee JY, Lee C. Inkjet-printed organic thin film transistors based on TIPS pentacene with insulating polymers. Journal of Materials Chemistry C. 2013;1(5):914-23.

95. Zhao K, Wodo O, Ren D, Khan HU, Niazi MR, Hu H, et al. Vertical Phase Separation in Small Molecule:Polymer Blend Organic Thin Film Transistors Can Be Dynamically Controlled. Advanced Functional Materials. 2016;26(11):1737-46.

96. Patrick Augustijns MB. Solvent Systems and Their Selection in Pharmaceutics and Biopharmaceutics: Springer, New York; 2007. 480 p.

97. Sunagawa I. Crystals: Growth, Morphology, & Perfection: Cambridge University Press; 2005.

98. Li XR, Smaal WTT, Kjellander C, van der Putten B, Gualandris K, Smits ECP, et al. Charge transport in high-performance ink-jet printed single-droplet organic transistors based on a silylethynyl substituted pentacene/insulating polymer blend. Organic Electronics. 2011;12(8):1319-27.

99. Madec M-B, Crouch D, Llorente GR, Whittle TJ, Geoghegan M, Yeates SG. Organic field effect transistors from ambient solution processed low molar mass semiconductor-insulator blends. Journal of Materials Chemistry. 2008;18(27):3230-6.

100. He Z, Li D, Hensley DK, Rondinone AJ, Chen J. Switching phase separation mode by varying the hydrophobicity of polymer additives in solution-processed semiconducting small-molecule/polymer blends. Applied Physics Letters. 2013;103(11).

101. Liu S, Wang WM, Briseno AL, Mannsfeld SCB, Bao Z. Controlled Deposition of Crystalline Organic Semiconductors for Field-Effect-Transistor Applications. Advanced Materials. 2009;21(12):1217-32.

102. Wo S, Headrick RL, Anthony JE. Fabrication and characterization of controllable grain boundary arrays in solution-processed small molecule organic semiconductor films. Journal of Applied Physics. 2012;111(7):073716.

103. Lee SS, Kim CS, Gomez ED, Purushothaman B, Toney MF, Wang C, et al. Controlling Nucleation and Crystallization in Solution-Processed Organic Semiconductors for Thin-Film Transistors. Advanced Materials. 2009;21(35):3605-+.

104. Tello M, Chiesa M, Duffy CM, Sirringhaus H. Charge Trapping in Intergrain Regions of Pentacene Thin Film Transistors. Advanced Functional Materials. 2008;18(24):3907-13.

105. Horowitz G, Hajlaoui ME. Grain size dependent mobility in polycrystalline organic field-effect transistors. Synthetic Metals. 2001;122(1):185-9.

106. Park B, Jeon HG, Choi J, Kim YK, Lim J, Jung J, et al. High-performance organic thin-film transistors with polymer-blended small-molecular semiconductor films, fabricated using a pre-metered coating process. Journal of Materials Chemistry. 2012;22(12):5641-6.

107. Park JH, Lim H, Cheong H, Lee KM, Sohn HC, Lee G, et al. Anisotropic mobility of small molecule-polymer blend channel in organic transistor: Characterization of channel materials and orientation. Organic Electronics. 2012;13(7):1250-4.

108. Ohe T, Kuribayashi M, Yasuda R, Tsuboi A, Nomoto K, Satori K, et al. Solution-processed organic thin-film transistors with vertical nanophase separation. Applied Physics Letters. 2008;93(5).

109. Kang J, Shin N, Jang DY, Prabhu VM, Yoon DY. Structure and properties of small molecule-polymer blend semiconductors for organic thin film transistors. J Am Chem Soc. 2008;130(37):12273-+.

110. Su Y, Liu J, Zheng L, Ding Z, Han Y. Polymer assisted solution-processing of rubrene spherulites via solvent vapor annealing. Rsc Advances. 2012;2(13):5779-88.

111. Kim JJ, Lee HM, Park JW, Cho SO. Patterning of rubrene thin-film transistors based on electron irradiation of a polystyrene dielectric layer. Journal of Materials Chemistry C. 2015;3(11):2650-5.

112. Naden AB, Loos J, MacLaren DA. Structure-function relations in diF-TES-ADT blend organic field effect transistors studied by scanning probe microscopy. Journal of Materials Chemistry C. 2014;2(2):245-55.

113. Smith J, Heeney M, McCulloch I, Malik JN, Stingelin N, Bradley DDC, et al. Percolation behaviour in high mobility p-channel polymer/small-molecule blend organic field-effect transistors. Organic Electronics. 2011;12(1):143-7.

114. Yun L, Huabin S, Yi S, Kazuhito T. Patterning technology for solution-processed organic crystal field-effect transistors. Science and Technology of Advanced Materials. 2014;15(2):024203.

115. Niazi MR, Li R, Qiang Li E, Kirmani AR, Abdelsamie M, Wang Q, et al. Solution-printed organic semiconductor blends exhibiting transport properties on par with single crystals. Nature communications. 2015;6:8598.

116. Madec MB, Butterworth S, Taboada P, Heenan R, Geoghegan M, Yeates SG. The influence of directed pi-pi interactions in solution on the thin film organic semiconductor device properties of small molecule polymer blends. Soft Matter. 2011;7(15):7065-70.

117. Niazi MR, Li R, Abdelsamie M, Zhao K, Anjum DH, Payne MM, et al. Contact-Induced Nucleation in High-Performance Bottom-Contact Organic Thin Film Transistors Manufactured by Large-Area Compatible Solution Processing. Advanced Functional Materials. 2015:n/a-n/a.

118. Hamaguchi A, Negishi T, Kimura Y, Ikeda Y, Takimiya K, Bisri SZ, et al. Single-Crystal-Like Organic Thin-Film Transistors Fabricated from Dinaphtho[2,3-b:2′,3′-f]thieno[3,2-b]thiophene (DNTT) Precursor–Polystyrene Blends. Advanced Materials. 2015:n/a-n/a.

119. Ohe T, Kuribayashi M, Tsuboi A, Satori K, Itabashi M, Nomoto K. Organic Thin-Film Transistors with Phase Separation of Polymer-Blend Small-Molecule Semiconductors: Dependence on Molecular Weight and Types of Polymer. Applied Physics Express. 2009;2(12).

120. Kwon J-H, Shin S-I, Kim K-H, Cho MJ, Kim KN, Choi DH, et al. Organic thin film transistors using 6,13-bis(tri-isopropylsilylethynyl)pentacene embedded into polymer binders. Applied Physics Letters. 2009;94(1).

121. Jo PS, Duong DT, Park J, Sinclair R, Salleo A. Control of Rubrene Polymorphs via Polymer Binders: Applications in Organic Field-Effect Transistors. Chemistry of Materials. 2015;27(11):3979-87.

122. Hunter BS, Ward JW, Payne MM, Anthony JE, Jurchescu OD, Anthopoulos TD. Low-voltage polymer/small-molecule blend organic thin-film transistors and circuits fabricated via spray deposition. Applied Physics Letters. 2015;106(22):223304.

123. Pitsalidis C, Pappa AM, Hunter S, Laskarakis A, Kaimakamis T, Payne MM, et al. High mobility transistors based on electrospray-printed small-molecule/polymer semiconducting blends. Journal of Materials Chemistry C. 2016;4(16):3499-507.

124. Jin Lee S, Kim Y-J, Young Yeo S, Lee E, Sun Lim H, Kim M, et al. Centro-Apical Self-Organization of Organic Semiconductors in a Line-Printed Organic Semiconductor: Polymer Blend for One-Step Printing Fabrication of Organic Field-Effect Transistors. Scientific Reports. 2015;5:14010.

125. Kaimakamis T, Pitsalidis C, Papamichail A, Laskarakis A, Logothetidis S. Organic transistors based on airbrushed small molecule-insulating polymer blends with mobilities exceeding 1 cm2 V-1 s-1. RSC Advances. 2016;6(99):97077-83.

126. Yuan YB, Giri G, Ayzner AL, Zoombelt AP, Mannsfeld SCB, Chen JH, et al. Ultra-high mobility transparent organic thin film transistors grown by an off-centre spin-coating method. Nature communications. 2014;5:3005.

127. Jurchescu OD, Subramanian S, Kline RJ, Hudson SD, Anthony JE, Jackson TN, et al. Organic Single-Crystal Field-Effect Transistors of a Soluble Anthradithiophene. Chemistry of Materials. 2008;20(21):6733-7.

128. Stingelin-Stutzmann N, Smits E, Wondergem H, Tanase C, Blom P, Smith P, et al. Organic thin-film electronics from vitreous solution-processed rubrene hypereutectics. Nat Mater. 2005;4(8):601-6.

129. Chen J, Shao M, Xiao K, He Z, Li D, Lokitz BS, et al. Conjugated Polymer-Mediated Polymorphism of a High Performance, Small-Molecule Organic Semiconductor with Tuned Intermolecular Interactions, Enhanced Long-Range Order, and Charge Transport. Chemistry of Materials. 2013;25(21):4378-86.

130. Hayashi Y, Kanamori H, Yamada I, Takasu A, Takagi S, Kaneko K. Facile fabrication method for p⁄n-type and ambipolar transport polyphenylenevinylene-based thin-film field-effect transistors by blending C60 fullerene. Applied Physics Letters. 2005;86(5):052104.

131. Babel A, Wind JD, Jenekhe SA. Ambipolar Charge Transport in Air-Stable Polymer Blend Thin-Film Transistors. Advanced Functional Materials. 2004;14(9):891-8.

132. Xu X, Xiao T, Gu X, Yang X, Kershaw SV, Zhao N, et al. Solution-Processed Ambipolar Organic Thin-Film Transistors by Blending p- and n-Type Semiconductors: Solid Solution versus Microphase Separation. ACS Applied Materials & Interfaces. 2015.

133. Kang M, Hwang H, Park W-T, Khim D, Yeo J-S, Kim Y, et al. Ambipolar Small-Molecule:Polymer Blend Semiconductors for Solution-Processable Organic Field-Effect Transistors. ACS Applied Materials & Interfaces. 2016.

134. Park JH, Lee KH, Mun S-j, Ko G, Heo SJ, Kim JH, et al. Self-assembly of organic channel/polymer dielectric layer in solution process for low-voltage thin-film transistors. Organic Electronics. 2010;11(10):1688-92.

135. Lee WH, Lim JA, Kwak D, Cho JH, Lee HS, Choi HH, et al. Semiconductor-Dielectric Blends: A Facile All Solution Route to Flexible All-Organic Transistors. Advanced Materials. 2009;21(42):4243-+.

136. Lee SJ, Kim YJ, Yeo SY, Lee E, Lim HS, Kim M, et al. Centro-Apical Self-Organization of Organic Semiconductors in a Line-Printed Organic Semiconductor: Polymer Blend for One-Step Printing Fabrication of Organic Field-Effect Transistors. Scientific Reports. 2015;5.

137. Chung YS, Shin N, Kang J, Jo Y, Prabhu VM, Satija SK, et al. Zone-Refinement Effect in Small Molecule−Polymer Blend Semiconductors for Organic Thin-Film Transistors. J Am Chem Soc. 2011;133(3):412-5.

138. Li Y, Liu C, Lee MV, Xu Y, Wang X, Shi Y, et al. In situ purification to eliminate the influence of impurities in solution-processed organic crystals for transistor arrays. Journal of Materials Chemistry C. 2013;1(7):1352-8.

139. Hunter S, Chen J, Anthopoulos TD. Microstructural Control of Charge Transport in Organic Blend Thin-Film Transistors. Advanced Functional Materials. 2014;24(38):5969-76.

140. Hunter S, Anthopoulos TD. Observation of Unusual, Highly Conductive Grain Boundaries in High-Mobility Phase Separated Organic Semiconducting Blend Films Probed by Lateral-Transport Conductive-AFM. Advanced Materials. 2013;25(31):4320-6.

141. Rivnay J, Jimison LH, Northrup JE, Toney MF, Noriega R, Lu S, et al. Large modulation of carrier transport by grain-boundary molecular packing and microstructure in organic thin films. Nat Mater. 2009;8(12):952-8.

142. Zhang Y, Zhou H, Seifter J, Ying L, Mikhailovsky A, Heeger AJ, et al. Molecular Doping Enhances Photoconductivity in Polymer Bulk Heterojunction Solar Cells. Advanced Materials. 2013;25(48):7038-44.

143. Salzmann I, Heimel G. Toward a comprehensive understanding of molecular doping organic semiconductors (review). Journal of Electron Spectroscopy and Related Phenomena. 2015;204, Part A:208-22.

144. Mor GK, Jones D, Le TP, Shang Z, Weathers PJ, Woltermann MKB, et al. Contact Doping with Sub-Monolayers of Strong Polyelectrolytes for Organic Photovoltaics. Advanced Energy Materials. 2014;4(13).

145. Zhou X, Pfeiffer M, Huang JS, Blochwitz J, Werner A, Leo K. Inverted OLEDs with Electrically Doped Carrier Injection and Transport Layers. MRS Online Proceedings Library Archive. 2002;725:P9.11 (4 pages).

146. Lim E, Jung B-J, Chikamatsu M, Azumi R, Yoshida Y, Yase K, et al. Doping effect of solution-processed thin-film transistors based on polyfluorene. Journal of Materials Chemistry. 2007;17(14):1416-20.

147. Abe Y, Hasegawa T, Takahashi Y, Yamada T, Tokura Y. Control of threshold voltage in pentacene thin-film transistors using carrier doping at the charge-transfer interface with organic acceptors. Applied Physics Letters. 2005;87(15):153506.

148. Mei JG, Diao Y, Appleton AL, Fang L, Bao ZN. Integrated Materials Design of Organic Semiconductors for Field-Effect Transistors. J Am Chem Soc. 2013;135(18):6724-46.

149. Anthopoulos TD. Unconventional chemical doping of organic semiconducting materials. Unconventional chemical doping of organic semiconducting materials. 2013:WO 2013098648 A1.

150. Paterson AF, Treat ND, Zhang W, Fei Z, Wyatt-Moon G, Faber H, et al. Small Molecule/Polymer Blend Organic Transistors with Hole Mobility Exceeding 13 cm2 V−1 s−1. Advanced Materials. 2016;28(35):7791-8.

151. Han Y, Barnes G, Lin Y-H, Martin J, Al-Hashimi M, AlQaradawi SY, et al. Doping of Large Ionization Potential Indenopyrazine Polymers via Lewis Acid Complexation with Tris(pentafluorophenyl)borane: A Simple Method for Improving the Performance of Organic Thin-Film Transistors. Chemistry of Materials. 2016.

152. Meerheim R, Olthof S, Hermenau M, Scholz S, Petrich A, Tessler N, et al. Investigation of C60F36 as low-volatility p-dopant in organic optoelectronic devices. Journal of Applied Physics. 2011;109(10):103102.

153. Solomeshch O, Yu YJ, Goryunkov AA, Sidorov LN, Tuktarov RF, Choi DH, et al. Ground-State Interaction and Electrical Doping of Fluorinated C60 in Conjugated Polymers. Advanced Materials. 2009;21(44):4456-60.

154. Qi Y, Sajoto T, Barlow S, Kim E-G, Brédas J-L, Marder SR, et al. Use of a High Electron-Affinity Molybdenum Dithiolene Complex to p-Dope Hole-Transport Layers. J Am Chem Soc. 2009;131(35):12530-1.

155. Ma L, Lee WH, Park YD, Kim JS, Lee HS, Cho K. High performance polythiophene thin-film transistors doped with very small amounts of an electron acceptor. Applied Physics Letters. 2008;92(6):063310.

156. Li J, Rochester CW, Jacobs IE, Friedrich S, Stroeve P, Riede M, et al. Measurement of Small Molecular Dopant F4TCNQ and C60F36 Diffusion in Organic Bilayer Architectures. ACS Applied Materials & Interfaces. 2015;7(51):28420-8.

157. Smets Y, Stark CB, Schmitt F, Edmonds MT, Lach S, Wright CA, et al. Doping efficiency and energy-level scheme in C60F48-doped zinc-tetraphenylporphyrin films. Organic Electronics. 2013;14(1):169-74.

158. Edmonds MT, Wanke M, Tadich A, Vulling HM, Rietwyk KJ, Sharp PL, et al. Surface transfer doping of hydrogen-terminated diamond by C60F48: Energy level scheme and doping efficiency. Journal of Chemical Physics. 2012;136(12):124701.

159. Mori T, Fujikawa H, Tokito S, Taga Y. Electronic structure of 8-hydroxyquinoline aluminum/LiF/Al interface for organic electroluminescent device studied by ultraviolet photoelectron spectroscopy. Applied Physics Letters. 1998;73(19):2763-5.

160. Wei P, Oh JH, Dong G, Bao Z. Use of a 1H-Benzoimidazole Derivative as an n-Type Dopant and To Enable Air-Stable Solution-Processed n-Channel Organic Thin-Film Transistors. J Am Chem Soc. 2010;132(26):8852-3.

161. Rossbauer S, Muller C, Anthopoulos TD. Comparative Study of the N-Type Doping Efficiency in Solution-processed Fullerenes and Fullerene Derivatives. Advanced Functional Materials. 2014;24(45):7116-24.

162. Khim D, Baeg K-J, Caironi M, Liu C, Xu Y, Kim D-Y, et al. Control of Ambipolar and Unipolar Transport in Organic Transistors by Selective Inkjet-Printed Chemical Doping for High Performance Complementary Circuits. Advanced Functional Materials. 2014;24(40):6252-61.

163. Méndez H, Heimel G, Opitz A, Sauer K, Barkowski P, Oehzelt M, et al. Doping of Organic Semiconductors: Impact of Dopant Strength and Electronic Coupling. Angewandte Chemie International Edition. 2013;52(30):7751-5.

164. Méndez H, Heimel G, Winkler S, Frisch J, Opitz A, Sauer K, et al. Charge-transfer crystallites as molecular electrical dopants. Nature communications. 2015;6:8560.

165. Salzmann I, Heimel G, Duhm S, Oehzelt M, Pingel P, George BM, et al. Intermolecular Hybridization Governs Molecular Electrical Doping. Physical Review Letters. 2012;108(3):035502.

166. Aziz EF, Vollmer A, Eisebitt S, Eberhardt W, Pingel P, Neher D, et al. Localized Charge Transfer in a Molecularly Doped Conducting Polymer. Advanced Materials. 2007;19(20):3257-60.

167. Zalar P, Kuik M, Henson ZB, Woellner C, Zhang Y, Sharenko A, et al. Increased Mobility Induced by Addition of a Lewis Acid to a Lewis Basic Conjugated Polymer. Advanced Materials. 2014;26(5):724-7.

168. Mendez H, Heimel G, Winkler S, Frisch J, Opitz A, Sauer K, et al. Charge-transfer crystallites as molecular electrical dopants. Nature communications. 2015;6.

169. Kim JH, Yun SW, An B-K, Han YD, Yoon S-J, Joo J, et al. Remarkable Mobility Increase and Threshold Voltage Reduction in Organic Field-Effect Transistors by Overlaying Discontinuous Nano-Patches of Charge-Transfer Doping Layer on Top of Semiconducting Film. Advanced Materials. 2013;25(5):719-24.

170. Belasco J, Mohapatra SK, Zhang Y, Barlow S, Marder SR, Kahn A. Molecular doping and tuning threshold voltage in 6,13-bis(triisopropylsilylethynyl)pentacene/polymer blend transistors. Applied Physics Letters. 2014;105(6):063301.

171. Vanoni C, Tsujino S, Jung TA. Reduction of the contact resistance by doping in pentacene few monolayers thin film transistors and self-assembled nanocrystals. Applied Physics Letters. 2007;90(19):193119.

172. Lee C-T, Chen H-C. Performance improvement mechanisms of organic thin-film transistors using MoOx-doped pentacene as channel layer. Organic Electronics. 2011;12(11):1852-7.

173. Zschieschang U, Weitz RT, Kern K, Klauk H. Bias stress effect in low-voltage organic thin-film transistors. Applied Physics A. 2009;95(1):139-45.

174. Singh S, Mohapatra YN. Trap Kinetics in Solution-Processed Organic Thin-Film Transistors. Ieee Electron Device Letters. 2016;37(1):35-8.

175. Wei P, Menke T, Naab BD, Leo K, Riede M, Bao Z. 2-(2-Methoxyphenyl)-1,3-dimethyl-1H-benzoimidazol-3-ium Iodide as a New Air-Stable n-Type Dopant for Vacuum-Processed Organic Semiconductor Thin Films. J Am Chem Soc. 2012;134(9):3999-4002.

176. Hein MP, Zakhidov AA, Lüssem B, Jankowski J, Tietze ML, Riede MK, et al. Molecular doping for control of gate bias stress in organic thin film transistors. Applied Physics Letters. 2014;104(1):013507.

177. Olthof S, Mehraeen S, Mohapatra SK, Barlow S, Coropceanu V, Brédas J-L, et al. Ultralow Doping in Organic Semiconductors: Evidence of Trap Filling. Physical Review Letters. 2012;109(17):176601.

178. Tietze ML, Burtone L, Riede M, Lüssem B, Leo K. Fermi level shift and doping efficiency in p-doped small molecule organic semiconductors: A photoelectron spectroscopy and theoretical study. Physical Review B. 2012;86(3):035320.

179. Pfeiffer M, Leo K, Zhou X, Huang JS, Hofmann M, Werner A, et al. Doped organic semiconductors: Physics and application in light emitting diodes. Organic Electronics. 2003;4(2–3):89-103.

180. Yoon S, Cho J, Lee H-K, Park S, Son HJ, Chung DS. Effects of 2,3,5,6-tetrafluoro-7,7,8,8-tetracyanoquinodimethane doping on diketopyrrolopyrrole-based, low crystalline, high mobility polymeric semiconductor. Applied Physics Letters. 2015;107(13):133302.

181. Naab BD, Himmelberger S, Diao Y, Vandewal K, Wei P, Lussem B, et al. High Mobility N-Type Transistors Based on Solution-Sheared Doped 6,13-Bis(triisopropylsilylethynyl)pentacene Thin Films. Advanced Materials. 2013;25(33):4663-7.

182. Singh S, Mohapatra SK, Sharma A, Fuentes-Hernandez C, Barlow S, Marder SR, et al. Reduction of contact resistance by selective contact doping in fullerene n-channel organic field-effect transistors. Applied Physics Letters. 2013;102(15).

183. Olabisi O, Adewale K. Handbook of Thermoplastics: Taylor & Francis; 1997.

184. Jacobs IE, Aasen EW, Oliveira JL, Fonseca TN, Roehling JD, Li J, et al. Comparison of solution-mixed and sequentially processed P3HT:F4TCNQ films: effect of doping-induced aggregation on film morphology. Journal of Materials Chemistry C. 2016;4(16):3454-66.

185. Pingel P, Schwarzl R, Neher D. Effect of molecular p-doping on hole density and mobility in poly(3-hexylthiophene). Applied Physics Letters. 2012;100(14).

186. Ha SD, Kahn A. Isolated molecular dopants in pentacene observed by scanning tunneling microscopy. Physical Review B. 2009;80(19).

187. Kleemann H, Schuenemann C, Zakhidov AA, Riede M, Luessem B, Leo K. Structural phase transition in pentacene caused by molecular doping and its effect on charge carrier mobility. Organic Electronics. 2012;13(1):58-65.

188. Pahner P, Kleemann H, Burtone L, Tietze ML, Fischer J, Leo K, et al. Pentacene Schottky diodes studied by impedance spectroscopy: Doping properties and trap response. Physical Review B. 2013;88(19):195205.

189. Blochwitz J, Fritz T, Pfeiffer M, Leo K, Alloway DM, Lee PA, et al. Interface electronic structure of organic semiconductors with controlled doping levels. Organic Electronics. 2001;2(2):97-104.

190. Olthof S, Tress W, Meerheim R, Lüssem B, Leo K. Photoelectron spectroscopy study of systematically varied doping concentrations in an organic semiconductor layer using a molecular p-dopant. Journal of Applied Physics. 2009;106(10):103711.

191. Tiwari SP, Potscavage WJ, Jr., Sajoto T, Barlow S, Marder SR, Kippelen B. Pentacene organic field-effect transistors with doped electrode-semiconductor contacts. Organic Electronics. 2010;11(5):860-3.

192. Fan CL, Lin WC, Chang HS, Lin YZ, Huang BR. Effects of the F4TCNQ-doped pentacene interlayers on performance improvement of top-contact pentacene-based organic thin-film transistors. Materials. 2016;9(1).

193. Minari T, Darmawan P, Liu C, Li Y, Xu Y, Tsukagoshi K. Highly enhanced charge injection in thienoacene-based organic field-effect transistors with chemically doped contact. Applied Physics Letters. 2012;100(9).

194. Li J, Zhang X-W, Zhang L, Khizar ul H, Jiang X-Y, Zhu W-Q, et al. Improving organic transistor performance through contact-area-limited doping. Solid State Communications. 2009;149(41-42):1826-30.

195. Ante F, Kaelblein D, Zschieschang U, Canzler TW, Werner A, Takimiya K, et al. Contact Doping and Ultrathin Gate Dielectrics for Nanoscale Organic Thin-Film Transistors. Small. 2011;7(9):1186-91.

196. Heimel G, Romaner L, Zojer E, Bredas J-L. The Interface Energetics of Self-Assembled Monolayers on Metals. Accounts of Chemical Research. 2008;41(6):721-9.

197. Hong JP, Park AY, Lee S, Kang J, Shin N, Yoon DY. Tuning of Ag work functions by self-assembled monolayers of aromatic thiols for an efficient hole injection for solution processed triisopropylsilylethynyl pentacene organic thin film transistors. Applied Physics Letters. 2008;92(14):2008-10.

198. Kobayashi S, Nishikawa T, Takenobu T, Mori S, Shimoda T, Mitani T, et al. Control of carrier density by self-assembled monolayers in organic field-effect transistors. Nat Mater. 2004;3(5):317-22.

199. Chu C-W, Li S-H, Chen C-W, Shrotriya V, Yang Y. High-performance organic thin-film transistors with metal oxide/metal bilayer electrode. Applied Physics Letters. 2005;87(19):193508.

200. Kano M, Minari T, Tsukagoshi K. Improvement of subthreshold current transport by contact interface modification in p-type organic field-effect transistors. Applied Physics Letters. 2009;94(14):143304.

201. Soeda J, Hirose Y, Yamagishi M, Nakao A, Uemura T, Nakayama K, et al. Solution-Crystallized Organic Field-Effect Transistors with Charge-Acceptor Layers: High-Mobility and Low-Threshold-Voltage Operation in Air. Advanced Materials. 2011;23(29):3309-14.

202. Hählen T, Vanoni C, Wäckerlin C, Jung TA, Tsujino S. Surface doping in pentacene thin-film transistors with few monolayer thick channels. Applied Physics Letters. 2012;101(3):033305.

203. Maddalena F, Meijer EJ, Asadi K, de Leeuw DM, Blom PWM. Doping kinetics of organic semiconductors investigated by field-effect transistors. Applied Physics Letters. 2010;97(4).

204. Pacher P, Lex A, Proschek V, Etschmaier H, Tchernychova E, Sezen M, et al. Chemical Control of Local Doping in Organic Thin-Film Transistors: From Depletion to Enhancement. Advanced Materials. 2008;20(16):3143-8.

205. Das A, Dost R, Richardson TH, Grell M, Wedge DC, Kell DB, et al. Low cost, portable, fast multiparameter data acquisition system for organic transistor odour sensors. Sensors and Actuators B: Chemical. 2009;137(2):586-91.

206. Toccoli T, Pallaoro A, Tonezzer M, Coppedè N, Iannotta S. OFET for gas sensing based on SuMBE grown pentacene films. Solid-State Electronics. 2008;52(3):417-21.

207. Song X, Wang L, Fan Q, Wu Y, Wang H, Liu C, et al. Role of oxygen incorporation in electronic properties of rubrene films. Applied Physics Letters. 2010;97(3).

208. So W-y, Wikberg JM, Lang DV, Mitrofanov O, Kloc CL, Siegrist T, et al. Mobility-independent doping in crystalline rubrene field-effect transistors. Solid State Communications. 2007;142(9):483-6.

209. Nishi T, Kanai K, Ouchi Y, Willis MR, Seki K. Oxygen effects on the interfacial electronic structure of titanyl phthalocyanine film: p-type doping, band bending and Fermi level alignment. Chemical Physics. 2006;325(1):121-8.

210. Maliakal AJ, Chen JYC, So W-Y, Jockusch S, Kim B, Ottaviani MF, et al. Mechanism for Oxygen-Enhanced Photoconductivity in Rubrene: Electron Transfer Doping. Chemistry of Materials. 2009;21(22):5519-26.

211. Lu C-K, Meng H-F. Hole doping by molecular oxygen in organic semiconductors: Band-structure calculations. Physical Review B. 2007;75(23).

212. Liao H-H, Yang C-M, Liu C-C, Horng S-F, Meng H-F, Shy J-T. Dynamics and reversibility of oxygen doping and de-doping for conjugated polymer. Journal of Applied Physics. 2008;103(10).

213. Zhao W, Qi Y, Sajoto T, Barlow S, Marder SR, Kahn A. Remote doping of a pentacene transistor: Control of charge transfer by molecular-level engineering. Applied Physics Letters. 2010;97(12).

214. Kobayashi H, Kobayashi N, Hosoi S, Koshitani N, Murakami D, Shirasawa R, et al. Hopping and band mobilities of pentacene, rubrene, and 2,7-dioctyl[1]benzothieno[3,2-b][1]benzothiophene (C8-BTBT) from first principle calculations. The Journal of Chemical Physics. 2013;139(1):014707.

215. Soeda J, Hirose Y, Yamagishi M, Nakao A, Uemura T, Nakayama K, et al. Solution-Crystallized Organic Field-Effect Transistors with Charge-Acceptor Layers: High-Mobility and Low-Threshold-Voltage Operation in Air. Advanced Materials. 2011;23(29):3309-+.

216. Ling MM, Bao Z. Thin Film Deposition, Patterning, and Printing in Organic Thin Film Transistors. Chemistry of Materials. 2004;16(23):4824-40.

217. Baikie ID, Grain AC, Sutherland J, Law J. Dual Mode Kelvin Probe: Featuring Ambient Pressure Photoemission Spectroscopy and Contact Potential Difference. Energy Procedia. 2014;60:48-56.

218. Flewitt PEJ, Wild RK. Physical Methods for Materials Characterisation, Second Edition: CRC Press; 2015.

219. Izawa T, Miyazaki E, Takimiya K. Molecular ordering of high-performance soluble molecular semiconductors and re-evaluation of their field-effect transistor characteristics. Advanced Materials. 2008;20(18):3388-92.

220. Bronstein H, Leem DS, Hamilton R, Woebkenberg P, King S, Zhang WM, et al. Indacenodithiophene-co-benzothiadiazole Copolymers for High Performance Solar Cells or Transistors via Alkyl Chain Optimization. Macromolecules. 2011;44(17):6649-52.

221. McCulloch I, Ashraf RS, Biniek L, Bronstein H, Combe C, Donaghey JE, et al. Design of Semiconducting Indacenodithiophene Polymers for High Performance Transistors and Solar Cells. Accounts of Chemical Research. 2012;45(5):714-22.

222. Zhang X, Bronstein H, Kronemeijer AJ, Smith J, Kim Y, Kline RJ, et al. Molecular origin of high field-effect mobility in an indacenodithiophene-benzothiadiazole copolymer. Nature communications. 2013;4:2238.

223. Klauk H. Organic Electronics: Materials, Manufacturing, and Applications: Wiley; 2006.

224. Tessler N, Solomeshch O. Derivatized fullerene-based dopants for organic semiconductors. Derivatized fullerene-based dopants for organic semiconductors. 2013:US 8431434 B2.

225. Gakh AA, Tuinman AA, Adcock JL, Sachleben RA, Compton RN. SELECTIVE SYNTHESIS AND STRUCTURE DETERMINATION OF C60F48. J Am Chem Soc. 1994;116(2):819-20.

226. Bulusheva LG, Okotrub AV, Boltalina OV. Electronic Structure of the Fluorinated Fullerene C60F48. The Journal of Physical Chemistry A. 1999;103(48):9921-4.

227. Tadich A, Edmonds MT, Ley L, Fromm F, Smets Y, Mazej Z, et al. Tuning the charge carriers in epitaxial graphene on SiC(0001) from electron to hole via molecular doping with C60F48. Applied Physics Letters. 2013;102(24):241601.

228. Rietwyk KJ, Wanke M, Vulling HM, Edmonds MT, Sharp PL, Smets Y, et al. Fluorination of the diamond surface by photoinduced dissociation of C60F48. Physical Review B. 2011;84(3):035404.

229. Myerson AS. Handbook of Industrial Crystallization: Second Edition. Second Edition ed: Butterworth-Heinemann, Boston; 2001. 332 p.

230. Sangwal K. Additives and Crystallization Processes: From Fundamentals to Applications: Wiley & Sons, New Jersey; 2007. 468 p.

231. Byrappa K, Ohachi T. Crystal Growth Technology: Springer, New York; 2003. 590 p.

232. Kullaiah Byrappa TO. Crystal Growth Technology: Springer-Verlag Berlin Heidelberg; 2003. 590 p.

233. Lada M, Starink MJ, Carrasco M, Chen L, Miskiewicz P, Brookes P, et al. Morphology control via dual solvent crystallization for high-mobility functionalized pentacene-blend thin film transistors. Journal of Materials Chemistry. 2011;21(30):11232-8.

234. Chang JJ, Chi CY, Zhang J, Wu JS. Controlled Growth of Large-Area High-Performance Small-Molecule Organic Single-Crystalline Transistors by Slot-Die Coating Using A Mixed Solvent System. Advanced Materials. 2013;25(44):6442-7.

235. Li X, Kjellander BKC, Anthony JE, Bastiaansen CWM, Broer DJ, Gelinck GH. Azeotropic Binary Solvent Mixtures for Preparation of Organic Single Crystals. Advanced Functional Materials. 2009;19(22):3610-7.

236. Han S, Yu X, Shi W, Zhuang X, Yu J. Solvent-dependent electrical properties improvement of organic field-effect transistor based on disordered conjugated polymer/insulator blends. Organic Electronics. 2015;27:160-6.

237. Chang JF, Sun BQ, Breiby DW, Nielsen MM, Solling TI, Giles M, et al. Enhanced mobility of poly(3-hexylthiophene) transistors by spin-coating from high-boiling-point solvents. Chemistry of Materials. 2004;16(23):4772-6.

238. Dohr M, Werzer O, Shen Q, Salzmann I, Teichert C, Ruzie C, et al. Dynamics of Monolayer-Island Transitions in 2,7-Dioctyl-benzothienobenzthiophene Thin Films. Chemphyschem. 2013;14(11):2554-9.

239. Wan J, Li Y, Ulbrandt JG, Smilgies D-M, Hollin J, Whalley AC, et al. Transient phases during fast crystallization of organic thin films from solution. APL Mater. 2016;4(1):016103.

240. Alberga D, Mangiatordi GF, Torsi L, Lattanzi G. Effects of Annealing and Residual Solvents on Amorphous P3HT and PBTTT Films. The Journal of Physical Chemistry C. 2014;118(16):8641-55.

241. Tsutsumi Jy, Matsuoka S, Inoue S, Minemawari H, Yamada T, Hasegawa T. N-type field-effect transistors based on layered crystalline donor-acceptor semiconductors with dialkylated benzothienobenzothiophenes as electron donors. Journal of Materials Chemistry C. 2015;3(9):1976-81.

242. Tsao HN, Cho DM, Park I, Hansen MR, Mavrinskiy A, Yoon DY, et al. Ultrahigh Mobility in Polymer Field-Effect Transistors by Design. J Am Chem Soc. 2011;133(8):2605-12.

243. Mei J, Kim DH, Ayzner AL, Toney MF, Bao Z. Siloxane-Terminated Solubilizing Side Chains: Bringing Conjugated Polymer Backbones Closer and Boosting Hole Mobilities in Thin-Film Transistors. J Am Chem Soc. 2011;133(50):20130-3.

244. Kang I, Yun HJ, Chung DS, Kwon SK, Kim YH. Record High Hole Mobility in Polymer Semiconductors via Side-Chain Engineering. J Am Chem Soc. 2013;135(40):14896-9.

245. Zhang W, Han Y, Zhu X, Fei Z, Feng Y, Treat ND, et al. A Novel Alkylated Indacenodithieno[3,2-b]thiophene-Based Polymer for High-Performance Field-Effect Transistors. Advanced Materials. 2015:n/a-n/a.

246. Chang J, Chi C, Zhang J, Wu J. Controlled Growth of Large-Area High-Performance Small-Molecule Organic Single-Crystalline Transistors by Slot-Die Coating Using A Mixed Solvent System. Advanced Materials. 2013;25(44):6442-7.

247. Giri G, Verploegen E, Mannsfeld SCB, Atahan-Evrenk S, Kim DH, Lee SY, et al. Tuning charge transport in solution-sheared organic semiconductors using lattice strain. Nature. 2011;480(7378):504-U124.

248. Luo C, Kyaw AKK, Perez LA, Patel S, Wang M, Grimm B, et al. General Strategy for Self-Assembly of Highly Oriented Nanocrystalline Semiconducting Polymers with High Mobility. Nano Lett. 2014;14(5):2764-71.

249. Sirringhaus H, Wilson RJ, Friend RH, Inbasekaran M, Wu W, Woo EP, et al. Mobility enhancement in conjugated polymer field-effect transistors through chain alignment in a liquid-crystalline phase. Applied Physics Letters. 2000;77(3):406-8.

250. Funahashi M, Sonoda A. High electron mobility in a columnar phase of liquid-crystalline perylene tetracarboxylic bisimide bearing oligosiloxane chains. Journal of Materials Chemistry. 2012;22(48):25190-7.

251. Hu H, Zhao K, Fernandes N, Boufflet P, Bannock JH, Yu L, et al. Entanglements in marginal solutions: a means of tuning pre-aggregation of conjugated polymers with positive implications for charge transport. Journal of Materials Chemistry C. 2015;3(28):7394-404.

252. Zhao K, Khan HU, Li R, Hu H, Amassian A. Carrier Transport Enhancement in Conjugated Polymers through Interfacial Self-Assembly of Solution-State Aggregates. ACS Applied Materials & Interfaces. 2016;8(30):19649-57.

253. Kleinhenz N, Persson N, Xue Z, Chu PH, Wang G, Yuan Z, et al. Ordering of Poly(3-hexylthiophene) in Solutions and Films: Effects of Fiber Length and Grain Boundaries on Anisotropy and Mobility. Chemistry of Materials. 2016;28(11):3905-13.

254. Noriega R, Rivnay J, Vandewal K, Koch FPV, Stingelin N, Smith P, et al. A general relationship between disorder, aggregation and charge transport in conjugated polymers. Nat Mater. 2013;12(11):1038-44.

255. Paterson AF, Treat ND, Zhang W, Fei Z, Wyatt-Moon G, Faber H, et al. Small Molecule/Polymer Blend Organic Transistors with Hole Mobility Exceeding 13 cm V^{-1} s^{-1}. Advanced Materials. 2016:n/a-n/a.

256. Hardigree JFM, Katz HE. Through Thick and Thin: Tuning the Threshold Voltage in Organic Field-Effect Transistors. Accounts of Chemical Research. 2014;47(4):1369-77.

257. Kang B, Choi HH, Cho K. 65.2: Invited Paper: Bias-Stress-Induced Charge Trapping in Flexible Polymer Gate Dielectrics in Organic TFTs. SID Symposium Digest of Technical Papers. 2015;46(1):966-8.

258. Lee WH, Choi HH, Kim DH, Cho K. 25th Anniversary Article: Microstructure Dependent Bias Stability of Organic Transistors. Advanced Materials. 2014;26(11):1660-80.

259. Mathijssen SGJ, Colle M, Gomes H, Smits ECP, de BB, McCulloch I, et al. Dynamics of threshold voltage shifts in organic and amorphous silicon field-effect transistors. ADVANCED MATERIALS. 2007;19:2785-.

260. Pernstich K, Haas S, Oberhoff D, Goldmann C, Gundlach D, Batlogg B, et al. Threshold voltage shift in organic field effect transistors by dipole monolayers on the gate insulator. Journal of Applied Physics. 2004;96(11):6431-8.

261. Hosseini AR, Wong MH, Shen YL, Malliaras GG. Charge injection in doped organic semiconductors. Journal of Applied Physics. 2005;97(2).

262. Miyadera T, Minari T, Tsukagoshi K, Ito H, Aoyagi Y. Frequency response analysis of pentacene thin-film transistors with low impedance contact by interface molecular doping. Applied Physics Letters. 2007;91(1):013512.

263. Sun X, Di C-a, Liu Y. Engineering of the dielectric–semiconductor interface in organic field-effect transistors. Journal of Materials Chemistry. 2010;20(13):2599-.

264. Park JH, Lee YT, Lee HS, Lee JY, Lee K, Lee GB, et al. Origin of Bias-Stress Induced Instability in Organic Thin-Film Transistors with Semiconducting Small-Molecule/Insulating Polymer Blend Channel. ACS Applied Materials & Interfaces. 2013;5(5):1625-9.

265. Hwang DK, Fuentes-Hernandez C, Kim J, Potscavage WJ, Kim S-J, Kippelen B. Top-Gate Organic Field-Effect Transistors with High Environmental and Operational Stability. Advanced Materials. 2011;23(10):1293-8.

266. Hwang DK, Fuentes-Hernandez C, Kim JB, Potscavage Jr WJ, Kippelen B. Flexible and stable solution-processed organic field-effect transistors. Organic Electronics. 2011;12(7):1108-13.

267. Kim Y-H, Anthony JE, Park SK. Polymer blended small molecule organic field effect transistors with improved device-to-device uniformity and operational stability. Organic Electronics. 2012;13(7):1152-7.

268. Ford MJ, Wang M, Phan H, Nguyen TQ, Bazan GC. Fullerene Additives Convert Ambipolar Transport to p-Type Transport while Improving the Operational Stability of Organic Thin Film Transistors. Advanced Functional Materials. 2016;26(25):4472-80.

269. Ryu KK, Nausieda I, He DD, Akinwande AI, Bulovic V, Sodini CG. Bias-Stress Effect in Pentacene Organic Thin-Film Transistors. IEEE Transactions on Electron Devices. 2010;57(5):1003-8.

270. Wang SD, Minari T, Miyadera T, Aoyagi Y, Tsukagoshi K. Bias stress instability in pentacene thin film transistors: Contact resistance change and channel threshold voltage shift. Applied Physics Letters. 2008;92(6).

271. Ahmed R, Simbrunner C, Schwabegger G, Baig MA, Sitter H. The role of metal contacts in the stability of n-type organic field effect transistors. Applied Physics a-Materials Science & Processing. 2014;117(4):2235-40.

272. Yan Y, She XJ, Zhu H, Wang SD. Origin of bias stress induced instability of contact resistance in organic thin film transistors. Organic Electronics. 2011;12(5):823-6.

273. Sinno H, Fabiano S, Crispin X, Berggren M, Engquist I. Bias stress effect in polyelectrolyte-gated organic field-effect transistors. Applied Physics Letters. 2013;102(11):113306.

274. Scott JC. Metal–organic interface and charge injection in organic electronic devices. Journal of Vacuum Science & Technology A. 2003;21(3):521-31.

275. Kahn A, Koch N, Gao W. Electronic structure and electrical properties of interfaces between metals and π-conjugated molecular films. Journal of Polymer Science Part B: Polymer Physics. 2003;41(21):2529-48.

276. Meijer E, Gelinck G, Van Veenendaal E, Huisman B-H, De Leeuw D, Klapwijk T. Scaling behavior and parasitic series resistance in disordered organic field-effect transistors. Applied physics letters. 2003;82(25):4576-8.

277. Vinciguerra V, La Rosa M, Nicolosi D, Sicurella G, Occhipinti L. Modeling the gate bias dependence of contact resistance in staggered polycrystalline organic thin film transistors. Organic electronics. 2009;10(6):1074-81.

278. Li F, Nathan A, Wu Y, Ong BS. Organic Thin Film Transistor Integration: A Hybrid Approach: Wiley; 2011.

279. Schmid G, Waser R. Nanotechnology: Volume 4: Information Technology II: Wiley; 2008.

280. Diao Y, Tee BCK, Giri G, Xu J, Kim DH, Becerril HA, et al. Solution coating of large-area organic semiconductor thin films with aligned single-crystalline domains. Nat Mater. 2013;12(7):665-71.

281. Yang HC, Shin TJ, Yang L, Cho K, Ryu CY, Bao ZN. Effect of mesoscale crystalline structure on the field-effect mobility of regioregular poly(3-hexyl thiophene) in thin-film transistors. Advanced Functional Materials. 2005;15(4):671-6.

282. Tseng H-R, Ying L, Hsu BBY, Perez LA, Takacs CJ, Bazan GC, et al. High Mobility Field Effect Transistors Based on Macroscopically Oriented Regioregular Copolymers. Nano Lett. 2012;12(12):6353-7.

283. Jurchescu OD, Baas J, Palstra TTM. Effect of impurities on the mobility of single crystal pentacene. Applied Physics Letters. 2004;84(16):3061-3.

284. Jimison LH, Toney MF, McCulloch I, Heeney M, Salleo A. Charge-Transport Anisotropy Due to Grain Boundaries in Directionally Crystallized Thin Films of Regioregular Poly(3-hexylthiophene). Advanced Materials. 2009;21(16):1568-+.

285. Gbabode G, Dohr M, Niebel C, Balandier J-Y, Ruzié C, Négrier P, et al. X-ray Structural Investigation of Nonsymmetrically and Symmetrically Alkylated [1]Benzothieno[3,2-b]benzothiophene Derivatives in Bulk and Thin Films. ACS Applied Materials & Interfaces. 2014;6(16):13413-21.

286. Kilby JS. Invention of the integrated circuit. IEEE Transactions on Electron Devices. 1976;23(7):648-54.

287. Kang SM, Leblebici Y. Cmos Digital Integrated Circuits: Tata McGraw-Hill; 2003.

288. Rabaey JM, Chandrakasan AP, Nikolić B. Digital Integrated Circuits, 2/e: Pearson Education; 2003.

289. Gelinck G, Heremans P, Nomoto K, Anthopoulos TD. Organic Transistors in Optical Displays and Microelectronic Applications. Advanced Materials. 2010;22(34):3778-98.

290. Petti L, Münzenrieder N, Vogt C, Faber H, Büthe L, Cantarella G, et al. Metal oxide semiconductor thin-film transistors for flexible electronics. Applied Physics Reviews. 2016;3(2):021303.

291. Labram JG, Lin Y-H, Anthopoulos TD. Exploring Two-Dimensional Transport Phenomena in Metal Oxide Heterointerfaces for Next-Generation, High-Performance, Thin-Film Transistor Technologies. Small. 2015(41).

292. Lin Y-H, Faber H, Labram JG, Stratakis E, Sygellou L, Kymakis E, et al. High Electron Mobility Thin-Film Transistors Based on Solution-Processed Semiconducting Metal Oxide Heterojunctions and Quasi-Superlattices. Advanced Science. 2015;2(7):1500058-n/a.

293. Smith J, Bashir A, Adamopoulos G, Anthony JE, Bradley DDC, Hamilton R, et al. Air-stable solution-processed hybrid transistors with hole and electron mobilities exceeding 2 cm2v-1 s-1. Advanced Materials. 2010;22(32):3598-602.

294. Oh MS, Hwang DK, Lee K, Choi WJ, Kim JH, Im S, et al. Pentacene and ZnO hybrid channels for complementary thin-film transistor inverters operating at 2V. Journal of Applied Physics. 2007;102(7):076104.

295. Kim JB, Fuentes-Hernandez C, Kim SJ, Choi S, Kippelen B. Flexible hybrid complementary inverters with high gain and balanced noise margins using pentacene and amorphous InGaZnO thin-film transistors. Organic Electronics. 2010;11(6):1074-8.

296. Na JH, Kitamura M, Arakawa Y. Organic/inorganic hybrid complementary circuits based on pentacene and amorphous indium gallium zinc oxide transistors. Applied Physics Letters. 2008;93(21):213505.

297. Fortunato E, Barquinha P, Martins R. Oxide Semiconductor Thin-Film Transistors: A Review of Recent Advances. Advanced Materials. 2012;24(22):2945-86.

298. Li YV, Mourey DA, Loth MA, Zhao DA, Anthony JE, Jackson TN. Hybrid Inorganic/organic complementary circuits using PEALD ZnO and ink-jet printed diF-TESADT TFTs. Organic Electronics. 2013;14(10):2411-7.

299. Kim JB, Fuentes-Hernandez C, Hwang DK, Potscavage Jr WJ, Cheun H, Kippelen B. Vertically stacked hybrid organic–inorganic complementary inverters with low operating voltage on flexible substrates. Organic Electronics. 2011;12(1):45-50.

300. Myny K, Smout S, Rockelé M, Bhoolokam A, Ke TH, Steudel S, et al. A thin-film microprocessor with inkjet print-programmable memory. Scientific Reports. 2014;4:7398.

301. Rockelé M, Pham D-V, Hoppe A, Steiger J, Botnaras S, Nag M, et al. Low-temperature and scalable complementary thin-film technology based on solution-processed metal oxide n-TFTs and pentacene p-TFTs. Organic Electronics. 2011;12(11):1909-13.

302. Guo X, Feng L, Cui Q, Xu X. Low Voltage Organic/Inorganic Hybrid Complementary Inverter With Low Temperature All Solution Processed Semiconductor and Dielectric Layers. IEEE Electron Device Letters. 2014;35(5):542-4.

303. Pecunia V, Banger K, Sou A, Sirringhaus H. Solution-based self-aligned hybrid organic/metal-oxide complementary logic with megahertz operation. Organic Electronics. 2015;21:177-83.

304. Ozgur U, Hofstetter D, Morkoc H. ZnO Devices and Applications: A Review of Current Status and Future Prospects. Proceedings of the IEEE. 2010;98(7):1255-68.

305. Lin Y-H, Faber H, Zhao K, Wang Q, Amassian A, McLachlan M, et al. High-Performance ZnO Transistors Processed Via an Aqueous Carbon-Free Metal Oxide Precursor Route at Temperatures Between 80–180 °C. Advanced Materials. 2013;25(31):4340-6.

306. Kim M-G, Kanatzidis MG, Facchetti A, Marks TJ. Low-temperature fabrication of high-performance metal oxide thin-film electronics via combustion processing. Nat Mater. 2011;10(5):382-8.

307. Faber H, Lin Y-H, Thomas SR, Zhao K, Pliatsikas N, McLachlan MA, et al. Indium Oxide Thin-Film Transistors Processed at Low Temperature via Ultrasonic Spray Pyrolysis. ACS Applied Materials & Interfaces. 2015;7(1):782-90.

308. Lin Y-H, Thomas SR, Faber H, Li R, McLachlan MA, Patsalas PA, et al. Al-Doped ZnO Transistors Processed from Solution at 120 °C. Advanced Electronic Materials. 2016;2(6):1600070-n/a.

309. Hwan Hwang Y, Seo J-S, Moon Yun J, Park H, Yang S, Ko Park S-H, et al. An /`aqueous route/' for the fabrication of low-temperature-processable oxide flexible transparent thin-film transistors on plastic substrates. NPG Asia Mater. 2013;5:e45.

Appendix A

List of publications

Journal articles

A. F. Paterson, N. D. Treat, W. Zhang, Z. Fei, G. Wyatt-Moon, H.Faber, G. Vourlias, P. A. Patsalas, O. Solomeshch, N. Tessler, M. Heeney, T. D. Anthopoulos, "Small Molecule/Polymer Blend Organic Transistors with Hole Mobility Exceeding 13 cm2/Vs", Advanced Materials, DOI: 10.1002/adma.201601075, (2016)

I. Isakov§, **A. F. Paterson**§, O, Solomeshch, N. Tessler, Qiang Zhang, Jun Li, Xixiang Zhang, Zhuping Fei, Martin Heeney and Thomas D. Anthopoulos, "Hybrid complementary circuits based on p-channel organic and n-channel metal oxide transistors with balanced carrier mobilities of up to 10 cm^2/Vs", Applied Physics Letters, DOI: 10.1063/1.4972988, (2016)

§ These authors contributed equally.

A. F. Paterson, Y.-H. Lin, A. D. Mottram, O. Solomeshch, N. Tessler, Z. Fei, M. Heeney, M. R. Niazi, A. Amassian, T. D. Anthopoulos, "The Role of Molecular Doping in 3rd Generation Small-Molecule/Polymer Organic Blend Systems for Organic Transistors". To be submitted.

J. Panidi, **A. F. Paterson**, Z. Fei, Y. Han, G. Vourlias, P. A. Patsalas, M. Heeney, T. D. Anthopoulos, "Remarkable Enhancement of Hole Mobility in Several *p*-type Small-Molecule/Polymer Blend-Based Organic Transistors via Simple Addition of the Lewis Acid $B(C_6F_5)_3$". Submitted.

Prizes and Awards

A. F. Paterson, N. D. Treat, W. Zhang, Z. Fei, G. Wyatt-Moon, H.Faber, G. Vourlias, P. A. Patsalas, O. Solomeshch, N. Tessler, M. Heeney, T. D. Anthopoulos, "Organic Small-Molecule / Polymer Blend Transistors with Hole Mobility Values of 13 cm^2/Vs Enabled via Moderate Molecular *p*-Doping", Centre for Plastic Electronics Annual Symposium 2016, Prize for Best Poster – 1st Prize

Appendix B

Effect of solvent blending on 3rd generation blend microstructure

As part of the development of the 3rd generation blend, the blend materials (C_8-BTBT:C_{16}IDT-BT:$C_{60}F_{48}$) were investigated in a range of solvents. The solvents were tested individually, as well as combined to produce solvent blends. The following table summarises a range of polarised optical microscope images for the *p*-doped C_8-BTBT:C_{16}IDT-BT:$C_{60}F_{48}$ blend in representative individual solvents and representative solvent blends. Two post-deposition annealing techniques were used to investigate the microstructures, demonstrating the range of morphologies that this blend system offers.

Solvents	**Blend temperature treatment**	
	120°C anneal, then quenched to room temperature	**120°C anneal, then cooled slowly to room temperature**
Anisole 50% CB 50%	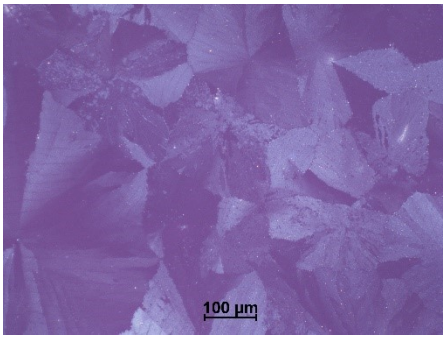	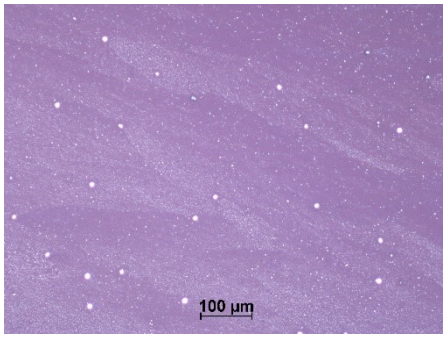
Anisole 50% THF 50%	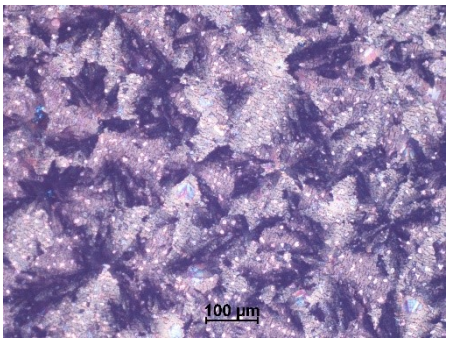	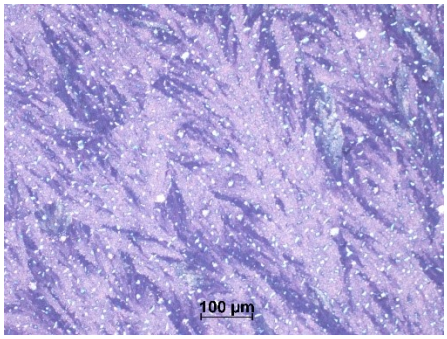

Anisole	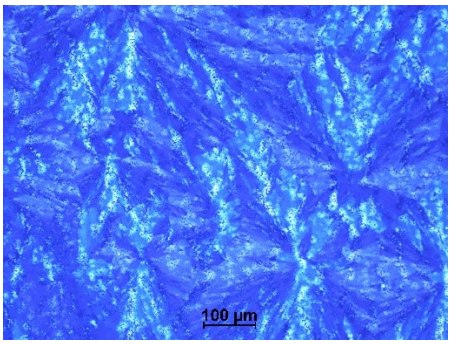	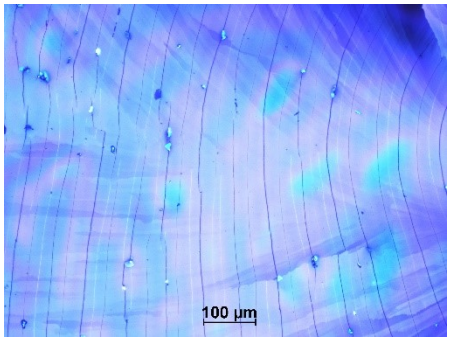
THF	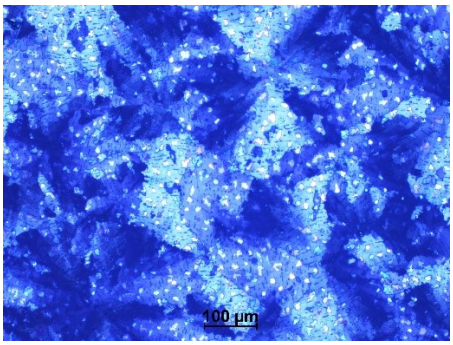	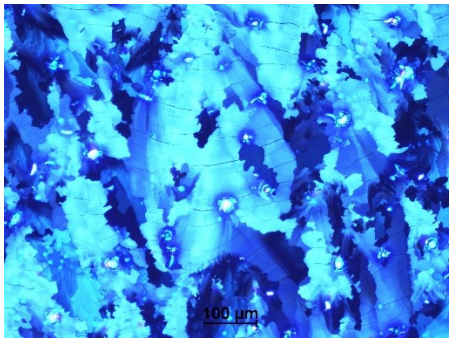
Tetralin 40% THF 60%	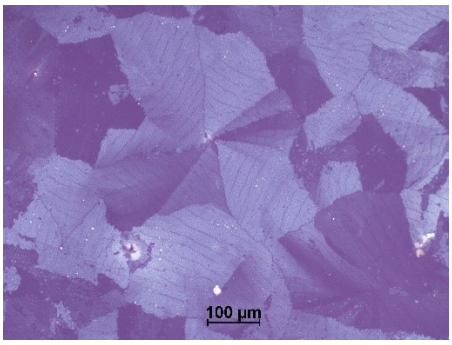	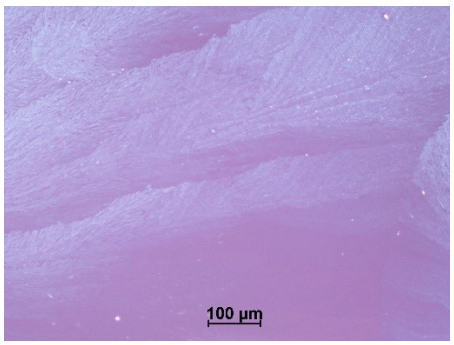
Tetralin 75% CB 25%	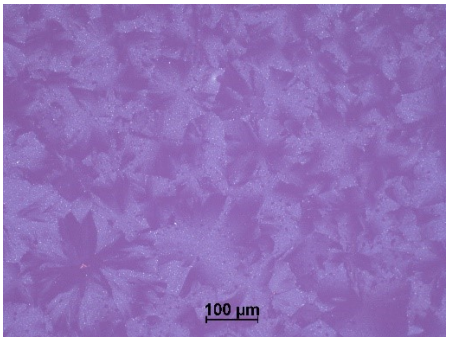	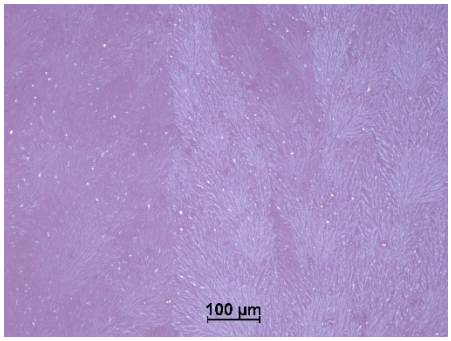

Tetralin 25% CB 75%	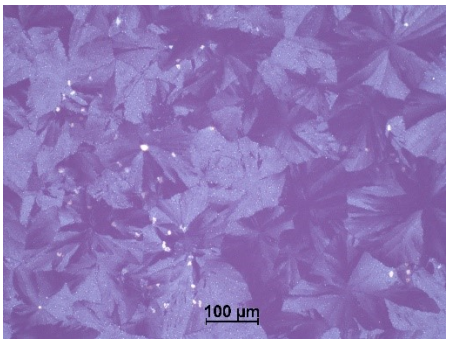	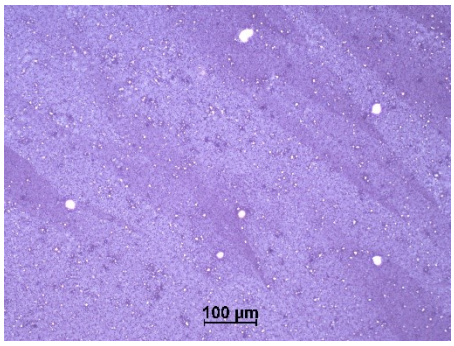
Tetralin 50% THF 50%	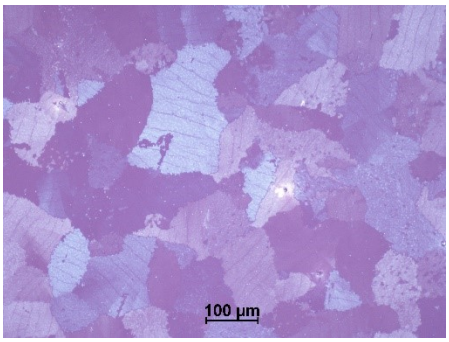	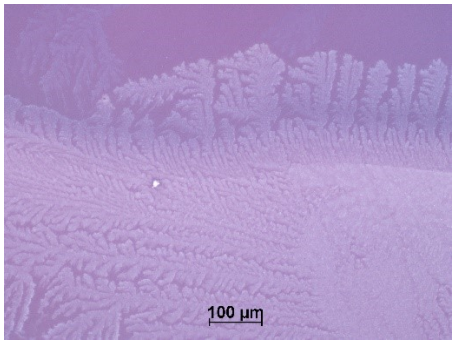
Tetralin 25% THF 75%	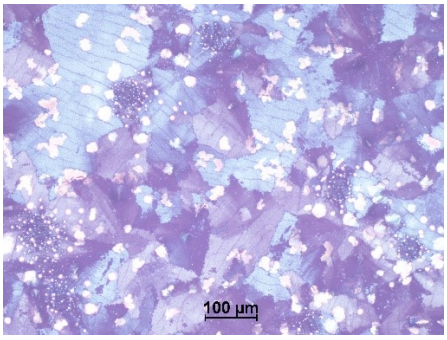	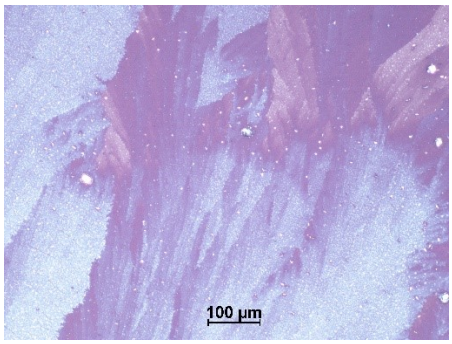

Appendix C

Content reuse permission licenses

JOHN WILEY AND SONS LICENSE
TERMS AND CONDITIONS

Jan 01, 2017

This Agreement between Alexandra Paterson ("You") and John Wiley and Sons ("John Wiley and Sons") consists of your license details and the terms and conditions provided by John Wiley and Sons and Copyright Clearance Center.

License Number	4020100399370
License date	Jan 01, 2017
Licensed Content Publisher	John Wiley and Sons
Licensed Content Publication	Advanced Materials
Licensed Content Title	Small Molecule/Polymer Blend Organic Transistors with Hole Mobility Exceeding 13 cm2 V−1 s−1
Licensed Content Author	Alexandra F. Paterson,Neil D. Treat,Weimin Zhang,Zhuping Fei,Gwenhivir Wyatt-Moon,Hendrik Faber,George Vourlias,Panos A. Patsalas,Olga Solomeshch,Nir Tessler,Martin Heeney,Thomas D. Anthopoulos
Licensed Content Date	Jul 4, 2016
Licensed Content Pages	8
Type of use	Dissertation/Thesis
Requestor type	Author of this Wiley article
License Number	4020100399370
License date	Jan 01, 2017
Licensed Content Publisher	John Wiley and Sons

JOHN WILEY AND SONS LICENSE
TERMS AND CONDITIONS

Dec 31, 2016

This Agreement between Alexandra Paterson ("You") and John Wiley and Sons ("John Wiley and

Sons") consists of your license details and the terms and conditions provided by John Wiley and Sons and Copyright Clearance Center.

License Number	4012500610208
License date	Dec 19, 2016
Licensed Content Publisher	John Wiley and Sons
Licensed Content Publication	Advanced Materials
Licensed Content Title	Charge Transport in Disordered Organic Materials and Its Relevance to Thin-Film Devices: A Tutorial Review
Licensed Content Author	Nir Tessler,Yevgeni Preezant,Noam Rappaport,Yohai Roichman
Licensed Content Date	May 7, 2009
Licensed Content Pages	21
Type of use	Dissertation/Thesis
Requestor type	University/Academic
Format	Print and electronic
Portion	Figure/table

JOHN WILEY AND SONS LICENSE
TERMS AND CONDITIONS

Dec 31, 2016

This Agreement between Alexandra Paterson ("You") and John Wiley and Sons ("John Wiley and Sons") consists of your license details and the terms and conditions provided by John Wiley and Sons and Copyright Clearance Center.

License Number	4001920965439
License date	Dec 04, 2016
Licensed Content Publisher	John Wiley and Sons
Licensed Content Publication	Angewandte Chemie International Edition
Licensed Content Title	Doping of Organic Semiconductors: Impact of Dopant Strength and Electronic Coupling
Licensed Content Author	Henry Méndez,Georg Heimel,Andreas Opitz,Katrein Sauer,Patrick Barkowski,Martin Oehzelt,Junshi Soeda,Toshihiro Okamoto,Jun Takeya,Jean-Baptiste Arlin,Jean-Yves Balandier,Yves Geerts,Norbert Koch,Ingo Salzmann
Licensed Content Date	Jun 19, 2013
Licensed Content Pages	5
Type of use	Dissertation/Thesis
Requestor type	University/Academic
Format	Print and electronic
Portion	Figure/table

JOHN WILEY AND SONS LICENSE
TERMS AND CONDITIONS

Dec 31, 2016

This Agreement between Alexandra Paterson ("You") and John Wiley and Sons ("John Wiley and Sons") consists of your license details and the terms and conditions provided by John Wiley and Sons and Copyright Clearance Center.

License Number	4001461222172
License date	Dec 03, 2016
Licensed Content Publisher	John Wiley and Sons
Licensed Content Publication	Advanced Materials
Licensed Content Title	Solution-Processed Small Molecule-Polymer Blend Organic Thin-Film Transistors with Hole Mobility Greater than 5 cm2/Vs
Licensed Content Author	Jeremy Smith,Weimin Zhang,Rachid Sougrat,Kui Zhao,Ruipeng Li,Dongkyu Cha,Aram Amassian,Martin Heeney,Iain McCulloch,Thomas D. Anthopoulos
Licensed Content Date	Apr 10, 2012
Licensed Content Pages	6
Type of use	Dissertation/Thesis
Requestor type	University/Academic
Format	Print and electronic
Portion	Figure/table

JOHN WILEY AND SONS LICENSE
TERMS AND CONDITIONS

Dec 31, 2016

This Agreement between Alexandra Paterson ("You") and John Wiley and Sons ("John Wiley and Sons") consists of your license details and the terms and conditions provided by John Wiley and Sons and Copyright Clearance Center.

License Number	4001441346788
License date	Dec 03, 2016
Licensed Content Publisher	John Wiley and Sons
Licensed Content Publication	Advanced Materials
Licensed Content Title	Observation of Unusual, Highly Conductive Grain Boundaries in High-Mobility Phase Separated Organic Semiconducting Blend Films Probed by Lateral-Transport Conductive-AFM
Licensed Content Author	Simon Hunter,Thomas D. Anthopoulos
Licensed Content Date	May 24, 2013
Licensed Content Pages	7
Type of use	Dissertation/Thesis
Requestor type	University/Academic

Format	Print and electronic
Portion	Figure/table